E-16-M19
#6

Research in Underwater Explosions

S. Menon
School of Aerospace Engineering
Georgia Institute of Technology
Atlanta, Georgia 30332-0150

Final Report
Under Grant N00014-91-J-1963

Submitted to
Office of Naval Research
Code 1132P
800 N. Quincy Street
Arlington, VA 22217

October 14, 1998

Research in Underwater Explosions

S. Menon
School of Aerospace Engineering
Georgia Institute of Technology
Atlanta, Georgia 30332-0150

1. Introduction

Underwater detonation of explosive material converts the unstable material into a more stable gas void at high temperature and pressure. The high pressure of the remnants of an underwater detonation sets forth an expansion-collapse cycle of the resulting underwater explosion bubble which is repeated several times before the bubble goes through interface instabilities and eventually disintegrates into a cloud of smaller bubbles. The interface instability problem is an interesting and complex subject and has recently been addressed based on experimental and analytical methods by Menon and Lal (1998). Various instability mechanisms at play during the bubble oscillation cycles were addressed and it was shown that the Rayleigh-Taylor instability occurs during the bubble collapse and plays a major role in the eventual collapse of the bubble. The presence of a solid surface in the vicinity of a pulsating bubble manifests itself as an asymmetry in the flow field. A dominant feature in the collapse of a bubble in such a flow is the development of a reentrant water jet. The asymmetry in the flow causes one side of the bubble to accelerate inward more rapidly than the opposite side resulting in a high-speed reentrant jet which pierces the bubble in the direction of its migration and produces an impact pressure much larger than the explosion pressure. This increased pressure on the surface can cause structural damage especially when the explosion energy (and hence the bubble size) is large. Other asymmetries (i.e., gravity or a free surface) can also cause the formation of the reentrant jet. The jets caused by gravity are directed upward and those caused by free surfaces are directed away from them.

This report summarizes the pertinent results obtained under this research program. Most of the details of this effort are given in the Appendices attached to this summary report and therefore, avoided here for brevity. In the following, a brief summary of the experimental and numerical efforts is given.

2. Experimental Studies

A series of experiments were carried out to investigate underwater explosions in shallow water (1 atmosphere ambient pressure) to understand the dynamics of bubble-wall interaction in such flows and to investigate feasibility of targeting and destroying mines buried in beaches. In this configuration (shown in Fig. 1), the free water surface is close enough to the bubble-wall

interaction region to allow it to play a role in modifying the dynamics of the bubble collapse. The free surface provides a constant pressure boundary in close proximity to the wall. It is known that the bubble moves away from the free surface and a reentrant jet is formed which pierces the bubble in the direction of its migration. Since, both the Bjerknes force and the buoyancy force, the two competitive forces acting on a bubble near a free surface, act in the same direction, the presence of the free surface above the bubble collapse region is likely to increase the net impact pressure on the wall. Another issue that was investigated is the behavior of the impact process when the rigid surface is buried below a layer of sand, as would be the case for buried mines. Some interesting results have been obtained and summarized in the papers in the Appendices.

Underwater explosion experiments near a solid boundary were conducted in a wooden tank of dimension 2 m $\times$ 1.5 m $\times$ 1.5 m, coated with fiberglass resin from inside. The tank has windows on three sides for optical imaging. The underwater explosion bubble is generated by centrally igniting a mixture of an explosive gas (either Hydrogen or Carbon Monoxide) and oxygen contained in a hand-blown glass globe over a steel plate of dimension 36.83 cm $\times$ 60.96 cm $\times$ 0.635 cm (shown in Fig. 2). Two different sizes of glass globes were used for present experiments with average radii of 2.54 cm and 3.2 cm. The glass globe has an electric spark ignition system connected to a 3000V DC power supply that ignites the premixed fuel-air stoichiometric mixture contained in the globe. The explosion takes place at a constant volume until the globe bursts. Since the experiments were conducted in a laboratory shallow water setup and using a gaseous explosive mixture, the bubbles are relatively smaller (although much larger than cavitation bubbles) than those observed in deep-sea explosions. Recently, Menon and Lal (1998) addressed the dynamics and instability issues of such a bubble in free field and they showed by means of extensive geometric and dynamic similarity analyses that the explosion bubble thus formed is a reasonable subscale approximation of a deep sea underwater explosion bubble. They have presented detailed scaling parameters, energy partitioning and also various interface instability mechanisms. Repeatability and experimental uncertainty have also been addressed and it has been shown in particular that repeated experiments produced error bands for the explosion pressure, maximum radius and time period of 5.88%, 3.7% and 6.06%, respectively.

The pressure inside the bubble during its oscillation was measured by a KISTLER transducer that is mounted inside the plug. Additionally, eight KISTLER pressure transducers were mounted on the plate as shown in Fig. 2 to obtain a surface distribution of the impact pressure field. These dynamic pressure transducers have low and high frequency response of 0.001 Hz and 50 kHz, respectively, and the resonant frequency of 300 kHz. They are, therefore, well suited for the current experiments as the bubble oscillation frequency (time period of approximately 15 ms) lies well within the above mentioned bounds. Signals from these pressure transducers were digitized using National Instrument's AT-MIO-16X analog-to-digital converter board, and were recorded into a microcomputer. Ten-channel data recording was performed with a sustained sampling rate of 10,000 samples per second per channel.

The distance between the globe and the plate was varied to investigate the effect of solid wall location relative to the explosion. The plate was later covered with sand or clay to simulate explosion over a buried wall. The thickness layer of sand and clay above the instrumented plate was also varied to determine how the porous material above the plate modifies the impact pressure. The water surface was lowered to study shallow water bubble-wall, bubble-sand-wall and bubble-clay-wall interactions. Either direct overhead floodlights or an argon-ion laser sheet which lies in a vertical plane perpendicular to the camera axis illuminated the tank. The optical recording of the bubble motion was performed by a CCD enhanced digital video camera at a speed of 1000 frames per second in order to obtain a full screen image.

Underwater explosion bubbles are created near an exposed or buried rigid boundary by detonating a mixture of oxygen and Carbon Monoxide in glass globes submerged in a water tank. A variable depth of either play sand or general purpose purge clay is used to bury a solid steel plate in order to simulate explosion over a buried rigid boundary. Eight pressure transducers mounted on the plate are used to map the pressure distribution on the plate and instrumented tubes and plugs measure pressure inside and outside the bubbles. A cinematography technique is employed to capture entire interaction process. There exists a critical distance above the plate where the reentrant water jet produces the maximum impact pressure on the plate. The jets formed by the explosions above this distance have to pierce the water layer between the bubble and the plate and hence yield lower impact pressures. The growth of bubbles formed by explosions below the critical distance is inhibited by the presence of the plate and hence their maximum sizes are comparatively restrained. The water jet is very focused and symmetrical about the center of impact. The effect of covering the flat plate with sand or clay is in general, to reduce the impact pressure and to smooth its distribution over the plate. However, when an explosion occurs very close to the sand surface loose sand particles are ejected and displaced as the bubble expands. This reduces the effective sand thickness and as a result, an increased impact pressure is achieved. This recovery of impact pressure increases in shallow water cases due to the free surface effect. Explosions were also carried out above clay surface to view the shape of the crater formed. Results show that double craters (i.e., secondary crater within the primary crater is formed for certain initial locations of the explosive above the surface

3. Numerical Studies

A series of numerical experiments were performed using a 3D finite element code called ALE3D that was obtained from Lawrence Livermore Laboratory. Results of these studies are given in the Appendices attached to this report. Here, we briefly summarize the pertinent results.

3.1 Bubble-Wall Interactions

An unsteady, 3D finite-element compressible code (ALE3D) has been successfully applied to study underwater explosions. Results clearly demonstrate that the ALE3D code can be used for bubble explosions. The basic code has been validated using shallow water explosion data. It has been shown that nearly all the features observed in experiments have been captured in these studies. There is excellent qualitative and reasonable quantitative agreement with the experimental data.

Results show that during collapse of a freely oscillating bubble, the bubble loses spherical symmetry and the bubble interface becomes unstable due to the excitation of Rayleigh-Taylor instability. Stability analysis confirms that this instability can occur and energy partition analysis indicates that there is a reasonable amount of energy missing that could be used to excite this instability. This verifies the earlier experimental demonstration that R-T instability is one of the primary mechanisms in bubble collapse and breakdown. The simulation of the collapse of a bubble near a rigid wall showed that the jet velocity and the impact pressure on the wall are functions of the explosion pressure and the distance of the bubble from the wall. The results indicate that for a given explosion pressure there is an optimal distance of the bubble from the wall for which we obtain maximum impact pressure. This trend and the peak impact pressure are in good agreement with the experimental results. It has been shown that the optimal location is due to two different physical effects as the bubble collapses near the wall. The evolution of the

vortex ring bubble, reported in earlier experimental and numerical studies, is also accurately predicted.

Some limitations of the current ALE3D code have also been identified. However, most of these limitations can be corrected by proper modifications to the code. Current effort is directed towards this goal so that more realistic (i.e., using real explosives) deep and shallow water explosion studies can be carried out. Extension to the code to handle sand surface properties is also being investigated for eventual study of explosions near buried surface.

3.2 Shaped Charge Explosions

The dynamics of bubbles formed during underwater explosions is numerically investigated using an Arbitrary Lagrangian-Eulerian, three-dimensional finite-element code. The collapse of bubbles formed by spherical, cylindrical and shaped charge explosion near a rigid wall has been simulated. It is shown here that the impact signature (the pressure footprint on a rigid surface) is a direct function of the explosive shape and explosion energy distribution. Shape modifications are studied here to understand the correlation between the explosive properties (shape, size and, energy/volume) and the impact process. Analysis of the simulations demonstrate that the final stages of the collapse, including the formation of a vortex ring bubble and a high velocity re-entrant jet, are successfully captured for all the simulated cases. The jet velocity and the impact pressure on the wall are functions of the explosion pressure and the distance from the wall. The results indicate that, for a given explosion energy, there is an optimal distance above (or below) the wall which results in the maximum impact pressure on the wall. For spherical explosions, this trend and the magnitude of the peak impact pressure are in good agreement with the experimental results. Spherical explosions result in the maximum peak impact pressure on the wall when compared to other shaped charges (for the same initial energy density and location) and is due to the highly focused impinging jet formed when the spherical bubble collapse. For other shaped explosions, the peak impact pressure is lower but proper shaping of the initial explosive increases the impact footprint. Simulations indicate that it is possible to correlate the initial explosive shape to the impact pressure and footprint size. These results suggests that by properly shaping the explosive charge it will be possible to increase the impact area, thereby, controlling the effect of explosion bubble collapse near a rigid surface.

3.3 Detonation Cord Explosions

Simulations of underwater detonation cord mesh explosion have been carried out using a three-dimensional arbitrary Lagrangian-Eulerian finite-element code. Earlier, this code was successfully employed to capture both qualitatively and quantitatively the dynamics of underwater explosions near rigid surfaces. In this study, the code was used to study the effect of detonation cord explosions on a stainless steel rod placed vertically within the mesh. This metal rod mimicked the trigger arm of a buried mine. The explosion strength was chosen to be larger than the yield strength of the metal rod. It was shown that when the metal rod is placed directly in the center of the mesh, the explosion bubble collapse causes a very high pressure along the diagonal axes and results in the rod getting squeezed and lengthened. On the other hand, when the rod was placed away from the mesh center, asymmetric forces are generated so that in all cases, fracture of the rod into multiple pieces occurs. These results demonstrate that to ensure repeatable destruction of a buried mine, asymmetric design of detonation cord (by changing energy density and/or geometry) is desired. Further calculations are planned to determine if an optimum design of the detonation mesh exists.

4. Conclusions

This report gives all the recent results obtained under this project. Both numerical and experimental studies were carried out to address the same physical problem. The problem of interest is the dynamics of gas bubble explosions underwater and its subsequent interaction with rigid and porous walls (i.e., rigid wall buried under sand). Of particular emphasis was the investigation of an earlier (previous year) observation that even when the rigid wall is not directly exposed to the explosion, it still feels a strong impact pressure. In terms of direct payoff this should be of considerable interest to NAVY since this maybe a means to target and explode buried mines on beaches without direct human involvement. Our experiments were performed in shallow water configurations so that the effects of both the wall and the free surface (as in natural beachfront) are simulated. Results described in the attached Appendices clearly demonstrate the key results of this study.

Our numerical studies developed the ALE3D code (from Lawrence Livermore Lab) to study these explosions. We have shown that the code is capable of capturing all the necessary features of the bubble-wall interaction and has been validated against the experimental data. This code is different from the codes currently being employed by NSWC (Indian Head) but has the same capabilities (actually more since it can also be used to investigate structural failure and crack propagation).

Publications under this Grant (ordered as in the Appendix)

Menon, S. and Lal, M., "On the Dynamics and Instability of Bubbles formed during Underwater Explosions," *Experimental Thermal and Fluid Science Journal*, Vol. 16, pp. 305-321, 1998.

Menon, S. and Pannala, S., "Dynamics of Underwater Explosion," *International Journal of Multiphase Flows*, 1998 (under revision).

Menon, S. and Lal, S., "Experimental Studies of Underwater Explosions near Exposed and Buried Rigid Surfaces," *J. of Fluids and Structures* (to be submitted), 1998.

Lal, M. and Menon, S. "Dynamics of Interaction of Two Underwater Explosion Bubbles," under preparation, 1998.

Menon, S. "Simulations of Underwater Shaped Charge Explosions near Rigid Surfaces," under preparation, 1998.

Menon, S. and Plachco, L. "Simulations of Underwater Mine Destruction Using Detonation Cord Explosives," under preparation, 1998.

Menon, S. and Pannala, S., "Simulations of Underwater Explosion Bubble Dynamics using an Arbitrary Lagrangian-Eulerian Formulation," Proceedings of the1997 ASME Fluids Engineering Meeting, Vancouver, BC, June 22-26, 1997, FEDSM97-3492.

Pannala, S. and Menon, S., "Numerical Studies of Bubble Collapse and Rebound near a Wall," Proceedings of the1997 ASME Fluids Engineering Meeting, Vancouver, BC, June 22-26, 1997, FEDSM97-3244.

Lal, M. and Menon, S., "Interaction of Two Underwater Explosion Bubbles," Proceedings of the ASME Fluid Engineering Division Summer Meeting, San Diego, FED Vol. 1, pp. 595-600,1996.

ELSEVIER

Experimental Thermal and Fluid Science 16 (1998) 305–321

Experimental Thermal and Fluid Science

On the dynamics and instability of bubbles formed during underwater explosions

Suresh Menon *, Mihir Lal

School of Aerospace Engineering, Georgia Institute of Technology, Atlanta, GA 30332-0150, USA

Received 14 February 1997; received in revised form 8 August 1997; accepted 12 August 1997

Abstract

Dynamics of explosion bubbles formed during underwater detonations are studied experimentally by exploding fuel (hydrogen and/or carbon monoxide)–oxygen mixture in a laboratory water tank. Sub-scale explosions are instrumented to provide detailed histories of bubble shape and pressure. Using geometric and dynamic scaling analyses it has been shown that these sub-scale bubbles are reasonable approximations of bubbles formed during deep sea underwater explosions. The explosion bubble undergoes pulsation and loses energy in each oscillation cycle. The observed energy loss, which cannot be fully explained by acoustic losses, is shown here to be partly due to the excitation of instability at the interface between the gaseous bubble and the surrounding water. Various possible mechanisms for the dissipation of bubble energy are addressed. The analysis of the experimental data gives quantitative evidence (confirmed by recent numerical studies) that the Rayleigh–Taylor instability is excited near the bubble minimum. The dynamics of the bubble oscillation observed in these experiments are in good agreement with experimental data obtained from deep sea explosions

Keywords: Underwater explosion; Bubble dynamics; Bubble instability; Fluid dynamics; Interface instabilities; Explosion bubble; Rayleigh–Taylor instabilities

1. Introduction

The dynamics of pulsating bubbles of hot gases at high temperature and pressures formed during an underwater explosion of solid explosives are still not very well understood. During an underwater explosion, a significant portion of the explosion energy is carried away by the detonation shock wave and is imparted into the surrounding water. The gas bubble left behind rapidly expands due to high internal pressure generated during the explosion. However, due to the high inertia of water, the bubble overexpands and its internal pressure drops below the pressure of the surrounding water. As a result, the bubble, once reaching the maximum radius, collapses and eventually reaches a bubble minimum. The collapse process is then reversed and the bubble expands again when the internal pressure exceeds the water pressure. Depending upon the remnant energy available, the bubble can undergo multiple oscillations that are highly damped and exhibit a nearly cuspoid behavior at the minimum size. The bubble pulsation is not indefinite since the thermodynamic internal energy available for the oscillation continuously decreases during the oscillation process till eventually the bubble loses its coherence and breaks up into a cloud of smaller bubbles that quickly disperse.

Although some sources of the observed energy loss have been identified in the past (for example, the radiation of shock wave and acoustic energy to the surrounding medium, the cooling of the hot bubble, mass loss and compressibility effects that occur near the bubble minimum) the bubble collapse process cannot be fully explained by these mechanisms [1–4]. The deviation of the bubble shape from sphericity [5] and various interface instability mechanisms (for example, the Kelvin–Helmholtz shear instability [6,7], the Rayleigh–Taylor [7,8] and Birkhoff [9,10] instabilities and Landau–Darrieus evaporative instability [11,12]) have all been proposed [13] to account for additional energy loss. However, no clear quantifiable evidence has been obtained so far, and it is still not clear how all these instabilities (if at all) interact and contribute to bubble collapse.

* Corresponding author. Tel.: +1 404 894 9126; fax: +1 404 894 2760; e-mail: menon@falcon.ae.gatech.edu.

0894-1777/98/$19.00
PII: S0894-1777(97)10038-3

Detailed measurements and imaging of pulsating bubbles formed during deep sea explosions are very difficult due to a variety of obvious reasons [14] and, therefore, there is insufficient data available to analyze the bubble collapse process. Controlled experiments, such as the ones described here, can be used to investigate the physical processes that contribute to the bubble instability. Since the experiments were conducted in a laboratory shallow water setup and using a gaseous explosive mixture (with significantly lower energy release), the bubbles are relatively smaller (although much larger than cavitation bubbles) than those observed in deep sea explosions. Therefore, the results have to be justified for their relevance to large scale underwater explosions. Using both geometric and dynamic scaling analyses (e.g., [13]), it is shown that the present experiments reasonably simulate deep sea bubble dynamics. Also, it has been shown earlier [15] that the explosion temperature is quite comparable to deep sea detonation temperature. It will be demonstrated here that although the explosion pressure is much lower when compared to deep sea detonations, the scaling parameters for the subsequent bubble pulsations have a relatively weak dependence on the explosion pressure.

2. Experimental procedure and typical results

Underwater explosion experiments were conducted in a water tank of dimension 2 m × 1.5 m × 1.5 m. The tank, shown in Fig. 1, has windows on three sides for optical imaging. The explosion bubble is generated by centrally igniting a mixture of explosive gases (e.g., Hydrogen and/or Carbon monoxide), oxidizer (Oxygen), and sometimes inert gases (Helium and Argon) in a hand-blown glass globe. The glass globe, which is shown in Fig. 2, weighs about 5–6 g and has an average diameter of 6.34 cm. Thus, the initial explosion source is of the order of the globe diameter. The gaseous explosive mixture is ignited in the glass globe by using an electric spark generated by spark wires placed inside the glass globe and connected to a 3000 volt DC power supply. The explosion takes place as in the constant volume combustion bomb of Flock et al. [16], until the globe breaks. Because of the water inertia, the combustion process is essentially completed at constant volume.

To simulate free-field explosions, the glass globe is supported around 0.65 m below the water free surface by two thin steel wires (of diameter 1 mm) that span the tank width between two windows (Fig. 1) and attached to the walls by means of four suction cups. The method used to support the glass globe allows one to mimic free-field explosions. However, due to buoyancy effects the bubble will (and does) migrate upwards. However, this migration process is noticeable only after the completion of the first oscillation and is similar to that observed in deep sea explosions [1]. Since, as shown below, the bubble interface instability is initiated during the first oscillation, it is assumed that the physics controlling the bubble instability is only weakly affected

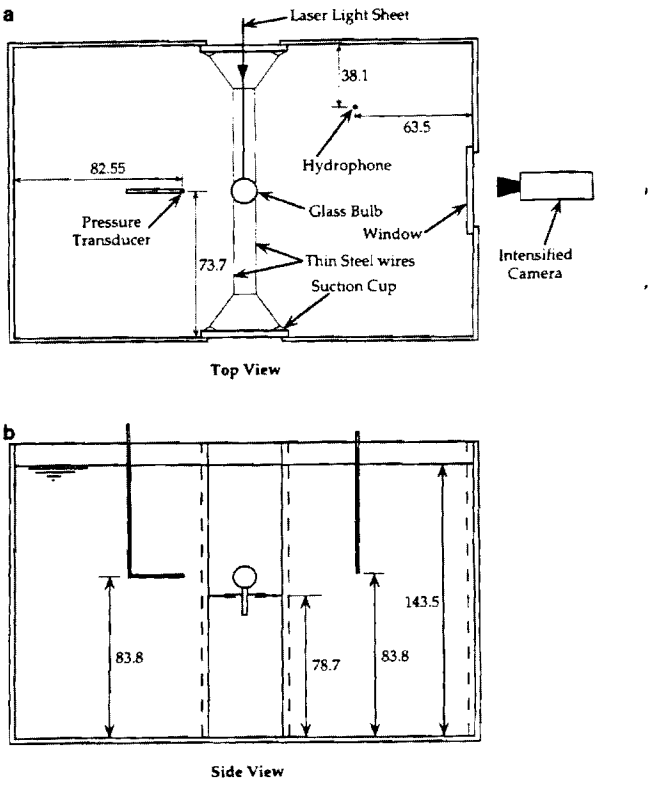

Fig. 1. Schematic of the test facility. (a) Top view; (b) Side view.

by buoyancy. The effect of buoyancy may become important during the later stages of the bubble oscillation. As the bubble begins to migrate upwards, some of the bubble energy could be lost to the vertical motion of the water and to the initiation of shear induced instabil-

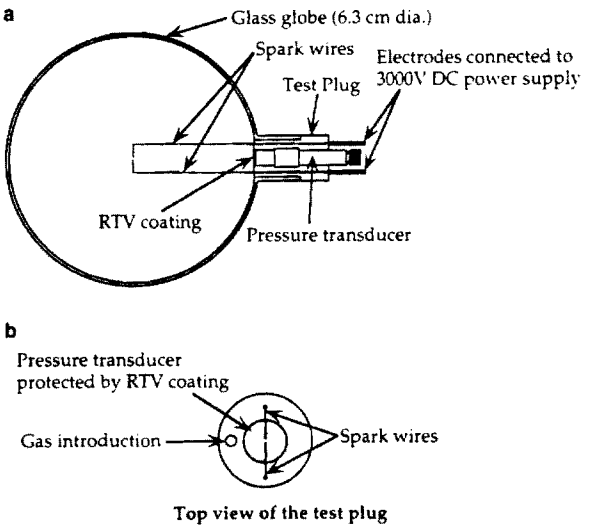

Fig. 2. Schematic of the glass bulb used for the explosions: (a) View of the glass bulb and the pressure transducer; (b) Top view of the bulb.

ities (i.e., Kelvin–Helmholtz) which could contribute to the eventual collapse of the bubble. These issues are discussed further in Section 4.

The pressure response (due to the propagation of acoustic waves) in the water surrounding the bubble is recorded during these experiments. To record the acoustic wave reflections from the walls, a hydrophone (Bruel & Kjaer Model No. 8103), with a frequency range of 0.1 Hz–180 kHz and a working pressure of up to 4×10^6 Pa, is installed in the tank close to the wall. This hydrophone is used primarily as an event marker and to record the strength of the wall-reflected acoustic waves. The pressure data in the surrounding water ahead of the oscillating bubble is obtained by using KISTLER dynamic piezoelectric pressure transducers as shown in Fig. 1. These transducers are fitted at the end of stainless steel (0.5 in. diameter) tubes which are bent at right angles so that the transducer faces towards the bulb. The range of these transducers is 0–35 bar which is sufficient for the present sub-scale experiments. These transducers have low frequency response of 0.001 Hz, high frequency response of 50 kHz and have the resonant frequency of 300 kHz. The bubble oscillation time period in the present experiments is nominally about 15 ms which yields a frequency lying well within the frequency bounds of the transducers. Analysis of the pressure signals from the transducers located at different positions (as shown in Fig. 1) showed that the pressure response ahead of the bubble is nearly independent of the location of the transducer and, therefore, most of the data presented here are from a single (the same) transducer.

To measure the pressure inside the bubble, the glass globe is equipped with another KISTLER dynamic pressure transducer (range 0–35 bar) coated slightly with RTV cement to protect it against the thermal loads generated upon ignition (see Fig. 2). The signals from the pressure transducers and the hydrophone are recorded using a PRESTON analog-to-digital converter and a HP 1000 A-700 computer at a sampling rate of 20,000 samples/s, per channel giving a temporal resolution of 50 μs. Data are continuously recorded until the bubble completely disintegrates.

To investigate the bubble instability process, direct imaging of the bubble during its pulsation is carried out using a high speed, CCD enhanced video camera (Kodak Ektapro EM Motion Analyzer Model No. 1012). To obtain the optical record, the tank is illuminated by either direct flood lights or an argon-ion laser sheet. Although the camera is capable of recording at a speed of 10,000 frames/s, images were obtained at 6000 and 4000 frames/s so that the full bubble can be viewed during its oscillation. Most of the images analyzed and reported in this study were obtained at 4000 frames/s. At this speed, the typical image size was 239×48 pixels and all the images were recorded in a video recorder using two speeds (30 frames/s and 5 frames/s) for image analysis.

Table 1 summarizes the various types of explosive mixtures studied in the present experiments. A variation in the fuel–air mixture changes not only the molecular weight (M) and the combustion product but also changes the explosion pressure (P_0), the peak pressure at bubble minimum (P_1) and γ (the ratio of specific heats), which depends on both the combustion product and explosion temperature. Since both carbon monoxide and hydrogen have similar heat release on molar basis (284 kJ/mol for CO and 242 kJ/mol for H_2), the explosion temperature is nearly the same for different stoichiometric fuel–oxygen mixtures considered here. When an inert gas is mixed with the fuel–oxygen mixture, some of the explosion energy is used to raise the temperature of the inert gas to the explosion temperature. This results in a reduction of the peak temperature achieved during the explosion. However, as shown by Strahle and Liou [15], when the inert gas was added to change the molecular weight (i.e., from 12.98 to 36.33), only a slight variation in explosion temperature (a variation between 3038 and 3372 K) occurred. Therefore, the temperatures achieved in all these experiments are considered comparable (and also comparable to deep sea explosion temperature of 2900 K [5]). Furthermore, since the specific heats of combustion products (water vapor and CO_2) have only a weak dependence on temperature [17], γ does not change appreciably in the temperature range of interest. Therefore, all values of γ in Table 1 have been computed at a reference temperature of 3200 K, which suffices for the purpose of qualitative study of the bubble dynamics for different gas mixtures. Values of P_0, P_1 and P_1/P_0 listed in Table 1 are those measured experimentally in this study and ϕ denotes equivalence ratio of the fuel–oxygen mixture, which is defined as $\phi = (F/O)/(F/O)_{\text{stoichiometric}}$. Here, (F/O) indicates fuel to oxygen ratio, and, $\phi = 1$ indicates a stoichiometric mixture, $\phi < 1$ a fuel-lean mixture and $\phi > 1$ a fuel-rich mixture.

Analysis of the results summarized in Table 1 shows that the explosion and the first minimum pressures depend on the equivalence ratio of gas mixture. Stoichiometric mixtures without any inert gas produce the strongest explosion pressure P_0 and, also, have the largest peak pressure at the first bubble minimum P_1. The pressure P_1 is of the same order (in some cases larger) than the explosion pressure for these cases. Increasing the inert gas content or decreasing the equivalence ratio weakens the explosion and, hence, decreases the corresponding bubble pressure. Although all these cases were analyzed, only representative results are shown in this paper.

Fig. 3(a) shows the pressure trace recorded by the test plug transducer for two typical explosions. The signal shows the signature of the explosion (the first maximum in the pressure), followed by the second pressure maximum corresponding to the first bubble minimum that occurs approximately 15 ms after the first peak. The subsequent peaks approximately represent the pressure maxima achieved during the second and third bubble pulsations, respectively. These peaks are much lower suggesting a significant energy loss near the first bubble minimum. This loss mechanism is addressed in detail in

Table 1
Bubble explosion test conditions

Group	No.	Gas mixture composition	M	ϕ	P_0 (kPa)	P_1/P_0	γ
1st	1	CO(67%) + O_2(33%)	29.34	1	848.1	1.0791	1.1535
	2	CO(60%) + O_2(30%) + He(10%)	26.81	1	1020.4	0.8894	1.1663
	3	CO(50%) + O_2(25%) + He(25%)	23.00	1	1199.7	0.7564	1.1901
	4	CO(40%) + O_2(20%) + He(40%)	19.20	1	985.9	0.8494	1.2218
	5	CO(37.5%) + O_2(18.75%) + He(43.75%)	18.25	1	748.8	1.0944	1.2315
2nd	6	CO(25%) + O_2(75%)	31.00	0.167	887.2	1.0333	1.2071
	7	CO(25%) + O_2(50%) + Ar(25%)	32.99	0.25	1006.6	0.9658	1.2353
	8	CO(25%) + O_2(50%) + He(25%)	24.00	0.25	891.0	0.9745	1.2353
	9	CO(33%) + O_2(67%)	30.67	0.25	894.0	1.0066	1.1936
	10	CO(25%) + O_2(25%) + Ar(50%)	34.98	0.5	1268.6	0.9568	1.2725
	11	CO(25%) + O_2(25%) + Ar(25%) + He(25%)	25.99	0.5	936.9	0.9614	1.2725
	12	CO(25%) + O_2(25%) + He(50%)	17.00	0.5	900.7	0.9771	1.2725
	13	CO(33%) + O_2(33%) + Ar(33%)	33.32	0.5	978.6	0.9763	1.2276
	14	CO(33%) + O_2(33%) + He(33%)	21.34	0.5	950.8	0.9885	1.2276
	15	CO(50%) + O_2(50%)	30.00	0.5	1020.2	1.0491	1.1713
	16	CO(75%) + O_2(25%)	29.00	1.5	1162.5	0.9902	1.1737
3rd	17	CO(20%) + H_2(20%) + O_2(20%) + Ar(40%)	28.38	1	1137.6	0.9861	1.2331
	18	CO(20%) + H_2(20%) + O_2(20%) + Ar(20%) + He(20%)	21.19	1	1054.9	0.9812	1.2331
	19	CO(20%) + H_2(20%) + O_2(20%) + He(40%)	14.00	1	985.9	1.0226	1.2331
	20	CO(25%) + H_2(25%) + O_2(25%) + Ar(25%)	25.49	1	1213.5	1.0831	1.2005
	21	CO(25%) + H_2(25%) + O_2(25%) + He(25%)	16.51	1	1185.9	1.1058	1.2005
	22	CO(30%) + H_2(30%) + O_2(30%) + Ar(10%)	22.60	1	1220.4	1.0296	1.1759
	23	CO(30%) + H_2(30%) + O_2(30%) + He(10%)	19.01	1	985.9	1.1775	1.1759
	24	CO(33%) + H_2(33%) + O_2(33%)	20.68	1	1123.8	1.0266	1.1626
4th	25	H_2(40%) + O_2(20%) + Ar(40%)	23.19	1	1181.8	1.0007	1.2456
	26	H_2(60%) + O_2(30%) + Ar(10%)	14.80	1	994.1	0.9288	1.1867
	27	H_2(67%) + O_2(33%)	12.01	1	1034.2	0.8902	1.1729
	28	H_2(60%) + O_2(30%) + He(10%)	11.21	1	934.4	0.9822	1.1867

this paper. Fig. 3(b) and (c) show, respectively, the pressure signatures recorded by the transducer in the water outside the bubble and by the hydrophone near the tank wall. The higher frequency signals observed in Fig. 3(b) and (c) are indicative of the acoustic reflections from the walls of the tank. Since the frequency of this pressure fluctuation is higher and the amplitude significantly lower (by at least an order of magnitude when compared to the explosion pressure and the pressure at the first bubble minimum), it is expected that the acoustic reflections from the walls do not significantly contaminate the bubble instability process.

This issue was recently addressed using a full three-dimensional, numerical simulation of the experimental configuration [18]. Very similar high frequency pressure fluctuations at comparable amplitudes were observed in the calculations. The possibility of acoustic interference or excitation of interface instability (discussed below) was also investigated by moving the walls further out and by replacing the rectangular tank walls with a shell. Computed results showed excellent agreement with the experimental data for the bubble pressure, and analysis of the results showed that, although there are some subtle effects of acoustic reflection from the laboratory tank walls (such as a slight decrease in the first oscillation period), the overall dynamics of the bubble oscillation was qualitatively and quantitatively very similar. It was, therefore, concluded that acoustic reflections from the walls are not causing any significant modifications of the bubble oscillation.

Fig. 4 shows the typical variation of the bubble radius (nondimensionalized by the initial bubble size, R_0 which is assumed in the present experiments to be the glass globe size since the explosion is completed before the bubble begins to expand) as a function of time (nondimensionalized by a time scale $\tau_s = R_0/\sqrt{(P_0/\rho_l)}$, where, P_0 is the explosion pressure and ρ_l is the density of water) for two typical explosions using stoichiometric mixtures of H_2–O_2 and CO–O_2. Consistent with the pressure signature seen in Fig. 3, Fig. 4 clearly shows how quickly the bubble weakens regardless of the fuel–oxygen mixture used. The magnitude of the maximum bubble radius, the pressure maximum at the first bubble minimum and the period of oscillation vary with the changes in the explosive mixture. However, the qualitative behavior of the rapid energy loss is quite similar and, therefore, Fig. 4 is representative of all the cases studied here.

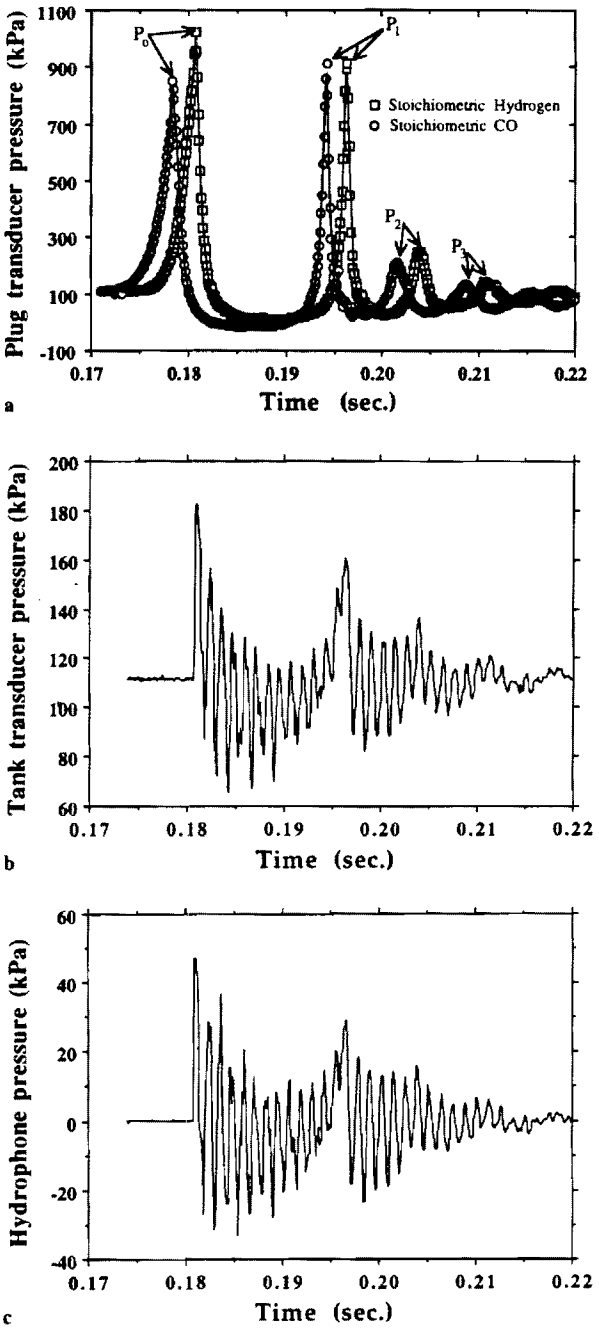

Fig. 3. Pressure signature recorded by the transducer in the test plug, water and hydrophone: (a) Pressure signature from the test plug transducer. Traces are shown for stoichiometric H_2–O_2 and CO–O_2 mixtures. Both mixtures show the explosion pressure peak (P_0) and the subsequent pressure maxima at the bubble minima. Notice that the pressure peak at the first bubble minimum (P_1) is much larger than the subsequent peaks suggesting that a rapid energy loss is occurring; (b) Pressure signature recorded by the transducer in the water; (c) Pressure signature recorded by the hydrophone near the tank wall.

The maximum bubble radius achieved during the second pulsation is significantly lower than the maximum reached during the first pulsation for all fuel mixtures.

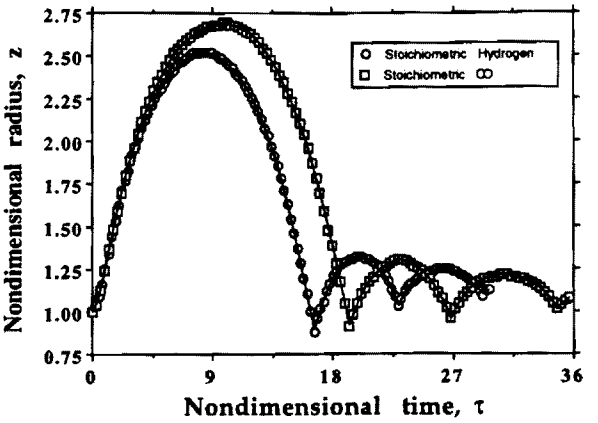

Fig. 4. Typical variation of the bubble radius determined from the bubble image data (shown in terms of the nondimensionalized radius $z = R/R_0$) as a function of time (in terms of the nondimensionalized time $\tau = t/\tau_s$) for stoichiometric mixtures of H_2–O_2 and CO–O_2.

As shown in Fig. 4, for both H_2–O_2 and CO–O_2 stoichiometric mixtures, the second bubble maximum is roughly 0.26 of the maximum achieved during the first oscillation (correcting for the initial bubble size which is unity in the non-dimensional coordinate used in Fig. 4). The decrease in the bubble maximum relative to the second bubble maximum is not that significant for the third pulsation. This suggests that most of the energy loss occurs either prior to or during the second bubble pulsation. The time period for pulsation also decreases with the second pulsation requiring around 33% of the time required to complete the first oscillation. The bubble radius variation observed in the present experiments is remarkably similar to that of deep sea explosions. For example, data from an explosion of 250 g of tetryl at a depth of 91 m [5] showed that the bubble radius maximum reached during the second pulsation was around 0.56 of maximum achieved during the first pulsation, and the time period for the second pulsation was 79% of the time required to complete the first pulsation. Data from TNT explosions [14] at greater depths (e.g., 152 m) also suggested a similar (0.61) reduction of second bubble maximum when compared to the first maximum. However, the deep sea data suggests that the losses are not as severe as observed in the laboratory. There could be many reasons for this discrepancy. For example, in the laboratory setup, the bulb holder (which contains the spark igniter and the pressure transducer) could be playing a role in damping the bubble oscillation, resulting in the observed reduction in the second bubble oscillation. In addition, much larger energy release occurs during TNT and pentolite explosions [1,3,4] which could result in relatively large amounts of energy left after the first oscillation. In general, however, this (qualitative) comparison suggests that the rapid decrease in the bubble size during multiple pulsations captured in the current experiments is reasonably similar to that observed in deep sea explosions.

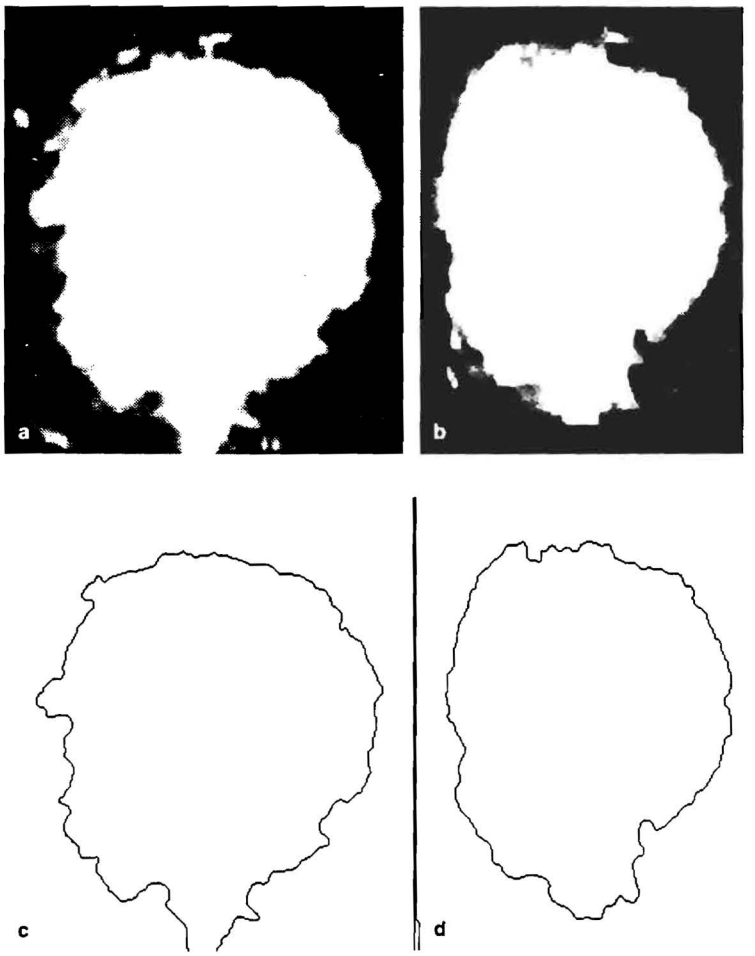

Fig. 5. Typical bubble images near the first bubble minimum. The video images have been purposely blurred to enhance the bubble shape. (a) and (b) are 0.25 msec apart near the first bubble minimum for the H_2–O_2 explosion; (c) and (d) are bubble shapes extracted from the video images shown in (a) and (b), respectively.

To investigate bubble instability, the bubble images were analyzed. Typical bubble images near bubble minimum extracted from the video are shown in Fig. 5 for the stoichiometric H_2–O_2 explosion (as a typical example). To analyze these images, the video frames were digitized and the bubble interface was extracted by enhancing the contrast. To enhance the bubble edge, these images were purposely blurred. Then, the contour of the bubble was traced using a commercially available image processing software and converted into a binary data file. The digitized images (corresponding to Fig. 5(a) and (b)) are shown in Fig. 5(c) and (d), respectively. The bubble contours shown in Fig. 5(c) and (d) clearly suggest that the bubble interface is corrugated and that both small and large wavelength corrugations exist along the bubble interface.

There are various possibilities for the observed interface corrugation. One possibility is that the glass fragments (formed from the bulb during the initial explosion) are causing the observed corrugation. To determine this, a series of experiments were carried out by coating the glass with black paint and then visualizing the explosion using back lighting. Under this condition, the glass fragments became clearly identified. Fig. 6(a) and (b) show, respectively, typical images near the first bubble maximum and minimum. It appears that in all the experiments, the glass fragments are typically long thin fragments (approximately 2–3 mm in width and 20 mm in length) that move outwards with the bubble during the expansion phase. Thus, it is feasible that the corrugation seen on the interface near the bubble maximum is due to the presence of the glass fragments. However, it appears that the bubble collapse is much faster than the inward motion of the fragments and the glass fragments are lagging behind. Thus, it is likely that the large wavelength interface corrugations seen near the first bubble minimum are not directly due to the presence of the glass fragments in the surrounding water.

Another possibility for the interface corrugation near the bubble minimum is the excitation of interface instabilities. There are various forms of possible instabilities and these are discussed in more detail in Section 4. To

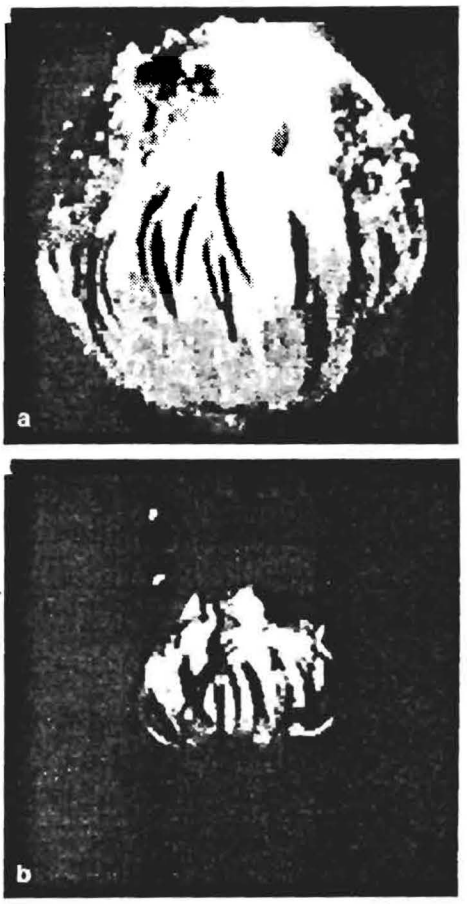

Fig. 6. Typical bubble images near (a) the first bubble maximum and (b) the first bubble minimum. These figures clearly show long and thin glass fragments.

determine the structure of the bubble interface it is necessary to determine the deviation of the bubble diameter from its initial spherical shape. To obtain the bubble diameter, the x and y coordinates along the bubble contour are determined by differentiating the white pixels from the black ones, then the bubble diameters at azimuthal positions spaced equally at one degree along the circumference are determined. Thus, for each bubble image, 360 bubble radii are computed. The reference bubble radius (reported in Fig. 4) is then determined by averaging all these radii. Since this method of computing bubble radii is based on counting an integral number of pixels, the maximum error incurred in measuring the bubble radius at any azimuth is limited to 3.5%. Obviously, this error is the lowest at bubble maximum. To identify the most unstable wavelength(s) of the interface corrugation, the radius data at each azimuthal location is normalized by the average radius, and Fast Fourier Transform (FFT) of these normalized bubble radius data is carried out to obtain the power spectral density of the corrugated interfacial waveform. The results of this analysis are discussed in more detail in Sections 4 and 5.

2.1. Experimental uncertainties

In order to determine the experimental uncertainities, several experiments were conducted under same experimental conditions for stoichiometric $CO–O_2$ explosion mixture and, initial radius, R_0, explosion pressure, P_0, maximum bubble radius, R_{max}, and time period of oscillation, T, were measured. Then, the quantities $P_0/(4\pi R_0^3/3)$, R_{max}/R_0 and T/τ_s were tabulated and their maximum, minimum and mean values were used to find error bands. The error bands for the three quantities mentioned above were found to be 5.88%, 3.7% and 6.06%, respectively.

3. Scaling analysis

In the present experiments, the explosion pressure is of the order of only 10 bar, while in a deep sea explosion it is of the order of 100 kbar [5,14]. In view of this discrepancy, the applicability of the present data for deep sea explosions must be examined. In this section, it will be shown that nearly all the geometric and the dynamic parameters required to ensure proper scaling are preserved between the current sub-scale experiments and deep sea explosion.

The noncompressive radial motion is the simplest approximation to the true motion of the gas bubble, where it is assumed that the motion of the surrounding water is entirely radial and there are no migration and buoyancy effects. This motion is expressed mathematically [5] as:

$$r\frac{d^2r}{dt^2}+\frac{3}{2}\left(\frac{dr}{dt}\right)^2=\frac{P_r-P_l}{\rho_l}. \tag{1}$$

where r is the instantaneous bubble radius, P_r is the pressure inside the bubble (assumed uniform throughout the bubble), P_l is the pressure in the water at the explosion depth, and ρ_l is the density of water. Eq. (1) has been extensively studied, for example, by Herring [19] and later by Trilling [20] who included acoustic energy losses and modified Eq. (1) for bubble motion with spherical symmetry to obtain the following equation (often called the Trilling–Herring equation):

$$\left(1-2C\frac{dz}{d\tau}\right)\frac{d^2z}{d\tau^2}+\frac{3}{2z}\left(1-\frac{4}{3}C\frac{dz}{d\tau}\right)\left(\frac{dz}{d\tau}\right)^2 = \frac{P^*-\tilde{P}}{z}+C\frac{dP^*}{d\tau}. \tag{2}$$

Here z is the normalized bubble radius ($z=r/R_0$) and C is the acoustic loss factor. The quantities P^*, $\tilde{P}$ and C are respectively, P_r/P_0, P_l/P_0 and $\sqrt{P_0/\rho_l}/c_l$, where, c_l is the speed of sound in water. Eqs. (1) and (2) have been investigated extensively in the past [13]. Various other forms of this equation have also been studied, for example, the Rayleigh–Plesset equation that has been extended to include surface tension effects, compressibility of the liquid and mass transfer at the interface [21–24]. In

the present study, we will limit ourselves to the forms given in Eqs. (1) and (2) since the focus of this study is not on the numerical investigation of the bubble instability problem.

The Herring–Trilling equation, Eq. (2), can be solved to obtain the temporal variation of the bubble radius. However, it is clear from the image data (Figs. 5 and 6) that the one-dimensional assumption is clearly violated (due to the loss of sphericity) as the bubble collapses and nears the bubble minimum. Therefore, it is likely that the solution of the one-dimensional model (even with various factors such as mass transfer, compressibility, etc. included) will not agree with the experimental data especially near the first bubble minimum and for subsequent pulsations. This can be demonstrated by solving Eq. (2) numerically, starting with $z = 1$ and $dz/d\tau = 0$ and $\tau = 0$ using a perfect gas law for adiabatic expansion, i.e., $P^* = z^{-3\gamma}$.

The comparison of the computed variation of bubble radius with time is shown in Fig. 7 for both H_2–O_2 and CO–O_2 stoichiometric mixtures. Only the first pulsation is shown here since the numerical model (2) includes only acoustic losses and does not agree with the experimentally observed rapid decay in bubble radius with subsequent pulsations. Clearly, there is very good agreement between the measured and numerically predicted bubble radius for the first expansion phase. A similar observation has been made earlier [15]. As the bubble collapses and approaches the bubble minimum, the computed radius begins to deviate from the experimental data. Especially near the bubble minimum, the computed radius is larger than the experimentally observed value suggesting that additional losses are occurring in the experiments as discussed in Section 3.2.

The first two terms in Eq. (2) represent the change rate of the water kinetic energy, and the two terms on the right-hand-side are related to the mechanical work rate of the gas bubble on the water and the energy loss due to acoustic radiation, respectively. Eq. (1), when integrated with respect to time (using appropriate initial conditions) yields

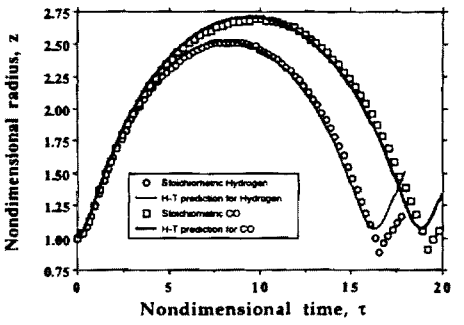

Fig. 7. Comparison of the numerical prediction using the Herring–Trilling (H–T) one-dimensional equation and the experimental data for the H_2–O_2 and the CO–O_2 explosion cases. Symbols show the current experimental data and the solid curves show the H–T numerical prediction.

$$\frac{3}{2}\left(\frac{4\pi}{3}\rho_l r^3\right)\left(\frac{dr}{dt}\right)^2 + \frac{4\pi}{3}P_l r^3 + E(r) = Y, \tag{3}$$

where $E(r)$ is the internal energy and is defined later in Eq. (5). Y is a constant of integration and represents the total energy associated with the radial flow of water. The internal energy is relatively unimportant over much of the expansion. Therefore, setting $dr/dt = 0$ in Eq. (3) gives an estimate for the energy Y in terms of R_{max} at sufficiently expanded stage of the motion [5, pp. 274–275]:

$$Y = \frac{4\pi}{3}P_l R_{max}^3. \tag{4}$$

As shown below, Y is related to the bubble oscillation period and modified forms of Y are used in Section 3.2 to study the energy partitioning issues.

3.1. Geometric and dynamic similarity analysis

The above expressions can be used to estimate parameters necessary to carry out scaling analysis of the present data. For solid explosives, such as TNT [5, p. 274], there is a very weak dependence of Y on P_r; namely, $Y \approx 6E(r)/(P_r)^{1/5}$. Furthermore, since

$$E(r) = \frac{P_r V(r)}{\gamma - 1} = \frac{4\pi P_r r^3}{3(\gamma - 1)}, \tag{5}$$

$E(r)$ and Y can be eliminated from Eqs. (4) and (5) to yield an expression for R_{max}/r:

$$\left(\frac{R_{max}}{r}\right)^3 = \frac{6P_r^{4/5}}{(\gamma - 1)P_l}. \tag{6}$$

Since, $P_r \approx nP_0$ [where $n = O(1)$] when $r = R_{min}$, it can be seen that R_{max}/R_{min} has an extremely weak dependence on P_0, i.e., $R_{max}/R_{min} \propto (P_0)^{4/15}$. Comparing the explosion pressures of gas explosion (approximately 10 bar) and deep sea explosion (approximately 100 kbar), it would seem that the bubble amplitude ratio, R_{max}/R_{min} for gas explosion would still be roughly 12 times smaller than that for deep sea explosion. However, since $P_l \propto (d + 10.33)$, where d is the explosion depth in meters (e.g., 91 m [5]), and since, in the present study, the ambient pressure, P_l is much lower than that for a deep sea explosion, the bubble amplitude ratio for shallow water tests becomes comparable to that for deep sea explosions. The period of bubble oscillation, T, can be shown to be proportional to $Y^{1/3}$ and inversely proportional to $(P_l)^{5/6}$ and, therefore, using Eq. (6) can be expressed as $T \propto \sqrt{\rho_l/P_l}R_{max}$.

To be useful for practical scaling studies, the bubble motion should preserve both geometric and dynamic similarities [13]. Geometric similarity implies invariance of R_{max}/d and R_{max}/R_{min} and dynamic similarity essentially implies invariance of the Froude number, $Fr = U^2/gL$, which in turn implies an invariance of T^2/R_{max}. Estimates for these parameters for the first bubble oscillation are given below for both the present experiments and the past deep sea studies.

For the present experiments of gas explosion, $R_{max} \approx 3R_0$, $R_{min} \approx R_0$, $R_0 \approx 3.15$cm, $T \approx 0.015$s, and

$d = 0.6477$ m. This gives $R_{max}/(d + 10.33) \approx 8.607 \times 10^{-3}$, $R_{max}/R_{min} \approx 3$, and $T^2/R_{max} \approx 2.381 \times 10^{-5}$ s^2/cm. In a deep sea explosion of 249.5 grams of tetryl charge fired at a depth of 91.44 m below the water surface [5, p. 271], $R_{max} = 45.11$ cm, $R_{min} \approx 12.7$ cm, $R_0 = 3.5$ cm, $T \approx 0.028$ s, and $d = 91.44$ m. This gives $R_{max}/(d + 10.33) \approx 4.432 \times 10^{-3}$, $R_{max}/R_{min} \approx 3.55$, and $T^2/R_{max} \approx 1.738 \times 10^{-5}$ s^2/cm. Data from TNT explosions at a depth of 152 m [14] suggests similar results: $R_{max}/(d + 10.33) \approx 2.55 \times 10^{-3}$, $R_{max}/R_{min} = 2.255$, and $T^2/R_{max} \approx 1.596 \times 10^{-5}$ s^2/cm. Scaling analysis of the amplitude of the bubble oscillation can also be carried out by defining an equilibrium radius R_e which is defined as the radius of the bubble when the pressure inside it equals the hydrostatic pressure at the explosion depth [3]. The present results suggest that $R_{max_1}/R_e = 1.6212$ and $R_{max_2}/R_e = 0.853$, whereas the experimental data [5] suggest: $R_{max_1}/R_e = 1.48$ and $R_{max_2}/R_e = 1.03$. Here, the subscripts 1 and 2 denote, respectively, the first and second bubble maxima. These comparisons clearly suggest that the present experiments preserve reasonably close geometric and dynamic similarities for all the parameters expect for R_{max}/d.

3.2. Energy partition

As noted earlier, the explosion energy can be redistributed among the various modes (e.g., shock wave energy, potential, kinetic and dissipated energies, etc.) initiated by the explosion. Previous studies [3,4,14] have attempted to use the experimentally obtained data from deep sea studies to evaluate how the total energy from explosion is partitioned between these modes. In the present study, particular interest lies in determining how much of the energy is available for exciting the bubble instability (to be discussed in Section 4). Vokurka [4] suggested that the energy balance for an expanding system (i.e., as the shock wave propagates outwards and the bubble begins to expand after the explosion) can be written as:

$$\Delta E_{ie} = \Delta E_{pe} + \Delta E_{de} + E_k. \tag{7}$$

where ΔE_{pe} and ΔE_{ie} are, respectively, the change in potential and internal energy of the gas bubble (from its initial state at time $t = 0$), ΔE_{de} is the energy dissipated and E_k is the liquid kinetic energy. Estimates for each of these terms can be obtained from the experimental data. The total (nondimensional) energy available for the explosion is determined from the relation $\overline{E}_0 = QW/E_0$, where Q is the detonation energy per kg of explosive, W is the weight in kg of the explosive and $E_0 = 4\pi R_0^3 p_l/3$ is the energy of the initial gas volume. For a stoichiometric hydrogen–oxygen mixture, $Q = 242$ kJ/mol of hydrogen and using representative values for the current experiments, one obtains: $\overline{E}_0 = 66.8735$. This is total amount of explosion energy which is to be distributed into various modes defined in Eq. (7) as the bubble expands. The change in internal energy (nondimensionalized using E_0) as the bubble expands and reaches bubble maximum can be written as [4]:

$$\Delta\overline{E}^e_{ie_1} = \overline{E}_{ie_0} - \overline{E}_{ie} = \left(\frac{P_0}{P_l}\right)\left[1 - \left(\frac{r}{R_0}\right)^{-3(\gamma-1)}\right]/(\gamma - 1), \tag{8}$$

where the subscript 1 indicates the first bubble oscillation and the superscript e indicates that the energy estimates is obtained during the expansion phase. The change in the potential energy (again nondimensionalized by E_0) is:

$$\Delta\overline{E}^e_{pe_1} = \left[\left(\frac{r}{R_0}\right)^3 - 1\right]. \tag{9}$$

Here, $r(> R_0)$ is the instantaneous bubble radius as the bubble expands from its initial diameter R_0 to its first maximum bubble radius R_{max_1}. Further, if one assumes that $E_k \approx 0$ near the first bubble maximum [4], an estimate for the energy dissipated can be obtained as: $\overline{E}^e_{de_1} = \Delta\overline{E}^e_{ie_1} - \Delta\overline{E}^e_{pe_1}$. Estimates for all these quantities are given in Table 2. As can be seen from Table 2, approximately 26% of the energy is dissipated as the bubble expands and reaches its first maximum. Previous studies [1,3] suggest that this dissipated energy is entirely carried away by the shock wave and the remaining energy (74%) at the first bubble maximum is the total energy available for the bubble collapse and subsequent oscilla-

Table 2
Energy partition of a typical stoichiometric H_2–O_2 explosion case

r	$\overline{E}$	Energy partition	Total energy available for next pulsation (% of $\overline{E}_0$)	Total energy lost (% of $\overline{E}_0$)
$r = R_0$	$\overline{E}_0$	66.8735	66.8735 (100%)	0 (0%)
$r = R_{max,1}$	$\overline{E}^e_{ie_1}$	34.4235	49.3259 – (73.76%)	17.5476 – (26.24%)
	$\Delta\overline{E}^e_{pe_1}$	14.9024		
$r = R_{min,1}$	$\overline{E}^e_{ie_1}$	39.4041	39.0911 – (58.46%)	27.7824 – (41.54%)
	$\Delta\overline{E}^e_{pe_1}$	−0.3130		
$r = R_{max,2}$	$\overline{E}^e_{ie_2}$	37.1503	38.4688 – (57.52%)	28.4047 – (42.48%)
	$\Delta\overline{E}^e_{pe_1}$	1.3185		

tions. The current estimate of 26% for the dissipated energy (which may or may not be totally associated with the shock wave) is lower than the value computed by Vokurka [4] who estimated for a TNT explosion [14] that approximately 50% of the total energy was dissipated as the bubble reached the first maximum. However, note that E_0 (and hence, P_0 and R_{max_1}) was much larger for the deep sea TNT explosion and, as a result, the difference between Eqs. (8) and (9) will be substantially larger than for the present case.

A similar analysis can be carried out for the contraction phase (i.e., as the bubble collapses from the first bubble maximum and reaches its first minimum) and then for the second expansion phase as the bubble rebounds to its second maximum. For the contraction phase, the energy balance can be written as in Eq. (7) except that now, the energy available for the various modes is limited to the amount left after 26% of the explosion energy has been dissipated. The energy balance at this stage is quite crucial since the observed large decrease in the second bubble maximum suggests that a significant amount of energy is dissipated either during the first bubble contraction or during the second bubble expansion. An estimate of the energy dissipated can be inferred by estimating the changes in the internal and potential energy as the bubble reaches, respectively, the first minimum and the second maximum by assuming that at both the first minimum and the second maximum, $E_k \approx 0$. For example, during the contraction phase, the change in potential energy can be written as [4]:

$$\Delta\bar{E}^{c}_{pe_1} = \left(\frac{R_{max_1}}{R_0}\right)^3\left[1-\left(\frac{r}{R_{max_1}}\right)^3\right], \tag{10}$$

where, $r(< R_{max_1})$ is the instantaneous bubble radius as the bubble contracts from the first maximum bubble radius R_{max_1} and reaches its first minimum. The superscript c indicates the contraction phase. The change in internal energy can also be expressed in terms of the bubble properties as

$$\Delta\bar{E}^{c}_{ie_1} = \left(\frac{1}{\gamma-1}\right)\left(\frac{P_{max_1}}{P_l}\right)\left(\frac{R_{max_1}}{R_0}\right)^3\left[\left(\frac{r}{R_{max_1}}\right)^{-3(\gamma-1)}-1\right]. \tag{11}$$

Using $\gamma = 1.173$ and the experimentally measured pressure at the first bubble maximum, $P_{max_1} = 8.0826$ kPa, in Eqs. (10) and (11) one can obtain $\Delta\bar{E}^{c}_{ie_1}$ and $\Delta\bar{E}^{c}_{pe_1}$ at the first bubble minimum i.e., when $r = R_{min_1}$. Table 2 gives estimates for these energies at the first bubble minimum as well as the amount of energy dissipated, $\Delta\bar{E}^{c}_{de_1}$ during the first contraction of the bubble and the internal energy of the bubble at the first minimum, $\bar{E}^{c}_{ie_1}$. To obtain the energy partition at the second bubble maximum, the energy left after $\Delta\bar{E}^{c}_{de_1}$ is first subtracted from the available energy and then partitioned using Eqs. (8) and (9), except for the subscript 2 (indicating the second pulsation).

The results show very interesting trends. It appears that around 15% of the total energy ($\bar{E}_0 = 66.8735$) is dissipated between the first bubble maximum and the first bubble minimum, and a very negligible part (less than 0.1%) of the total energy is dissipated between the first bubble minimum and the second bubble maximum. In terms of the actual energy available after the first expansion, $\bar{E}^{e}_{ie_1} + \Delta\bar{E}^{e}_{pe_1}$ (i.e., after the 26% energy dissipated near the first bubble maximum is removed), the energy dissipated by the first minimum is around 21% of the available energy. Thus, nearly 42% of the total available energy is dissipated in first oscillation cycle. Between the first bubble minimum and the second bubble maximum, the amount of energy dissipated is negligible and the bubble radius data (Fig. 4) suggests that beyond the second oscillation, the energy loss is similar to the losses occurring during the second pulsation. Thus, this energy partition study shows that a significant amount of the explosion energy is dissipated during the first bubble pulsation. Clearly, some of this dissipated energy (during the first expansion phase) is carried away by the shock wave; however, there still appears to be a significant amount of energy that cannot be accounted for by the internal and potential energies associated with the bubble after the first pulsation. A similar conclusion has been obtained in earlier studies [1,4,22,25] where it was suggested that this dissipation may be due to various phenomena such as (i) turbulence induced in the water, (ii) mass loss from the gaseous bubble, (iii) Taylor instability at the interface, and (iv) gas cooling and steam condensation near the interface. However, none of the above studies were able to clearly identify the mechanism(s) behind the observed energy loss. As demonstrated in Section 4, the present study suggests that the energy loss is likely to be related to the excitation and amplification of interface instabilities.

4. Bubble interface instability

Analysis of the bubble images (e.g., (Fig. 5(c) and (d)) showed that significant corrugation of the bubble interface occurs near bubble minimum. Past studies [13,15] have suggested that this corrugation is the result of the bubble interface undergoing some sort of instability. Although various sources of instability (both hydrodynamic and evaporative) have been proposed it is still not clear how these instabilities contribute to the bubble interface collapse. However, if these instabilities do occur then it would explain the (so far) unexplained loss of energy during the first bubble pulsation. Therefore, an attempt was made in this study to identify the sources of the bubble interface instability and to determine, using theoretical stability analysis, if these instabilities are possible for the test conditions.

Two types of hydrodynamic instability mechanisms have been proposed: Rayleigh–Taylor (RT) and Kelvin–Helmholtz (KH) instability. The RT instability occurs when there are two fluids of different densities adjacent to each other and the lighter fluid is accelerated towards the denser fluid while the KH instability re-

quires the presence of a shear motion along the circumference of the bubble. The evaporative instability, often called the Landau–Darrieus (LD) instability [11], is a much more complex process and is due to the mass and heat transfer occurring across the bubble interface.

4.1. Hydrodynamic instabilities

Both or either of the RT and KH instability could play a role in destabilizing the bubble interface leading to the bubble collapse. Here, these two instabilities are addressed to identify their importance.

4.1.1. Rayleigh–Taylor instability

As shown by Birkhoff [9], for the case of underwater bubble, collapsing bubbles are unstable even though the denser liquid (water) is being accelerated towards the lighter vapor (explosion product), with surface tension having negligible effect on instability. He further showed that the general instability criteria allow two types of instability: the classical RT instability, which occurs at large wavelengths (small wave numbers) and has an exponential growth rate and the Birkhoff instability, which occurs at small wavelengths (large wave numbers) and has an algebraic growth rate. For small perturbations in bubble radius, the distorted interface $r(\phi, t)$ in spherical coordinates can be expressed in terms of Legendre polynomials by:

$$r(\phi, t) = R(t) + \sum_{n=1}^{\infty} b_n(t) P_n(\cos\phi). \tag{12}$$

where $R(t)$ is the mean bubble radius, ϕ is the bubble polar variable and n is the order of Legendre polynomial with the corresponding amplitude b_n. The differential perturbation equation can be obtained, in the absence of gravity, for the condition of constant internal pressure as [10]

$$\frac{d^2 b_n}{d\tau^2} + \frac{3}{z}\frac{dz}{d\tau}\frac{db_n}{d\tau} - A b_n = 0. \tag{13}$$

where A is given by [26]:

$$A = \left([n(n-1) - (n+1)(n+2)(\rho_2/\rho_1)](d^2z/d\tau^2) - (n-1)n(n+1)(n+2)(\sigma/P_0R_0)/z^2\right) / (z[n + (n+1)(\rho_2/\rho_1)]). \tag{14}$$

Here ρ_1 is the density of water, ρ_2 is the density of the gas in the bubble, σ is the surface tension and z is the dimensionless radius, $R(t)$. The general stability criteria for the stability of the Eq. (13) was derived by Birkhoff [10] and shown to be:

$$A < 0 \quad \text{and} \quad 6A\frac{dR}{dt} + R\frac{dA}{dt} < 0. \tag{15}$$

The first criterion in Eq. (15) reduces to the familiar RT stability criterion, $d^2R/dt^2 < 0$, for $\rho_1 \gg \rho_2$ and negligible surface tension effects. The second criterion is the Birkhoff stability criterion and entails that R^6A should be a decreasing function of time for stability. Fig. 8 shows the variation of A for different values of n for the H_2–O_2 explosion case of Fig. 7. Here a value of 70 dynes/cm for the surface tension of water, σ, has been assumed. Except for $n = 1$ (which corresponds to translation of the bubble center rather than deformation of the spherical shape), it can easily be observed that the Birkhoff stability criterion is violated as the bubble approaches the minimum radius. These stability criteria have been discussed in [27] where the stability of the growth phase has been analyzed and the preferentially amplified wavelength has been shown. The expansion and collapse of a large two-phase bubble of hot water in a tank of cold water has been shown in [28], where the growing interface has been shown to undergo RT instabilities of high wavenumber of 10.

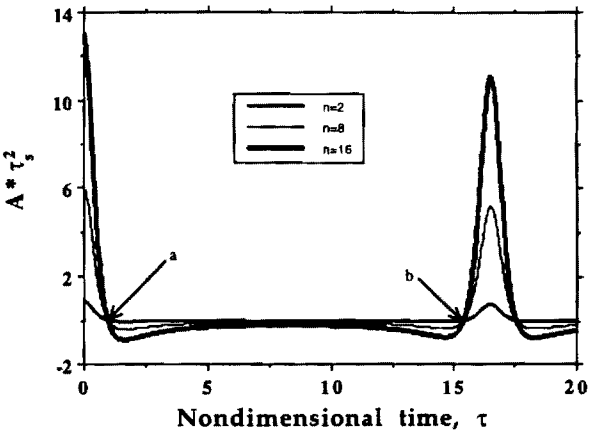

Fig. 8. The variation of A with time for the H_2–O_2 explosion case for different values of n.

The stability of Eq. (13) can be studied using Liapunov's theorems for nonlinear systems [29] by constructing a positive-definite Liapunov functional. Consider the second order differential equation $x'' + f(x)x' + g(x) = 0$, where $x' = dx/d\tau$ and in the state variable notation where $x_1 = x$ and $x_2 = x'$, the energy functional can be expressed as $V(x_1, x_2) = x_2^2/2 + U(x_1)$. If $g(x)$ is continuously differentiable, $g(0) = 0$ and $xg(x) > 0$ for all nonzero x, then $U(x_1)$ can be selected as $U(x_1) = \int_0^{x_1} g(s)\,ds$. According to Liapunov's theorem, a sufficient condition for the stability of the system of above mentioned second order differential equation in a region of state space is $V > 0$ and $W \equiv dV/d\tau < 0$. Considering $x = b_n$, one obtains $f(x) = (3dz/d\tau)/z$ and $g(x) = -Ax$ from Eq. (13). The Liapunov's energy functional becomes $V = x_2^2/2 - Ax_1^2/2$, which will be positive for all negative values of A. Therefore, by considering the range of τ defined by the points a and b in Fig. 8, one obtains $V > 0$. Since $W = -3(dz/d\tau)x_2^2/z$, a sufficient condition for the stability of the system defined by Eq. (13) becomes $dz/d\tau > 0$. Fig. 9 shows $dz/d\tau$. It can easily be inferred that the bubble growth is stable and the Liapunov stability criterion is violated during the bubble collapse phase.

Another method to study the stability of a second order differential equation with time-varying coefficients, like Eq. (13), is by means of the (so called) phase plane method [30]. In this method, the system trajectory is

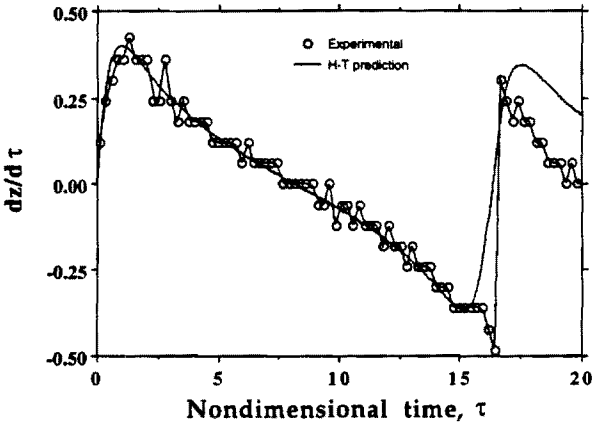

Fig. 9. The variation of first time derivatives of radius as a function of time for the first bubble oscillation of the H_2–O_2 explosion case. Results from the numerical calculations using the H–T equation (solid curve) is also shown to indicate reasonable agreement with the experimental data.

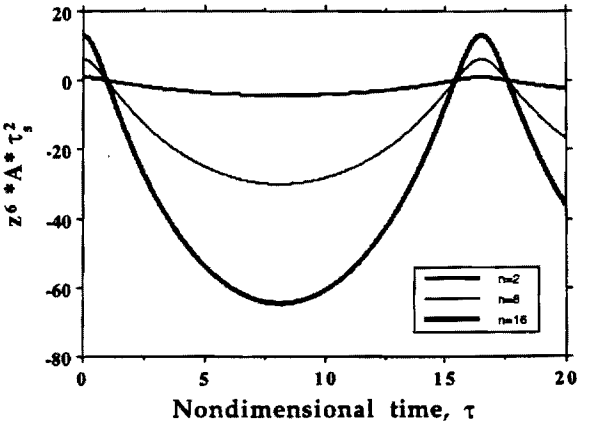

Fig. 10. The variation of R6A with time for the H_2–O_2 explosion case.

plotted in the state space. One can employ the delta method and Eq. (13) can be rewritten as $dx_2/dx_1 = -(x_1+\delta)/x_2$, where $\delta = 3(dz/d\tau)x_2/z - (1+A)x_1$ can be assumed constant over an infinitesimal interval $\Delta\tau$. The integrated form of this equation is $x_2^2 + (x_1+\delta)^2 = r^2$, where r is the constant of integration. One can start with an initial point $P(x_{1_0}, x_{2_0})$ at $\tau = 0$ and calculate δ and r. Next, an infinitesimal arc of radius r is drawn through P with center at $(-\delta, 0)$. The time required to move from the initial point to the next point in the phase plot is given by

$$\Delta\tau = \sin^{-1}\left\{\frac{x_{1_0}+\Delta x_1+\delta}{r}\right\} - \sin^{-1}\left\{\frac{x_{1_0}+\delta}{r}\right\} = \cos^{-1}\left\{\frac{x_{2_0}-\Delta x_2}{r}\right\} - \cos^{-1}\left\{\frac{x_{2_0}}{r}\right\}, \quad (16)$$

which can be rearranged to solve for Δx_1 and Δx_2 in terms of $\Delta\tau$. Thus, the coordinates of the next point in the state space separated by $\Delta\tau$ from the initial point P can easily be computed and a forward marching scheme can be set forth by updating the initial point and incrementing time by $\Delta\tau$ in each step. By making $\Delta\tau$ sufficiently small, this method can produce a set of values of $x_1 = b_n$ and $x_2 = db_n/d\tau$ with τ without actually solving Eq. (13). Since, this set of data is all one needs to investigate the stability or instability of Eq. (13), a phase plot is actually not needed. One can start with any arbitrarily small nonzero initial values of x_1 and x_2, and study their variations as time progresses. It is interesting to note that for $n > 1$ the qualitative variations of x_1 and x_2 with τ is quite independent of the choice of their initial values. Furthermore, the values of x_1 and x_2 grow rapidly without limit as the bubble minimum is reached and they keep growing even when the second pulsation starts indicating that the bubble minimum is unstable.

To examine the second criterion of Birkhoff's instability, the quantity R^6A (again in terms of the nondimensional variable z) estimated from the experimental data is shown in Fig. 10 for the H_2–O_2 mixture case. Interestingly enough, this quantity decreases continuously till bubble radius maximum and, thereafter it increases. Thus, based on the criteria established by Birkhoff, the conditions near bubble minimum can give rise to catastrophic instability. This is consistent with the observation seen earlier (in Fig. 7 and in experiments, [5]) that the rate of change of bubble radius is virtually discontinuous near bubble minima. To correlate the various regions of potential instability, the bubble radius time history along with the different regions for potential instability are shown in Fig. 11. Three regions are identified in this figure. In region A, $dR/dt < 0$, $d^2R/dt^2 < 0$, in region B, $dR/dt < 0$ or $dr/dt > 0$, $d^2R/dt^2 > 0$ and, in region C, $dR/dt > 0$, $d^2R/dt^2 < 0$. Clearly, the second criterion of Birkhoff suggests that the region B is unstable to perturbation.

The above analysis suggests that the bubble is unstable to perturbation near the bubble minimum and is susceptible to both RT and Birkhoff type of interface instability. To determine which of these instabilities is dominant, it is necessary to determine the most unstable

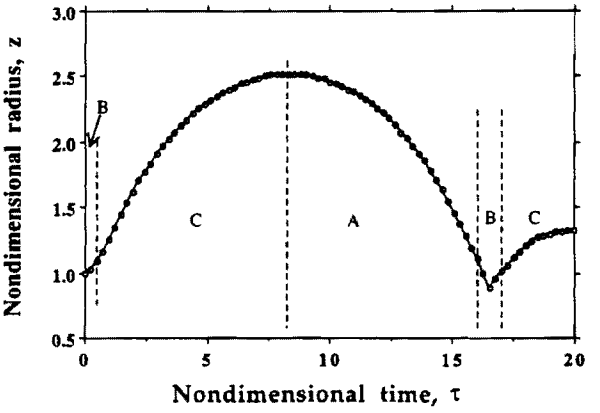

Fig. 11. Stability margins as suggested by Birkhoff [9] for the first bubble pulsation shown in terms of the nondimensional radius z and time τ. Based on Birkhoff's analysis, region B which occurs near the first bubble minimum is unstable to perturbations.

wavelength of the instability. It was noted earlier [13], that within the range of the maximum wavelength (which is determined by the size of the bubble) and the minimum wavelength (which depends on the effects of the surface tension), there exists a preferentially amplified most unstable wavelength. To determine this, the power spectral density of the bubble diameter near bubble radius minimum (obtained by carrying out FFT analysis of the bubble diameter, as described in Section 2) was analyzed and is shown in Fig. 12 for the H_2–O_2 mixture as a function of c/λ. Here, c is the bubble circumference and λ is the wavelength. Two curves are shown in the figure corresponding to 1 ms and 0.5 ms just prior to bubble minimum. It can be seen that there is a peak in power spectral density (which is actually the square root of the sum of the squares of mode amplitude coefficients, and should occur at integral fractions of bubble circumference because a periodic trace is being analyzed) for a value of the wavelength, which though large, is finite. Infinite wavelength corresponds to the mean bubble radius, and is, consequently, accompanied by a large peak (which is removed from these plots to facilitate comparison of the amplification of the other smaller wavelengths).

Fig. 12 clearly shows that the large wavelength instability is most dominant and the power spectral density of the largest wavelength increases as the bubble minimum is approached. Such a large-wavelength perturbation is characteristic of the RT type of interface instability which grows with an exponential growth rate. The general criteria of Birkhoff are satisfied suggesting that both RT and Birkhoff instabilities can be (and do get) excited near bubble minimum. However, since the effect of surface tension is always stabilizing and its effect increases rapidly with increasing n [26], it is plausible that, although Birkhoff-type of instability occurs near bubble minimum, it may be stabilized by the surface tension effect. The fact that the high wavenumber instability is not observed in the bubble diameter spectra suggests that even though the Birkhoff instability may be excited first near bubble minimum, the stabilizing effect of surface tension is suppressing the small wavelength disturbances, while, due to its exponential growth rate, the large wavelength RT instability becomes more dominant and, thereby, controls the growth of the bubble interface instability.

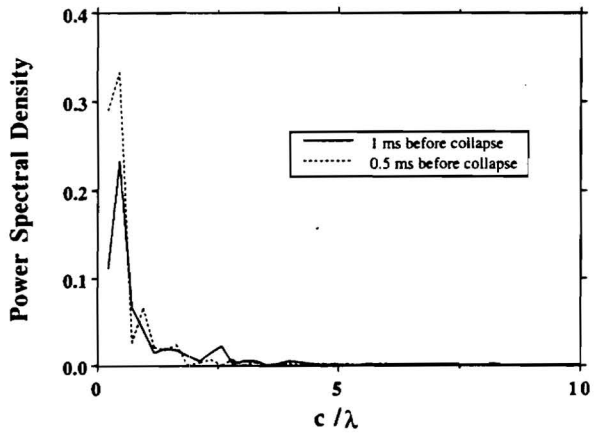

Fig. 12. Power spectral density analysis of the bubble diameters for the H_2–O_2 explosion case. The dotted and the solid curves correspond, respectively, to the bubble data 0.5 ms and 1 ms just prior to collapse. Results show that the large wavelength RT instability is dominant near the first bubble minimum.

These results were confirmed using a full three-dimensional numerical simulation of the bubble explosion using an advanced finite-element code ALE3D [18,31]. Results showed that as the bubble collapses, a large wavelength variation appears on the bubble interface. A typical result is shown in Fig. 13. This wave-like interface corrugation seen in the computations occurred in all test cases, including simulations with the tank walls moved outwards and changed from rectangular to spherical geometry. These computations were carried out without including the glass bulb and other experimental artifacts, such as, the pressure transducer and the spark. Thus, it appears that the formation of the interface corrugation is a physical property of the bubble dynamics.

4.1.2. Kelvin–Helmholtz instability

Yet another fundamental instability mechanism is the KH instability, which occurs when there is a shearing motion at the interface. A dispersion relation for gravity waves with a shear velocity U tangential to the interface in the upper fluid [6,8] can be given as:

$$\Omega_{KH} = -ik\frac{U\rho_2}{(\rho_1+\rho_2)} \pm \left[k^2U^2\frac{\rho_1\rho_2}{(\rho_1+\rho_2)^2} - kg\frac{(\rho_1-\rho_2)}{(\rho_1+\rho_2)}\right]^{\frac{1}{2}}. \quad (17)$$

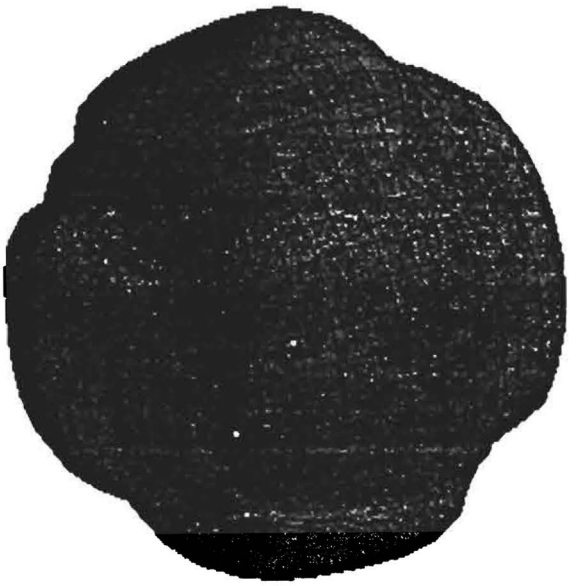

Fig. 13. Numerically predicted (using ALE3D) bubble shape near the first bubble minimum clearly showing the presence of large wavelength RT instability.

where Ω_{KH} is the growth rate, k is the wave number and g is the local acceleration (note that for the present case, the local acceleration is given by R_0/τ_s^2). The stability criterion can be shown to be [6]

$$(\rho_1 - \rho_2)g > kU^2\rho_2, \tag{18}$$

which, for the particular case of water–gas interface ($\rho_1 \gg \rho_2$) reduces to $\rho_1 g > kU^2\rho_2$. Since, $\rho_1 \gg \rho_2$ and g can also be very large near bubble minimum, the quantity $\rho_1 g/\rho_2$ is usually very large and the condition given by Eq. (18) is not difficult to satisfy suggesting that KH instability will not become relevant unless the tangential shear velocity U becomes very significant. Such shear motion would occur in the initially symmetric situation only if some interface corrugation has already occurred.

Fig. 14 shows a plot of the distance of the bubble center from the reference (unexploded) bubble location as a function of time. It can be seen that between the explosion and the first bubble maximum, there is negligible upward migration of the bubble (this justifies the earlier neglection of buoyancy effect for the study of RT instability). However, as time progresses, the bubble migrates upwards at an almost linear rate. Fig. 14 can be used to estimate the migration velocity which is determined to be approximately, 104.17 cm/s. The quantity $\rho_1 g/\rho_2$ assumes a value of approximately $2 \times 10^8\,\mathrm{m/s^2}$, for example, for stoichiometric H_2–O_2 mixture near bubble minimum. A surface corrugation of wavenumber as large as $150\,\mathrm{m^{-1}}$ ($c/\lambda \approx 30$) would also require a tangential shear velocity of magnitude larger than 1000 m/s to violate the stability criterion given by Eq. (18). Therefore, it is concluded that KH instability does not play a major role in the initiation of the bubble instability process.

4.2. Evaporative instability

When mass transfer is induced at the interface in the form of evaporation or condensation, the Landau–Darrieus evaporative instability can also contribute to the interface distortion. Mass transfer across the gas–water interface can occur through several mechanisms: evaporation, condensation, dissolution of product gases into water, explosive boiling of superheated liquids, and direct entrainment of gases into the liquid water [13]. In the present case, it is possible that due to presence of hot combustion products in the bubble, the surrounding water layer could be made to vaporize. However, the actual evaluation of the evaporation rate is not possible without detailed heat and mass transfer calculations since both the evaporative kinetics and the diffusion processes enter into the heat and mass transfer problem in a complex manner [12]. In order to determine the mass flux, j, the energy equation in spherical coordinates in presence of spherical symmetry,

$$\frac{\partial T}{\partial t} + \frac{R^2 R}{r^2}\frac{\partial T}{\partial r} = D\left(\frac{\partial^2 T}{\partial r^2} + \frac{2}{r}\frac{\partial T}{\partial r}\right), \tag{19}$$

has to be solved in the liquid surrounding the bubble, subject to the boundary conditions. Here, T is the temperature, r is the radial coordinate measured from the bubble center, and D is the thermal diffusivity of water. The boundary condition at the bubble interface is given by:

$$4\pi R^2 k\left(\frac{\partial T}{\partial r}\right)_{r=R} = -\frac{\mathrm{d}}{\mathrm{d}t}\left(\frac{4}{3}\pi R^3 L\rho_v\right). \tag{20}$$

where k is the thermal conductivity of water, L is the latent heat of vaporization, and ρ_v is the density of vapor. This boundary condition simply states that the heat required for evaporation of the liquid is supplied by the hot bubble by means of conduction through the interface. To solve Eq. (19), a transformation to the Lagrange coordinates can be implemented by defining $h = [r^3 - R^3(t)]/3$, so that the interface always lies at $h = 0$. Two finite difference equations are obtained for Eqs. (19) and (20) in terms of the space step, Δh and time step, Δt. The computation starts with an initial temperature distribution in water. A tridiagonal and diagonally dominant matrix equation is obtained and solved for the unknown temperatures at the grid points at later time Δt [32]. Thus a forward marching scheme in time can be set to determine the temperature distribution in water with bubble motion. The temperature of water at the interface determines the mass flux across the interface at any time.

The above equations were numerically solved for the experimental test conditions. Results showed that the interface temperature during the bubble expansion is around 344 K which is lower than the temperature needed to evaporate the water surrounding the bubble. Therefore, it is concluded that LD instability is not likely to occur near the bubble maximum.

In summary, it appears that both Birkhoff and RT instabilities can contribute to the interface instability near the bubble minimum. Near the bubble minimum, the interface becomes highly corrugated and the flow becomes locally turbulent. A portion of the bubble energy could be dissipated into heat in the local turbulent flow as the

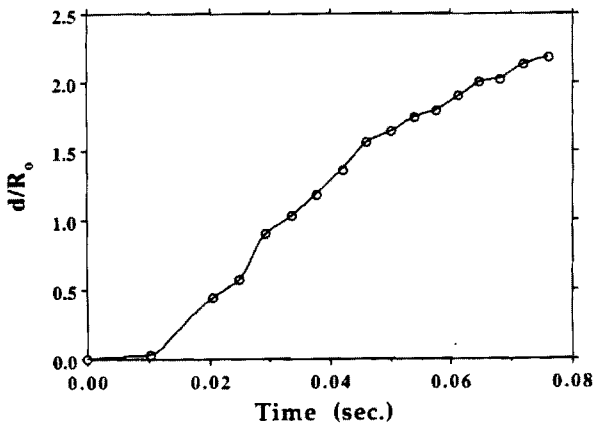

Fig. 14. Upward migration of the bubble center from its original location as a function of time. The vertical motion due to buoyancy is negligible only for the first bubble pulsation. Using a linear fit to this data, a migration velocity of around 104 cm/s is estimated for the present case.

bubble reaches its minimum. Of the hydrodynamic instabilities, the B-instability is likely to be excited first. However, the surface tension effect tends to stabilize the small wavelength (high wavenumber) B-instability, whereas, due to its exponential growth, the large wavelength (low wavenumber) RT instability becomes dominant. The excitation of RT instability extracts (or dissipates) significant amounts of total energy (as estimated in Section 3). This may explain the observed rapid decrease in the bubble size and pulsation amplitude after the first oscillation. As the bubble continues to pulsate (albeit with a significantly reduced amplitude), the effect of buoyancy causes an upward migration of the bubble. This can result in an effective shear velocity (however, data suggests that this velocity is not large enough to contribute sufficiently to cause the excitation of the KH instability).

5. Practical significance/usefulness

The dynamics of underwater explosions are of considerable interest due to the well known effects of the bubbles formed during the explosion. Many of the past and present studies are motivated by the need to characterize the mechanism by which these bubbles interact with underwater surfaces, such as, submarines, etc. The erosive and destructive nature of cavitation bubbles (usually these are very small micro-bubbles) on turbine blades and propellers are well known. However, when bubbles are formed due to large explosions near a surface, more destructive interaction occurs, since, the collapse process results in the formation of a water jet that impacts the surface with a peak pressure much larger (by an order of magnitude) than the original explosion pressure [4,5]. The dynamics of such large-scale bubble–surface interaction is not well understood. The present study forms the first phase of an ongoing investigation on the effects of bubble dynamics. Understanding the basic mechanism of bubble oscillation is the first step towards investigation of more complex fluid–structure interactions. For example, bubble–bubble interactions were recently used [33] to enhance the remnant energy in one bubble (at the expense of the other) so that the stronger bubble is less susceptible to instability and can maintain its coherence for a longer period. This has implications for focusing underwater bubble explosions.

6. Conclusions

This paper discusses results obtained in an experimental investigation of gaseous bubbles formed during underwater explosions. Experiments were carried out in a sub-scale laboratory test facility using gaseous fuel–oxygen mixtures as the explosion source. The typical bubble images and the pressure signatures (both outside and inside the bubble) were recorded during these experiments for a range of test conditions. Using both geometric and dynamic scaling analyses it has been demonstrated that the characteristic nondimensional parameters for the current experiments are reasonably similar to those measured in deep sea explosions. Thus, the present results have practical implications for understanding the characteristics of high-explosive deep sea explosions (which are very difficult to quantify).

Partition analysis of the total energy released during a typical explosion showed that nearly 26% of the total explosion energy is dissipated (or lost) during the first bubble expansion phase and another 15% of the total available energy is dissipated during the first contraction phase. As a result, the bubble size and the oscillation amplitude is decreased significantly after the first pulsation. This rapid decrease in bubble size and amplitude is similar to observations of deep sea explosions. Past studies attributed this observed decrease partly to the energy dissipated by the initial shock wave and partly to some unaccounted mechanism(s). The analysis of the present data suggests that the unaccounted-for energy goes into interface instability.

Various sources of the interface instability have been evaluated in the present study using the experimental data and stability analysis. Results suggest that neither the evaporative LD instability nor the KH instability are likely to play an observable role in the interface instability. However, near the bubble minimum, the hydrodynamic RT and Birkhoff instabilities are excited. It has been shown here that although the Birkhoff instability is excited first, surface tension efects damp the high wavenumber, small wavelength Birkhoff instability. However, the RT instability (with its exponential growth rate) is not damped and eventually dominates the interface instability. This study confirms earlier conjectures [1,3,13] that hydrodynamic interface instabilities play a major role in the energy loss process and the rapid decrease in bubble size and oscillation dynamics.

7. Recommendations

The current experiments were limited to shallow water, gaseous explosions. Although scaling analysis demonstrates that the present results are meaningful for real deep sea explosions, this needs to be confirmed by carrying out similar controlled explosions under higher pressure. Some such studies have been conducted in the past but the data acquired under these conditions are very limited and difficult to interpret. More detailed measurements are needed for realistic explosives (e.g., pentolite).

Nomenclature

English letters

b_n	amplitude of Legendre polynomial, m
c_l	speed of sound in water, m/s

C	acoustic loss factor $\left(=\sqrt{P_0/\rho_l}/c_l\right)$, nondimensional
d	explosion depth, m
D	thermal diffusivity of water, m^2/s
$E(r)$	internal energy of the bubble, J
k	wavenumber, m^{-1}
L	latent heat of vaporization, J/kg
M	molecular weight, gm/mole
P_r	pressure inside bubble, KPa
P^*	normalized pressure $(=P_r/P_0)$, nondimensional
$\tilde{P}$	normalized pressure $(=P_l/P_0)$, nondimensional
r	instantaneous bubble radius, cm
t	time, s
T	bubble oscillation period, s
Y	total energy associated with the radial flow of water, J
z	normalized bubble radius, nondimensional

Greek Symbols

γ	ratio of specific heats, dimensionless
λ	wavelength, m
σ	surface tension of water, dynes/cm
τ	time $(=t/\tau_s)$, nondimensional
τ_s	time scale $\left(=R_0/\sqrt{P_0/\rho_l}\right)$, s
ϕ	bubble polar variable, rad

Superscripts

c	contraction phase
e	expansion phase

Subscripts

0	initial state
1	corresponding to the first oscillation
2	corresponding to the second oscillation
de	dissipated energy
e	equilibrium state
ie	internal energy
k	kinetic energy
l	ambient state at the explosion depth
max	maximum state
min	minimum state
pe	potential energy

Acknowledgements

This work is supported by the Office of Naval Research under Grant No. N00014-91-J-1963 and monitored by Drs. Richard Miller and Judah Goldwasser. This paper is dedicated to the memory of the original investigator of this project, Regent's Professor Warren Strahle of the School of Aerospace Engineering, Georgia Institute of Technology.

References

[1] A.B. Arons, D.R. Yennie, Energy partition in underwater explosion phenomena, Rev. Mod. Phys. 20 (1948) 519–536.
[2] H.M. Sternberg, W.A. Walker, Calculated flow and energy distribution following underwater detonation of a pentolite sphere, Phys. Fluids 14 (1971) 1869–1878.
[3] K. Vokurka, A method for evaluating experimental data in bubble dynamics studies, Czech J. Phys. B 36 (1986) 600–615.
[4] K. Vokurka, Oscillations of gas bubbles generated by underwater explosions, Acta Technical Csav. 2 (1987) 162–172.
[5] R.H. Cole, Underwater Explosions, Princeton University Press, Princeton, 1948.
[6] G.B. Whitham, Linear and Nonlinear Waves, John Wiley, New York, 1974.
[7] B. Sturtevant, Rayleigh–Taylor instability in compressible fluids, in: H. Groenig (Ed.), Sixteenth International Symposium on Shock Tubes and Waves, VCH, 1988, pp. 89–100.
[8] G.I. Taylor, The instability of liquid surfaces when accelerated in a direction perpendicular to their planes, Part I, Proc. Roy. Soc. Lond. A 201 (1950) 192–195.
[9] G. Birkhoff, Note on Taylor instability, Quart. Appl. Math. 12 (1954) 306–309.
[10] G. Birkhoff, Stability of spherical bubbles, Quart. Appl. Math. 13 (1956) 451–453.
[11] L.D. Landau, E.M. Lifshitz, Fluid Mechanics, Pergamon Press, London, 1987.
[12] A. Prosperetti, M.S. Plesset, The stability of an evaporating interface, Phys. Fluids 27 (1984) 1590–1602.
[13] J.E. Shepherd, Interface Effects in Underwater Explosions, Conventional Weapons Underwater Explosions, ONR Workshop Report, 1988, pp. 43–83.
[14] A.B. Arons, J.P. Slifko, A. Carter, Secondary pressure pulses due to gas globe oscillation in underwater explosions: I. Experimental data, J. Acoust. Soc. Am. 20 (1948) 271–276.
[15] W. Strahle, S.G. Liou, Physical and chemical observations in underwater explosion bubbles, Sym. Comb. 25 (1994) 89–94.
[16] E.S. Flock, C.S. Marvin Jr., F.R. Caldwell, C.H. Roeder, NACA Report No. 682, 1940.
[17] G.J. Wylen, R.E. Sonntag, Fundamentals of Classical Thermodynamics, Wiley, New York, 1967.
[18] S. Menon, S. Pannala, Simulations of Underwater Explosion Bubble Dynamics Using an Arbitrary Lagrangian-Eulerian Formulation, ASME Fluids Engineering Division Summer Meeting (FEDSM97- 3492), Vancouver, Canada, June 1997.
[19] C. Herring, OSRD Report No. 236, 1941.
[20] L. Trilling, The collapse and rebound of a gas bubble, J. Appl. Phys. 23 (1952) 14–17.
[21] W. Lauterborn, Numerical investigation of nonlinear oscillations of gas bubbles in liquids, J. Acoust. Soc. Am. 59 (1976) 283–293.
[22] W. Hentschel, W. Lauterborn, Acoustic emission of single laser-produced cavitation bubbles and their dynamics, Appl. Sci. Res. 38 (1982) 225–230.
[23] A. Prosperetti, A generalization of the Rayleigh–Plesset equation of bubble dynamics, Phys. Fluids 25 (1982) 409–410.
[24] A. Prosperetti, A. Lezzi, Bubble dynamics in a compressible liquid. Part 1, First-order theory, J. Fluid Mech. 168 (1986) 457–478.
[25] J.W. Pritchett, Incompressible Calculations of Underwater Explosion Phenomena, Proceedings of the Second International Conference on Numerical Methods in Fluid Dynamics, Springer, Berlin, 1971, pp. 422–428.

[26] M.S. Plesset, On the stability of fluid flows with spherical symmetry, J. Appl. Phys. 25 (1954) 96–98.
[27] C.E. Brennen, Cavitation and Bubble Dynamics, Oxford University Press, New York, 1995.
[28] A.B. Reynolds, G. Berthoud, Analysis of EXCOBBULE two-phase expansion tests. Nucl. Eng. Design 67 (1981) 83–100.
[29] W.R. Kolk, R.A. Lerman, Nonlinear System Dynamics, Van Nostrand Reinhold, New York, 1992, pp. 179–216.
[30] D.P. Atherton, Nonlinear Control Engineering, Van Nostrand Reinhold, London, 1975, pp. 16–74.
[31] S. Pannala, S. Menon, Numerical Study of Bubble Collapse and Rebound Near a Wall, ASME Fluids Engineering Division Summer Meeting (FEDSM97-3244), Vancouver, Canada, 1997.
[32] M.D. Donne, M.P. Ferranti, The growth of vapor bubbles in superheated sodium, J. Heat Mass Transfer 18 (1975) 477–493.
[33] M.K. Lal, S. Menon, Interaction of Two Underwater Explosion Bubbles, ASME Fluids Engineering Division Summer Meeting, San Diego, 1996.

Simulations of Underwater Explosion Bubble Dynamics

S. Menon and S. Pannala
School of Aerospace Engineering
Georgia Institute of Technology
Atlanta, Georgia

Abstract

The dynamics of bubbles formed during underwater explosions is numerically investigated using an Arbitrary Lagrangian-Eulerian, three-dimensional finite-element code. Comparison of isolated bubble oscillation results with experimental data show good qualitative and quantitative agreement. Analysis using both stability considerations and energy balance estimates suggest that the excitation of Rayleigh-Taylor (R-T) instability is a major cause of interface instability during bubble collapse. The collapse of an explosion bubble near a rigid wall has also been simulated. The entire collapse process, including the formation of a vortex ring bubble and a high velocity re-entrant jet, are successfully captured in the simulations. The jet velocity and the impact pressure on the wall are functions of the explosion pressure and the distance of the bubble from the wall. The results indicate that, for a given explosion energy, there is an optimal distance of the bubble from the wall for which the impact pressure on the wall is maximum. This trend and the magnitude of the peak impact pressure are in good agreement with the experimental results. The evolution of the vortex ring bubble, reported in earlier experimental and numerical studies, is also accurately predicted. Available scaling laws for the time period and the peak velocities generated during bubble collapse are also reviewed in light of the current results. The present results are shown to obey many of the geometric and dynamic scaling laws when compared to deep sea explosions.

Key Words: Bubble Oscillation, Underwater Explosions, Dynamics, Rayleigh-Taylor Instability, Bubble Collapse, Gas Bubbles, Numerical Simulations, Impinging Jet.

1. INTRODUCTION

Vapor and gas bubble dynamics are of great practical interest in the prediction and prevention of cavitation erosion of marine propeller and turbine blades. The destructive nature of strong explosions near submerged rigid surfaces is also well known. Detailed reviews (e.g., Blake and Gibson, 1987; Prosperetti, 1982) have summarized past experimental and numerical results. Experimental studies are too many to list completely; however, most past studies focused on cavitation (small) bubbles. Among the studies that focused on large scale explosions are the studies reported in Cole (1948) for freely oscillating, deep sea explosion bubbles and the studies of bubble collapse near walls (e.g., Tomita and Shima, 1986). Bubble-bubble interactions have also been studied in the past (e.g., Warren and Rice, 1964). However, in most cases, due to difficulties in acquiring detailed data, only limited information has been obtained. Recently, experiments were carried out to investigate relatively large-scale bubble explosions (Menon and Lal, 1998a; Lal and Menon, 1996). These experiments were conducted in shallow water (1 atmosphere ambient pressure) due to an interest in understanding the dynamics of bubble oscillation and bubble-wall interaction in such flows (including the effect of a free water surface) and to investigate the feasibility of targeting mines buried in beaches. The data obtained from these experiments have been used to validate the numerical model discussed in this paper.

Numerical studies in the past range from simple 1-D analytic solutions (e.g., Lauterborn, 1976; Plesset, 1971; Prosperetti, 1982) to more complex 2D/3D studies. Many studies employed the Boundary Element Method (BEM) or its variants (e.g., Chahine and Perdue, 1988; Duncan and Zhang, 1991; Blake et al., 1986; Plesset and Chapman, 1971). BEM is computationally very efficient since only the flow on the boundary surface is computed which allows the reduction of the dimensionality of the problem by one. Past results have demonstrated that this approach can capture many features of the bubble oscillation and collapse process. However, this method has some inherent limitations. For example, BEM does not allow for variations of density and pressure inside the bubble even though studies suggest that considerable variations can occur at bubble minimum. In addition, the BEM fails at the point of jet formation, as the simple domain becomes double connected.

The flow evolution beyond the point of bubble collapse has been modeled using BEM by explicitly introducing vortex elements (e.g., Zhang and Duncan, 1994; Zhang et al., 1993; Best, 1993). This approach requires understanding where to introduce such vortex elements. Another assumption employed in BEM is that the ambient water is incompressible. This assumption need not be true in strong underwater explosions, especially near jet formation.

There are other assumptions used in past studies that are known to be questionable. For example, bubble shape is known to quickly deviate from sphericity at bubble maximum (radius), thereby, violating axisymmetric assumptions used in many past studies (e.g., Szymczak et al., 1993; Zhang and Duncan, 1994) and requiring full 3D treatment. Thus, simple 1-D, 2-D/axisymmetric or incompressible methods cannot completely resolve the bubble and the associated flow dynamics. Furthermore, simplified treatments cannot account for the interaction between the vapor and the liquid phases. To investigate the physics of such interaction, the details of the flow field both inside and outside the bubble is needed. Conventional numerical treatments (even using full 3D) such as Lagrangian or Eulerian techniques are also not practical, since the expansion and collapse of bubbles create severe fluid motion so that a Lagrangian approach (in which the grid points move with the fluid resulting in severe grid distortion) becomes inappropriate, while in an Eulerian approach, adequate resolution in the regions of interest is very difficult to achieve since the bubble's shape changes very rapidly.

A numerical method that includes both compressibility and an ability to capture the entire bubble collapse in complex configuration is used in this study. This numerical code combines lagrangian and eulerian features and is based on the Arbitrary Lagrangian-Eulerian (ALE) scheme developed at the Lawrence Livermore Laboratory. This code has been typically employed in the past to investigate structural fracture, and only limited studies of underwater explosion dynamics have been reported. Past attempts include 2D (e.g., Tipton et al., 1992) and 3D (e.g., Couch et al., 1996) studies of single bubble collapse. However, these studies provided only qualitative information and did not investigate the details of the collapse process. Furthermore, the ability of this code to capture accurately large

explosion bubble collapse has not yet been established. Validation under these conditions is necessary for the next phase of research as noted below.

In this paper, quantitative comparisons with experimental data is carried out to establish the ability of this code. In addition, the ALE3D code is also extended to investigate both single and double bubble explosions in free field and bubble collapse in the vicinity of a rigid wall. The motivation behind these studies is three fold. First, there are not that many 3D unsteady, compressible codes currently available to study such complex flow problems. For example, an Eulerian-Lagrangian (restricted) code called DYSMAS is currently used by the U. S. Navy to study underwater explosions. DYSMAS is made up of three different codes: an Eulerian solver, a Lagrangian solver and a coupler and is quite different from the ALE formulation. The ability and accuracy of this code to simulate complex bubble collapse and shock propagation is sometime very difficult (if not impossible) to verify since very little data is available for problems of interest. One of the objectives of the present study (using ALE3D) is to validate a code that can be used to investigate flow configurations that were studied using DYSMAS thereby proving an independent verification of the predicted results. The validation of the ALE3D code is discussed in this paper. Its application to complex problems of more practical interest will be reported in the future.

The second objective of this study is to investigate the dynamics of the bubble collapse. It was determined experimentally recently (Menon and Lal, 1998a) that during the bubble collapse, Rayleigh-Taylor interface instability is excited as the bubble reaches its minimum radius. Energy balance and stability analysis of the experimental data suggested that this instability could play a role in the bubble collapse and in its eventual breakdown. Earlier studies (e.g., Shephard, 1988) had suggested that hydrodynamic instability could be important in bubble collapse but until recently there had not been any clear evidence of this mechanism in both experimental and numerical data. The recent experiments only provide limited data due to the inherent difficulty in carrying out measurements. The present numerical study (under nearly identical conditions) provides an independent capability to address this fundamentally important issue. Since, the present numerical code is a

fully compressible solver it can capture interface instability due to density variation and therefore, can be used to address this issue. The results discussed in this paper clearly demonstrate that Rayleigh-Taylor interface instability is excited during the bubble collapse and that a portion of the bubble energy is being used to excite this instability. These results are discussed in some detail in this paper.

Finally, the third objective is to validate a simulation tool that can be utilized to investigate large (i.e., strong) underwater explosions near complex surfaces and the subsequent bubble-surface interactions. A numerical solver that can simulate simultaneously fluid dynamic and material surface interaction is needed. In the present study, ALE3D validation is carried out for bubble collapse near a rigid surface. However, the eventual goal is to study underwater explosion dynamics near surfaces buried beneath a sand surface. This type of study will require development and implementation of material models that mimic sand surface properties and is a focus of current research.

2. THE NUMERICAL METHOD

ALE3D (Anderson et al. 1994) is an explicit, 3D finite element code that simulates the fluid motion and elastic-plastic response on an unstructured grid. The grid may consist of arbitrarily connected hexahedral shell and beam elements. The ALE algorithm is implemented by carrying out a complete lagrangian calculation followed by an advection step. After each lagrangian step, a new mesh is created using a finite element based equipotential method to relax the distorted grid. In the Eulerian advection step, the fluid variables such as mass, density, energy, momentum and pressure are reevaluated on the new mesh by allowing fluid motion. The details of the constitutive models are described elsewhere (e.g., Steinberg, 1991) and, therefore, are not described here for brevity.

The advection step uses methods similar to those developed for 2D ALE code, CALE (Tipton, 1990), and the 3D Eulerian code, JOY (Couch et. al., 1983). For pure zones, a second order, monotonic advection algorithm is used (Van Leer, 1977). This advection

step can create mixed material elements (i.e., liquid and vapor). Material interfaces are not explicitly tracked but for the purpose of carrying out mixed element advection, they are inferred from volume fractions. Separate state variables are kept for each component of a mixed element. The well known compressible Euler equations are solved for the Eulerian advection step and therefore, are not shown here for brevity. Only the equations governing the Lagrangian step are summarized below. Further details of this code are given in the above mentioned references. The Lagrangian equations for conservation of mass, momentum and energy are given, respectively as:

$$\frac{d\rho}{dt} = -\rho \vec{\nabla} \bullet \vec{U} \tag{1}$$

$$\rho \frac{d\vec{U}}{dt} = -\vec{\nabla} p + \vec{F}_0 \tag{2}$$

$$\frac{d\varepsilon}{dt} = -p \frac{dv}{dt} + \dot{\varepsilon}_0 \tag{3}$$

where ρ is the mass density, $v = 1/\rho$ is the specific volume, $\vec{U}$ is the Lagrangian velocity, ε is the specific energy, p is the pressure, $\vec{F}_0$ is the force from the artificial viscosity and $\dot{\varepsilon}_0$ is the heating rate from the artificial viscosity. The artificial viscosity is part of the dissipative algorithm in the code since there is no natural viscous dissipation included in this formulation.

In ALE3D the proper choice of the equations of state for the various materials as required. Only a brief summary is given here primarily to highlight some of the features of the code. The explosion bubble is assumed to be of noncondensible steam and its equation of state is represented as: $p = (\Upsilon - 1)(1 + \mu)E$ where, γ is the ratio of specific heats, the relative volume is $\mu = \rho/\rho_0 - 1$ and E is the internal energy per unit volume.

The surrounding water is modeled using a Gruneisen form given as:

$$p = \frac{\rho_0\left(1+\left(1-\frac{\Upsilon_0}{2}\right)\mu-\frac{a}{2\mu^2}\right)}{\left(1-(S_1-1)\mu-S_2\frac{\mu^2}{\mu+1}-S_3\frac{\mu^3}{(\mu+1)^2}\right)}+(\Upsilon_0+a\mu)E \qquad (4)$$

For expanded material, the above expression is replaced by $p = \rho_0 C^2\mu + (\Upsilon_0 + a\mu)E$. Here, C is the intercept of the shock velocity-particle velocity curve (the Hugoniot curve), S_1, S_2 and S_3 are the coefficients of the slope of the shock velocity-particle velocity curve, Υ_0 is the Gruneisen gamma and "a" is the first order volume correction to γ. Our present interest is in underwater explosions in shallow water. Comparison of the pressure predicted by the above equation of state using available coefficients in the literature with the data obtained from NIST (1988) in the appropriate temperature and pressure range of interest showed significant discrepancies. In order to address this problem, water regime data was used to obtain new coefficients. It was determined that with these modified coefficients, the equation of state very closely agreed with the experimental results.

A limitation of the current ALE3D input structure is that it requires that the equation of state be in an analytical form (such as Eq. 5). The behavior of a material like water which has a discontinuous transition from steam to water can not be fully represented by an analytical form. Therefore, modifications were carried out to the coefficients to achieve a best fit to the experimental data. A more general approach would involve reading the data directly from tables rather than fitting it to an equation. This capability is currently being investigated for incorporation into the code. High explosive materials are also required to obey a specific form (many forms are included in ALE3D) of the state equation. Modifications are currently being studied to allow investigation of explosive materials and porous surfaces (e.g., sand) for which there are no analytical equation of state.

Another issue is that ALE3D is an inviscid code and surface tension effects are not included in this model. These limitations of the code are acceptable for the present study since the Reynolds numbers (Re) encountered in the flow based on the bubble diameter is the order of 100,000. Thus, neglecting viscous terms in the momentum and energy equations in such high Re flows should not significantly alter the results, as noted earlier (Wilkerson, 1989). Furthermore, the study of the hydrodynamic Rayleigh-Taylor instability can be carried using an inviscid model since this instability is due to density gradients in the flow. Neglecting surface tension is also considered acceptable since it was noted earlier (Plesset, 1954) that surface tension has a very limited stabilizing effect on the bubble interface and is only critical when there is very little pressure difference across the bubble interface (which is not the case in explosive bubbles). Other studies (e.g., Vokurka, 1985) also showed that surface tension effects are important for only very small bubble.

3. RESULTS AND DISCUSSION

In this section, the results obtained for the various cases are summarized and discussed. Wherever possible, comparison with experimental data is carried out to validate the simulated results. Analysis is also carried out to understand the fluid motion generated both inside and outside the bubble during collapse and to understand the dynamics of the instability occurring during collapse.

3.1 Bubble Oscillation Dynamics

Free field oscillating bubble collapse was simulated using test conditions similar to the experimental set-up of Menon and Lal (1998a) to enable direct comparison and to investigate the afore-mentioned interface instability seen in the experiments. The experiments were conducted in a water tank of dimension 2m x 1.5m x 1.5m. The underwater explosion bubble were generated in the experiments by centrally igniting a mixture of explosive gases (e.g., Hydrogen and/or Carbon Monoxide), oxidizer (Oxygen) in a hand-blown glass globe. The glass globe weighed about 5-6 grams, and had an average diameter of 6.34 cm. Thus, the initial explosion source is of the order of the globe diameter. The gaseous explo-

sive mixture was ignited by using an electrical spark generated by spark wires placed inside the glass globe and connected to a 3000 volts DC power supply. Further details are given elsewhere (Menon and Lal, 1998a).

In the present study, the computational domain, the bubble initial explosion energy, the bubble location and ambient conditions were all chosen identical to the values in the experiments. Thus, the freely oscillating bubble is modeled in the center of a 1.5 m x 1.5 m x 1.5 m tank filled with water (as in the experiments). The initial bubble diameter modeled is 6.34 cm, the initial explosion pressure is 9.34 atmospheres (again, as in the experiments) and the water pressure is 1 atmosphere. The only differences between the numerical treatment and the earlier experiments are that the effect of the glass bulb and the sting used to hold the electric spark assembly are not modeled. This omission is particularly important since it removes any possibility that these features of the experimental setup could play a role in exciting interface instability.

The ALE mesh treatment (i.e., mesh regridding) is applied to all the elements in the bubble and in the vicinity of the bubble. But away from the bubble where the bubble explosion does not cause much grid distortion, Lagrangian mesh treatment is used. The number of elements used to resolve the bubble and the surrounding water was varied to confirm that the results are grid independent. For a typical 3D simulation, 72,576 elements were used to discretize the domain., but as many as 220,000 elements were used for grid independence tests. Most of the results on the bubble dynamics discussed here (unless otherwise noted) are on the finest grid resolution. In addition to these studies, the effect of the computational domain (extent and shape) was also studied to ensure that the results do not depend upon these parameters.

Figures 1a and 1b show, respectively, the global grid and a close-up of the grid around the bubble. Most of the grid resolution is employed around the bubble and ALE region while the far field is resolved using a relatively coarse grid. Although various cases have been simulated, only characteristic results are discussed below to highlight the results.

Figures 2a and 2b show respectively, the pressure (normalized by the initial liquid pressure p_l which is 1 atmosphere) and the bubble radius (normalized by the bubble maximum radius, R_{max}) history during the first oscillation under various test conditions. Here, time is normalized by $\tau_l = R_{max}/(\sqrt{p_l/\rho_l})$ which is the characteristic time scale for the bubble to reach its maximum radius. Also, p_l is the ambient water pressure and ρ_l is the water density In Fig. 2a, the pressure in the bubble is compared with experimental data (Menon and Lal 1998a). It can be seen that the computed period of oscillation (around 15 ms), the peak pressure and the maximum radius (Fig. 2b) agrees well with data. It can also be seen that the shape and the extent of the computational domain do not play a major role in dictating bubble dynamics. This can be observed from Fig. 2a since the time period and peak pressure changed only by around 10% (increase) and 5% (decrease), respectively, when the walls are moved away by a factor of seven. Further increase in the wall locations did not significantly change the predicted pressure profile. Changing the outer boundary shape (from rectangular to spherical) also did not change the oscillation period and the bubble dynamics (discussed below). This suggests that the geometry of the outer domain does not significantly affect the local physics of the bubble oscillation and that "nearly" free-field explosion condition can be simulated when the walls are moved further away. However, to obtain "true" free field conditions, outflow boundary conditions are required. This feature is currently being investigated for implementation.

The bubble radius history (Fig. 2b) also shows similar agreement with data. During the contraction phase there are some differences between the calculations and the experiments. Note that, the experimental set-up employed a glass globe (which contained the stoichiometric fuel-air mixture) with a metal insert that contained the pressure transducer and the spark generator (Menon and Lal, 1998a) while these features were ignored in the numerical model. In addition, the effect of glass fragments have not been included in the numerical model. Thus, some discrepancies are expected.

In spite of these differences it is interesting to observe that the numerical and the experimental results are in relatively close agreement. This suggests that the experimental

artifacts (identified above) are not significantly modifying the dynamics of the bubble oscillation process. Therefore, the present numerical study serves to provide an independent validation of the results described earlier in Menon and Lal (1998a).

Figure 3a shows the time trace of the non-dimensional pressure in the tank close to a wall. It is very similar to the high frequency pressure oscillations as recorded by the tank transducer in the experiments (Menon and Lal, 1998a) and shown in Fig. 3b. The differences in the frequency content (the high frequency fluctuations are missing from the numerical data) may be attributed in part to coarse grid used in the far field (which would effectively damp high frequency waves). This is demonstrated in Fig. 3a using pressure data obtain on two different grid resolutions.

3.2 Bubble Instability during Collapse

The basic physics of bubble oscillation has been known for some time. The bubble grows after the explosion due to the high pressure inside the bubble. Because of inertia, this results in an over expansion and the pressure inside the bubble falls below the ambient (water) pressure. As a result, the bubble collapses and reaches a bubble minimum at which time the internal pressure again exceeds the external pressure. Thus, an oscillation process is set up and continues as long as there is sufficient energy available. However, energy is continuously lost during the oscillation. As a result, the maximum bubble size decreases during the subsequent oscillations and the bubble typically breaks up into smaller bubbles after 2-3 oscillations. The source of this energy loss leading to bubble collapse has been an issue of investigation for some time. Past studies (e.g., Arons et al., 1948; Pritchett, 1971; Plesset, 1971; Vokurka, 1987; Shepherd, 1988) have attempted to identify these sources. The propagation of the initial shock wave, acoustic losses, compressibility and heat transfer effects, mechanical work done on water and vapor, etc. have all been used to explain the energy loss. However, even when all these effects were included the total observed energy loss still could not be fully explained.

Other sources of energy loss and bubble breakdown have been proposed but without any detailed experimental or numerical proof. For example, onset of various interface instabilities have been suggested (Shepherd, 1988). Recent experimental studies focused on the instability mechanisms (Menon and Lal, 1998a) and the analysis suggested that during the collapse process, the Rayleigh-Taylor (R-T) instability occurs at the bubble interface. Analytically, R-T instability has been shown to occur for the case of underwater collapsing bubbles by Birkhoff (1956) even though the denser fluid (water) is being accelerated towards the lighter fluid (gaseous explosion product), with surface tension having negligible effect on instability. He further showed that the general instability criteria allows two types of instability: the classical R-T instability, which occurs at large wave lengths (small wave numbers) with an exponential growth rate, and the Birkhoff instability, which occurs at small wave lengths with an algebraic growth rate. Analysis of the experimental data (Menon and Lal, 1998a) showed that both instabilities are excited near bubble minimum but the Birkhoff instability is quickly overtaken by the exponentially growing R-T instability so that R-T instability eventually dominates.

Understanding the mechanism of bubble interface instability is important since this would partly explain the energy loss during oscillation and is a possible mechanism for the bubble breakdown. This phenomenon has never been numerical captured (at least to the present authors' knowledge). Thus, the present numerical results appear to be the first such demonstration in open literature. Figure 4a shows the computed bubble surface (only the rectangular computational domain case is shown since the spherical case gave identical result) at the maximum bubble radius and Figs. 4b and 4c show respectively, the bubble shape at its first minimum radius for the rectangular and spherical outer domains. Both these simulations were conducted using 220,000 cells (simulations using coarser grids also showed very similar structure and therefore, are not shown). For comparison, Fig. 4d shows a typical snapshot (at the bubble minimum) from the experiments. Note that Figs. 4b and 4c have been magnified (relative to Fig. 4a) to facilitate visualization. As can be seen, near the bubble minimum large-wavelength wave-like distortion appears along the bubble interface in remarkable similarity with the distortion seen the experimental picture. Note that, there are sufficient number of grid points in the azimuthal direction to reason-

ably resolve the bubble interface and it was confirmed that the interface distortion occurs independent of the grid resolution. It can also be seen that changing the computational domain either by increasing it or by changing the shape (see more discussions below) did not change the form or character of the wave-like distortion on the bubble surface. Thus, this interface distortion feature appears to be a physical phenomenon.

Figures 5a and 5b show, respectively, the velocity vector field at the bubble maximum in the vicinity of the bubble for the rectangular and spherical domains and Figs. 6a and 6b show respectively, the velocity vector field just after the bubble minimum for the rectangular and spherical domains. Figures 5a and 5b shows that the fluid (both the gas inside the bubble and the liquid outside) are undergoing an outward motion of the bubble. Changing the shape of the computational domain does not change the local fluid motion significantly. In Figs. 6a and 6b, the bubble is just starting to expand after reaching the minimum radius and the fluid has reversed direction and is in the outflow direction. It can be seen that near the bubble minimum the fluid motion has lost spherical symmetry. These figures show that both the bubble shape and the associated fluid motion in the vicinity of the bubble are relatively insensitive to the shape of the computational domain. Of course, the oscillation period and the bubble maximum radius are modified slightly when the outer domain is extended, as shown earlier in Figs. 2a and 2b, but the local fluid dynamics appears to be relatively insensitive.

As noted above, Figs. 6a and 6b show that fluid motion inside the bubble is no longer symmetric indicating a deviation from sphericity. This is consistent with observations made earlier (Cole, 1948). The deviation from sphericity and the formation of waves on the bubble interface are characteristics of Rayleigh-Taylor instability.

The R-T instability can also be inferred by analyzing the variation of the radius with time. As shown by Birkhoff (1956), for the case of underwater bubble, collapsing bubbles are unstable even though the denser liquid (water) is accelerated towards the lighter fluid (explosion product). He showed using a perturbation analysis of the one-dimensional Trilling equation (Trilling, 1952) that the general stability criteria is given by

$d^2R/dt^2 < 0$, where R(t) is the mean bubble radius. This criteria can be evaluated from the current numerical (and the earlier experimental) data. Figure 7a shows this quantity near bubble minimum. Clearly, near the bubble minimum the R-T stability criteria is violated and confirms that R-T instability is occurring near bubble minimum.

Another approach to analyze the bubble surface instability is to use Liapunov's theorem for nonlinear systems (Menon and Lal, 1998a; Kolk and Lerman, 1992). The sufficient condition for stability using this analysis for the bubble expansion and collapse process reduces to $dz/dt > 0$, where z is the normalized bubble radius ($z = r/R_0$). Figure 7b shows the variation of this quantity as a function of normalized time. It can be seen that the bubble growth phase is stable. However, the Liapunov stability criterion is violated during the bubble collapse phase. Thus, it appears that the Rayleigh-Taylor instability does occur as the bubble nears its minimum radius.

The analysis of the earlier experimental data indicated that both Birkhoff and Rayleigh-Taylor instabilities are likely to be excited near the bubble minimum. The Birkhoff stability criteria is part of the general stability criteria (see Menon and Lal, 1998a). The experimental data suggested that both types of instabilities are excited but that the exponentially growing R-T instability quickly dominates the interface distortion. The present analysis confirms that the general stability criteria is violated near the bubble minimum and the visualization of the bubble shape shows that the interface instability appears as a large wavelength distortion which is characteristics of R-T instability. No sign of Birkhoff instability (which is short wavelength, high frequency instability) is observed in the calculations. This may be due to lack of sufficient grid resolution to resolve the high frequency, short wavelength distortion even with the high resolution employed. Nevertheless, the results clearly confirm the earlier observation that R-T instability does occur during the bubble collapse phase.

3.3 Scaling Analysis

To be useful for practical applications, the bubble motion should preserve both geometric and dynamic similarities (Cole 1948). Geometric similarity implies invariance of R_{max}/d and R_{max}/R_{min} and dynamic similarity essentially implies invariance of the Froude number, $Fr=U^2/gL$, which in turn implies an invariance of T^2/R_{max}. Here, R_{min}, d and T are, respectively, the bubble minimum radius, water depth and time period of oscillation. Estimates for these parameters for the first bubble oscillation are given below for the present study and compared to the past deep sea studies.

For the present studies of gas explosion, $R_{max} \approx 3R_0$, $R_{min} \approx R_0$, $R_0 \approx 3.15$ cm (initial bubble size), $T \approx 0.015$ sec, and $d = 0.6477$ m. This gives $R_{max}/(d+10.33) \approx 8.607\times10^{-3}$, $R_{max}/R_{min} \approx 3$, and $T^2/R_{max} \approx 2.381\times10^{-5}$ s²/cm. In a deep sea explosion of 249.5 grams of tetryl charge fired at a depth of 91.44 m below the water surface [Cole 1949, page 271], $R_{max} = 45.11$ cm, $R_{min} \approx 12.7$ cm, $R_0 = 3.5$ cm, $T \approx 0.028$ sec, and $d = 91.44$ m. This gives $R_{max}/(d+10.33) \approx 4.432\times10^{-3}$, $R_{max}/R_{min} = 3.55$, and $T^2/R_{max} = 1.738\times10^{-5}$ s²/cm.

Data from TNT explosions at a depth of 152 m (Arons et al. 1948) suggests similar results: $R_{max}/(d+10.33) \approx 2.55\times10^{-3}$, $R_{max}/R_{min} = 2.255$, and $T^2/R_{max} = 1.596\times10^{-5}$ s²/cm. These comparisons suggest that the present study preserves reasonably close geometric and dynamic similarities with the past deep sea explosion data for all the parameters except for R_{max}/d (which is clearly impossible since current studies are in shallow water). This good agreement is primarily due to the fact that in the present study, $R_{min} \approx R_0$ whereas in deep sea studies they are significantly different.

3.4 Energy Loss Estimate

The explosion energy is redistributed among the various modes (e.g., shock wave energy, potential, kinetic and dissipated energies, etc.) initiated by the explosion. Earlier (Menon and Lal, 1998a) used the experimentally obtained data to evaluate how the total energy

from explosion is partitioned between these modes. The energy balance for an expanding system can be written as (e.g., Vokurka, 1987): $\Delta E_i = \Delta E_p + \Delta E_d + E_k$, where, ΔE_i and ΔE_p are respectively, the change in internal and potential energy of the gas bubble (from its initial state at time t=0), ΔE_d is the energy dissipated and E_k is the liquid kinetic energy. Estimates for each of these terms can be obtained (or approximated) from the simulation.

For the experiments, the total (nondimensional) energy was determined from the relation $\bar{E}_0 = QW/E_0$, where Q is the detonation energy per kg of explosive, W is the weight in kg of the explosive and $E_0 = 4\pi R_0^3 p_1/3$ is the energy of the initial gas volume. For a stoichiometric hydrogen-oxygen mixture, Q = 242 KJ/mole of hydrogen and using representative values it was determined that $\bar{E}_0 = 66.9$. In the present numerical study, the explosion pressure was matched to the experimental pressure which results in an energy estimate of $\bar{E}_0 = 56.5$. The discrepancies is likely to be due to the idealized estimate used in the experiments where it was assumed that the entire explosion energy is converted to pressure. No correction for incomplete combustion, energy to break up the glass bulb, and energy lost to the sting were included in the experimental estimate. Thus, the present numerical estimate is considered reasonable. $\bar{E}_0$ is total amount of explosion energy which is to be distributed into various modes as the bubble expands. The change in internal energy (nondimensionalized using E_0) as the bubble expands and reaches bubble maximum can be written as (Vokurka, 1987):

$$\Delta\bar{E}_i^e = \left(\frac{P_0}{P_1}\right)\left(\left[1-\left(\frac{r}{R_0}\right)^{-3(\gamma-1)}\right]/(\gamma-1)\right) \tag{5}$$

where the subscript 0 indicates the first bubble oscillation and the superscript e indicates the expansion phase. The change in potential energy (again nondimensionalized bE_0) is:

$$\Delta\bar{E}_p^c = \left[\left(\frac{r}{R_0}\right)^3 - 1\right] \tag{6}$$

Here, $r > R_0$ is the instantaneous bubble radius as the bubble expands from its initial diameter R_0 to its first maximum bubble radius R_{max}. Further, since $E_k \approx 0$ near the bubble maximum (Vokurka, 1987), an estimate for the energy dissipated based on the above relations suggests that approximately 14% of the energy is dissipated as the bubble expands and reaches its first maximum. This estimate is lower that the experimental result of 26% (Menon and Lal, 1998a). However, as mentioned earlier, this discrepancy may be due to uncertainties in the experimental estimate.

A similar analysis can be carried out for the contraction phase (i.e., as the bubble collapses from the bubble maximum and reaches its minimum radius). For the contraction phase the energy available is limited to the amount left after the above noted fraction of the explosion energy has been dissipated. However, the current numerical study is based on an inviscid code and thus, the energy lost from the bubble during the expansion phase is not fully dissipated. Some fraction is dissipated due to numerical and artificial dissipation in the numerical scheme. This fraction can be determined by determining the total energy in the computational domain during the calculation. Estimate suggests that approximately 3-4% of the energy is dissipated due to artificial dissipation.

The change in potential energy during the contraction phase can be written as (Vokurka, 1987):

$$\Delta\bar{E}_p^c = \left(\frac{R_{max}}{R_0}\right)\left[1 - \left(\frac{r}{R_{max}}\right)^3\right] \tag{7}$$

where, the superscript "c" indicates the contraction phase. The change in internal energy can also be expressed in terms of the bubble properties as:

$$\Delta\bar{E}_i^c = \left(\frac{1}{\gamma - 1}\right)\left(\frac{P_{max}}{P_1}\right)\left(\frac{R_{max}}{R_0}\right)^3\left[\left(\frac{r}{R_{max}}\right)^{-3(\gamma-1)} - 1\right] \tag{8}$$

Using the computed data in (7) and (8) it appears that around 15% of the total energy is dissipated between the first bubble maximum and minimum. This amount is in very

good agreement with the experimental estimate of 15%. Since it is estimated here that around 3-4% is numerically dissipated, it leaves around 11-12% unresolved. A possible avenue for this energy loss is in the excitation and amplification of the interface instabilities which lead to the eventual bubble collapse.

In summary, the above study confirms the earlier experimental observation that Rayleigh-Taylor instability occurs near the bubble minimum. Stability analysis confirms that this instability can occur and energy partition analysis indicates that there is a reasonable amount of energy missing that could be used to excite this instability.

3.5 Bubble-Wall Interactions

Bubble collapse near a rigid wall is of significant interest due to its ability to cause serious damage to the structure (cavitation damage of underwater propellers is a well known example). This is because when the bubble collapses near a rigid surface, a strong reentrant water jet is formed that is directed towards the wall. The peak impact pressure on the wall due to this water jet can be substantially higher than the explosion pressure. The dynamics of this collapse process has been under investigation for some time; however, experimental capability to record the effects of the interaction process is limited due to the difficulty in accessing the bubble collapse region. Past numerical studies have been able to capture the collapse process but, as noted before, such calculations resorted to obtaining information from experiments to ensure that the simulation's initial conditions agreed with experimental data. Furthermore, earlier studies did not fully resolve the fluid motion both outside and inside the collapsing bubble. Thus, the earlier studies failed to fully explain the dynamics of the impact process and the effect of initial bubble location on the measured impact pressure on the wall.

In the present study, the impact process is investigated as a function of explosion strength, gravity orientation (i.e., wall above and below the bubble), and the bubble location relative to the wall. Conditions were chosen to mimic the experimental conditions as much as possible. For a typical simulation, a total of 25,000 elements are used to resolve

the bubble and the wall region and another 35,000 elements are used for the rest of the domain. Again, grid independence studies using over 200,000 elements were conducted to ensure that the results were grid independent. Characteristic results that highlight some interesting physics of the problem are discussed here.

Three cases are analyzed here to highlight the various physical phenomena associated with the bubble collapse near a wall and its dependence on the proximity of the wall. These cases correspond to an initial bubble location of 5 cm (case 1), 6.34 cm (case 2) and 4 cm (case 3) above the wall (gravity inhibiting case, i.e., bubble above the wall as in the experiments, Menon and Lal, 1998b), respectively. Figures 8a-c show the velocity field at various stages of the collapse for case 1. At the bubble maximum, the bubble is almost spherical but begins to distort as it collapses. Since there is less volume of water between the wall and the bubble during the collapse, the pressure drop is quite large relative to the pressure drop on other sides of the bubble. This pressure differential further forces the bubble towards the wall. This migration of the bubble causes the water surrounding the bubble to be directed away relative to the bubble geometric center and thereby, creating a higher pressure on the upper side of the bubble away from the wall resulting in the well known Bjerknes force (Blake et al., 1986). The iterative combination of these effects (as the bubble moves closer to the wall) cause the water to penetrate the bubble from the high pressure side and to form a high-speed water jet that impacts the rigid surface. As this jet impacts the rigid plate, a toroidal vortex ring bubble is formed, as shown in Fig. 8c. This ring bubble qualitatively compares well with those observed in both experiments (e.g., Tomita and Shima, 1986; Vogel et al., 1989) and in numerical studies (Best, 1993; Szymczak et al., 1993; Zhang and Duncan, 1994).

Figures 9a and 9b show, respectively, the velocity fields for cases 2 and 3 at a time just before the jet formation. Comparison with Fig. 8b indicates that when the bubble is farthest from the wall (case 2) it has time to collapse to a smaller volume and thus, generates higher velocities while in case 3, the bubble cannot collapse as much as the other two cases and thus, lower velocities are observed. The implication of these differences on the impact pressure generated on the wall is discussed below.

Figure 10 compares the time traces of peak impact pressure on the rigid wall for the three cases. The non-dimensional time periods (scaled with the time scale, τ_1), are 2.021, 2.017 and 2.048, respectively, for the three cases. The peak velocities are observed slightly before the jet impacts the wall. These velocities scaled with non-dimensional velocity scale based on the ambient (water) pressure and water density ($\sqrt{P_1/\rho_1}$) are 6.9, 7 and 6.4, respectively. These values compare well with earlier results (e.g., Chahine and Perdue, 1988; Blake et al., 1986). It can be observed that even though case 2 generated the maximum velocity, it does not correspond to the maximum peak impact pressure. This is because the jet loses some of its kinetic energy as it penetrates through the water layer between the toroidal bubble and the wall. In case 1, the lower and the upper bubble surfaces are closer to (in fact just touching) the wall before impingement and thus, there is no water layer for the jet to penetrate. This results in higher impact pressures on the wall. On the other hand, for case 3, the bubble is so close to the wall that it does not have the freedom to fully expand before collapsing. As a result, the overall jet speed achieved in this case is lower than case 1 and as a result, the impact pressure is lower than for case 1.

These results suggest that due to two different physical reasons, there is an optimum distance above the wall for which a peak impact pressure is achieved. This has been confirmed by direct comparison with experimental data. Figure 11 shows the peak impact pressure (normalized by the initial explosion pressure) variation with normalized distance of the bubble center above the wall. Two sets of numerical results for gravity inhibiting case (with wall below the bubble) and gravity aided case (wall above the bubble) are compared to the experimental data (gravity inhibiting case). Both these cases show similar behavior except that there is a slight shift to higher impact pressure for the gravity aided case. This agrees with physical intuition that buoyancy aids the migration of the bubble towards the wall and thus, enhances the impact process. It is likely that the effect of buoyancy will be more apparent for deep sea large-scale explosions. This is an issue currently under study.

It is clearly seen in Fig. 11 that the present numerical study has captured both the trend and the magnitudes of the peak impact pressures seen in the experiments for a range of initial bubble locations. The experimental data shows a slightly lower maximum peak impact pressure at a farther distance when compared to the numerical data. However, this discrepancy can be attributed primarily to the limitations of the experimental set up (Menon and Lal, 1998a; 1998b). As noted earlier, the experiments used a metal sting (which contained a pressure transducer) to hold the glass bulb that contained the explosive mixture. The presence of this sting and the glass fragments very close to the wall (not included in the numerical study) are likely to effect the measurements.

In spite of this discrepancy, it is encouraging to note that there is considerable agreement between the numerical and experimental results. This provides confidence in the capability of the simulation model and provides a research tool that can now be utilized for detailed studies of more realistic explosions both in shallow water and deep sea situations. Current studies (to be reported in the near future) are focused on bubble dynamics due to realistic high explosive shaped (e.g., cylindrical detonation cord) charge explosions near rigid surfaces.

Finally, Fig. 12 shows the variation of impact pressure along the wall for case 1 just after the jet formation. This figure shows that the jet is very narrow and is not spreading at all. This is reflected in the observed high impact pressure at the jet centerline. There is a rapid decay of pressure away from the impingement point which is very typical of stagnation point flows. The need to adequately resolve this highly coherent but narrow jet structure is one of the reason that makes it very difficult to simulate the bubble collapse process accurately using conventional schemes without causing prohibitive increase in computational cost. The ability of ALE3D to capture such a flow field without requiring enormous increase clearly demonstrates its capability.

4. CONCLUSIONS

In this paper, an unsteady, 3D finite-element compressible code has been successfully applied to study underwater explosions. Results clearly demonstrate that the ALE3D code can be used for bubble explosions. The basic code has been validated using shallow water explosion data. It has been shown that nearly all the features observed in experiments have been captured in these studies. There is excellent qualitative and reasonable quantitative agreement with the experimental data.

Results show that during collapse of a freely oscillating bubble, the bubble loses spherical symmetry and the bubble interface becomes unstable due to the excitation of Rayleigh-Taylor instability. Stability analysis confirms that this instability can occur and energy partition analysis indicates that there is a reasonable amount of energy missing that could be used to excite this instability. This verifies the earlier experimental demonstration that R-T instability is one of the primary mechanisms in bubble collapse and breakdown. The simulation of the collapse of a bubble near a rigid wall showed that the jet velocity and the impact pressure on the wall are functions of the explosion pressure and the distance of the bubble from the wall. The results indicate that for a given explosion pressure there is an optimal distance of the bubble from the wall which gives the maximum impact pressure. This trend and the peak impact pressure are in good agreement with the experimental results. It has been shown that the optimal location is due to two different physical effects as the bubble collapses near the wall. The evolution of the vortex ring bubble, reported in earlier experimental and numerical studies, is also accurately predicted.

Some limitations of the current ALE3D code have also been identified. However, most of these limitations can be corrected by proper modifications to the code. Current effort is directed towards this goal so that more realistic (i.e., using real explosives) deep and shallow water explosion studies can be carried out. Extension to the code to handle sand surface properties is also being investigated for eventual study of explosions near buried surface.

ACKNOWLEDGMENTS

This work is supported by the Office of Naval Research under grant No. N00014-91-J-1993. ALE3D, a product of Lawrence Livermore National Laboratories was used for the simulations in this paper.

REFERENCES

Anderson, S., Dube, E., Futral, S., Otero, I., and Sharp, R. 1994 Users Manual For ALE3D. Lawrence Livermore National Lab., CA.

Arons, A. B. and Yennie, D. R. 1948 Energy partition in underwater explosion phenomenon. *Rev. Mod. Phys.*, 20, 519-536.

Best, J. 1993 The formation of toroidal bubbles upon the collapse of transient cavities. *J. Fluid Mech.*, 251, 79-107.

Birkhoff, G. 1956 Stability of spherical Bubbles. *Quart. Appl. Math.*, 13, 451-453.

Blake, J. R., Taib, B. B., and Doherty, G. 1986 Transient cavities near boundaries. Part I. Rigid boundary. *J. Fluid Mech.*, 170, 479-497.

Blake, J. R. and Gibson, D. C. 1987 Cavitation bubbles near boundaries. *Annual review of fluid mechanics*, 153, 259-273.

Chahine, G. L., and Perdue, T. O. 1988 Simulation of the three-dimensional behavior of an unsteady large bubble near a structure. 3rd International Colloquium on Bubbles and Drops, Monterey, CA.

Cole, R. H. 1948 Underwater Explosions. Princeton University Press, Princeton.

Couch, R., Albright, E. and Alexander, N. 1983 JOY Computer Code. Lawrence Livermore Laboratory, CA, UCID-19688.

Couch, R. and Faux, D. 1996 Simulation of underwater explosion benchmark experiments with ALE3D. UCRL-CR-123819, Lawrence Livermore National Laboratory, Livermore, CA.

Duncan, J. H., and Zhang, S. 1991 On the interaction of a collapsing cavity and a compliant wall. *J. of Fluid Mech.*, 226, 401-423.

Kolk, W. R., and Lerman, R. A. 1992 Nonlinear system dynamics, Van Nostrand Reinhold, New York, 179-216.

Lal, M. K., and Menon, S. 1996 Interaction of two underwater explosion bubbles.

ASME FED, 1, 595-600.

Lauterborn, W. 1976 Numerical investigation of nonlinear oscillations of gas Bubbles in liquids. *J. Acoust. Soc. Am.*, 59, 283-293.

Menon, S. and Lal, M. K. 1998a On the dynamics and instability of bubbles formed during underwater explosions. *Experimental Thermal and Fluid Science Journal, to appear.*

Menon, S. and Lal, M. K. 1998b Experimental studies of underwater explosions near exposed and buried rigid surfaces. Under preparation.

NIST 1988 Thermophysical Properties of Water (Steam). NIST Standard Reference Database 10, U. S. Dept. Commerce.

Plesset, M. S. 1954 On the stability of fluid flows with spherical symmetry, *J. Appl. Phys.*, 25, 96-98.

Plesset, M. S. 1971 The dynamics of cavitation bubbles. *J. Appl. Mech.*, 16, 277-282.

Plesset, M. S. and Chapman, R. B. 1971 Collapse of an initially spherical cavity in the neighborhood of a solid boundary. *J. of Fluid Mech.*, 47, 283-290.

Pritchett, J. W. 1971 Incompressible calculations of underwater explosion phenomena, Proceedings of the second international conference on numerical methods in fluid dynamics, Springer, 422-428.

Prosperetti, A. 1982 A generalization of the Rayleigh-Plesset equation of bubble dynamics. *Phys. Fluids*, 25, 409-410.

Shepherd, J. E. 1988 Interface effects in underwater explosions. Proc. Conventional Weapons Underwater Explosions, ONR Workshop Report, 43-88.

Steinberg, D. 1991 Equation of state and strength properties of selected materials. Lawrence Livermore Natn. Lab., Livermore, CA, UCRL-MA-106439.

Szymczak, W. G., Rogers, J. C. W., Solomon, J. M. and Berger A. E. 1993 A numerical algorithm for hydrodynamic free boundary problems. J. *Comput. Phys.*, 106, 319-336.

Tomita. Y., and Shima. A. 1986 Mechanisms of impulsive pressure generation and damage pit formation by bubble collapse. *J. Fluid Mech.*, 169, 535-564.

Tipton, R. E. 1990 CALE User Manual. Lawrence Livermore Laboratory.

Tipton, R. E., Steinberg, D. J., and Tomita, Y. 1992 Bubble expansion and collapse near a rigid wall. *JSME*, 35, 67-75.

Trilling, L. 1952 The collapse and rebound of a gas bubble, *J. Appl. Phys.*, 23, 14-17.

Van Leer, B. 1977 Towards the ultimate conservative difference scheme. IV. A new approach to numerical convection. *J. Comp. Phys.*, 23, 276-299.

Vogel, A., Lauterborn, W. and Timm, R. 1989 Optical and acoustic investigations of the dynamics of laser-produced cavitation bubbles near a solid boundary. *J. Fluid Mech.*, 206, 299-338.

Vokurka, K. 1985 On Rayleigh's model of a freely oscillating bubble. *Czech. J. Phys. B*, 35, 121-132.

Vokurka, K. 1987 Oscillations of gas bubbles generated by underwater explosions, *Acta Technical Ssav.* 2, 162-172.

Warren, G. R. and Rice, T. W. 1964 The interaction of the gas bubbles from two adjacent underwater explosions. Foulness Division Note 9-64, Atomic Weapons Research Establishment, United Kingdom Atomic Energy Authority.

Wilkerson, S. A. 1989 Boundary integral technique for explosion bubble collapse analysis. ASME, Energy-sources technology conference and exhibition, Houston, 1989.

Zhang, S., Duncan, J. H. and Chahine, G. L. 1993 The final stage of the collapse of a cavitation bubble near a rigid wall. *J. Fluid Mech.*, 257, 147-181.

Zhang, S. and Duncan, J. H. 1994 On the non spherical collapse and rebound of a cavitation bubble. *Phys. Fluids*, 6, 2352-2362.

LIST OF FIGURES

Figure 9. Formation of the toroidal ring vortex bubble on the wall for various cases in terms of the velocity vector field. All solutions are at 15 ms (for case 1 see Fig. 8b). (a) Case 2, (b) Case 3.

Figure 10. Comparison of the impact pressure on the plate below the bubble for various initial bubble locations (cases 1-3).

Figure 11. Normalized (by initial explosion pressure) maximum impact pressure on the wall as a function of initial bubble location above the wall. ALE3D results are compared to the experimental data (Menon and Lal, 1998b).

Figure 12. Variation of the pressure on the wall away from the jet stagnation point. Plot shows that the impinging jet is narrow and highly focussed. This results in a high impact pressure.

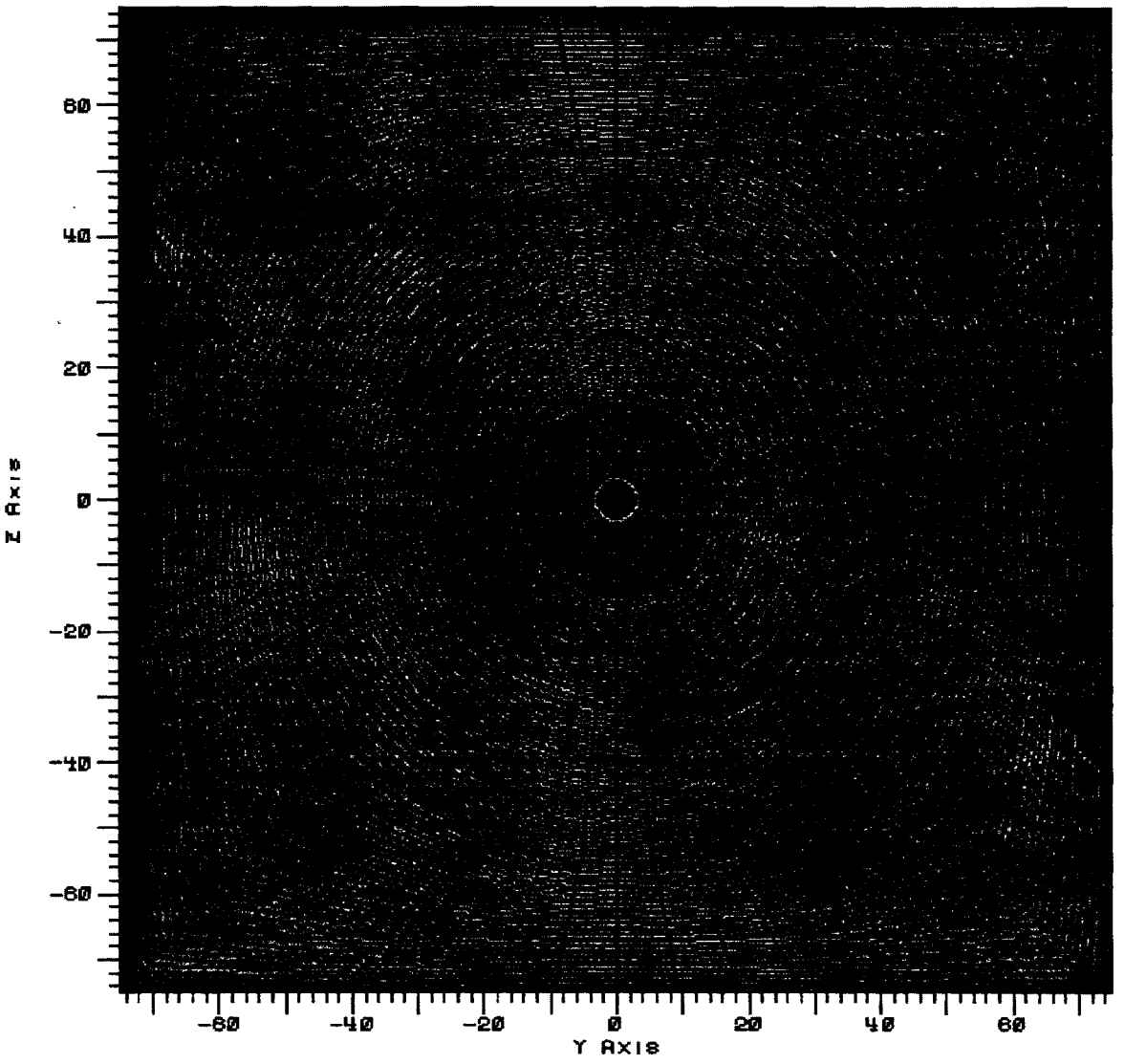
60
40
20
0
-20
-40
-60
Z Axis
-60
-40
-20
0
20
40
60
Y Axis

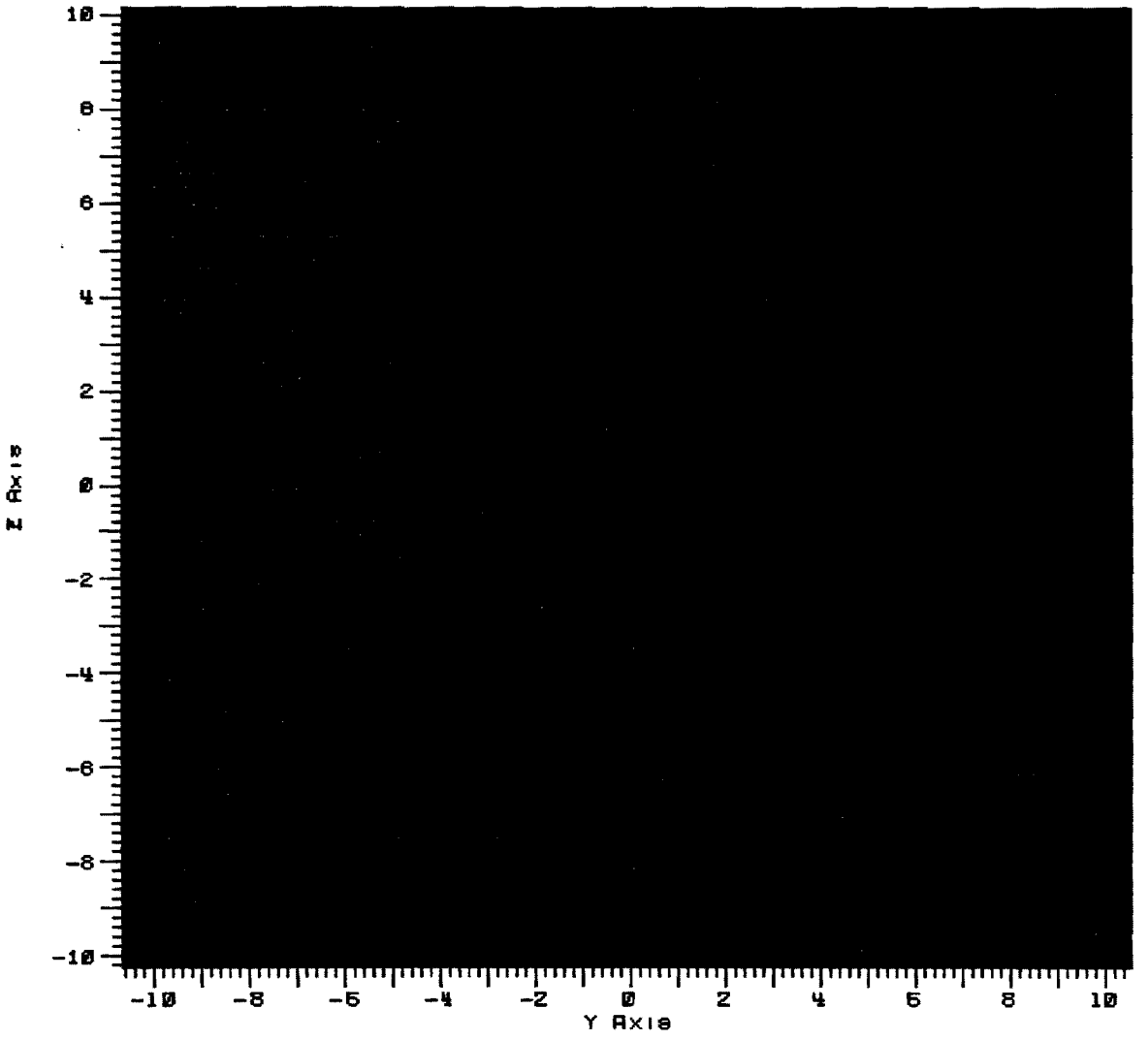
10
8
6
4
2
0
-2
-4
-6
-8
-10
Z Axis
-10
-8
-6
-4
-2
0
2
4
6
8
10
Y Axis

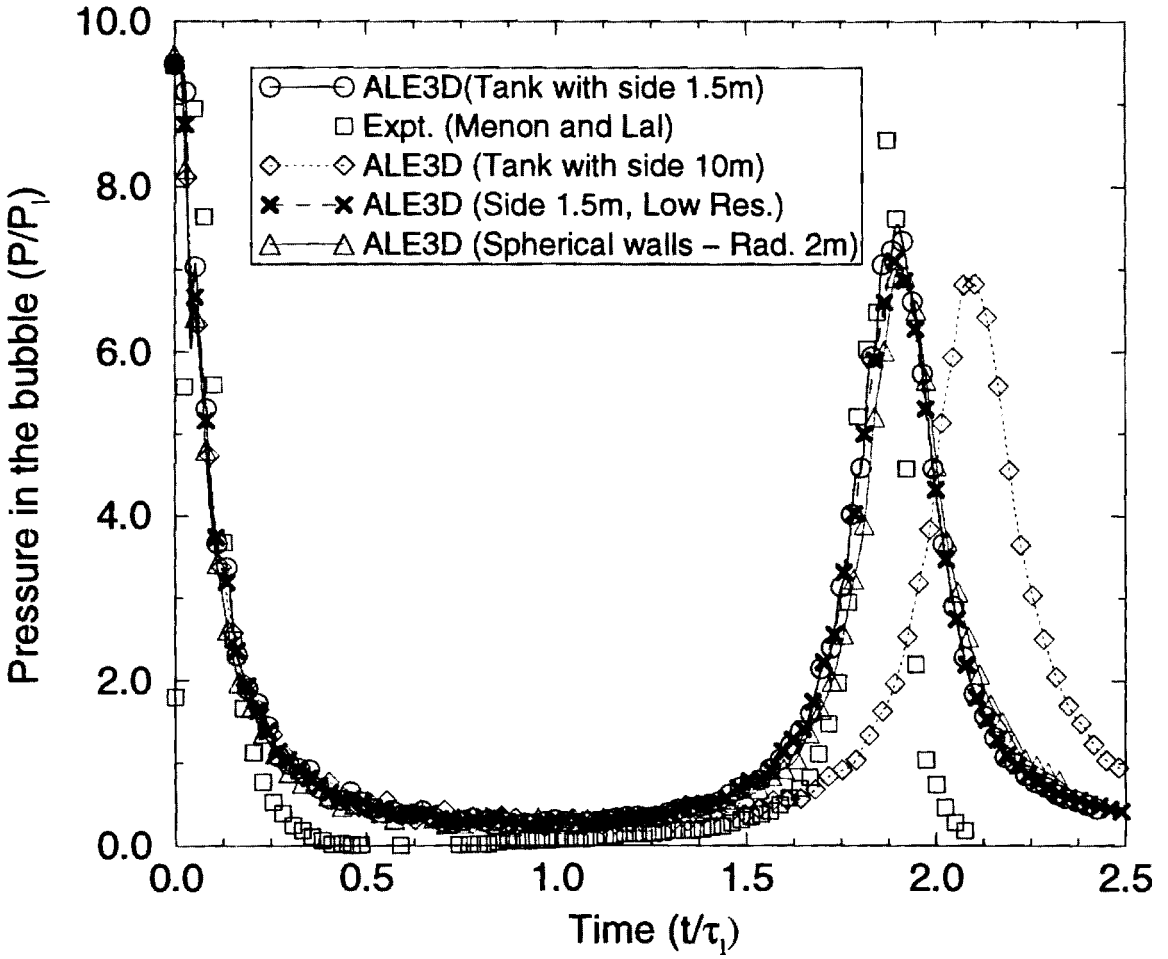
ALE3D(Tank with side 1.5m)
Expt. (Menon and Lal)
ALE3D (Tank with side 10m)
ALE3D (Side 1.5m, Low Res.)
ALE3D (Spherical walls – Rad. 2m)
Pressure in the bubble (P/P$_I$)
Time (t/τ_I)
10.0
8.0
6.0
4.0
2.0
0.0
0.0
0.5
1.0
1.5
2.0
2.5

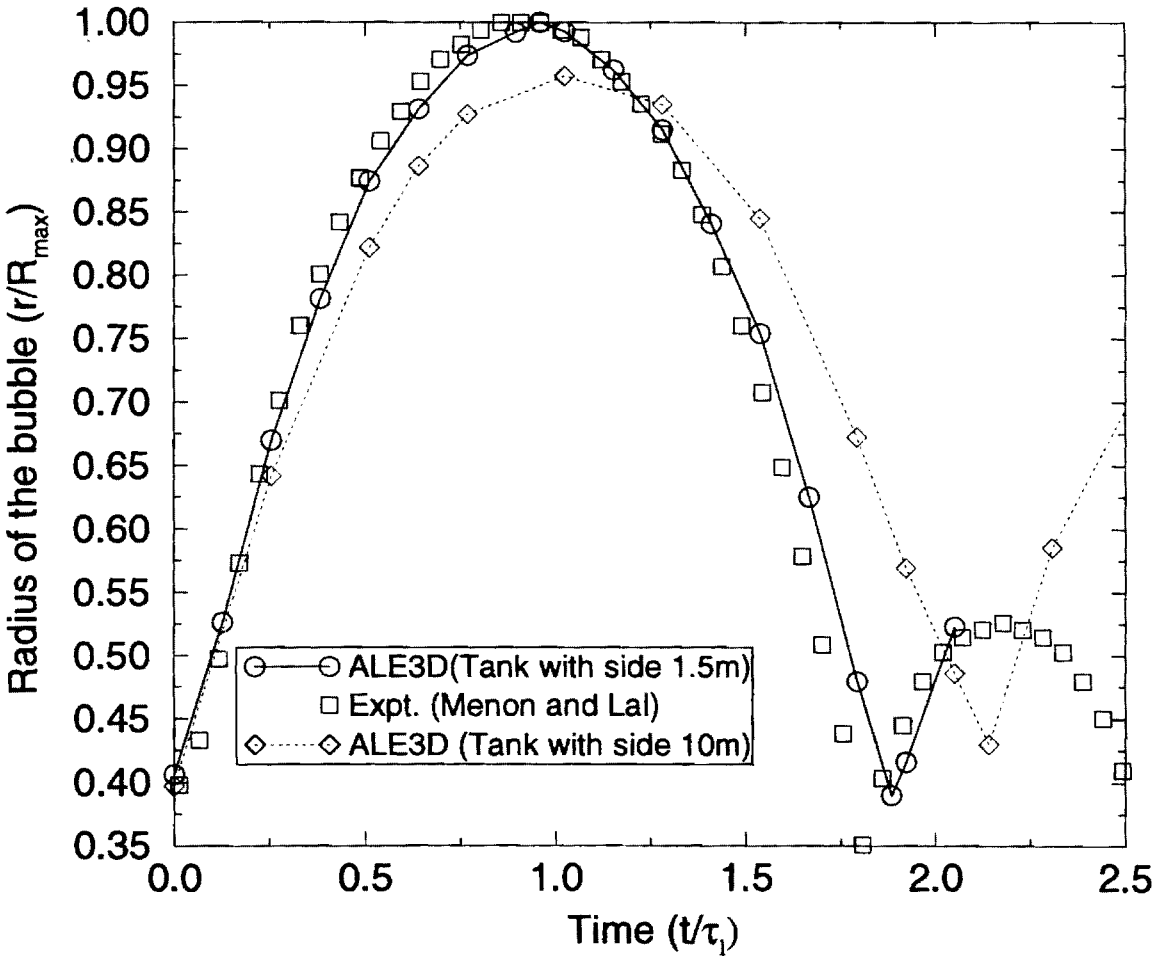
1.00
0.95
0.90
0.85
0.80
0.75
0.70
0.65
0.60
0.55
0.50
0.45
0.40
0.35
Radius of the bubble (r/R_max)
0.0
0.5
1.0
1.5
2.0
2.5
Time (t/τ_1)
ALE3D(Tank with side 1.5m)
Expt. (Menon and Lal)
ALE3D (Tank with side 10m)

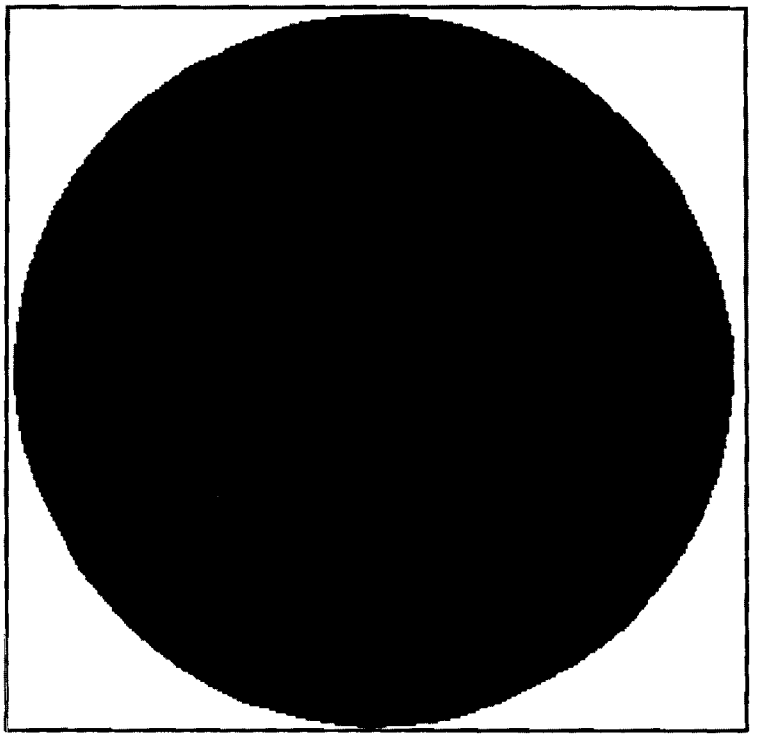

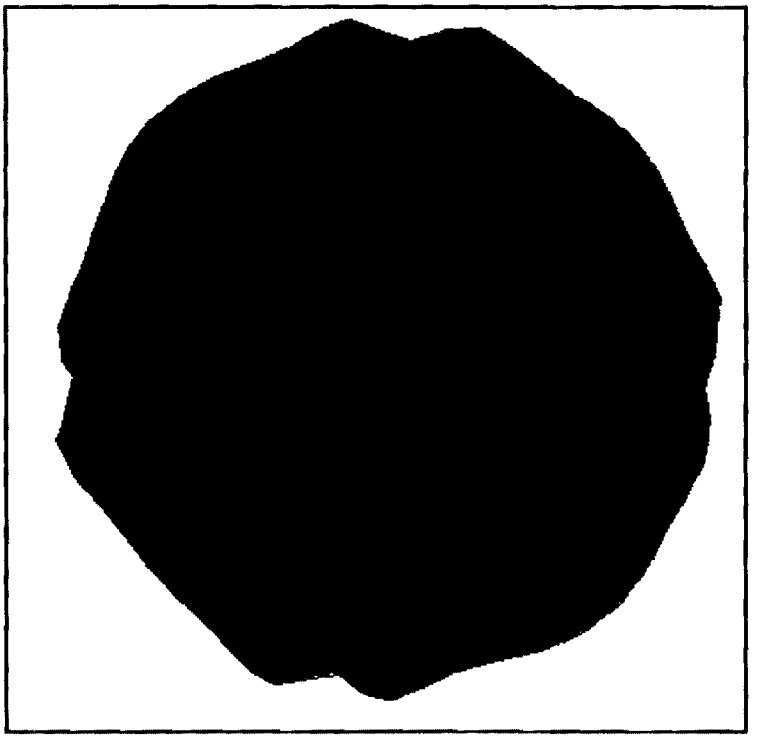

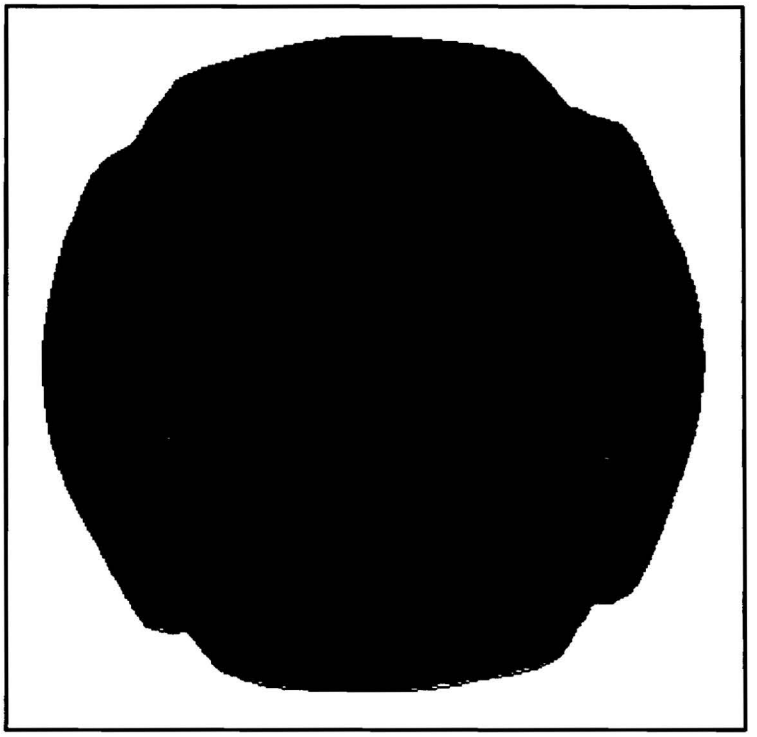

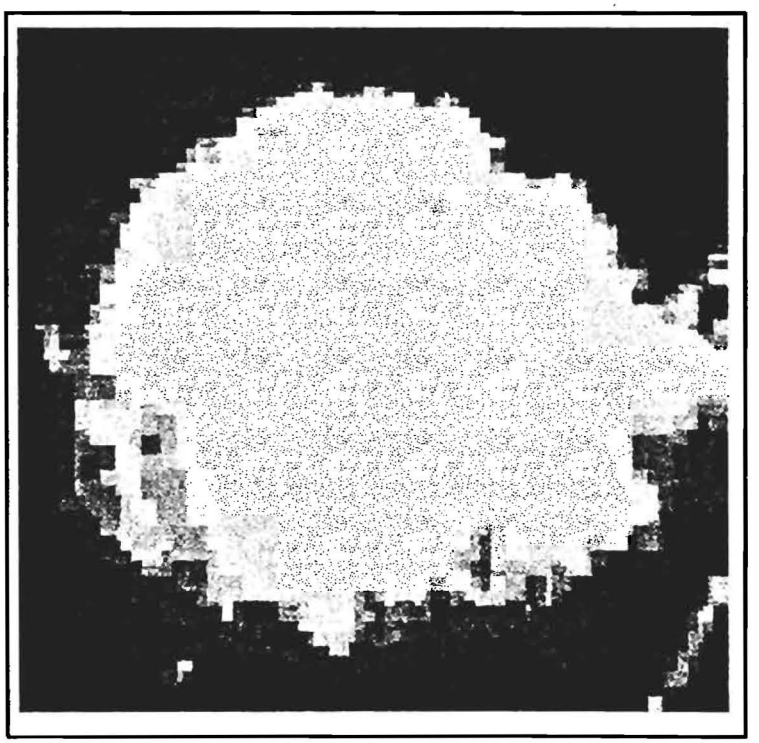

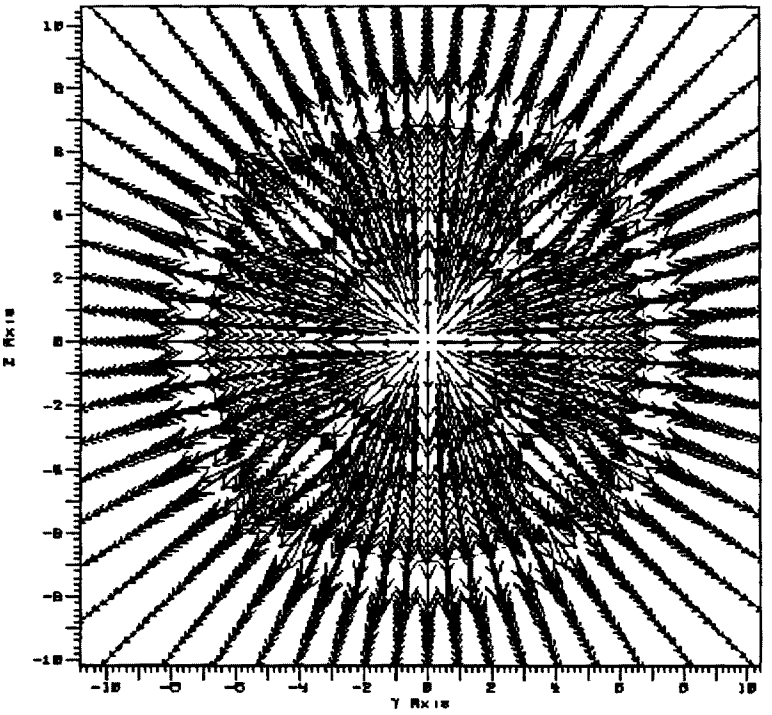
Z Axis
Y Axis

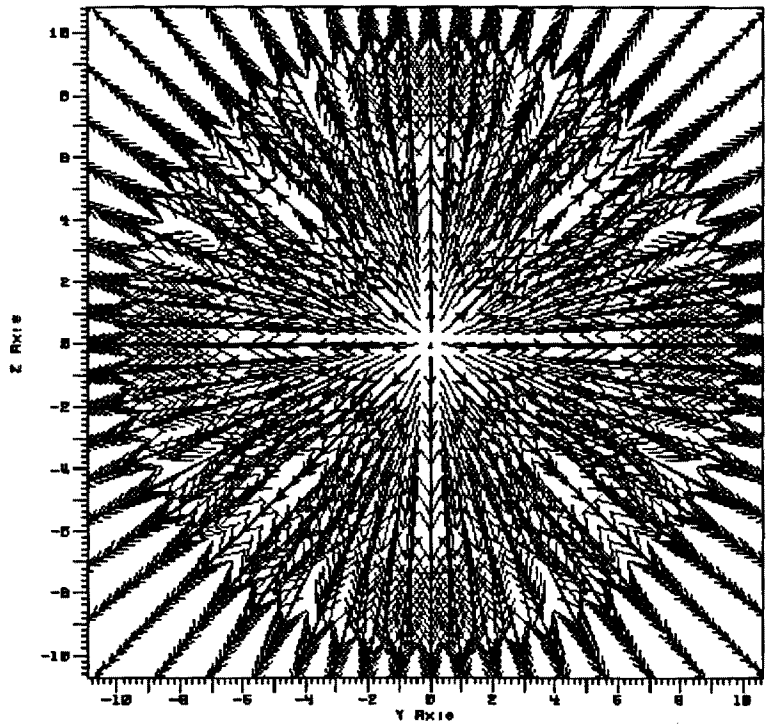
Z Axis
Y Axis

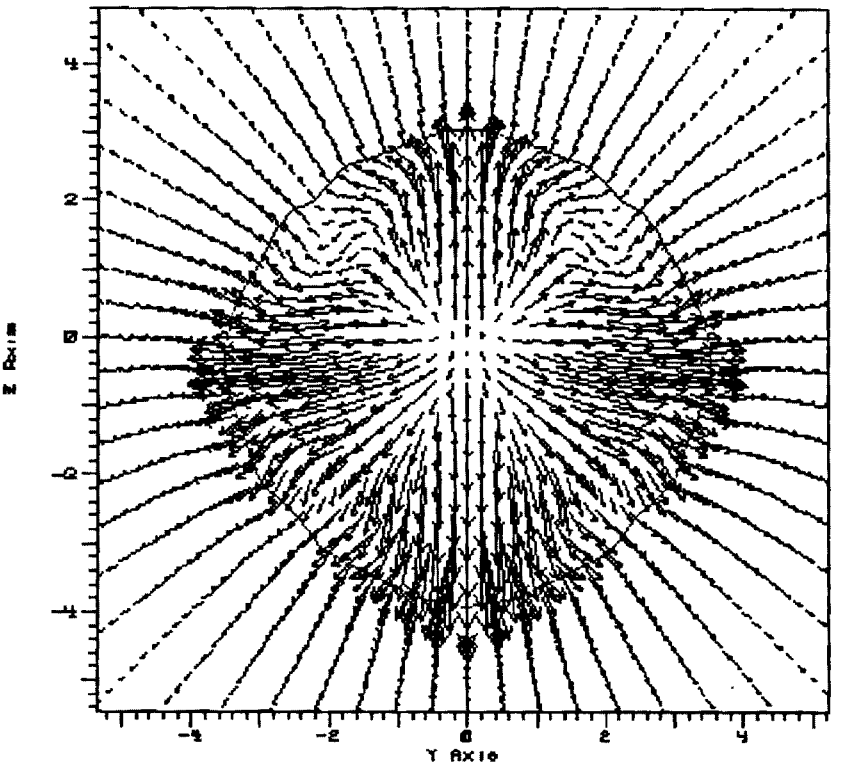
Z Axis
4
2
0
-2
-4
-4
-2
0
2
4
Y Axis

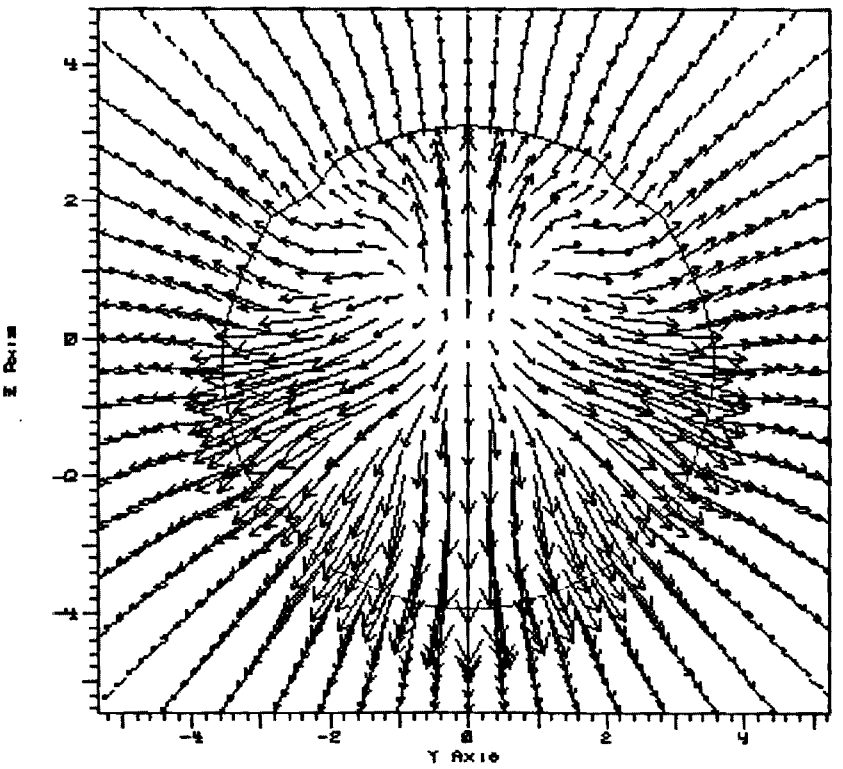
Z Axis
4
2
0
-2
-4
-4
-2
0
2
4
Y Axis

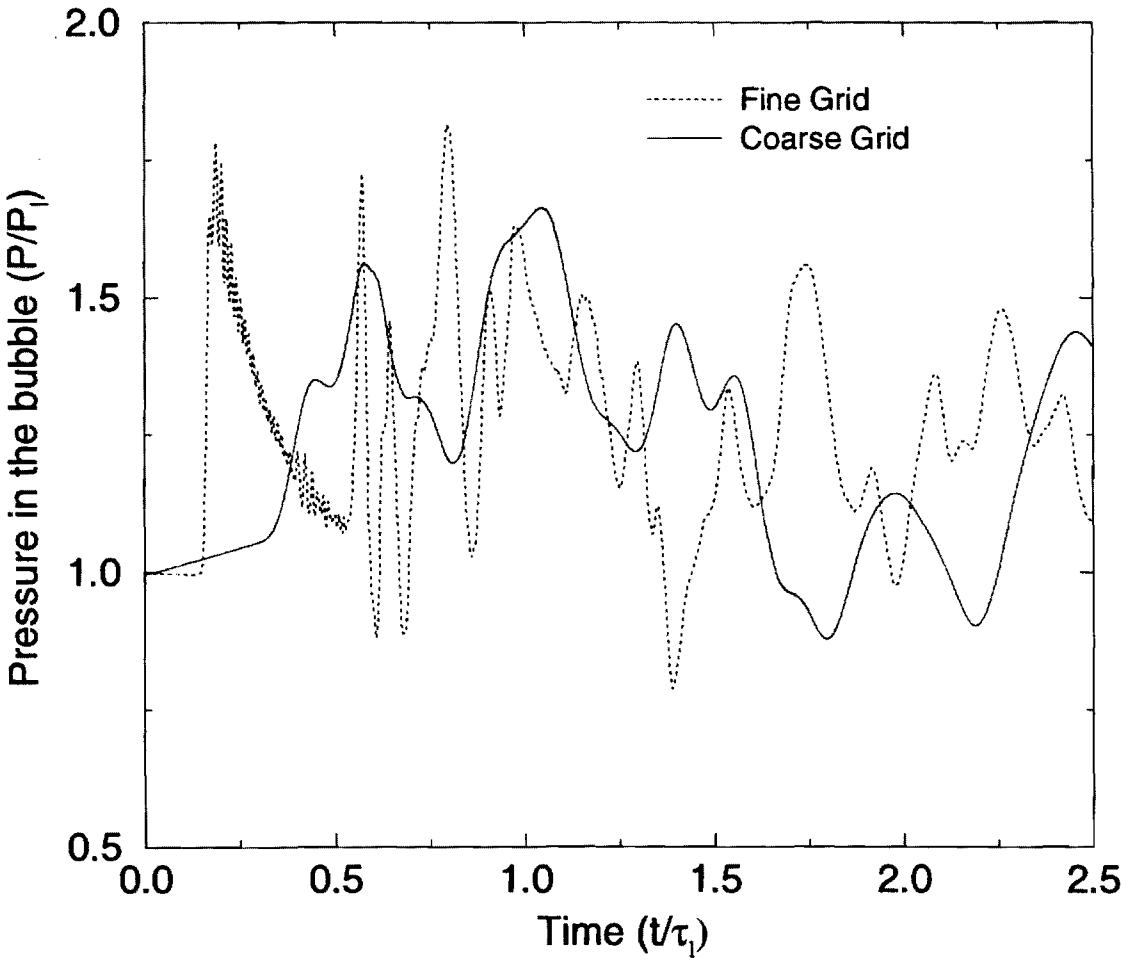
Fine Grid
Coarse Grid
Pressure in the bubble (P/P$_l$)
Time (t/τ_l)
2.0
1.5
1.0
0.5
0.0
0.5
1.0
1.5
2.0
2.5

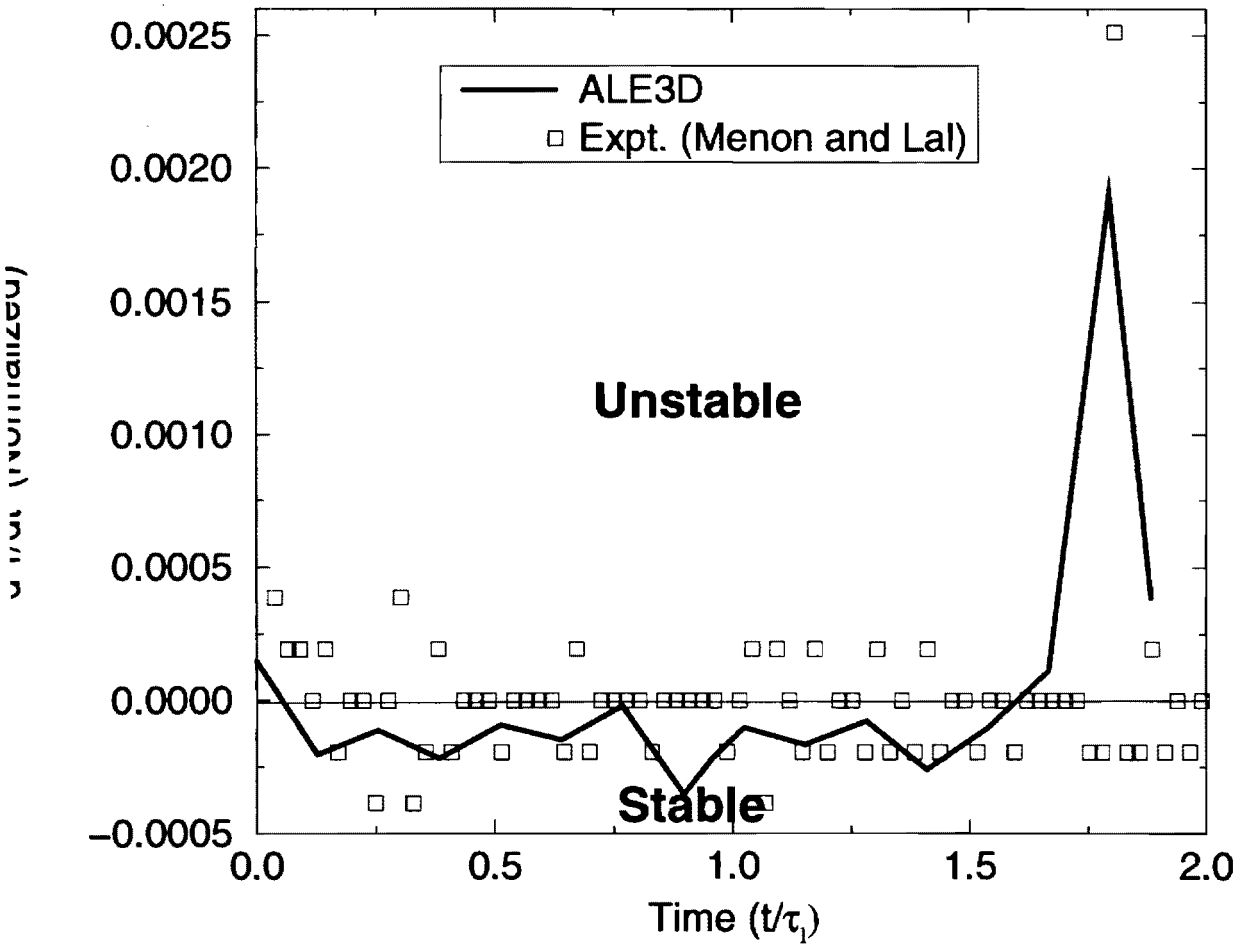
0.0025
0.0020
0.0015
0.0010
0.0005
0.0000
−0.0005
0.0
0.5
1.0
1.5
2.0
Time (t/τ1)
ALE3D
Expt. (Menon and Lal)
Unstable
Stable

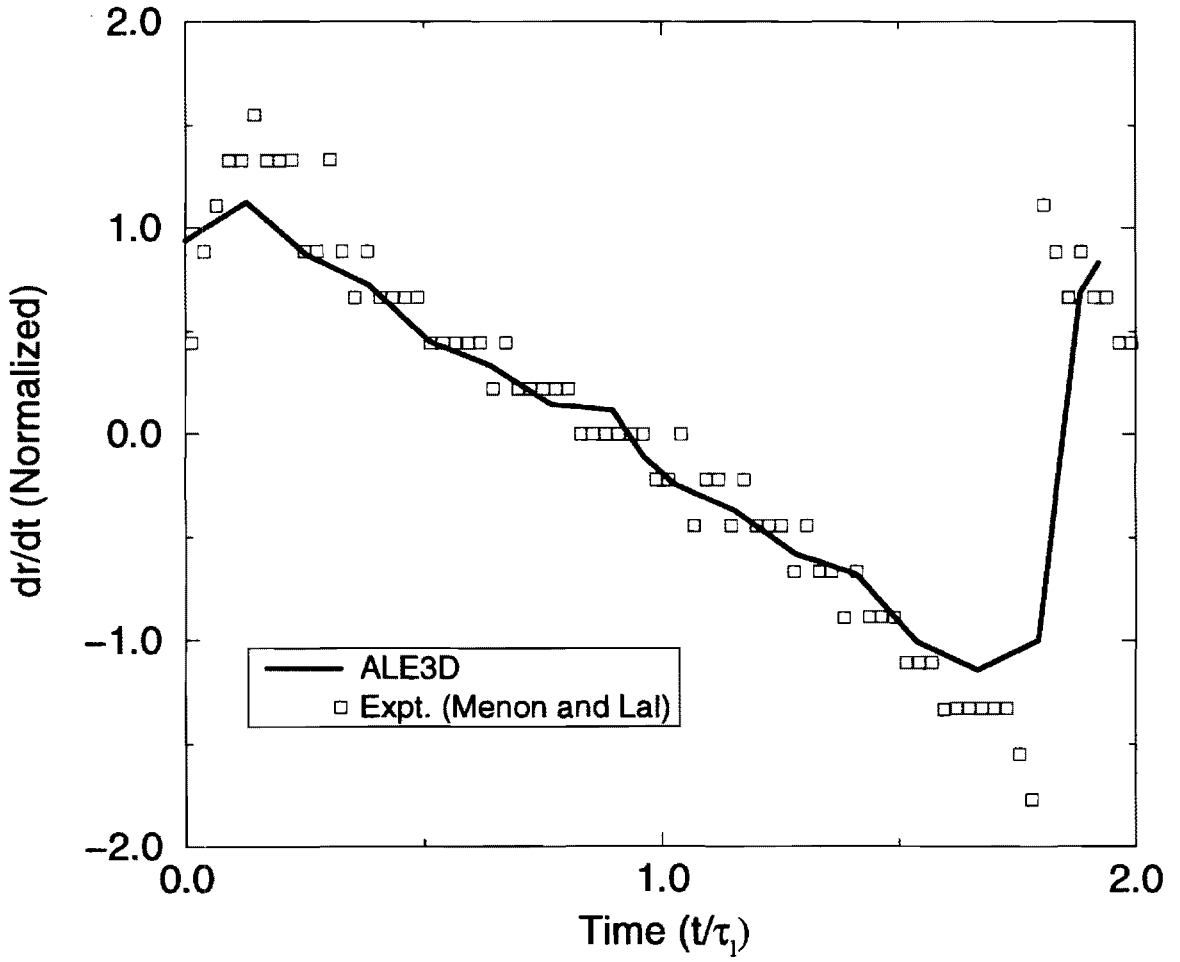
2.0
1.0
0.0
−1.0
−2.0
0.0
1.0
2.0
dr/dt (Normalized)
Time (t/τ1)
ALE3D
Expt. (Menon and Lal)

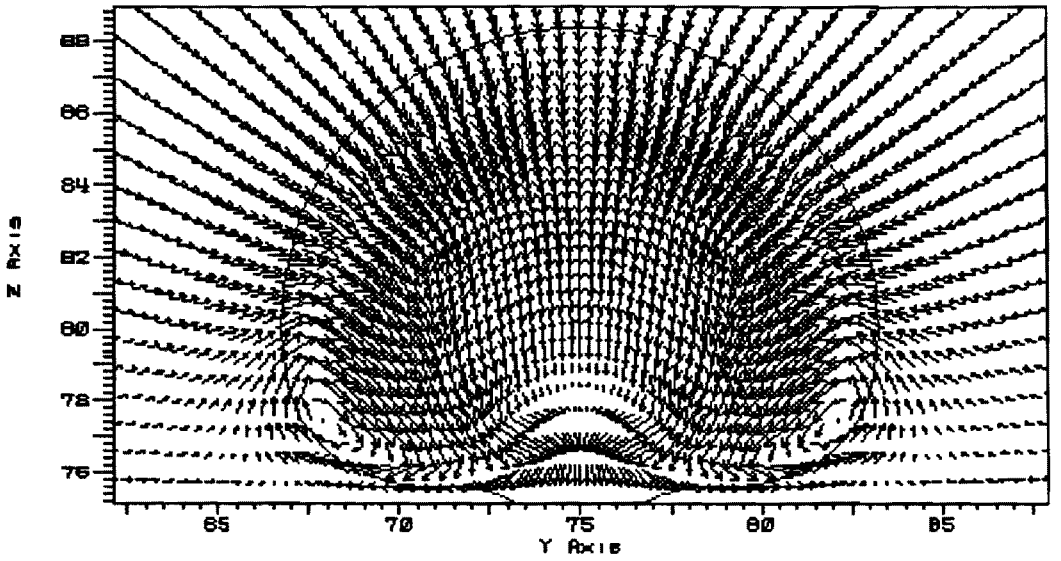
88
86
84
82
80
78
76
Z Axis
65
70
75
80
85
Y Axis

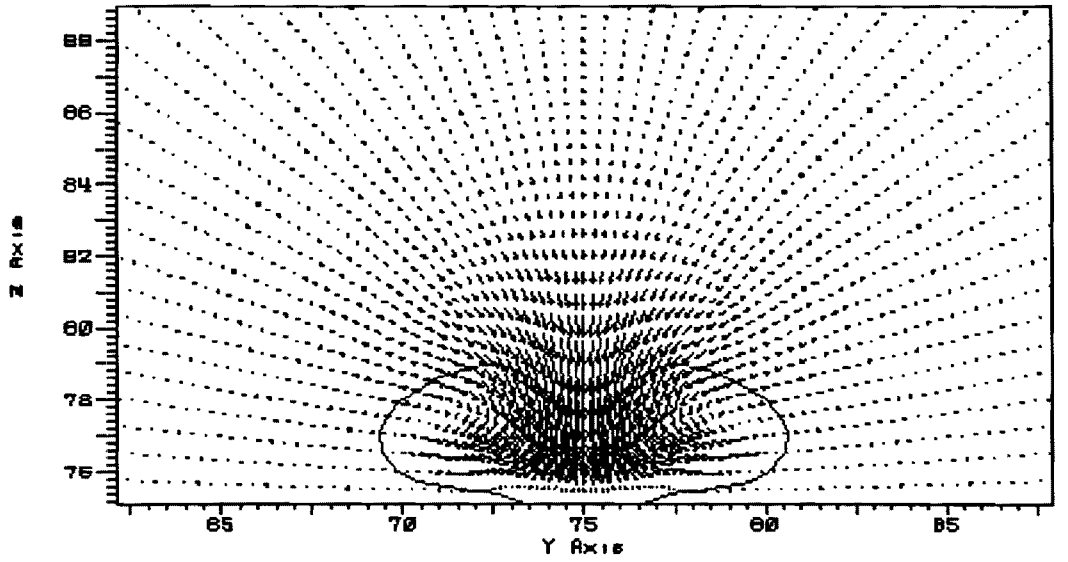
88
86
84
82
80
78
76
Z Axis
65
70
75
80
85
Y Axis

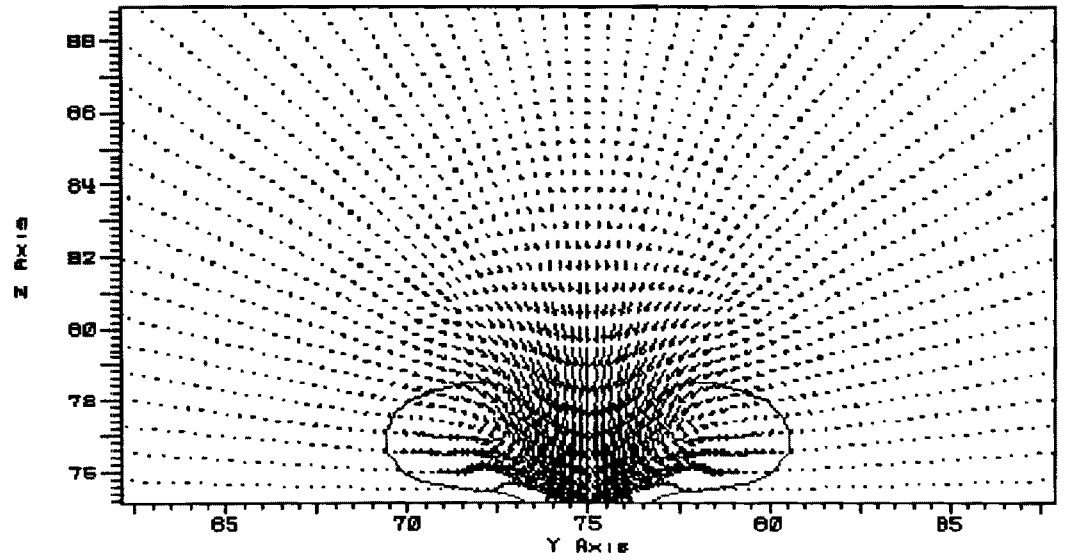
88
86
84
82
80
78
76
Z Axis
65
70
75
80
85
Y Axis

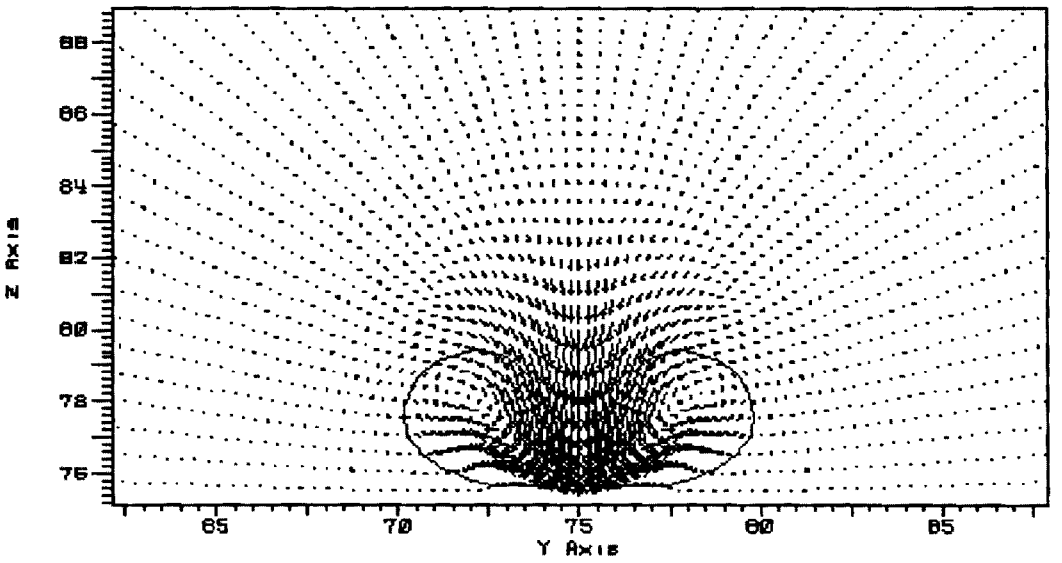
88
86
84
82
80
78
76
Z Axis
65
70
75
80
85
Y Axis

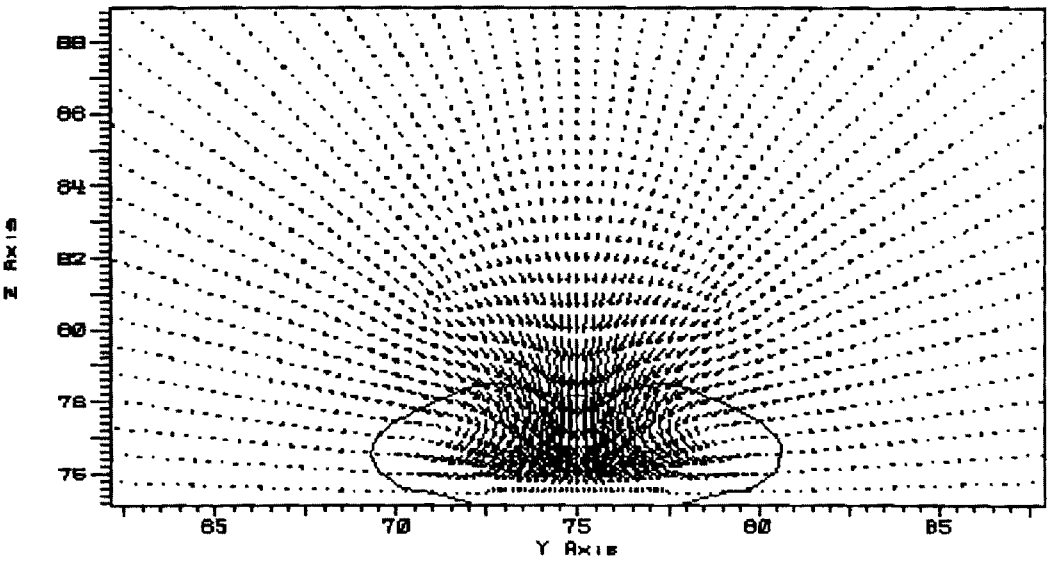
88
86
84
82
80
78
76
Z Axis
65
70
75
80
85
Y Axis

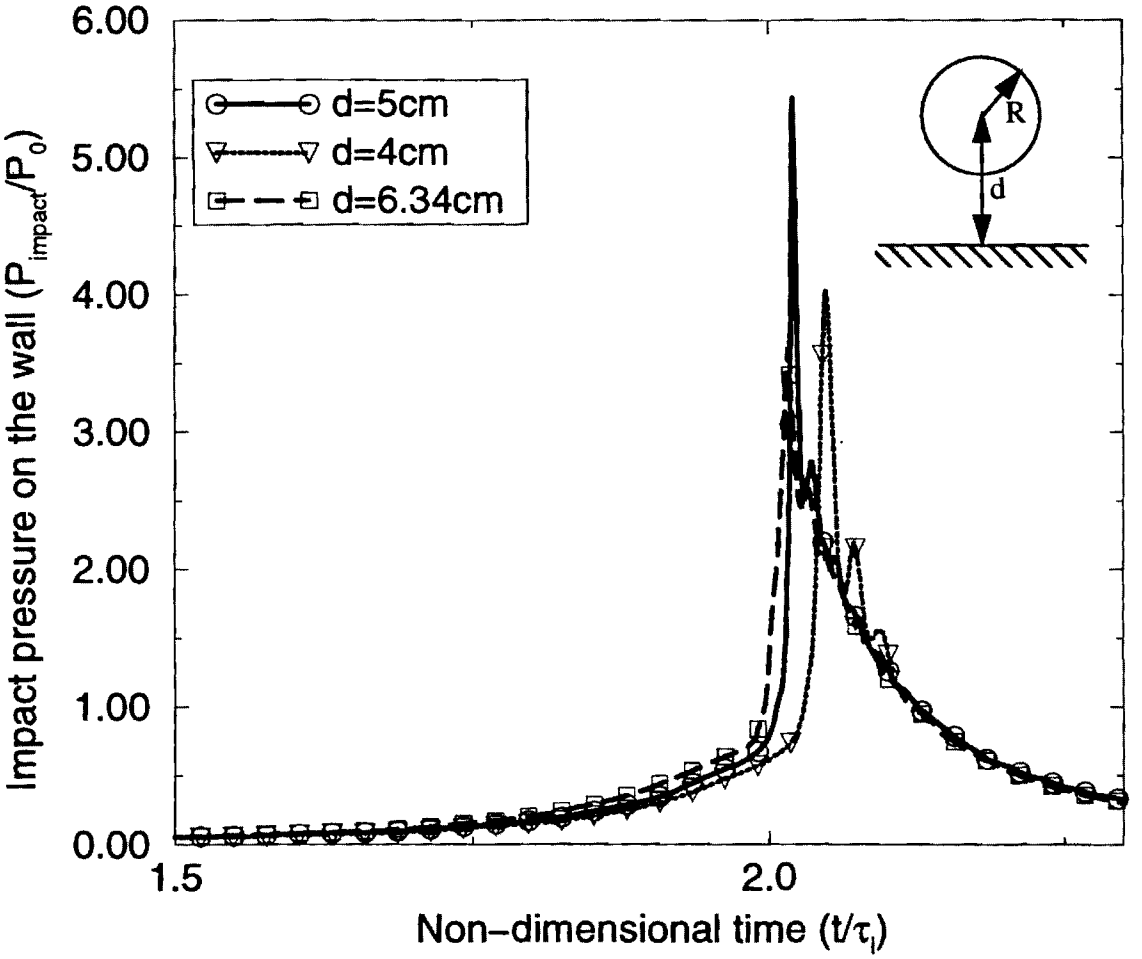
6.00
5.00
4.00
3.00
2.00
1.00
0.00
1.5
2.0
Impact pressure on the wall (P_{impact}/P_0)
Non-dimensional time (t/τ_1)
d=5cm
d=4cm
d=6.34cm
R
d

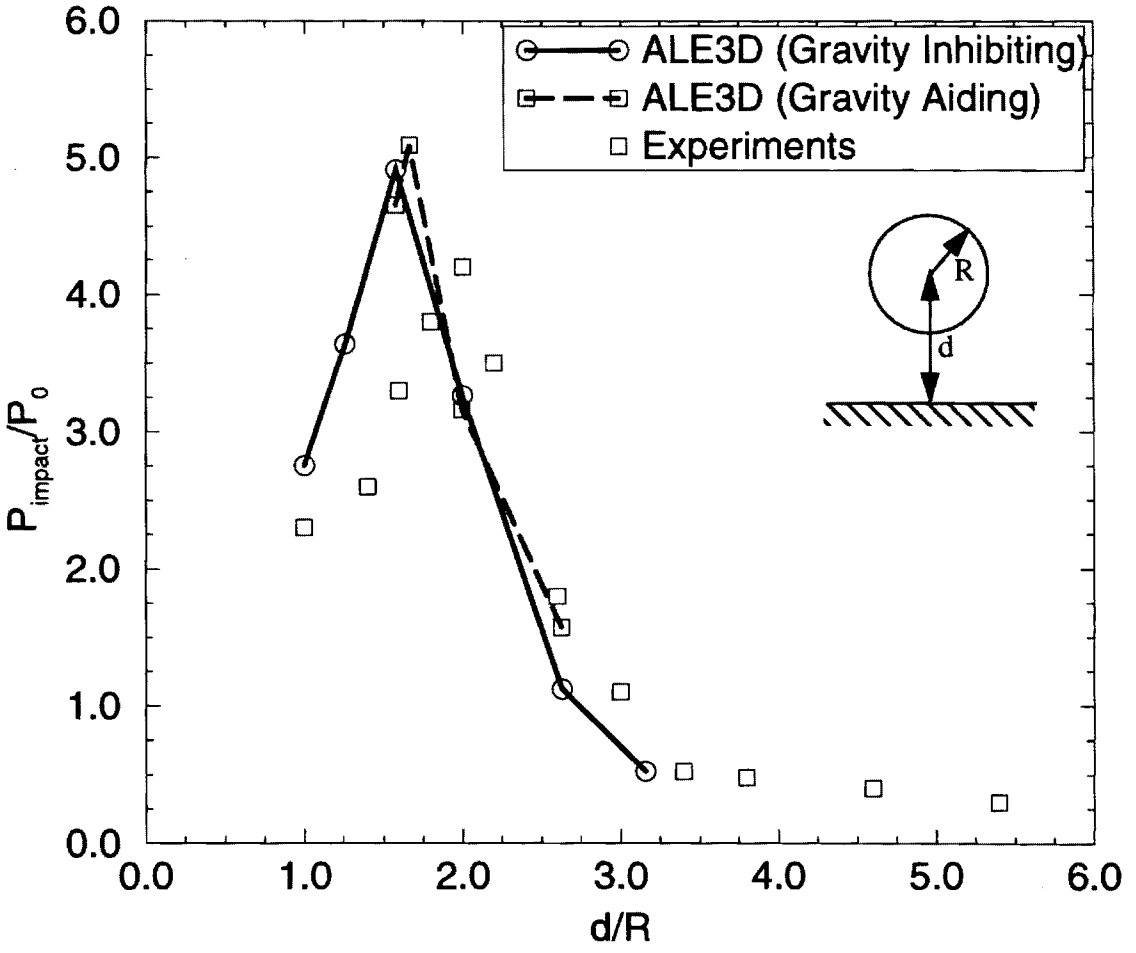
ALE3D (Gravity Inhibiting)
ALE3D (Gravity Aiding)
Experiments
R
d
P_{impact}/P_0
d/R
0.0
1.0
2.0
3.0
4.0
5.0
6.0

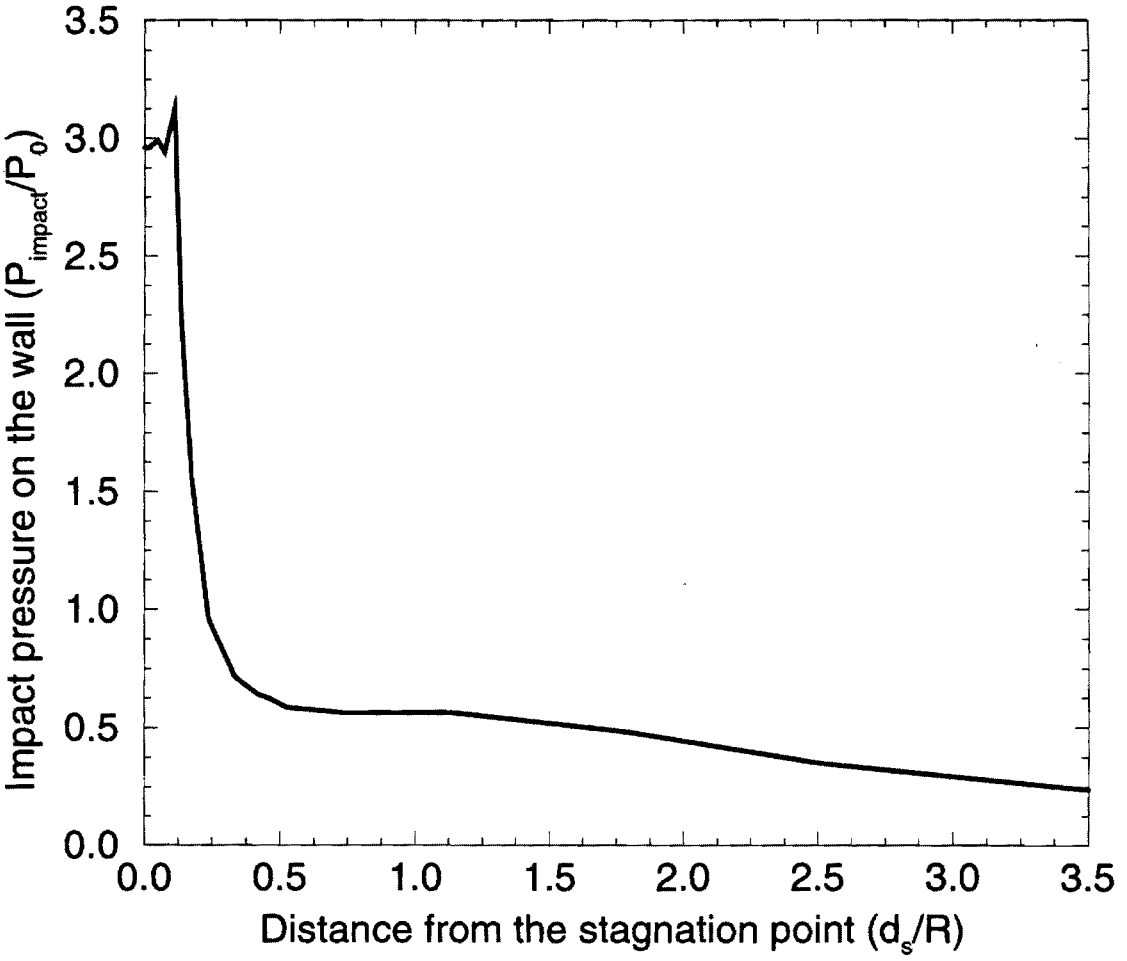
Impact pressure on the wall (P_{impact}/P_o)
3.5
3.0
2.5
2.0
1.5
1.0
0.5
0.0
0.0
0.5
1.0
1.5
2.0
2.5
3.0
3.5
Distance from the stagnation point (d_s/R)

Preliminary Draft (03/04/98)

Experimental Studies of Underwater Explosions near Exposed and Buried Rigid Surfaces

S. Menon and M. Lal
School of Aerospace Engineering
Georgia Institute of Technology
Atlanta, Georgia 30332-0150

To be submitted to
Journal of Fluids and Structures

ABSTRACT

Underwater explosion bubbles are created near an exposed or buried rigid boundary by detonating a mixture of oxygen and Carbon Monoxide in glass globes submerged in a water tank. A variable depth of either play sand or general purpose purge clay is used to bury a solid steel plate in order to simulate explosion over a buried rigid boundary. Eight pressure transducers mounted on the plate are used to map the pressure distribution on the plate and instrumented tubes and plugs measure pressure inside and outside the bubbles. A cinematographic technique is employed to capture entire interaction process. There exists a critical distance above the plate where the reentrant water jet produces the maximum impact pressure on the plate. The water jet is very focused and symmetrical about the center of impact. The effect of covering the flat plate with sand or clay is in general, to reduce the impact pressure and smoothen its distribution over the plate. However, when an explosion ocurrs very close to the sand surface loose sand particles are ejected and displaced as the bubble expands. The reduces the effective sand thickness and as a result, an increased impact pressure is achieved. This recovery of impact pressure increases in shallow water cases due to the free surface effect. Explosions were also carried out above clay surface to view the shape of the crater formed. Results show that double craters (i.e., secondary crater within the primary crater is formed for certain initial locations of the explosive above the surface.

1. INTRODUCTION

Underwater detonation of explosive material converts the unstable material into a more stable gas void at high temperature and pressure. The high pressure of the remnants of an underwater detonation sets forth an expansion-collapse cycle of the resulting underwater explosion bubble which is repeated several times before the bubble goes through interface instabilities and eventually disintegrates into a cloud of smaller bubbles. The interface instability problem is an interesting and complex subject and has recently been addressed based on experimental and analytical methods by Menon and Lal (1998). Various instability mechanisms at play during the bubble oscillation cycles were addressed and it was shown that the Rayleigh-Taylor instability occurs during the bubble collapse and plays a major role in the eventual collapse of the bubble.

The presence of a solid surface in the vicinity of a pulsating bubble manifests itself as an asymmetry in the flow field. A dominant feature in the collapse of a bubble in such a flow is the development of a reentrant water jet. The asymmetry in the flow causes one side of the bubble to accelerate inward more rapidly than the opposite side resulting in a high-speed reentrant jet which pierces the bubble in the direction of its migration and produces an impact pressure much larger than the explosion pressure. This increased pressure on the surface can cause structural damage especially when the explosion energy (and hence the bubble size) is large. Other asymmetries (i.e., gravity or a free surface) can also cause the formation of the reentrant jet. The jets caused by gravity are directed upward and those caused by free surfaces are directed away from them.

Much of the research activities in the area of underwater bubble dynamics have been focused on the behavior of cavitation bubbles. Vapor and gas bubble dynamics are of great

practical interest in prediction and prevention of cavitation erosion of marine propeller and turbine blades. The fact that the collapse of these tiny microbubbles near a solid boundary is also characterized by the formation of reentrant jets leading to formation of damage pits on the solid wall has led to the huge amount of research activity in the field. Researchers have resorted to experimental (e.g., laser induced bubbles) and various numerical (e. g., boundary-integral method) techniques to model and predict the behavior of cavitation bubbles. On the other hand, large bubbles are created by larger underwater explosion. These large bubble due to their tremendous destructive capabilities upon collapse near a rigid boundary find practical applications in underwater weaponry. However, detailed measurements and imaging of pulsating bubbles formed during deep sea explosions are very difficult due to a variety of obvious reasons and therefore, there is insufficient data available to analyze the dynamics of interaction of such large bubbles with a solid boundary. Controlled experiments as described in this paper can be very helpful in providing some insight into the problem.

Recently, a series of experiments were carried out to investigate underwater explosions in shallow water (1 atmosphere ambient pressure) to understand the dynamics of bubble-wall interaction in such flows and to investigate feasibility of targeting and destroying mines buried in beaches. In this configuration (shown in Fig. 1), the free water surface is close enough to the bubble-wall interaction region to allow it to play a role in modifying the dynamics of the bubble collapse. The free surface provides a constant pressure boundary in close proximity to the wall. It is known that the bubble moves away from the free surface and a reentrant jet is formed which pierces the bubble in the direction of its migration (e.g., Birkhoff, 1957; Blake and Gibson, 1981; Chahine, 1977; Chahine, 1982; Wilkerson, 1989). Since, both the Bjerknes force and the buoyancy force, the two competitive forces acting on a bubble near a free surface, act in the same direction, the presence of the free surface above the bubble collapse region is likely to increase the net impact pressure on the wall. Another issue that was investigated is the behavior of the

impact process when the rigid surface is buried below a layer of sand as would be the case for buried mines. Some interesting results have been obtained and summarized in this paper.

This paper reports the results of the experiments carried out in a laboratory water tank to study the interaction of a pulsating bubble created by underwater explosion of flammable gas contained in a glass globe with a nearby solid wall. The wall was later covered with sand or clay to simulate explosion over a buried wall. The location of the globe with respect to the wall was varied for a parametric study. The water surface was lowered to study shallow water interactions.

2. EXPERIMENTAL PROCEDURES

Underwater explosion experiments near a solid boundary were conducted in a wooden tank of dimension 2 m × 1.5 m × 1.5 m, coated with fiberglass resin from inside. The tank has windows on three sides for optical imaging. The underwater explosion bubble is generated by centrally igniting a mixture of an explosive gas (either Hydrogen or Carbon Monoxide) and oxygen contained in a hand-blown glass globe over a steel plate of dimension 36.83 cm × 60.96 cm × 0.635 cm (shown in Fig. 2). Two different sizes of glass globes were used for present experiments with average radii of 2.54 cm and 3.2 cm. The glass globe has an electric spark ignition system connected to a 3000V DC power supply that ignites the premixed fuel-air stoichiometric mixture contained in the globe. The explosion takes place at a constant volume until the globe bursts. Since the experiments were conducted in a laboratory shallow water setup and using a gaseous explosive mixture, the bubbles are relatively smaller (although much larger than cavitation bubbles) than those observed in deep sea explosions. Recently, Menon and Lal (1998) addressed the dynamics and instability issues of such a bubble in free field and they showed by means of extensive geometric and dynamic similarity analyses that the explosion

bubble thus formed is a reasonable subscale approximation of a deep sea underwater explosion bubble. They have presented detailed scaling parameters, energy partitioning and also various interface instability mechanisms. Repeatability and experimental uncertainty have also been addressed and it has been shown in particular that repeated experiments produced error bands for the explosion pressure, maximum radius and time period of 5.88%, 3.7% and 6.06%, respectively.

The pressure inside the bubble during its oscillation was measured by a KISTLER transducer which is mounted inside the plug. Additionally, eight KISTLER pressure transducers were mounted on the plate as shown in Fig. 2 to obtain a surface distribution of the impact pressure field. These dynamic pressure transducers have low and high frequency response of 0.001 Hz and 50 kHz, respectively, and the resonant frequency of 300 kHz. They are, therefore, well suited for the current experiments as the bubble oscillation frequency (time period of approximately 15 ms) lies well within the above mentioned bounds. Signals from these pressure transducers were digitized using National Instrument's AT-MIO-16X analog-to-digital converter board, and were recorded into a microcomputer. Ten channel data recording was performed with a sustained sampling rate of 10,000 samples per second per channel.

The distance between the globe and the plate was varied to investigate the effect of solid wall location relative to the explosion. The plate was later covered with sand or clay to simulate explosion over a buried wall. The thickness layer of sand and clay above the instrumented plate was also varied to determine how the impact pressure is affected by the porous material above the plate. The water surface was lowered to study shallow water bubble-wall, bubble-sand-wall and bubble-clay-wall interactions. The tank was illuminated by either direct overhead flood lights or an argon-ion laser sheet which lies in a vertical plane perpendicular to the camera axis. The optical recording of the bubble motion was performed by a CCD enhanced digital video camera at a speed of 1000 frames per second in order to obtain a full screen image.

3. VISUALIZATION OF THE BUBBLE-WALL INTERACTION

The collapse process near the wall (with and without the presence of the sand layer) was dynamically similar. Figure 3 shows a typical collapse process of a bubble near a rigid plate. The bubble expands subsequent to the explosion, however, the extend of the expansion (for a free field explosion, these bubbles were found to expand up to three times the initial diameter) depends on the relative position of the free surface and the rigid plate. As the bulb is brought closer to the plate, up to a certain distance an increase in the impact pressure is recorded by all transducers. If the distance between the bulb and the plate is further reduced beyond the certain distance, a reduction in the impact pressure is noted. The optimum distance is determined to be $d/R_o = 2$; where d is the distance between the bulb and plate, and R_o is the initial globe radius. Such an optimum distance was also observed in recent numerical studies (Menon and Pannala, 1998) where it was shown that this is due to effect of two different physics. When the bubble is too close to the wall it cannot fullu expand to its maximum diameter and thus, does not generate sufficient jet speed during collapse. On the other hand, when the bubble is too far away, there is a water layer between the callpasing bubble and the wall that the reentrant water jet has to penetrate. This also reduces the peak inpact pressure on the wall. When the bubble is at the optimum location, the bubble expands to its maximum and just touches the wall before undergoing the collapse process.

The pressure recorded by the transducer no. 8 located at the center of the plate and directly underneath the globe was found to be the maximum, $P_{Imp}/P_o = 4.19$ at the optimum distance, where P_{Imp} is the impact pressure on the plate at the center and P_o is the explosion pressure inside the bubble. Figure 4 shows the impact pressure (normalized by the explosion pressure) variation with distance from the plate. It also shows the pressure traces recorded by two off-center transducers (see Fig. 2 for locations). Although the impact pressure is noted to be

highest for $d/R_o = 2$, the actual magnitude of the pressure is much lower than the value at the central location. This implies that the impinging water jet is highly focused and does not spread at all. Figure 5 shows the distribution of the impact pressure on the plate and confirms earlier conjecture.

For a bubble collapse at the optimum distance, the time period of oscillation is found to be 19 ms, while it is around 15 ms in free field configuration. Therefore, as the bubble is brought close to the surface, an increase in the time period of oscillation is observed. If the bubble is brought further close to the surface beyond the optimum distance, the time period reduces slightly to 18 ms.

Experiments were also conducted to simulate underwater explosion over a buried surface as near a beach by covering the plate with varying depths of sand on the top. The typical parameters are identified in Fig. 1. The bubble collapse process optically obtained for this case is shown in Fig. 6. The bubble is once again attracted towards the plate and a reentrant jet is formed in the bubble in the direction of its migration. It can be seen from this figure that the bulb is almost touching the sand. The effect of covering the plate with sand is to reduce the impact pressure on the plate. Figure 7 shows the impact pressure at the center of the plate for various sand depths. When the plate is covered with the sand while maintaining the same distance between the plate and the bulb, a reduction in the impact pressure at the center of the plate is observed. However, when the sand depth is further increased so as to bring the bulb closer to the sand, a partial recovery of the impact pressure occurs as shown in Fig. 7. Here, the distance of the bubble from the sand surface becomes more important. An explosion close to the sand surface creates a crater in the sand. The sand particles are ejected or displaced from the center and are deposited at the rim of the crater in the form of ejecta. This process is quite similar to crater formation even when there is no water present as on planetary surfaces. The key result of the ejecta formation is that the effective sand thickness at the center decreases and this

in combination of the water jet can be attributed to slight recovery in the impact pressure. As the bubble is moved away from the plate, crater formation is not observed and the impact pressure is solely due to the water jet impact.

In order to simulate the explosion near a beach and to investigate the effect of the proximity of the free surface, the water depth, d_w, was lowered. Since water free surface is known to repel the bubble, the free surface should aid in the impact process. This was confirmed in the experiments. Figure 8 shows the impact pressure on the plate for cases with sand covering as a function of varying water depth. A lower water depth increases the impact pressure and decreases the time period of oscillation. The time period of oscillation of the bubble shown in Fig. 6 is about 16 ms. When the water depth is decreased for this experiment such that the bulb center is only about 10 cm below the free surface, the period of oscillation further reduces to 14 ms.

The water jet impinges on the flat plate almost symmetrically. This fact can be seen in Fig. 9 which shows the impact pressure distribution over the plate covered with 5.08 cm of sand. Notice also that the distribution of impact pressure is not as focused as it used to be for no sand cases (compare the pressure drop between center and off-center transducers from Fig. 4). Therefore, the effect of burying the flat plate under sand is to smoothen the impact pressure distribution. Figure 10 shows the impact pressure recorded at the plate center for varying distance of explosion over the sand and that of explosion depth. For shallow water cases, two peaks are observed with varying distance of explosion from the plate. Examination of the recorded images suggests that the second peak is due to similar dynamics as in no sand cases. That is, the peak corresponds to the case when the bubble touches the sand surface at its maximum diameter. The first peak, however, is due to the crating phenomena as discussed earlier as a case of explosion close to sand surface. This crating phenomena can be visually seen in next two figures. Figure 11 shows an explosion close to sand surface and does indeed exhibit

the crating phenomenon (the formation of the crater lip can be seen). Figure 12 corresponds to an explosion away from the sand surface and the bubble completes one oscillation cycles before it hits the plate. No crating is observed to be taking place. As the water depth is increased, the peaks in impact pressure vanish (Fig. 10). This signifies the fact that the water free surface actually helps in crating.

The dynamics of bubble collapse over a clay layer is very much identical to those corresponding to the sand. The explosion leaves behind a distinct crater in the clay and the shape and size of the crater depends on the proximity of the explosion and the mechanical properties of the clay. An explosion close to the clay surface makes a crater in which the existence of two craters can be identified. The outer (wider but shallow) crater can be attributed to the bubble expansion and the deeper inner crater is due to the impact of water jet. Figure 13 shows a typical digitally regenerated crater formed in a 7.6 cm thick clay layer by an explosion occurring 2.54 cm above the clay surface. As the explosion is moved away from the crater surface, the outer crater becomes non-existent and the inner crater becomes predominant. The issues concerning crating phenomena is still under investigation and the results will be reported in the future.

4. ANALYSIS OF THE RESULTS

The fact that the interaction of two bubbles oscillating in phase with each other is physically equivalent to that of a single bubble near a solid boundary was exploited by Lal and Menon (1998) to demonstrate how the water jets formed in the two bubbles violently collapse on to each other. The dominant feature of the asymmetric collapse of a bubble near a solid boundary is the possibility of a liquid/solid impact (the impact of the water jet on the solid surface) with the generation of a "water hammer" pressure given by (Field, 1993)

$$P_{wh} = V\rho_l C_l \rho_s C_s / (\rho_l C_l + \rho_s C_s) \approx V\rho_l C_l \qquad (1)$$

where V is the jet impact velocity and ρ_l, ρ_s and C_l, C_s are the densities and shock wave velocities of water and solid respectively. The speed of the reentrant jet in a bubble collapsing in a quiescent liquid near a solid wall at the time it impacts the opposite surface of the bubble is given by (Brennen, 1995)

$$U_j = \xi(\Delta P / \rho_l)^{1/2} \qquad (2)$$

where ξ is a constant and $\Delta p = p_\infty - p_m$. Here, p_∞ is the hydrostatic pressure at the explosion depth and p_m is the pressure inside the bubble at its maximum radius. The value of the constant ξ depends on the size of the bubble and its distance from the wall and has been empirically determined for the cavitation bubbles.

The situation where the bubble is initially located at a considerable distance away from the solid wall is also very interesting. The solid wall in such a case may never experience water hammer pressure because of the reason that the reentrant jet may never reach the solid wall. The reentrant jet may still be formed depending on the strength of Bjerknes force as compared to that of the buoyancy force. The reentrant jet upon hitting the opposite wall of the bubble produces a pressure pulse in the liquid of magnitude $\rho CV/2$, which can subsequently interact with the solid wall.

The penetration of the original bubble by the reentrant jet leads to the formation of two toroidal vortex bubbles. For the bubbles starting their oscillation at a moderate distance from the wall, the expansion and collapse is nearly spherical and the reentrant jet penetrates the fluid between the opposite wall of the bubble and the solid boundary while the bubble has already started its second oscillation cycle (i. e., rebounding). When the bubble is initially very close to

the solid wall, the bubble may never attain a spherical shape starting from the very beginning of the expansion phase. For instance, when the glass bulb is initially touching the solid wall, the ensuing bubble elongates in the direction perpendicular to the wall and there would be no amount of liquid trapped between the bubble and the wall. In fact, the graph of the peak pressure produced on the solid wall with respect to the initial distance of the globe from the wall shows that there is an optimum distance from the wall where the peak pressure on the plate is the maximum. A bubble which is farther from the wall collapses to a smaller size and can concentrate its energy over a smaller volume. Earlier numerical studies (Menon and Pannala, 1998; Pannala and Menon, 1997) have presented a detailed convincing argument for the existence of such an optimum distance. Besides, a jet that strikes the wall directly is more capable of damage in spite of its lower jet speed than the one with a higher jet velocity but has to first pierce the liquid volume between the bubble and the wall.

Experimental data indicate that the bubble becomes prolate quite early in the collapse phase, reaching about (12%) prolate just prior to the start of jet formation. Jet formation depends on the curvature of the bubble-liquid interface (Lauterborn and Bolle, 1975). The presence of a nearby solid boundary reduces the motion of the bubble wall closer to it. As the bubble first becomes elongated in the direction normal to the wall, the point of the bubble farthest from the wall will have the maximum curvature and therefore would be the prime candidate for the origin of jet formation. For the pressure difference, Δp, of 1 atm, Plesset and Chapman (1971) found the jet velocities for two cases of bubble location with respect to the solid wall to be around 130 and 170 m/sec, respectively. Perdue (1988) observed the maximum jet velocity to reach a value given by $11.1(\Delta p/\rho)^{1/2}$.

Since the underwater explosion bubbles in the present study are created by igniting a mixture of Carbon Monoxide and Oxygen, it may be assumed that the bubble contains the non-condensable contents. If this non-condensable gas is considered as ideal and if it is assumed that negligible

heat is exchanged with the surrounding fluid on the time scale of the bubble oscillation, then the pressure, P_b, exerted by the bubble contents can be expressed as

$$P_b = P_0 (R_0 / R)^{3\gamma} \tag{3}$$

where the subscript 0 denotes the initial condition and γ is the ratio of specific heats (Menon and Lal, 1998). Furthermore, the buoyancy parameter can be defined as

$$\delta = (\rho g R_m / P_\infty)^{1/2} \tag{4}$$

where R_m is the maximum bubble radius. Physically δ signifies the ratio of the bubble half-life to the time it would take a bubble of radius R_m to rise the order of one radius from rest due to buoyancy forces. If the bubble is close to a horizontal rigid boundary and is located a distance ζ_0 from it, then $\lambda = \zeta_0/R_m$ characterizes the Bjerknes attraction of the boundary.

The Kelvin Impulse of a bubble, I, is defined such that its time derivative equals the sum of all external force acting on the bubble including Bjerknes and buoyancy forces also. The Kelvin impulse physically corresponds to the impulsive force applied to the bubble surface to generate the observed flow, changing in response to the action of external forces. For motion over a rigid boundary, the Kelvin Impulse is found to be given by (Blake, 1988)

$$I \approx \left(2\sqrt{6}\pi / 9\lambda^2\right)\left[2\lambda^2\delta^2 B\left(\tfrac{11}{6}, \tfrac{1}{2}\right) - B\left(\tfrac{7}{6}, \tfrac{3}{2}\right)\right] \tag{5}$$

where B is the beta function and the Impulse is scaled with respect to $(R_m)^3(\rho p_\infty)^{1/2}$.

The null impulse state corresponds to a situation where the competing Bjerknes and buoyancy forces are approximately equal in their action. This state is given by

$$\lambda\delta = \left(B(\tfrac{7}{6},\tfrac{3}{2})/B(\tfrac{11}{6},\tfrac{1}{2})\right)^{1/2} = 0.442 \qquad (6)$$

No jetting is observed at this state and the bubble does not migrate in any direction.

All these properties will be verified for the flat plate case in the near future.

5. CONCLUSION

There exists a critical distance above the plate where the reentrant water jet produces the maximum impact pressure. The jets formed by the explosions above this distance have to pierce the water layer between the bubble and the plate and hence yield lower impact pressures. The growth of bubbles formed by explosions below the critical distance is inhibited by the presence of the plate and hence their maximum sizes are comparatively restrained. The water jet, however, is very focused and symmetrical about the center of impact. The effect of covering the flat plate with sand or clay is to reduce the impact pressure and smoothen its distribution over the plate. However, Loose sand particles are displaced during crater formation due to an explosion close to the sand surface. The formation of crater reduces effective sand thickness and a partial recovery in impact pressure is achieved. The water free surface enhances the crater foramtion and the pressure recovery is indeed substantial. Explosions close to the clay surface display formation of double craters.

ACKNOWLEDGMENT

This work is supported by the Office of Naval Research under Grant No. N00014-91-J-1963 and monitored by Drs. Richard Miller and Judah Goldwasser.

REFERENCES

Best, J. P. & Blake, J. R. 1994 An estimate of the Kelvin Impulse of a transient cavity. *Journal of Fluid Mechanics* **261,** 75-93.

Best, J. P. & Kucera, A. 1992 A numerical investigation of non-spherical rebounding bubbles. *Journal of Fluid Mechanics* **245,** 137-154.

Blake, J. R., Taib, B. B. & Doherty, G. 1986 Transient cavities near boundaries. Part 1. Rigid boundary. *Journal of Fluid Mechanics* **170,** 479-497.

Brennen, C. E. 1995 *Cavitation and bubble dynamics*, Oxford University Press, New York.

Chahine, G. L. & Bovis, A. G. 1983 Pressure field generated by nonspherical bubble collapse. *Transactions of the ASME* **105,** 356-363.

Chahine, G. L. & Perdue, T. O. 1988 Simulation of the three dimensional behavior of an unsteady large bubble near a structure. In *Proceedings 3rd International Colloquium on Drops and Bubbles,* Monterey, California.

Field, J. E. 1993 Experimental studies of bubble collapse. In *Bubble dynamics and Interface Phenomena* (eds J. R. Blake, J. M. Boulton-Stone & N. H. Thomas), pp. 17-31, Dordrecht: Kluwar Academic Publishers.

Hooton, M. C., Blake, J. R. & Soh, W. K. 1993 Behaviour of an underwater explosion bubble near a rigid boundary: theory and experiment. In *Bubble dynamics and Interface Phenomena* (eds J. R. Blake, J. M. Boulton-Stone & N. H. Thomas), pp. 421-428, Dordrecht: Kluwar Academic Publishers.

Kedrinskii, V. K. 1987 Hydrodynamics of explosions. *Zhurnal Priklandnoi Mekhaniki I Tekhnicheskoi Fiziki* **4,** 23-48.

Lal, M. K. & Menon, S. 1998 Dynamics of interaction of two underwater explosion bubbles. To appear shortly in *Journal of Fluids Engineering*.

Lauterborn, W. & Bolle, H. 1975 Experimental investigations of cavitation-bubble collapse in the neighbourhood of a solid boundary. *Journal of Fluid Mechanics* **72,** 391-399.

Lean, M. H. & Domoto, G. A. 1983 Application of the boundary element method to collapse of vapor bubbles in the neighborhood of a solid boundary. In *Proceedings Methodes Numeriques de l'Ingenieur, Comptes Rendus du Troisieme Congres International,* Paris, France.

Menon, S. & Lal, M. 1998 On the Dynamics and Instability of Bubbles Formed During Underwater Explosions. *International Journal of Experimental Heat Transfer, Thermodynamics and Fluid Mechanics*, In the press.

Pannala, S. & Menon, S. 1997 Numerical study of bubble collpase and rebound near a wall. In *Proceedings 1997 ASME Fluids Engineering Division Summer Meeting.*

Perdue, T. O. 1988 A numerical study of the interaction between a bubble and a rigid structure. In *Proceedings Cavitation and Multiphase Flow Forum - 1988 National Fluid Dynamics Congress,* Cincinnati, Ohio.

Plesset, M. S. & Chapman, R. B. 1971 Collapse of an initially spherical vapour cavity in the neighbourhood of a solid boundary. *Journal of Fluid Mechanics* **47(2),** 283-290.

Robinson, P. B. & Blake, J. D. 1993 Dynamics of cavitation bubble interactions. In *Bubble dynamics and Interface Phenomena* (eds J. R. Blake, J. M. Boulton-Stone & N. H. Thomas), pp. 55-64, Dordrecht: Kluwar Academic Publishers.

Tipton, R. E., Steinberg, D. J. & Tomita, Y. 1992 Bubble expansion and collapse near a rigid wall. *JSME International Journal* **35(1),** 67-75.

Tomita, Y. & Shima A. 1986 Mechanisms of impulsive pressure generation and damage pit formation by bubble collapse. *Journal of Fluid Mechanics* **169,** 535-564.

van der Meulen, J. H. J. & van Renesse, R. L. 1987 A study of the collapse of laser-induced bubbles in a flow near a boundary. In *Proceedings Cavitation and Multiphase Flow Forum - 1987 ASME Applied Mechanics, Bioengineering and Fluids Engineering Conference,* Cincinnati, Ohio.

Ward, B. & Emmony, D. C. 1990 Interactions of laser-induced cavitation bubbles with a rigid boundary. In *Proceedings 19th International Congress on High-Speed Photography and Photonics,* Cambridge, England.

Wilkerson, S. A. 1989 Boundary integral technique for explosion bubble collapse analysis. In *Proceedings The Energy Sources Technology Conference and Exhibition, ASME,* Houston, Texas.

Zhang, S., Duncan, J. H. & Chahine, G. L. 1992 Simulation of the final stage of bubble collapse near a rigid wall. In *Proceedings Cavitation and Multiphase Flow Forum - 1992 ASME Fluids Engineering Conference,* Los Angeles, California.

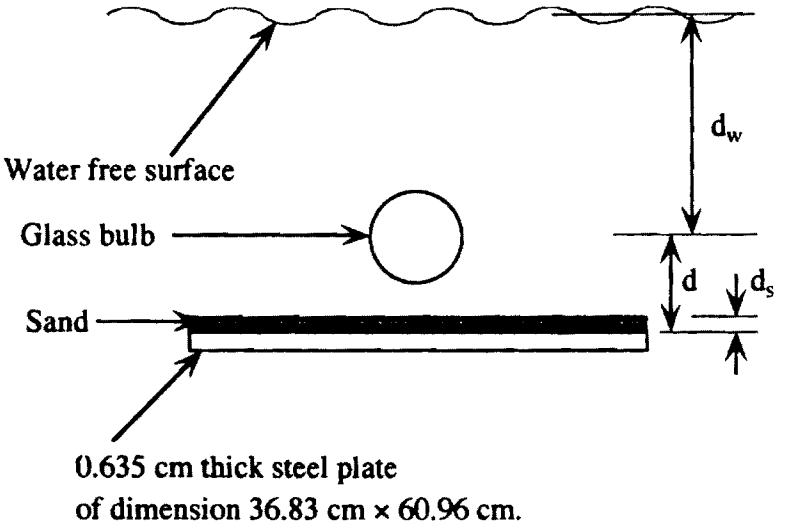

Fig. 1. Experimental setup for simulating explosion near an exposed or buried object. For exposed object, $d_s = 0$.

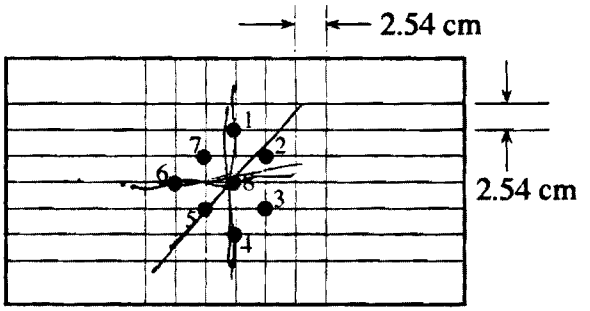

Fig. 2. Layout of pressure transducers on the plate

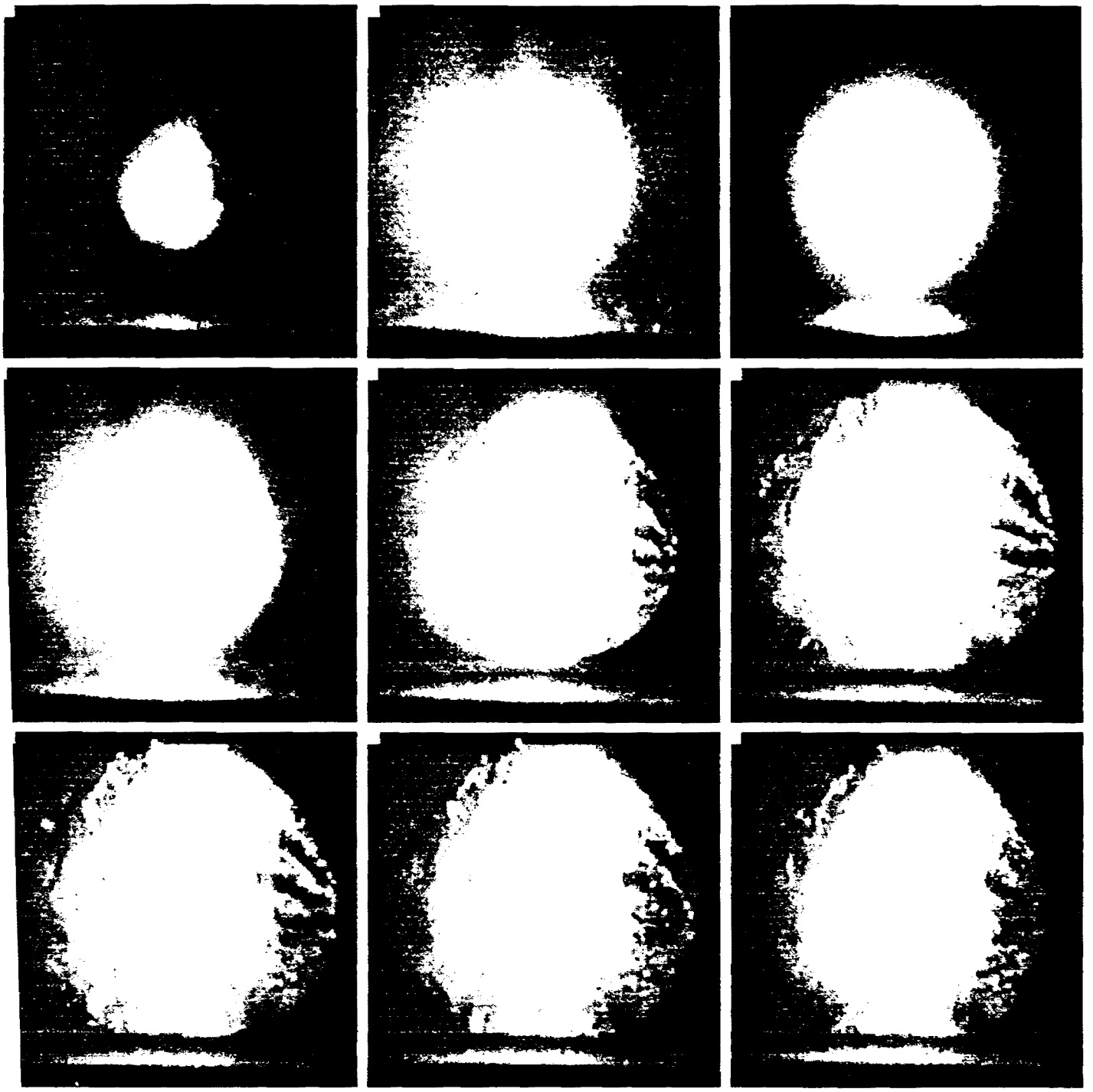

Fig. 3. Time sequence of bubble collapse near an exposed plate for $d/R_0 = 2$.

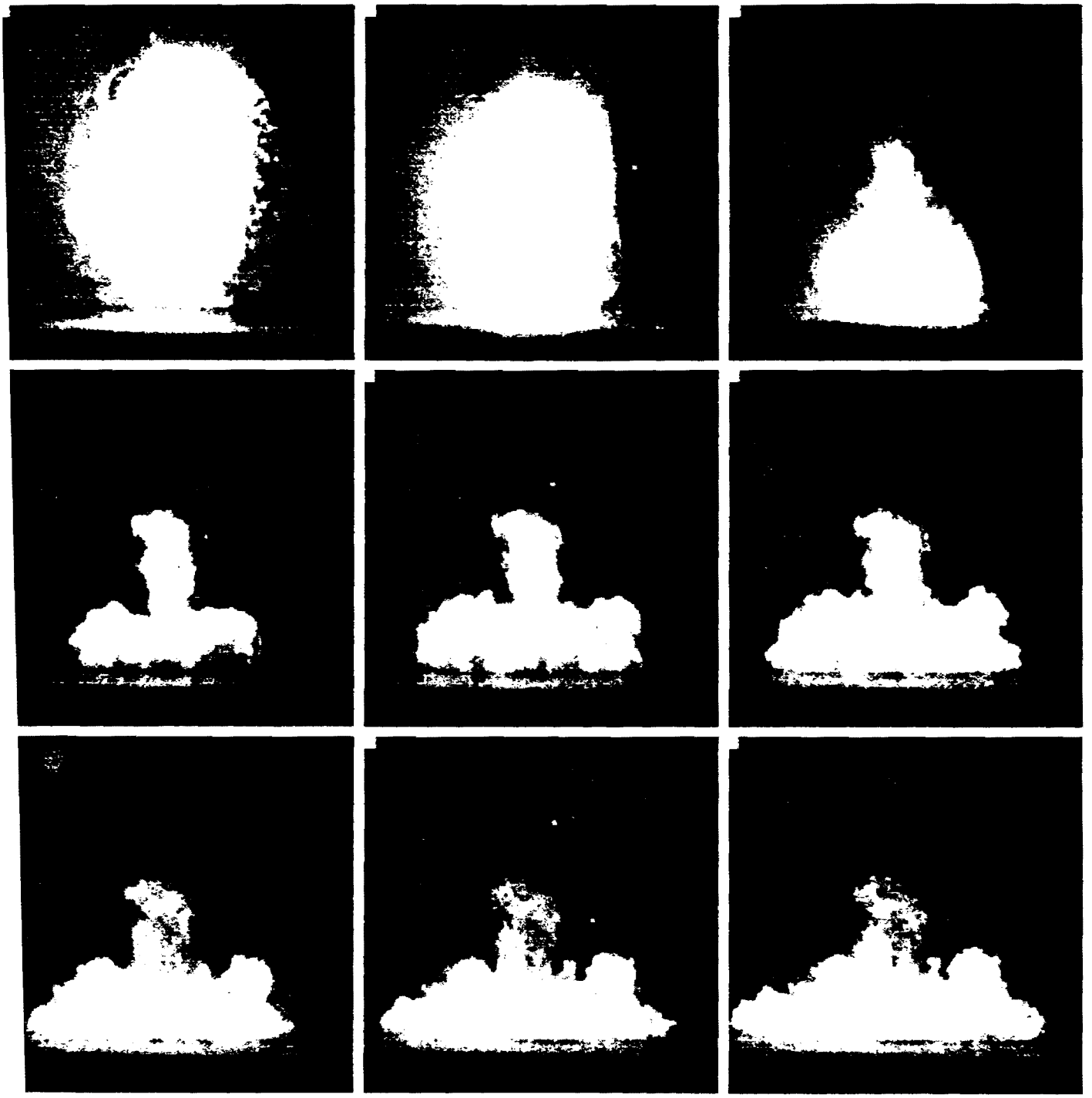

Fig. 3. (Continued)

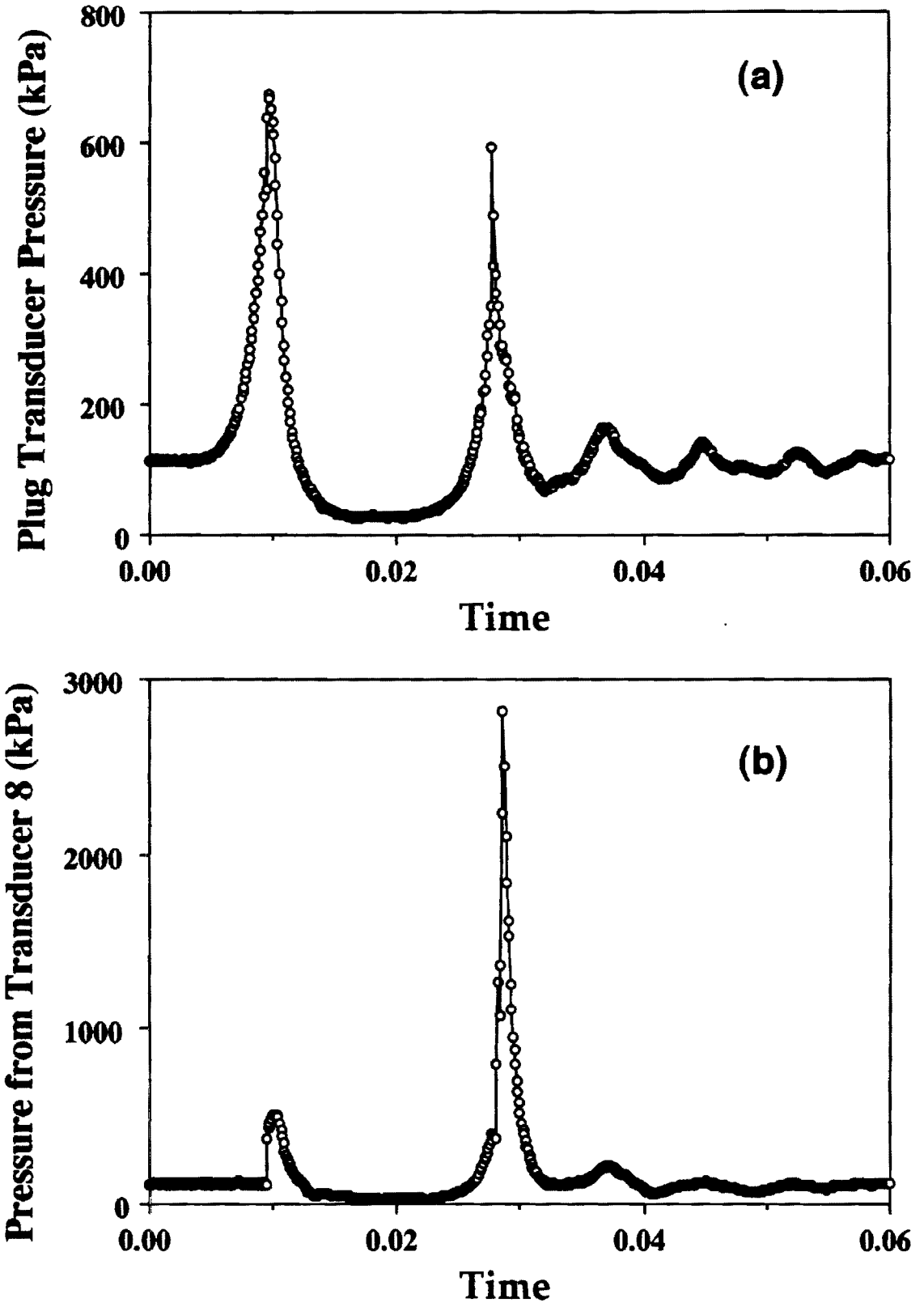

Fig. 4. Pressure time trace recorded by (a) the plug transducer; and (b-d) the plate transducers for the exposed plate case with $d/R_o = 2$.

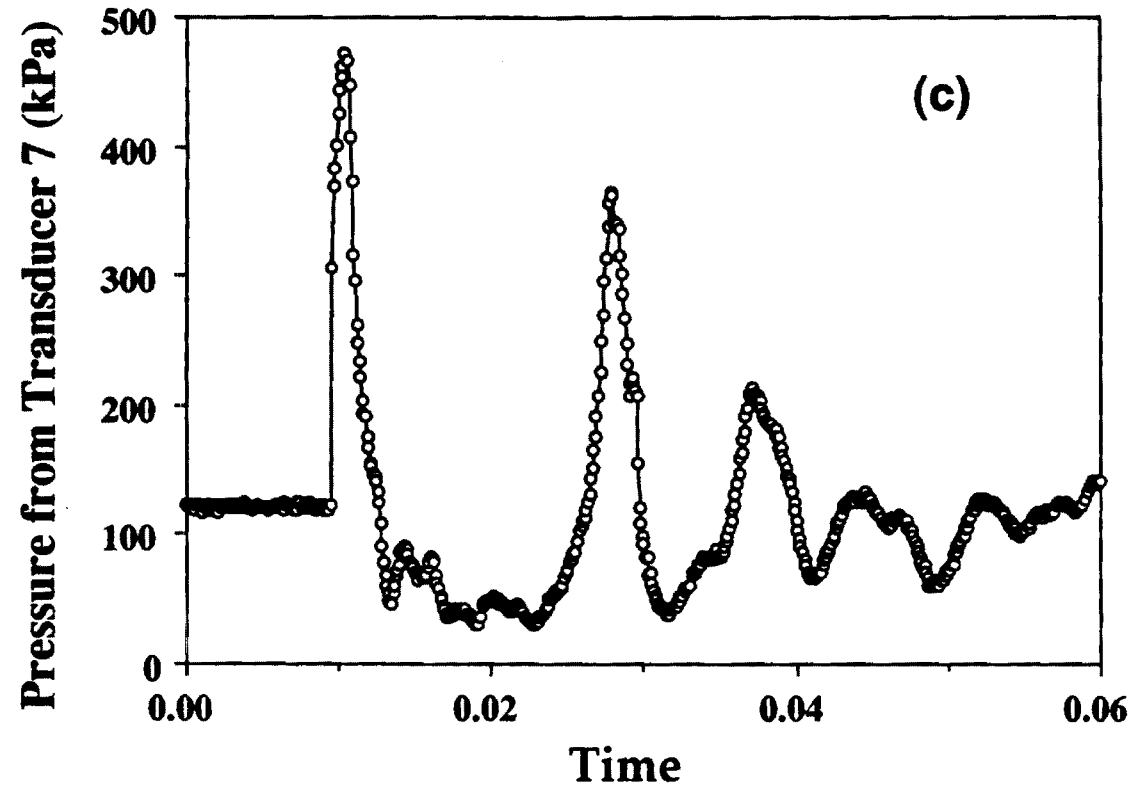

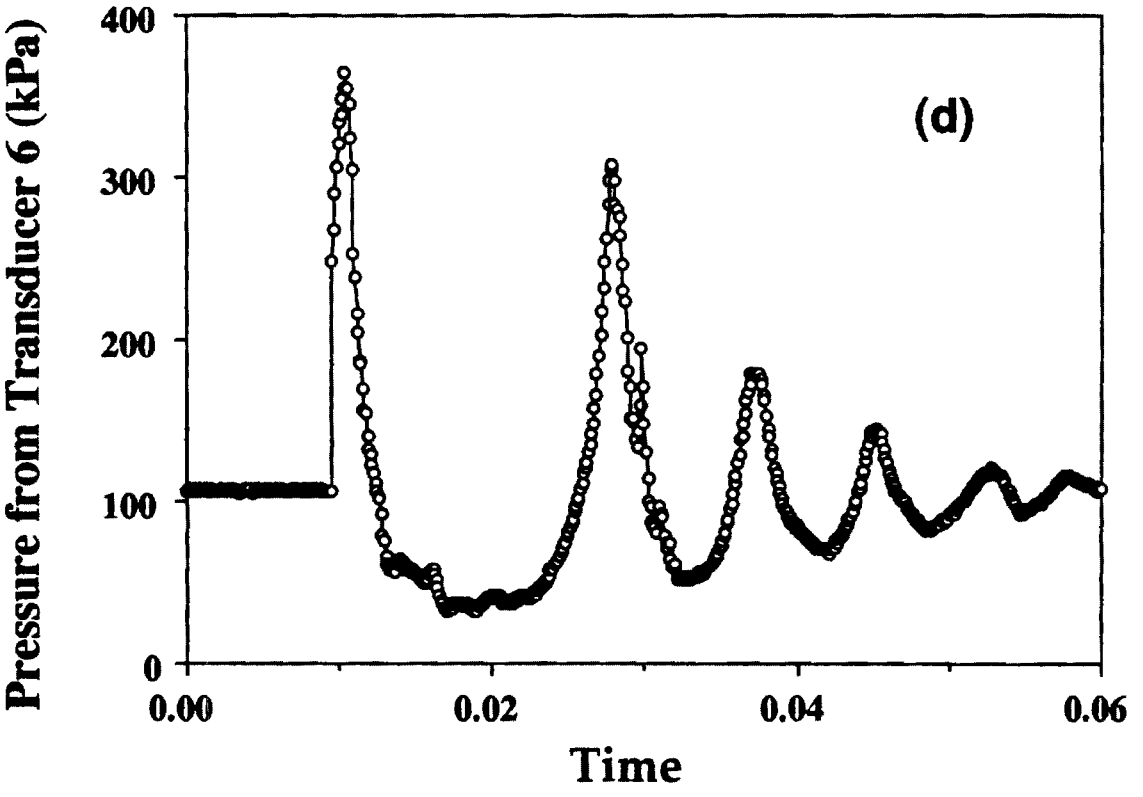

Fig. 4. (Continued)

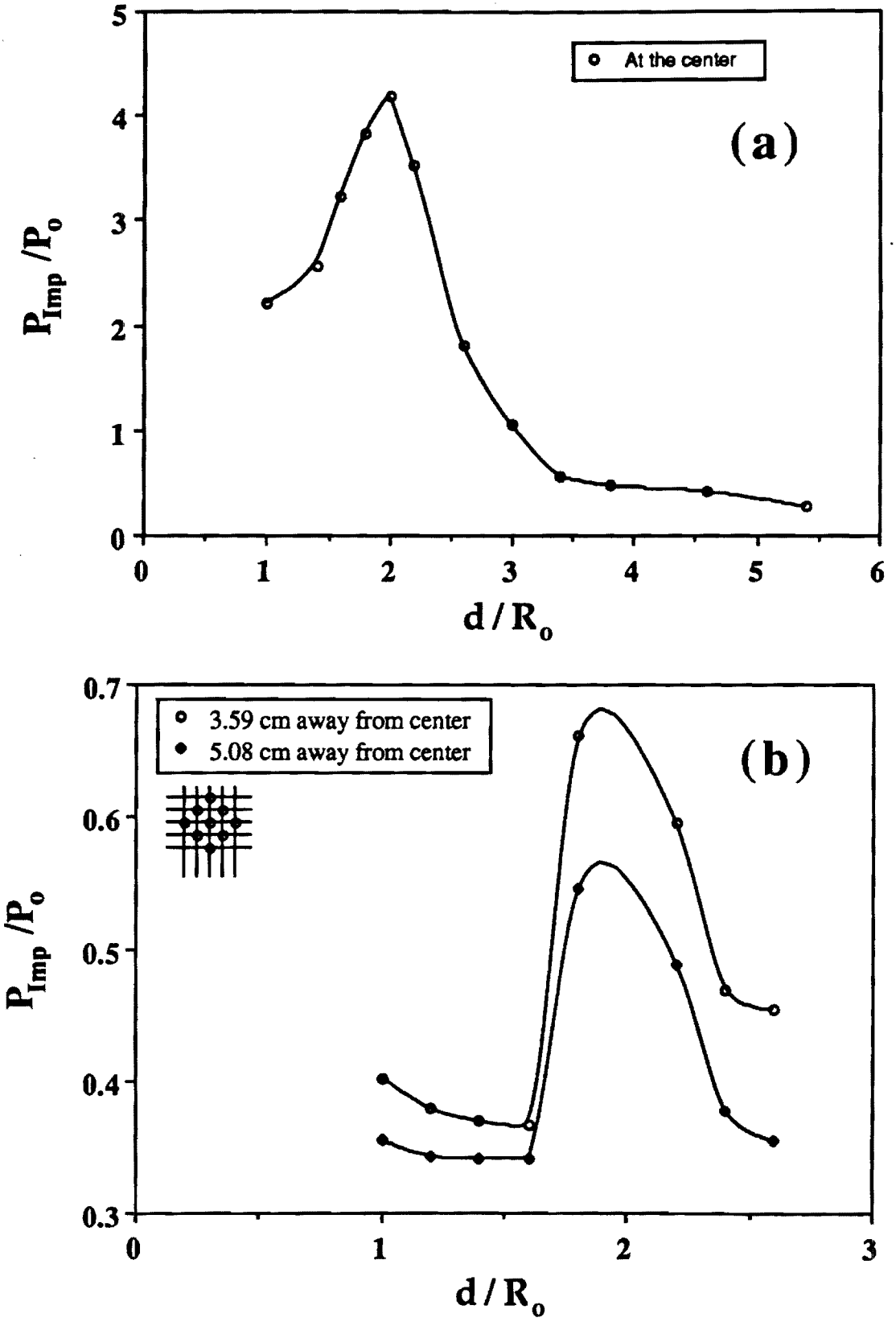

Fig. 5. Normalized impact pressure measured by (a) transducer no. 8; and (b) transducer no. 6 and 7 (away from the center) as a function of distance of the initial bulb from the plate.

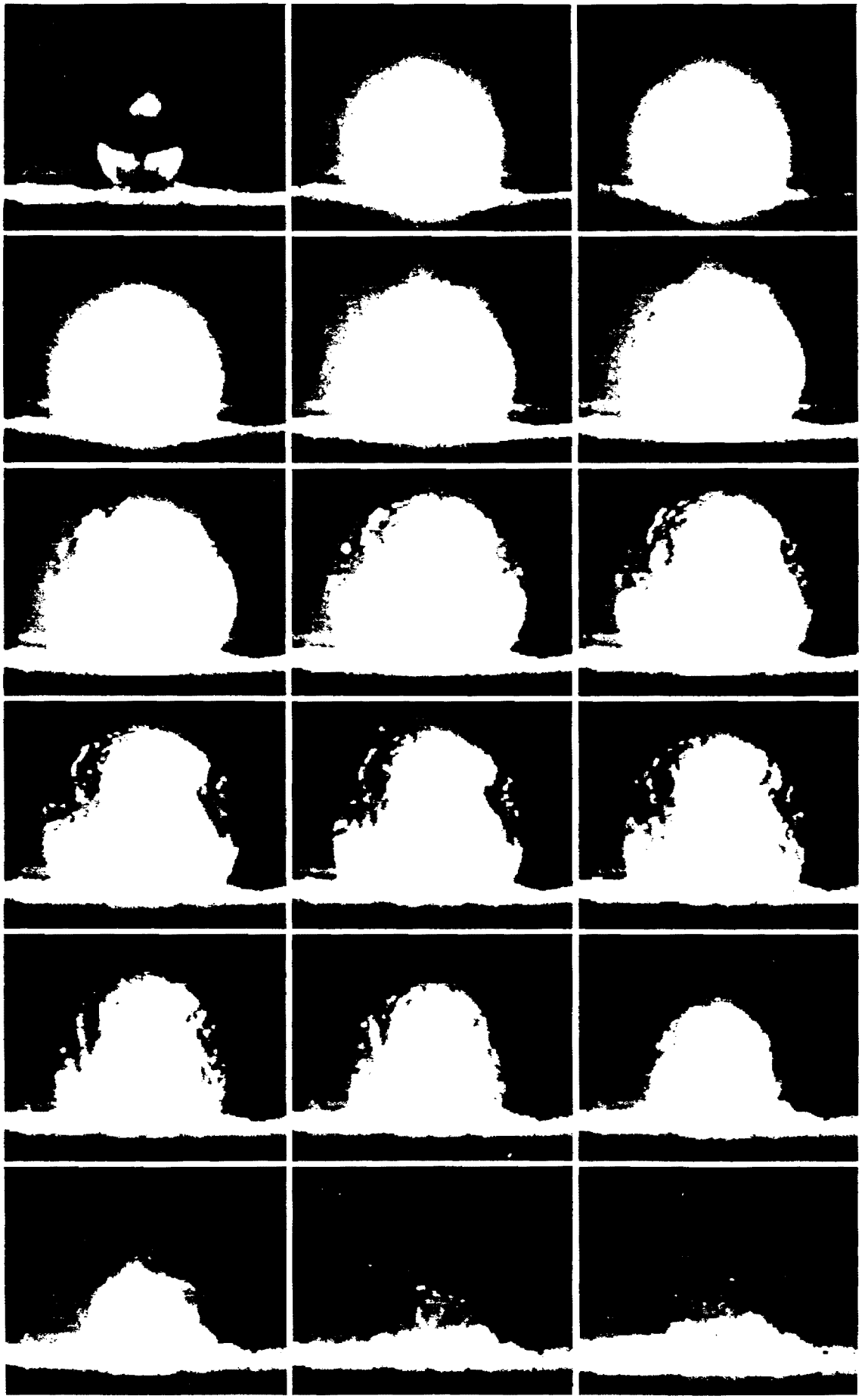

Fig. 6. Bubble collapse near a buried object. $d/R_0 = 2.4$, $d_s/R_0 = 1.1$ and $d_w/R_0 = 24$.

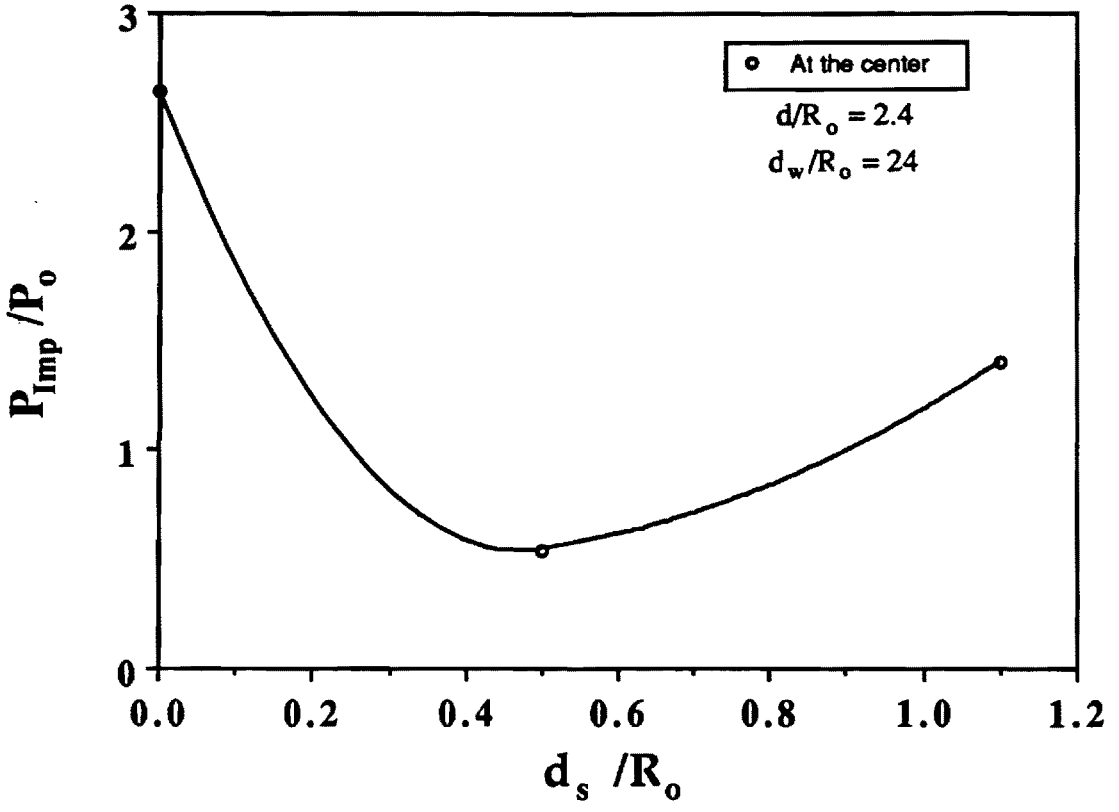

Fig. 7. Normalized impact pressure at the center as a function of sand layer thickness.

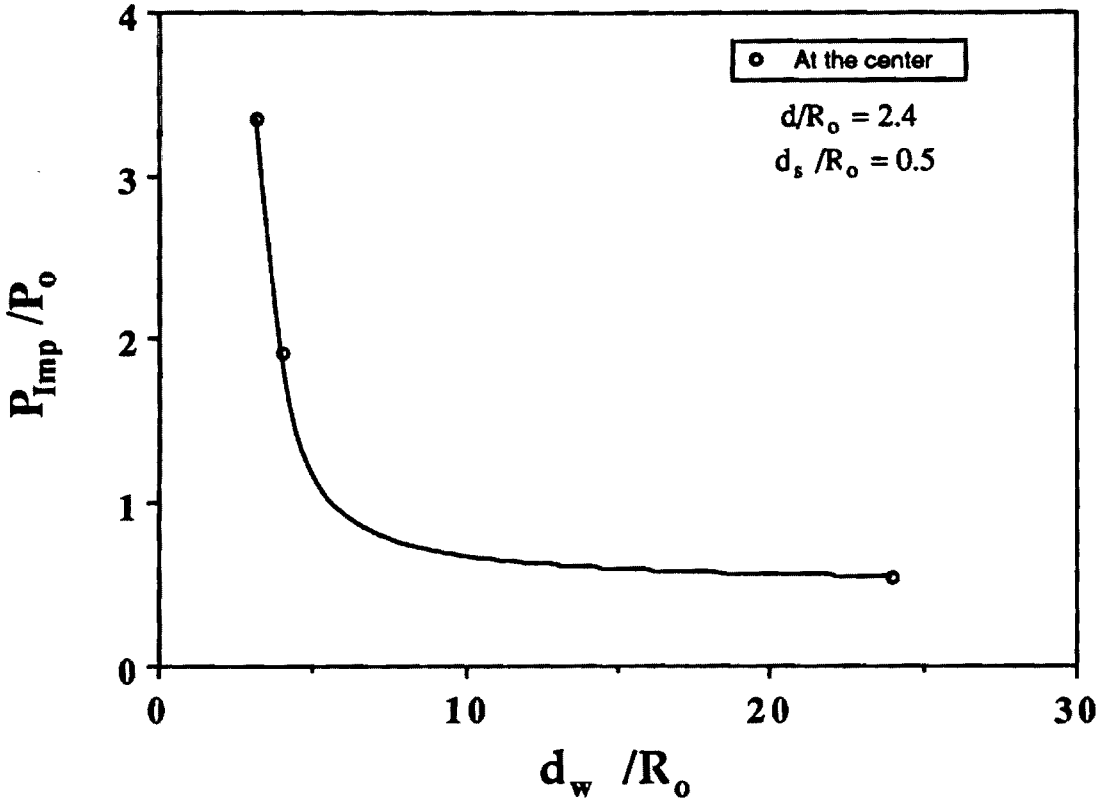

Fig. 8. Normalized impact pressure at the center as a function of the location of free water surface above the bubble.

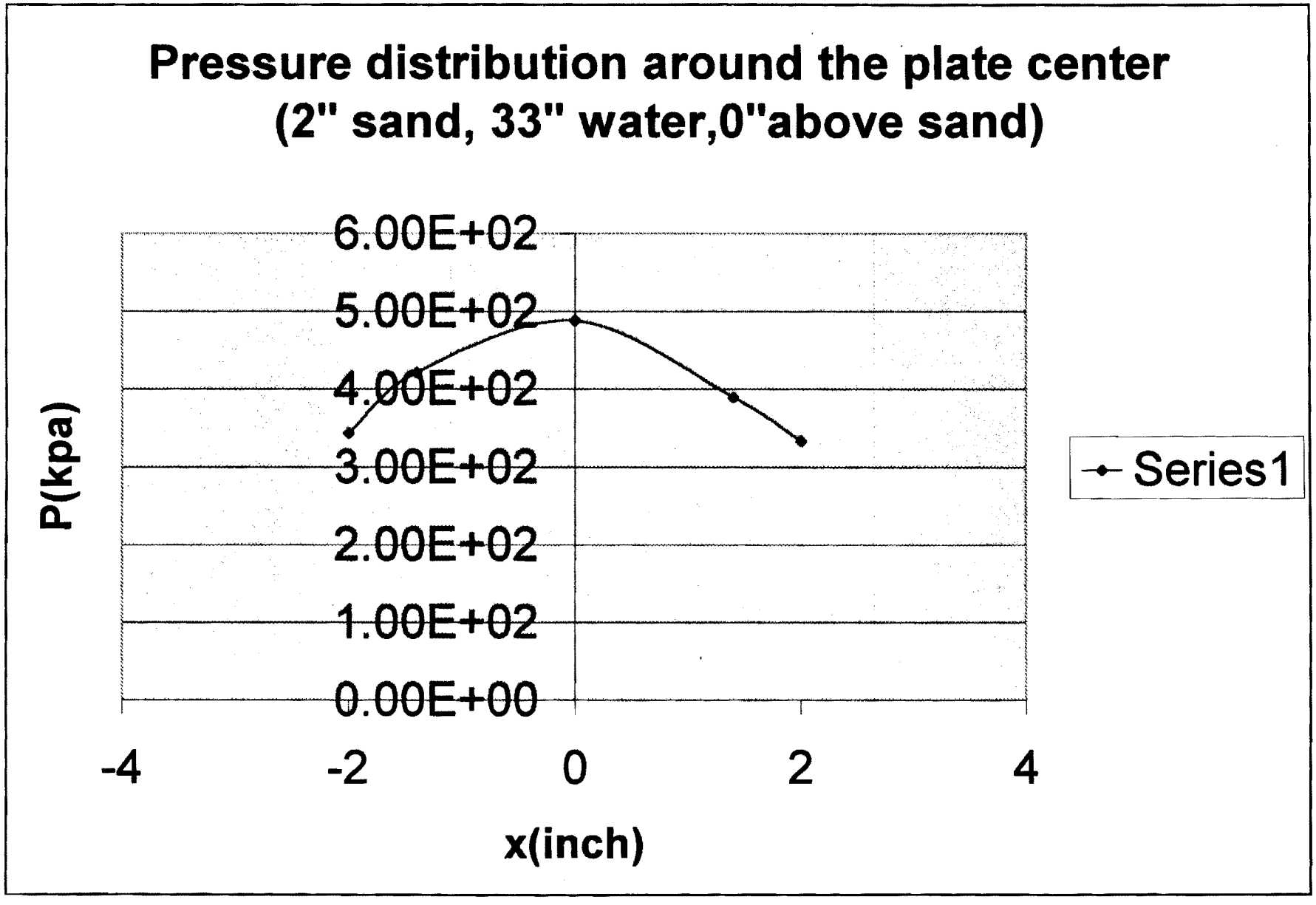
Pressure distribution around the plate center
(2" sand, 33" water,0"above sand)
6.00E+02
5.00E+02
4.00E+02
3.00E+02
2.00E+02
1.00E+02
0.00E+00
P(kpa)
-4
-2
0
2
4
x(inch)
Series1

Pressure variation at center versus the distance between the bulb and the solid surface.

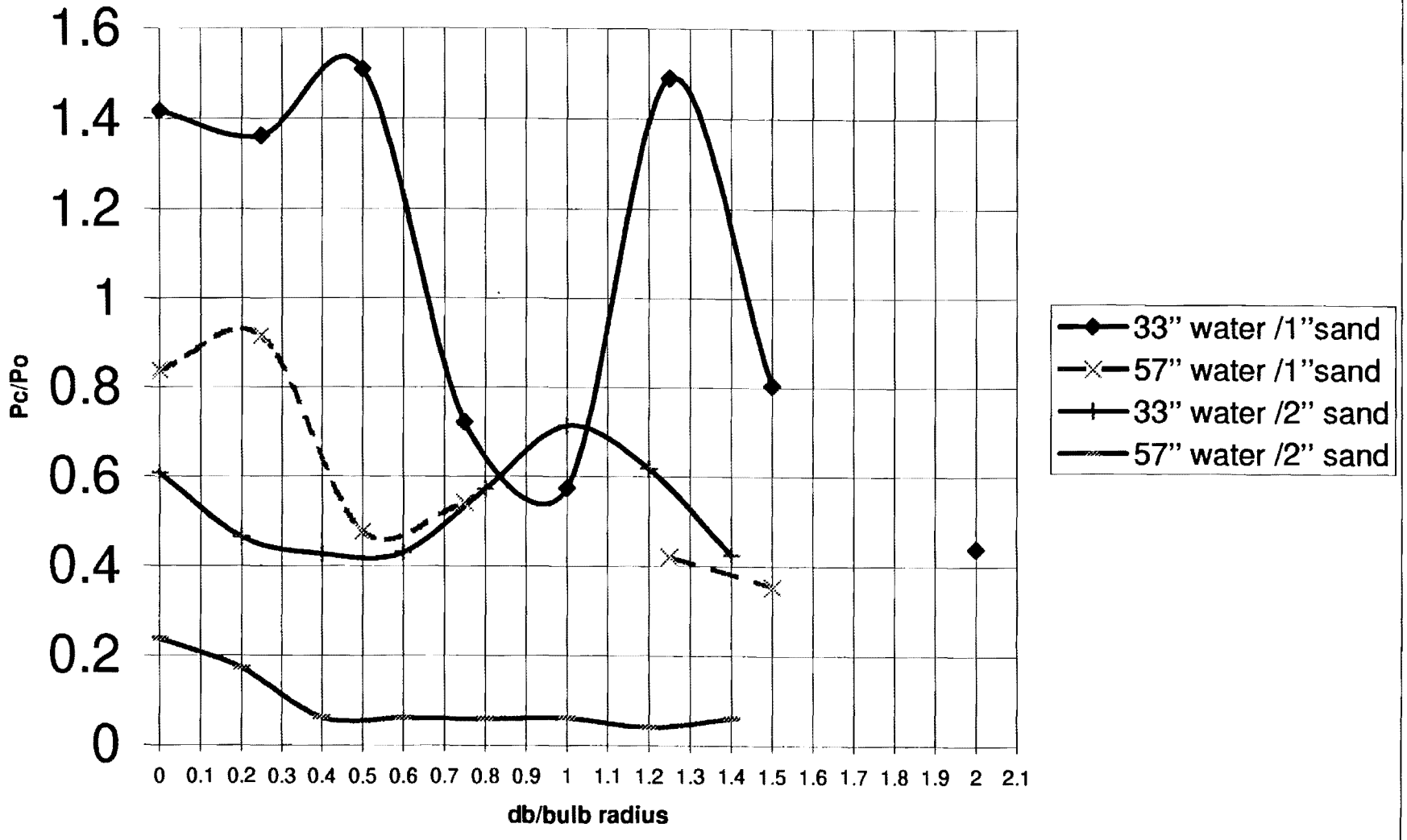

2" sand

33" water

0" above

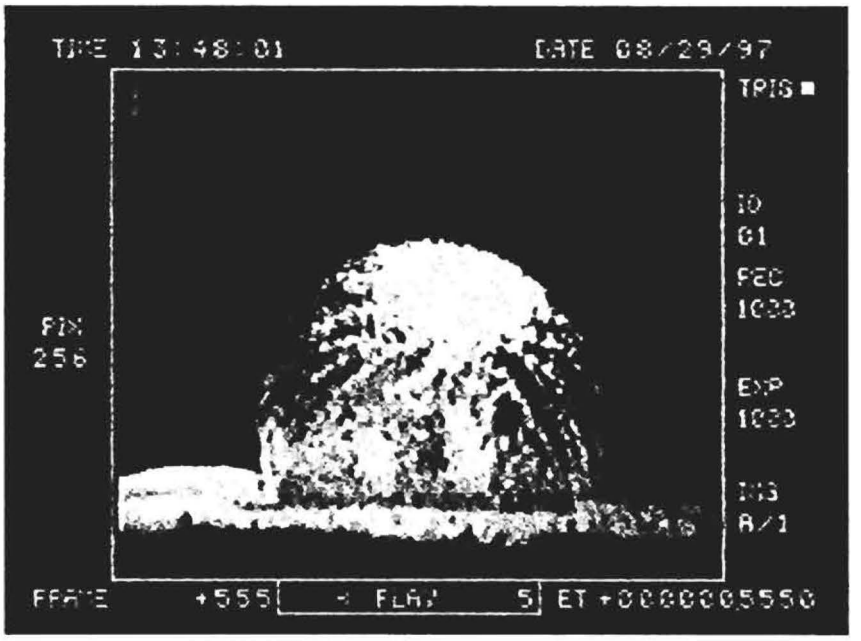

Fig 11

2" sacral
33" waist
0" above

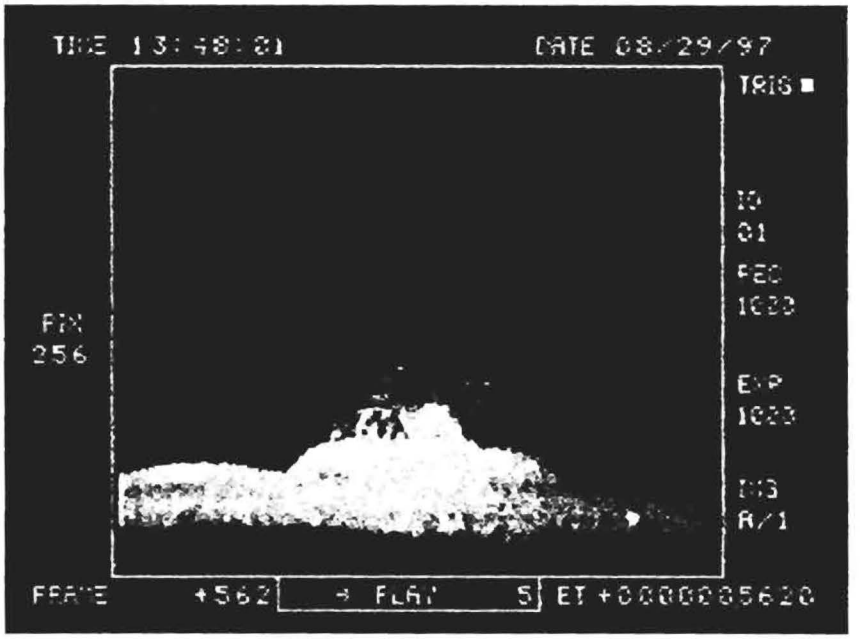

Fig 11 (cont)

11" sand
33" wide
2.5" above

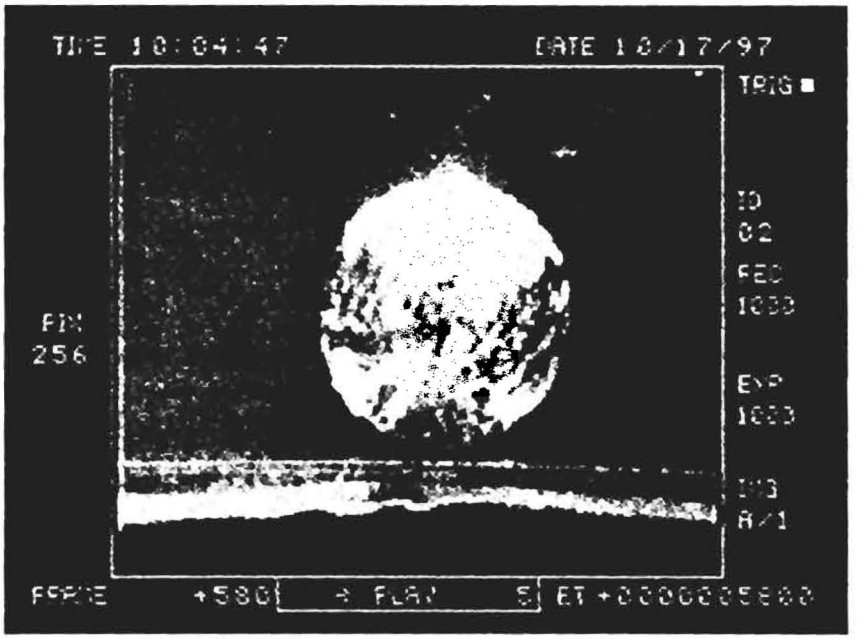

Fig 12

crater # 1

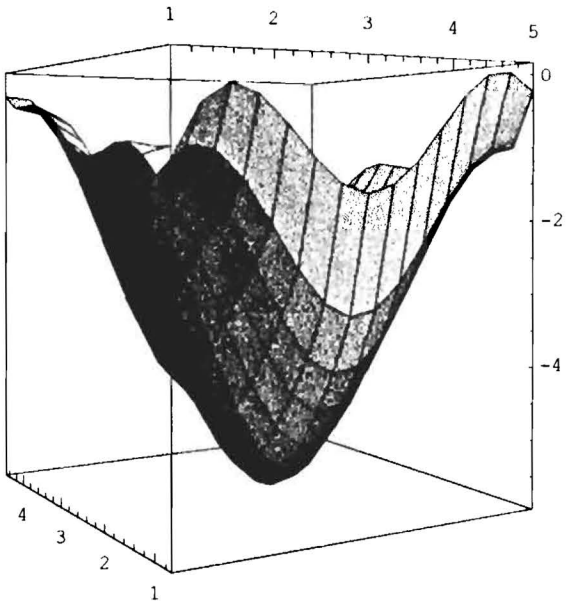

33" water

3" clay

bulb 0" above clay

Dynamics of Interaction of Two Underwater Explosion Bubbles

Mihir Lal
Post-Doctoral Fellow

Suresh Menon
Professor

School of Aerospace Engineering
Georgia Institute of Technology
Atlanta, GA 30332-0150

ABSTRACT

Underwater explosion bubbles are created by detonating a mixture of oxygen and Carbon Monoxide or Hydrogen in glass globes submerged in a water tank. A cinematographic technique is employed to capture entire interaction process in both horizontal and vertical configurations. Instrumented tubes and plugs measure pressure inside and outside the bubbles. Depending on the delay between two explosions and inter-bubble distance, the bubbles may either attract each other to form a single coalesced bubble, or they may violently repel each other. A violent interaction between the bubbles leads to an increased instability of the bubbles. When a coalesced bubble is formed by merging the energies of two bubbles, the resulting bubble has more residual energy and is more stable for successive oscillations. An out-of-phase oscillation generates a reentrant water jet which pierces the bubble in the direction of its migration. Experiments were also conducted to qualitatively and quantitatively study the interaction of a free surface with the explosion bubble(s).

Introduction

Much of the research activities in the area of underwater bubble dynamics has been focused on the behavior of cavitation bubbles. Cavitation bubble dynamics play very important role in underwater acoustics and in predicting and preventing propeller and turbine blade damage. These bubbles, however, seldom occur singly. Actual cavitation fields contain several thousands of

oscillating and translating microbubbles. Study of the behavior of a cloud of bubbles thus becomes inevitable and experimental (e.g., Chahine and Sirian, 1985; Tomita et al., 1984), numerical (e.g., Chahine and Liu, 1985; Chahine, 1991; Chahine and Duraiswami, 1992; Wang and Brennen, 1994) and analytical (e.g., Van Wijngaarden, 1972) techniques have all been developed. The simplest model that has been studied by the researchers is the interaction between two bubbles. Theoretical and numerical studies of the interaction of two spherical or nonspherical bubbles of same or different sizes (e.g., Fujikawa et al., 1985; Fujikawa and Takahira, 1986; Fujikawa and Takahira, 1988; Morioka, 1974; Serebryakov, 1992; Shima, 1971; Takahira, 1988) have also been carried out. Interesting experimental observations of the interaction of a gas bubble with a pressure wave (Shima and Tomita, 1988) or with a vapor bubble (Smith and Mesler, 1972) have also been made. However, most of these observations are for microbubbles and find applications in cavitation, erosion and related topics.

Large bubbles, such as those created by underwater explosion, owing to their tremendous inherent destructive capabilities upon collapse near a rigid boundary, find practical applications in underwater weaponry. Detailed measurements and imaging of pulsating bubbles formed during deep sea explosions are very difficult due to a variety of obvious reasons (e.g., Arons et al., 1948) and therefore, there is insufficient data available to analyze the dynamics of interaction of bubbles. Controlled experiments described here, are required to investigate the physical processes that contribute to the interaction of bubbles. These experiments were conducted in a laboratory shallow water setup using a gaseous explosive mixture. The observations reported here are of practical significance for buried mines detection in shallow water beaches, where the interaction of an explosion bubble with a solid boundary and water free surface is anticipated.

The interaction of two underwater explosion bubbles is a very interesting and complex phenomenon, because of the fact that one bubble is influenced by the time-delayed pressure or shock wave radiated from the adjacent bubble. Radial motion of the bubble may be greatly excited

or subdued due to the interaction depending on their temporal and spatial separations. Though some experimental work has been done on the interaction of gas bubbles with two adjacent underwater explosion bubbles, and it has been shown that strong and complicated interactions ensue, it appears that no detailed results on the interaction of two underwater explosion bubbles have been published in the public domain literature.

This paper reports the results of the experiments carried out in a laboratory water tank to study the interaction between two adjacent bubbles created by underwater explosion of flammable gas contained in glass globes. The globes were placed side-by-side either in a horizontal or a vertical plane. The distance between the two globes and their sizes were both varied. This paper also discusses the interaction of an explosion bubble with the water free surface.

Experimental Procedures

Underwater explosion experiments were conducted in a wooden tank of dimension 2 m × 1.5 m × 1.5 m, coated with fiberglass resin from inside. The tank, as shown in Fig. 1, has three windows on three sides for optical imaging. The underwater explosion bubble is generated by centrally igniting a mixture of an explosive gas (either Hydrogen or Carbon Monoxide) and oxygen contained in a hand-blown glass globe. Three different sizes of glass globes were used for present experiments with average radii of 2.9 cm, 3.2 cm, and 3.8 cm. The glass globe, as shown in Fig. 2, has an electric spark ignition system connected to a 3000V DC power supply. The explosion takes place at a constant volume until the globe bursts. Since the experiments were conducted in a laboratory shallow water setup and using a gaseous explosive mixture, the bubbles are relatively smaller (although much larger than cavitation bubbles) than those observed in deep sea explosions. Recently, Menon and Lal (1997) addressed the dynamics and instability issues of such a bubble in free field and they showed by means of extensive geometric and dynamic similarity analyses that the explosion bubble thus formed is a reasonable subscale approximation of a deep sea underwater explosion bubble. They have presented detailed scaling parameters, energy partitioning and also

various interface instability mechanisms. Repeatability and experimental uncertainty have also been addressed and it has been shown in particular that repeated experiments produced error bands for the explosion pressure, maximum radius and time period of 5.88%, 3.7% and 6.06%, respectively. A parallel numerical study using an Arbitrary Lagrangian-Eulerian (ALE3D) code was also carried to investigate bubble dynamics (Menon and Pannala, 1997). Comparison of the computed results with the experimental data for a single and double bubble oscillation showed excellent agreement.

The pressure response in the water around the bubbles were recorded during the experiments by means of 4 KISTLER dynamic piezoelectric pressure transducers fitted at the ends of 4 stainless steel (1.27 cm diameter) tubes bent at right angle, as shown in Fig. 1. A hydrophone is also mounted in the tank and is used for measuring acoustic pressure. Pressure inside the bubble during its oscillation is measured by another KISTLER transducer which is mounted inside the plug, as shown in Fig. 2. These dynamic pressure transducers have low and high frequency response of 0.001 Hz and 50 kHz, respectively, and the resonant frequency of 300 kHz. They are therefore well suited for the current experiments as the bubble oscillation frequency (time period of approximately 15 ms) lies well within the above mentioned bounds. Signals from these six pressure transducers and the hydrophone were digitized using National Instrument's AT-MIO-16X analog-to-digital converter board, and were recorded into a microcomputer. Eight channel data recording was performed with a sustained sampling rate of 10,000 samples per second per channel.

The tank was illuminated by either direct overhead flood lights or an argon-ion laser sheet which lies in a vertical plane perpendicular to the camera axis. The optical recording of the bubble motion was performed by a CCD enhanced digital video camera with a maximum speed of 6000 frames per second. Many of the experiments, however, were performed at a lower speed of 1000 frames per second in order to obtain a full screen image.

The two glass globes were supported inside the tank by means of a modified sting which made the pressure transducers mounted inside the two globes to face each other. This facilitated direct measurement of the fluctuation in the pressure inside one bubble due to its interaction with the other. A means for altering the distance between the two bubbles was provided by the six holes drilled in the supporting copper pipe (1.6 cm diameter) of Fig. 1. Experiments were conducted in primarily two configurations; a horizontal configuration, when the supporting pipe was horizontal, and a vertical configuration, when it was vertical. The former configuration prohibited the use of laser light sheet and only the flood lights were used for imaging, while the latter allowed the use of laser light sheet.

Experiments were also conducted to study the interaction of water free surface with the explosion bubble. The motivation for these experiments has obvious reasons. The free surface provides a constant pressure boundary in close proximity of the oscillating bubble. It is known that the bubble moves away from the free surface and a reentrant jet is formed which pierces the bubble in the direction of its migration (see e.g., Birkhoff, 1957; Blake and Gibson, 1981; Chahine, 1977; Chahine, 1982; Wilkerson, 1989). The observed lack of experimental data for interaction of a bubble with the water free surface (Wilkerson, 1989) motivated the current experiments.

Results and Discussion

The interaction process is highly dependent on the time delay between the two explosions. This time delay is related to a variety of hardware and bubble response characteristics, namely, the gas volume (globe size), the equivalence ratio of the fuel-oxygen mixture, and the gap between the two spark wires, etc. The actual delay (temporal separation) between two explosions is therefore measured from the recorded video images as the time elapsed between the instant when the individual globe bursts. It was therefore deemed necessary to conduct several experiments to

collect statistical information about the range of bubble behavior with respect to the delay between two explosions.

The entire spectrum of delay can be classified into two broad regions: in phase oscillation and out of phase oscillation (see e.g., Morioka, 1974; Shima, 1971; Smith and Mesler, 1972). In most of the past analytical, numerical or even experimental work on the interaction of two cavitation bubbles, interest has been focused primarily on the contraction phase of the bubble oscillation. This yields an in phase oscillation of identical bubbles as they both start collapsing at the same time following a sudden change in the ambient pressure. In phase oscillation is obtained when there is strictly no delay between the explosions. This is the simplest scenario and has been analyzed comprehensively.

Another interesting scenario is a 180^{o} out of phase oscillation and it can be best understood in the interaction of two identical explosion bubbles as a case where one bubble starts its oscillation cycle when the other has already reached its maximum radius. In fact, these are the two scenarios predicted by the analytical theories (Morioka, 1974). Morioka's (1974) theoretical analysis of natural frequencies of two pulsating bubbles predicts the existence of two natural frequencies corresponding to in phase and 180^{o} out of phase oscillations, respectively. Of course, in an experimental setup one can have any amount of delay between zero to 180^{o}, or even beyond 180^{o}. Two bubbles oscillating in phase behave in a nearly identical manner as a single bubble near a rigid boundary and therefore, are of considerable practical interest since it has been shown that the collapse of a bubble near a wall can cause significant damage. The bubbles have an increasing repulsive effect as the delay between two explosions increases, up to the point when they oscillate 180^{o} out of phase (Smith and Mesler, 1972).

Figure 3 shows an example for two underwater explosion bubbles oscillating in phase. The initial volume of the right glass globe is 94 ml and that of the left glass globe is 90.5 ml. They are

in a horizontal configuration and are initially separated by a distance d, where $d/R_0 = 2.32$. Both of them are filled with stoichiometric mixture of Carbon Monoxide and Oxygen. There is virtually no delay between two explosions (determined from the image data) and since the two globes have almost same volume, they burst also at the same time (time, t = 0 ms). Since the initial spatial separation between the globes was intentionally kept to a very small value so that a violent interaction can ensue, the bubbles soon come in contact with each other. They deviate more and more from sphericity as they expand with time, collapse violently on to each other and merge together to form a single coalesced bubble.

The plane surface where the two bubbles come in contact may be considered as a rigid boundary in an equivalent single bubble analogy. Figure 4 shows the relative position of this surface with respect to the initial globes' centers. Notice that this surface is almost perpendicular to the line joining the initial globes' centers and is located almost midway. The time period of oscillation of the bubbles shown in Fig. 3 is about 21 ms, while that of an identical bubble in free-field is less than 15 ms. Therefore, for two identical bubbles oscillating in phase, an increase in the bubble period is observed. A similar observation was made by Chahine (1991).

The pressure traces measured around the bubbles show that the bubble behavior is symmetrical. Figure 5 shows the pressure trace measured by the transducer mounted in the right plug. The first peak corresponds to the explosion pressure and a pressure fluctuation of about 700 kPa exhibited near bubble minimum (second peak) demonstrates the severity of collapse of the jets formed in two bubbles on to each other. Figure 6 shows the pressure signature recorded by a transducer mounted in a tube underneath the right globe (see Fig. 1). The pressure drops exponentially as one moves away from the bubble (Cole, 1948). A pressure drop of 70% (from 1000 kPa to 300 kPa) over a distance of 14 cm, and that of 80% (from 1000 kPa to 200 kPa; see Fig. 6) over a distance of 34 cm from the bubble center have been recorded by tank transducers.

The coalesced bubble quickly breaks into cloud of smaller bubbles which migrate upward due to buoyancy effect. The bubble contour is traced and 360 bubble radii are obtained at equal azimuth locations. These data are then Fourier analyzed and the results are shown in Fig. 7, which shows the power spectral density of the coalesced bubble's interface at three instants: just after it is formed and 1 and 5 ms after it collapses. Here c is the bubble circumference and λ is the wavelength. This technique of obtaining the power spectral density of bubble interface to quantify the interface corrugation has been described in detail by Menon and Lal (1997). Moreover, by using painted globes, they have clearly shown that the glass fragments which are typically long and thin, considerably lag the bubble motion during collapse phase and therefore do not contribute to the interface corrugation. It can be inferred from Fig. 7 that the coalesced bubble starts exhibiting pronounced and distributed peaks in power spectral density soon after collapse. A peak is actually the square root of the sum of the squares of mode amplitude coefficients and occurs at integral fractions of bubble circumference because a periodic trace is being analyzed. The coalesced bubble is therefore very unstable.

A single coalesced bubble does not form only in an in phase oscillation. Another situation where the formation of a single coalesced bubble has been observed repeatedly and most surprisingly, is associated with a nonzero time delay and a very short inter-bubble distance. This case is shown in Fig. 8. The initial volume of the right glass globe is 125 ml and that of the left glass globe is 127 ml. They are almost touching each other such that the initial separation distance between them, d, is given by $d/R_o = 2.1$. Both of them are filled with stoichiometric mixture of Carbon Monoxide and Oxygen. The right globe explodes first (at time t = 0 ms) and tries to encompass the left globe as the bubble grows. When the left globe explodes (at time t = 8 ms), the shock wave emitted by this bubble travels through the right bubble as is evident by its protruding pieces. The right bubble, however, maintains its coherence and sphericity. It seems that the energy of the left bubble is substantially transferred to the right bubble, and it does not even get a chance to expand to its maximum radius. A force field is generated such that when the right bubble

starts to collapse, the left bubble just merges into its predecessor to form a single coalesced bubble, which continues the oscillation cycle as a single explosion bubble. Since no jets are formed and the coalesced bubble is formed by merging the energies of two bubbles, it has more residual energy than that of the previous example and does not disintegrate into smaller bubbles so quickly. In fact, it is even more stable than a single explosion bubble in free field and can, therefore, be used for focusing bubble energy for enhancement of its destructive capabilities.

The available energy for successive pulsations of the coalesced bubble can be calculated using Vokurka's (1986 and 1987) energy balance analysis (e.g., Menon and Lal, 1997). The various formulae for this analysis are given in the cited references and are, therefore, avoided here for the sake of brevity. The energy, $E_0 = 4\pi R_0^3 P_l / 3$, where R_0 is the initial globe radius and P_l is the ambient hydrostatic pressure at the explosion depth, is used to nondimensionalize energy and the heat release of stoichiometric carbon monoxide is taken to be 284 KJ/mole (Strahle and Liou, 1994). The total nondimensional energy available for oscillation of the right bubble at time t = 0 can be given by $\overline{E}_0 = 78.439$ for an explosion depth of 0.65 m. The nondimensional internal and the potential energies of the right bubble at its maximum radius for an expansion ratio of $R_{max} / R_0 = 2.738$, are estimated to be 38.043 and 19.528, respectively. The energy dissipated into the surrounding water by a shock wave thus equals $20.868E_0$. Therefore, the energy available for successive oscillation of the right bubble at its maximum radius equals $57.571E_0$. A similar analysis for the left bubble for a smaller explosion pressure and expansion ratio of only 1.095 yields the value of the available energy at its maximum radius to be $11.916E_0$. The coalesced bubble should apparently have available energy of $69.487E_0$ for its successive oscillation, which is roughly 20.7% more than what a single explosion bubble should have in a free field condition. The coalesced bubble is, in fact, observed to oscillate for an extended period of time.

It is interesting to note that the explosion pressure for the left bubble (200 kPa) is only about 20% of what it would have been in a free field case. Thus, an expanding bubble inhibits the formation of another explosion bubble in its close proximity by reducing its explosion pressure. This may be the reason why the left bubble does not have sufficient energy to expand to its maximum radius. But, it certainly aids its predecessor to form a coalesced bubble with a greater energy. This time, the right plug transducer lies inside the coalesced bubble as it collapses. The collapse pressure recorded by this transducer is very high (2500 kPa). Except for the plug transducers, the pressure traces recorded by the right and left transducers are once again almost identical, indicating a symmetrical bubble behavior.

Similar dynamic behavior is exhibited by the interaction of bubbles formed by glass globes of initially different sizes. It is not possible, however, to obtain an in phase oscillation because of a simple reason that the two bubbles have different time periods of oscillation. On the other hand, the formation of a coalesced bubble by mergence of two bubbles, have also been exhibited by the bubbles of different sizes when the smaller bubble has been absorbed into the larger bubble. This kind of bubble dynamics is not feasible for large inter-bubble distance.

When the initial inter-globe distance is sufficiently large, the bubbles start repelling each other for a nonzero time delay. The repulsion force increases with the delay between the explosions, up to the point when they are oscillating 180^{o} out of phase. In this case, when the predecessor bubble collapses, the successor bubble reaches its maximum radius. At this point the pressure field is abruptly reversed and this causes the formation of a strong reentrant water jet in the successor bubble. An example of out of phase interaction is shown in Fig 9. The initial volume of the right glass globe is 94 ml and that of the left glass globe is 92.5 ml. Both of them are filled with stoichiometric mixture of Carbon Monoxide and Oxygen. They are in a horizontal configuration and are initially separated by a distance d, where $d/R_0 = 4$. Figure 9 shows the initial globes' locations. The right globe explodes first (at time t = 0 ms) and reaches its maximum radius when

the left globe explodes (at around t = 7.5 ms). A strong reentrant water jet is formed in the left bubble as it collapses. Figure 10 shows how this reentrant jet travels with time. Here, x denotes the location of the jet tip relative to the inertial frame (the tank) and x = 0 corresponds to the instant when the jet tip becomes visible for the first time. The formation of a strong reentrant water jet has also been observed for two bubbles of different sizes.

As the phase delay between two explosions increases beyond 180^{o}, the repulsion force as well as the water jet velocity decrease in magnitude. If the phase delay between two explosions increases beyond 360^{o} (i.e., if one bubble has already completed one oscillation cycle when the other bubble forms), the resulting interaction is very weak. In this case, though the predecessor bubble manages to create a depression in successor bubble at its maximum radius, formation of a jet is not observed.

The horizontal configuration is very important from a practical standpoint, as it can set a catastrophic bending vibration to a nearby rigid body if tuned properly. The vertical configuration is also equally important, as it can dramatically enhance the impact pressure of a single bubble when collapsed near a rigid body. It is speculated that if two bubbles are placed close to each other along an axis perpendicular to a nearby rigid body, and if these two bubbles are tuned to oscillate 180^{o} out of phase with each other, a water jet will be formed directed towards the rigid surface with a velocity which will be higher than that formed by the collapse of a single bubble under similar circumstances. When the interaction of two bubbles is studied in vertical configuration, the orientation of the gravitational force changes. The gravitational effects are known to be controlled by the size of the bubble. If the gravitational effects are dominant, an isolated bubble migrates in an upward direction. But, in the presence of a competing effect, such as another pulsating bubble above or below it, the dynamics of the bubble are controlled by its spatial and temporal separations from it. Therefore, two in phase bubbles separated by a short vertical distance attract each other. On the other hand, two out of phase bubbles separated by a short vertical distance repel each other

such that the top bubble migrates upward and the bottom one migrates downward and the jets formed in them pierces them in the directions of their migration. There is an upper bound to the distance between two identical out of phase bubbles in vertical configuration beyond which their interaction would cease to exist and its value can be easily estimated as described below.

Experiments were carried out to study the interaction of a free surface with an explosion bubble. A simple sting mount was used to support the glass globe and the depth of water in the tank was decreased in a step of 2.54 cm. At larger depths, the gravitational effects are dominant and the bubble migrates upward. Reduced water depths provide competing effects and the bubble starts to migrate downward. It was found that the bubble migration velocity smoothly changes its direction as well as its magnitude. Figure 11 shows the transition of bubble migration velocity with water depth. As two in phase bubbles are equivalent to a single bubble near a rigid boundary, similarly two out of phase bubbles are equivalent a single bubble near a free surface. The transition point of Fig. 11 can thus determine the maximum inter-bubble distance for which two identical out of phase bubbles in vertical configuration far away from water free surface would start interacting with each other. The maximum center-to-center distance between two identical interacting bubbles (of approximate volume of 230 ml) oscillating 180^{o} out-of-phase with each other was found to be $6.8R_0$, R_0 being the initial radius.

Conclusions

Underwater explosion experiments have been conducted in a water tank using flammable gases in glass globes to study the dynamics of interaction of two explosion bubbles in both horizontal and vertical configurations. The former configuration can excite a nearby submerged structure in bending vibration mode, while the latter can easily be tailored for the directionality and enhancement of the impact pressure resulting from the collapse of an underwater explosion bubble near a solid boundary. Depending on the delay between two explosions and inter-bubble distance, the bubbles may either attract each other to form a single coalesced bubble, or they may violently

repel each other. A violent interaction between the bubbles leads to an increased instability of the bubbles. If a coalesced bubble is formed by mergence of two bubbles, the resulting bubble has more residual energy and is more stable for successive oscillations. An out-of-phase oscillation generates a reentrant water jet which pierces the bubble. Water free surface repels the bubble and the transition point of bubble migration velocity determines the maximum inter-bubble distance required for the initiation of interaction between two out-of-phase pulsating bubbles.

Acknowledgment

This work is supported by the Office of Naval Research under Grant No. N00014-91-J-1963 and monitored by Drs. Richard Miller and Judah Goldwasser.

References

Arons, A. B., Slifko, J. P., and Carter, A., 1948, "Secondary Pressure Pulses Due to Gas Globe Oscillation in Underwater Explosions: I. Experimental Data," *The Journal of the Acoustical Society of America*, Vol. 20, pp. 271-276.

Birkhoff, G., and Zarantonello, E. H., 1957, *Jets, Wakes, and Cavities*, Academic Press Inc, New York, pp. 241-243.

Blake, J. R., and Gibson, D. C., 1981, "Growth and Collapse of a Vapor Cavity near a Free Surface," *Journal of Fluid Mechanics*, Vol. 111, pp. 123-140.

Chahine, G. L., 1977, "Interaction Between an Oscillating Bubble and a Free Surface," *Journal of Fluids Engineering*, Vol. 38, pp. 709-716.

Chahine, G. L., 1982, "Experimental and Asymptotic Study of Nonspherical Bubble Collapse," *Applied Scientific Research*, Vol. 38, pp. 187-197.

Chahine, G. L., and Liu, H. L., 1985, "A Singular Perturbation Theory of the Growth of a Bubble Cluster in a Superheated Liquid," *Journal of Fluid Mechanics*, Vol. 156, pp. 257-279.

Chahine, G. L., and Sirian, C. R., 1985, "Collapse of a Simulated Multibubble System," *ASME, Cavitation and Multiphase Flow Forum*, Albuquerque, New Mexico, pp. 78-81.

Chahine, G. L., 1991, "Dynamics of the Interaction of Non-Spherical Cavities," *Mathematical approaches in Hydrodynamics,* ed., T. Miloh, Society for Industrial Applications of Mathematics, Philadelphia, pp. 51-67.

Chahine, G. L., and Duraiswami, R., 1992, "Dynamical Interactions in a Multi-Bubble Cloud," *Transactions of the ASME*, Vol. 114, pp. 680-686.

Cole, R. H., 1948, *Underwater Explosions*, Princeton University Press, Princeton.

Fujikawa, S., Takahira, H., and Akamatsu, T., 1985, "Underwater Explosion of Two Spherical or Nonspherical Bubbles and Their Interaction With Radiated Pressure Waves," *Shock Waves and Shock Tubes*, Proceedings of the Fifteenth International Symposium, Berkeley, CA, pp. 737-744.

Fujikawa, S., and Takahira, H., 1986, "A Theoretical Study on the Interaction between Two Spherical Bubbles and Radiated Pressure Waves in a Liquid," *Acoustica*, Vol. 61, pp. 188-199.

Fujikawa, S., and Takahira, H., 1988, "Dynamics of Two Nonspherical Cavitation Bubbles in Liquids," *Fluid Dynamics Research*, Vol. 4, pp. 179-194.

Menon, S., and Lal, M., 1997, "On the Dynamics and Instability of Bubbles Formed During Underwater Explosions," *Experimental Thermal and Fluid Science Journal*, in press.

Menon, S., and Pannala, S., 1997, "Simulation of Underwater Explosion Bubbles using an Arbitrary Lagrangian-Eulerian Formulation," Proceeding of the 1997 ASME Fluid Engineering Division Summer Meeting, FEDSM97-3244.

Moroika, M., 1974, "Theory of Natural Frequencies of Two Pulsating Bubbles in Infinite Liquid," *Journal of Nuclear Science and Technology*, Vol. 11, pp. 554.

Serebryakov, V. V., 1992, "Expansion of Axisymmetric and Spherical Cavities, and Their Interactions," *Fluid Mechanics Research*, Vol. 21, No. 2, pp. 67-79.

Shepherd, J. E., 1988, "Interface Effects in Underwater Explosions," *Conventional Weapons Underwater Explosions*, ONR Workshop Report, pp. 43-83.

Shima, A., 1971, "The Natural Frequencies of Two Spherical Bubbles Oscillating in Water," *ASME Journal of Basic Engineering*, Vol. 93, pp. 426-432.

Shima, A., and Tomita, Y., 1988, "Impulsive Pressure Generation by Bubble/Pressure-Wave Interaction," *AIAA Journal,* Vol. 26, No. 4, pp. 434-437.

Smith, R. H., and Mesler, R. B., 1972, "A Photographic Study of the Effect of an Air Bubble on the Growth and Collapse of a Vapor Bubble near a Surface," *Journal of Basic Engineering*, pp. 933-942.

Strahle, W., and Liou, S. G., 1994, "Physical and Chemical Observations in Underwater Explosion Bubbles," *Symposium (International) on Combustion*, Vol. 25, pp. 89-94.

Takahira, H., 1988, "Nonlinear Oscillation of Two Spherical Gas Bubbles in a Sound Field," *ASME Cavitation and Multiphase Flow Forum*, pp. 1-4.

Tomita, Y., Shima, A., and Ohno, T., 1984, "Collapse of Multiple Gas Bubbles by a Shock Wave and Induced Impulsive Pressure," *Journal of Applied Physics*, Vol. 56, No. 1, pp. 125-131.

Van Wijngaarden, L., 1972, "On the Collective Collapse of a Large Number of Gas Bubbles in Water," *Proceedings of the 11th International Congress of Applied Mechanics*, Springer, Berlin, pp. 854-865.

Vokurka, K., 1986, "A Method for Evaluating Experimental Data in Bubble Dynamics Studies," *Czech. Journal of Physics*, B, Vol. 36, pp. 600-615.

Vokurka, K., 1987, "Oscillations of Gas Bubbles Generated by Underwater Explosions," *Acta Technica Csav*, Vol. 2, pp. 162-172.

Wang, Y. C., and Brennen, C. E., 1994, "Shock Wave Development in the Collapse of a Cloud of Bubbles," *Cavitation and Multiphase Flow Forum*, Vol. 194, pp. 15-19.

Wilkerson, S. A., 1989, "Boundary Integral Technique for Explosion Bubble Collapse Analysis," *Energy-Sources Technology Conference and Exhibition*, 89-OCN-2, Houston, Texas, pp. 1-12.

List of Figures

Figure 10. Reentrant water jet tip location and velocity for two bubbles of Fig 9 oscillating 180^{o} out-of-phase.

Figure 11. Bubble migration velocity for the interaction of a single bubble with water free surface.

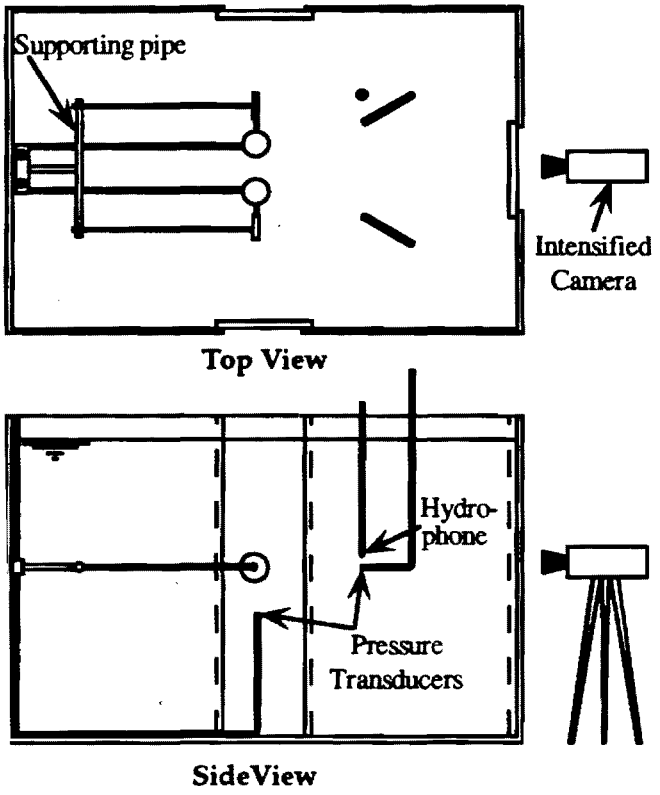
Supporting pipe
Intensified
Camera
Top View
Hydro-
phone
Pressure
Transducers
SideView

Figure 1

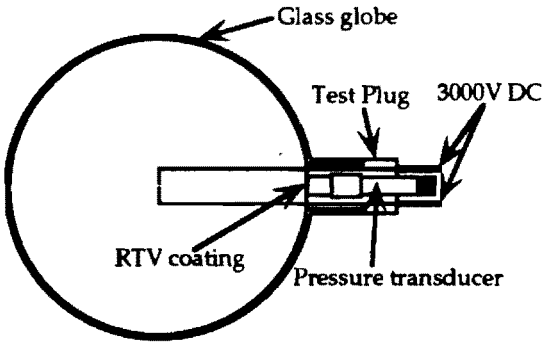

(a)

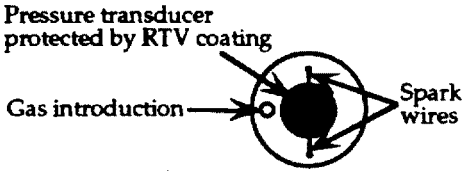

(b)

Top view of the test plug

Figure 2

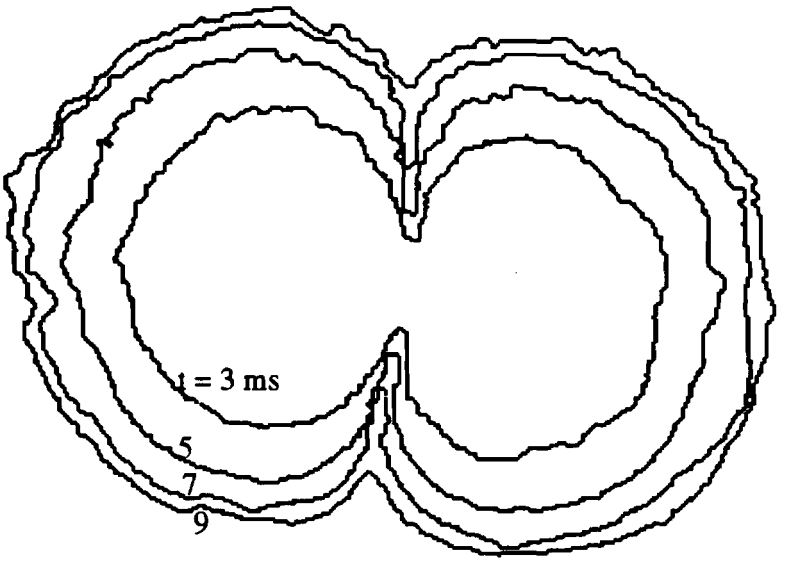

Figure 3a

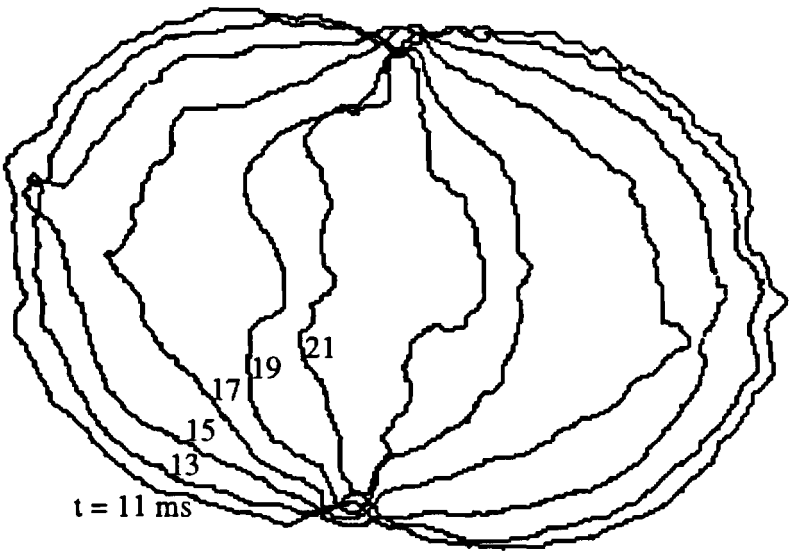

Figure 3b

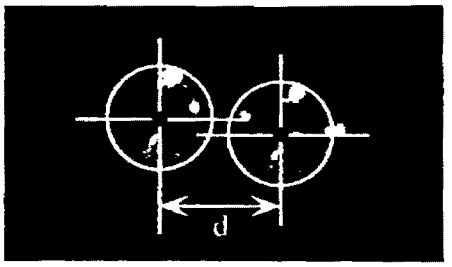

$d/R_o = 2.32$

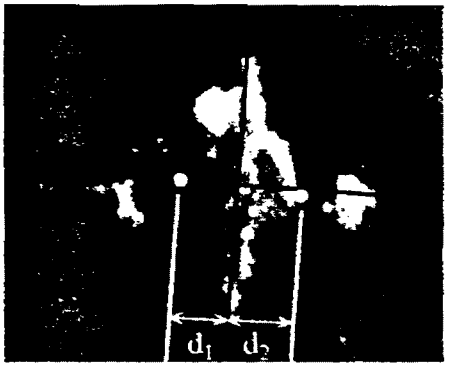

$d_1/R_o = 1.1$; $d_2/R_o = 1.22$

Figure 4

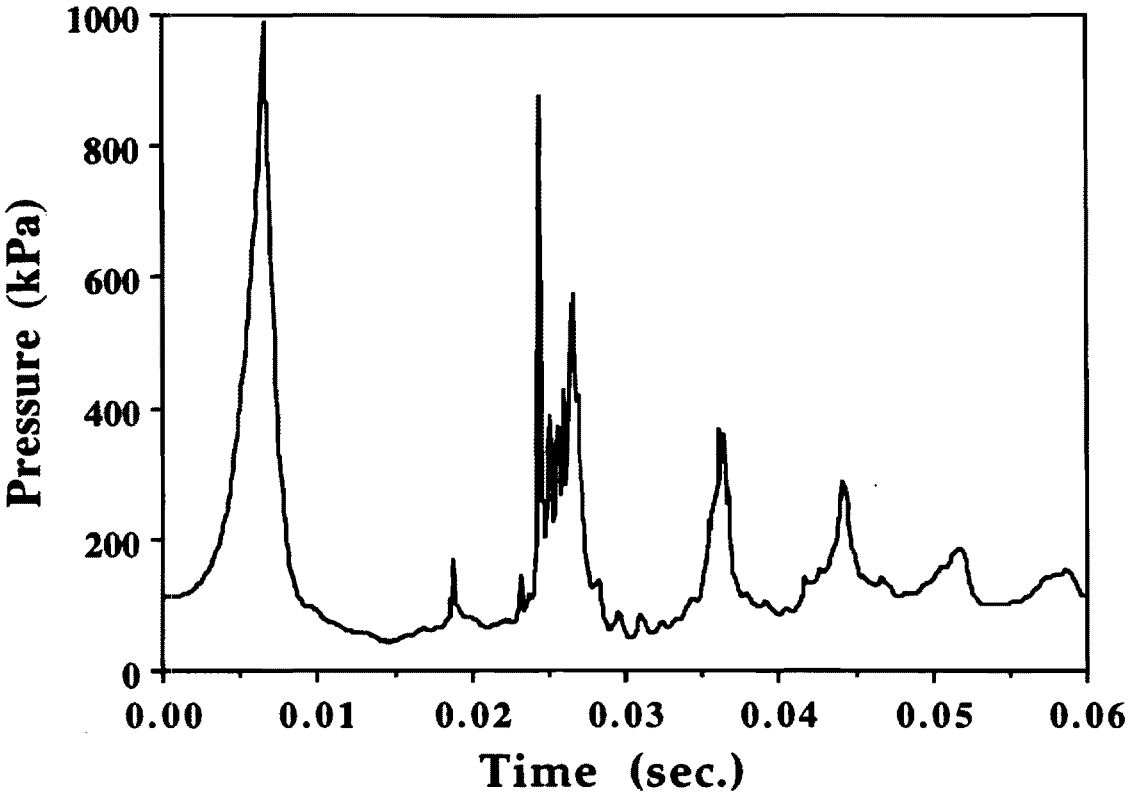
1000
800
600
400
200
0
Pressure (kPa)
0.00
0.01
0.02
0.03
0.04
0.05
0.06
Time (sec.)

Figure 5

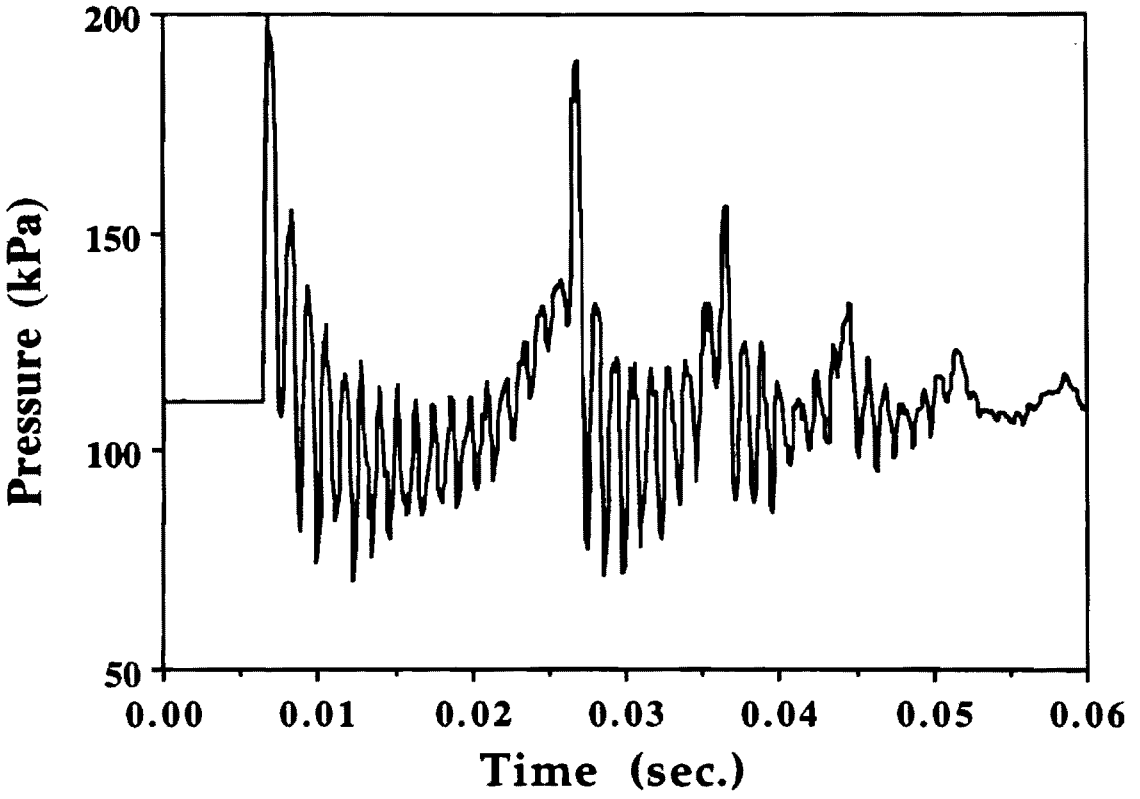
200
150
100
50
Pressure (kPa)
0.00
0.01
0.02
0.03
0.04
0.05
0.06
Time (sec.)

Figure 6

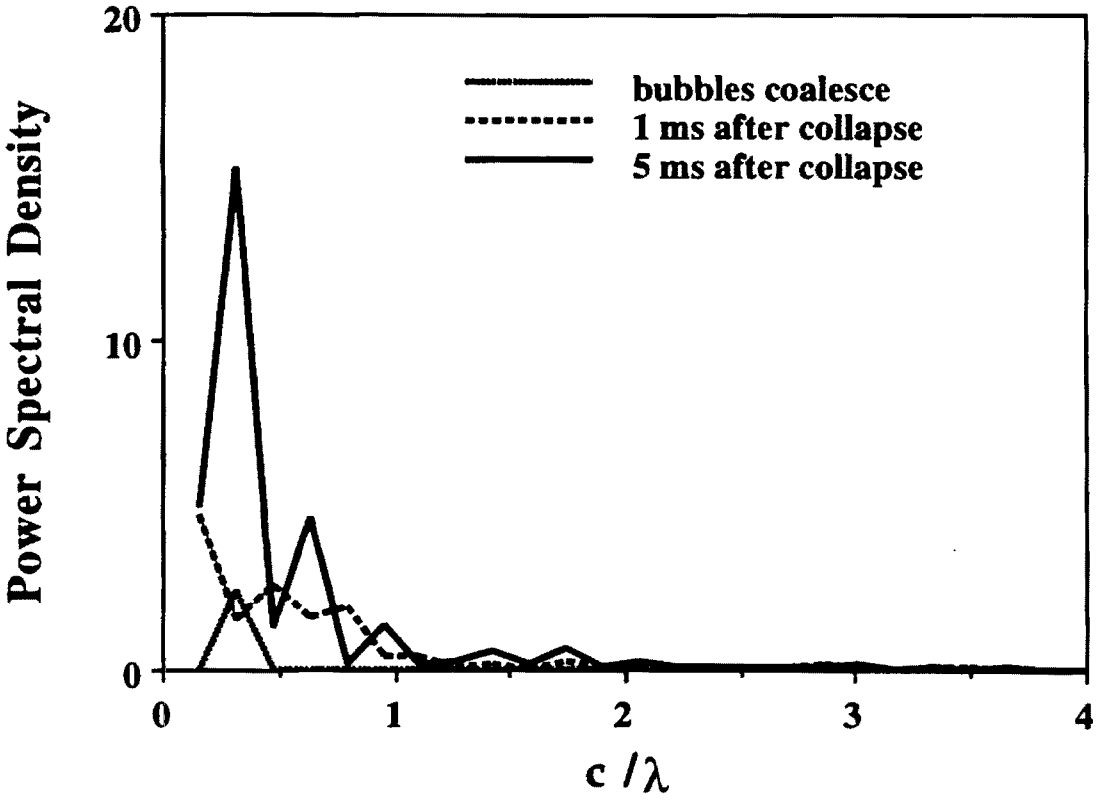
Power Spectral Density
20
10
0
0
1
2
3
4
c /λ
bubbles coalesce
1 ms after collapse
5 ms after collapse

Figure 7

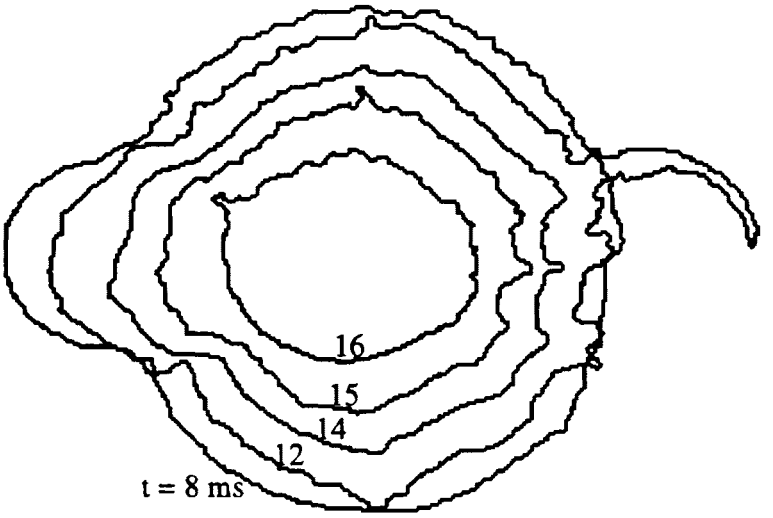

Figure 8

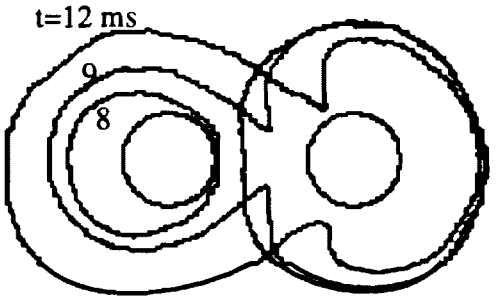

Figure 9a

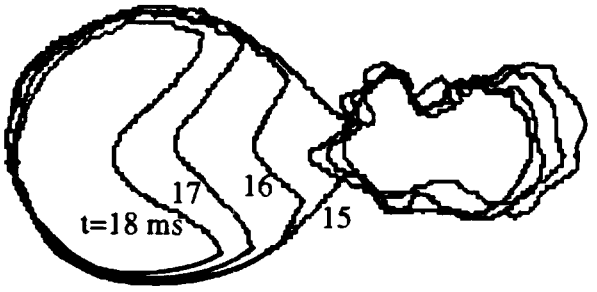

Figure 96

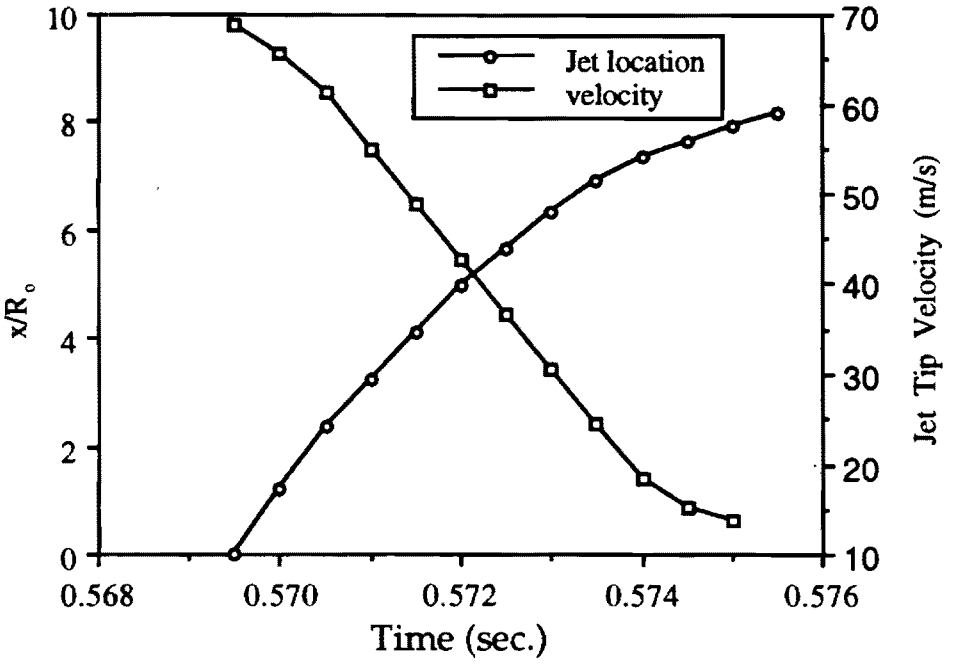
Jet location
velocity
x/R$_o$
Jet Tip Velocity (m/s)
Time (sec.)
0
2
4
6
8
10
10
20
30
40
50
60
70
0.568
0.570
0.572
0.574
0.576

Figure 10

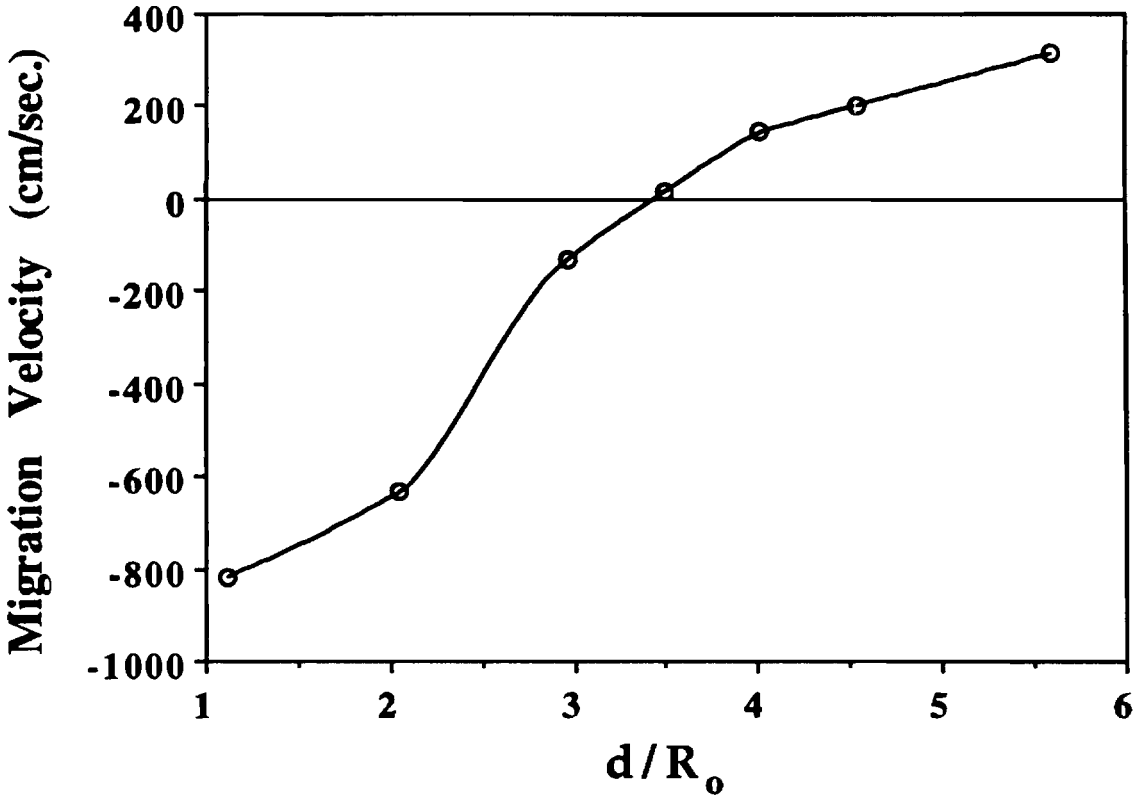
Migration Velocity (cm/sec.)
400
200
0
-200
-400
-600
-800
-1000
1
2
3
4
5
6
d/R$_o$

Figure 11

Preliminary Draft

Simulations of Underwater Mine Destruction Using Detonation Cord Explosives

S. Menon and L. Plachco
School of Aerospace Engineering
Georgia Institute of Technology
Atlanta, GA 30332-0150

Abstract

Simulations of underwater detonation cord mesh explosion have been carried out using a three-dimensional arbitrary Lagrangian-Eulerian finite-element code. Earlier, this code was successfully employed to capture both qualitatively and quantitatively the dynamics of underwater explosions near rigid surfaces. In thepresent study, this code was used to study the effect of detonation cord explosions on a stainless steel rod placed vertically within the mesh. This metal rod mimicked the trigger arm of a buried mine. The explosion strength was chosen to be larger than the yield strength of themetal rod. It was shown that when the metal rod is placed directly in the center of the mesh, the explosion bubble collapse causes a very high pressures along the diagonal axes and results in the rod getting squeezed and lengthened. On the other hand, when the rod was placed away from the mesh center, asymmetric forces are generated that results in the fracture of the rod into multiple pieces. These results demonstrate that to ensure repeatable destruction of a buried mine, asymmetric design of detonation cord (by changing energy density and/or geometry) is desired. Further calculations are planned to determine if an optimum design of the detonation mesh exists.

Introduction

Earlier studies (Menon and Pannala, 1998; Menon and Yang, 1998) using a three-dimensional Arbitrary Lagrangian-Eulerian (ALE3D) code have established that this code can capture with very good quantitative and qualitative accuracy the dynamics of explosion bubble collapse and the resulting impact pressure generated on the wall. The earlier studies were designed to evaluate the capability of the code and also to determine how the code could be utilized to develop explosive shape designs to achieve particular impact objectives.

A configuration of key interest in the present study is the behavior of explosion bubble collapse for more realistic devices such as a detonation cord net. This type of net is typically deployed on the surf zone of beaches and detonated to destroy buried mines. Due to the complexity of the explosion dynamics, field experiments do not provide detailed visualization of the explosion process and the consequent effect on the buried mine. Recent experiments in a shallow water test facility (Menon et al., 1998) of explosions near exposed and buried (under sand) surfaces have demonstrated that the bubble collapse does result in high impact pressure on the surface even when the surface is buried below a layer of sand. High speed imaging and pressure measurements were carried out to quantify the explosion dynamics and the behavior of the collapsing bubble for a range of parameters. It was determined that the peak impact pressure depends upon the explosion energy, the distance of initial charge above the surface and the sand thickness. Interestingly, it was also determined that the behavior of the sand under the impact force can also play a role in determining the impact pressure on the buried surface. A scaling relation has been obtained to correlate all the data. An attempt to model this complex multiphase behavior is currently underway.

In the present study, we focus on the behavior of detonation cord explosions and its impact of rigid bodies within its neighborhood. The availability of the ALE3D code at this stage provides us with an opportunity to investigate these types of problems. We limit our studies to the case of a single square mesh of detonation cord (made up of four cylindrical charges of same energy) that is located on the ground. Simulations of the explosion of this mesh was first carried out and then, a series of calculations were carried out with a metal (stainless steel) cylinder rod positioned in the center (Case D1), off-center (Case D2) and in the corner (Case D3). Figure 1 shows schematically the various cases studied. The rationale for the choice of this configuration is that buried mines have trigger arms that protrude, in some cases, above the ground. The goal of the detonation cord is to cause a pressure differential force on the arm which in turn would result in the movement of the arm resulting in trigering the detonation. However, field experiments in the past have produced mixed results in terms of the effect of explosion on the trigger arm (it appears the shape of the arm changes the dynamics of the interaction). The present study, albiet highly simplified at present hopefully will provide a preliminary understanding of the explosion dynamics. Subsequently, more realistic scenarios can be studied using this approach.

Results and Discussions

A key feature of the realistic strong underwater explosion is the formation and propagation of a strong shock wave upon the ignition and explosion. This detonation wave propagates at very high speed and can play a major role in the impact process. Earlier studies were carried out to mimic explosions that were carried out in our shallow water test facility. As such, the explosion energy was relatively low. The ALE3D capability has no limitations regarding the type of energy and the shape of the explosive charge. To demonstrate this, Fig. 2 shows the propagation of a detonation shock wave

formed when a high energy device is exploded in free field (only a quarter quadrant is shown). The impingement of such a strong shock wave on a surface can result in significant structural damage. Here, we will not attempt to simulate a real detonation cord energy (which is not available in open literature). Rather, we simulate a representative case using parameters similar to our earlier studies (Menon and Yang, 1998). Table 1 summarizes the test conditions and the properties of the detonation cord used.

Here, we discuss on the cases of the detonation net with the metal cylinder in the middle. Figures 3a-e show respectively, a time sequence of the velocity vector field in the x-y plane at a location just above the ground for case D1 (metal cylinder in the center of the net). The bubble shape is shown in these figures as a solid line. In Fig. 3a, the explosion bubble has reached its maximum and the flow is still outwards in all direction. In Fig. 3b, the bubble begins to collapse and results in a reversal of the fluid motion. However, it can be noted that although the collapse is symmetric, the inward motion of the fluid primarily occurs along the diagonal and the reflection of this incoming fluid from the cylinder results in an outward fluid motion in the x- and y- perpendicular directions. Due to the collapse along the diagonal axes, peak pressures are expected along these directions as will shown below. The key point to note from these figures is that the entire collapse process is symmetric. The implication of this symmetry on the structural forces on the metal cylinder is discussed below.

Figure 4a-c show respectively, three snapshots of the pressure contours in the same x-y plane and at the same location above the ground. As can be seen in Fig. 4c, the diagonal collapse of the impinging jet motion results in high local pressure along the diagonal axes. The pressure is relatively lower in the principal x- and y-axis directions. Thus, one can assumed that the metal cylinder is undergoing compression along the diagonal. If the metal yield strength is unable to withstand this force then it is likely to

undergo failure mode. In the present case, the metal rod is a stainless steel rod with an yield strength of 340 N-m. The initial explosion energy for the detonation cord around 503 N-m. Thus, it is likely that this could result in structural failure of the metal rod as observed in these calculations.

Further effects of the explosion and the explosion bubble collapse on the metal cylinder can be determined by visualization of the velocity vector field and the pressure field in the y-z plane. Figures 5a-e show respectively, a time sequence of the velocity field and Figs. 6a-e show the corresponding pressure contours in the y-z plane at x = xc (which is a plane through the center of the metal cylinder). The metal cylinder is shown in these figures as a solid lined object. The velocity vector field shows the initial outward motion (Fig. 5a) and then the beginning of the collapse (Fig. 5b).The flow impinges on the metal rod and then rebounds and flows away from the rod (Figs. 5d, e).

The pressure contours in the y-z plane shows the impact of the bubble collapse much more clearly. Initially (Figs. 6a,b) region of high pressure is seen on the sides of the rod and on the top region. However, overall the pressure contours are symmetric. It can be seen that as the bubble collapses (Figs. 6c-e) the high pressure region surrounds the bubble and the metal cylinder actually gets squeezed and becomes thinner and taller than its original size. The fluid-structure interaction simulated using ALE3D clearly demonstrate the ability of such simulations to understand this type of complex problem.

In summary, when the metal cylinder is place in the center of a detonation cord mesh then the explosion results in a symmetric flow pattern with the collapse occurring primarily in the diagonal directions. However, due to symmetry the stresses (mostly compressive) on the metal cylinder occur also symmetrically. As a result, the cylinder gets squeezed and elongates under the explosion force.

To understand the collapse dynamics more clearly, calculations were carried out with the metal cylinder located off-center along the x-axis (Case D2) and located at the corner (Case D3). It was expected that these positioning will make the collapse pattern non-symmetric and should result in unbalanced forces on the metal cylinder. This was observed in these calculations. In fact, due to the non-symmetric forces on the metal rod, the forces on the rod were large enough to fracture it. Some representative results for these cases are discussed below.

Figures 7a and 7b show respectively, the pressure contours in the x-y plane near the ground for the off-center case (case D2) and the corner case (Case D3). Since the metal rod was shifted in the positive x-direction the pressure rise is much higher on the left side of the rod. This can be observed by comparing to the earlier case of the rod located in the center. The collapse is still along the diagonal axis in both cases. This results in an asymmetric force on the metal rod.

The velocity vector fields do not show anything significantly different (other than some asymmetry in the flow motion) from the images shown in Figs. 3 and therefore, are not shown. Briefly, the collapse process still occurs along the diagonal with the fluid motion stronger in the left side (since the metal rod was placed off-center to the right and in the top right corner). We discuss below primarily the pressure contours to show the impact of the explosion on the metal rod.

Figures 8a-e shows respectively, the pressure contours in the y-z plane through the metal rod for the off-center case (the corresponding pressure contours for the corner case are not shown since the result was quite similar). The metal rod is shown as a light blue line in these figures and is explicitly marked in these figures. It can be seen that

immediately after the explosion, high pressure is observed on the rod near the ground and half-way above the ground (Figs 8a). This is due to the initial explosion shock impingement. This force appears to be sufficient to cause a fracture in the metal rod. Subsequently, as the bubble collapse and the pressure builds up asymmetrically the rod breaks up as seen in the subsequent figures. This can be clearly observed in Fig. 8c-e where the light blue line (representing the rod) appears as two distinct sections.

A similar result is observed in the case of the rod placed on the corner. It would appear from these simulations that when the metal rod is off-center in any way the forces on the rod become asymmetrical and causes the rod to fracture (if its strength is low enough which was true for the present case). On the other hand, when the rod was in the center of the mesh, due to symmetry the forces just squeezes the rod and lengthens it.

From design standpoint this suggests that to achieve a non-symmetrical force on the metal rod we need to device a detonation code mesh that is NOT symmetric in energy density and/or in geometrical design. Some characteristic configurations are planned for future studies to determine if an optimum design can be developed that will always result in the forces on the metal rod to be asymmetrical. From the standpoint of causing a structural change of the trigger arm of a buried mine, this approach may allow for the detonation cord explosive to trip the arm all the time. We hope to investigate these features in the near future.

Conclusions

Simulations of underwater detonation cord mesh explosion have been carried out using a three-dimensional arbitrary Lagrangian-Eulerian finite-element code. Earlier, this code was successfully employed to capture both qualitatively and quantitatively the dynamics of underwater explosions near rigid surfaces. In thepresent study, this code was used to study the effect of detonation cord explosions on a stainless steel rod placed vertically within the mesh. This metal rod mimicked the trigger arm of a buried mine. The explosion strength was chosen to be larger than the yield strength of themetal rod. It was shown that when the metal rod is placed directly in the center of the mesh, the explosion bubble collapse causes a very high pressures along the diagonal axes and results in the rod getting squeezed and lengthened. On the other hand, when the rod was placed away from the mesh center, asymmetric forces are generated that in all cases results in the fracture of the rod into multiple pieces. These results demonstrate that to ensure repeatable destruction of a buried mine, asymmetric design of detonation cord (by changing energy density and/or geometry) is desired. Further calculations are planned to determine if an optimum design of the detonation mesh exists.

References

Menon, S. and Lal, M. K. 1998 On the dynamics and instability of bubbles formed during underwater explosions. *Experimental Thermal and Fluid Science Journal, to appear.*

Menon, S., Lal, M., Placho, L. and Jaquelin, F. 1998a Collapse of underwater explosion bubbles near exposed and buried rigid surfaces. Under preparation.

Menon, S., Yang, B. and Placho, L. 1998b Simulations of underwater mine destruction using detonation cord explosive. Under preparation.

Menon, S. and Pannala, S 1998 Simulations of underwater explosion bubble dynamics. under revision., to appear in *J. of Multiphase Flows*..

LIST OF FIGURES

Figure 8. Time sequence of the pressure contours in the y-z plane at x = xc (through the center of the rod) for the off-center case D2. The location of the rod is highlighted. Note that as the asymmetric pressure builds up the rod fractures into multiple pieces.

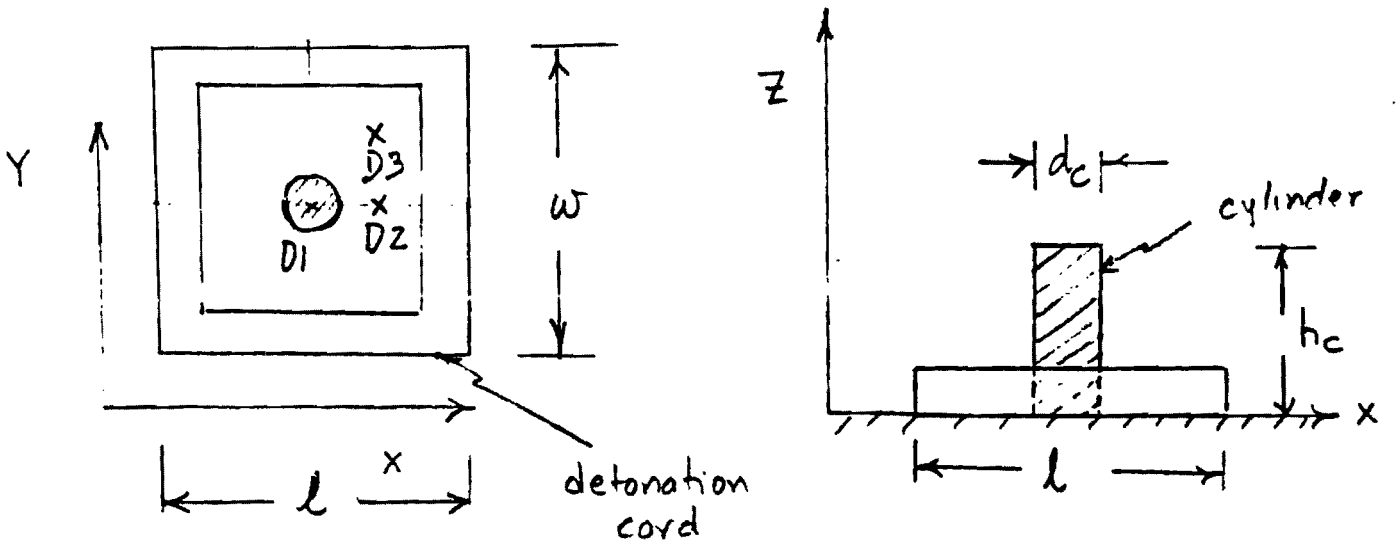

$l = 0.14\ m$

$w = 0.14\ m$

$d_c = 0.015\ m$

$h_c = 0.07\ m$

Total Energy of detonation cord = 503 N-m

Yield Strength of Cylinder = 340 N-m

Figure 1 : Locations for cases D1, D2, D3 are shown in Figure

Figure 2

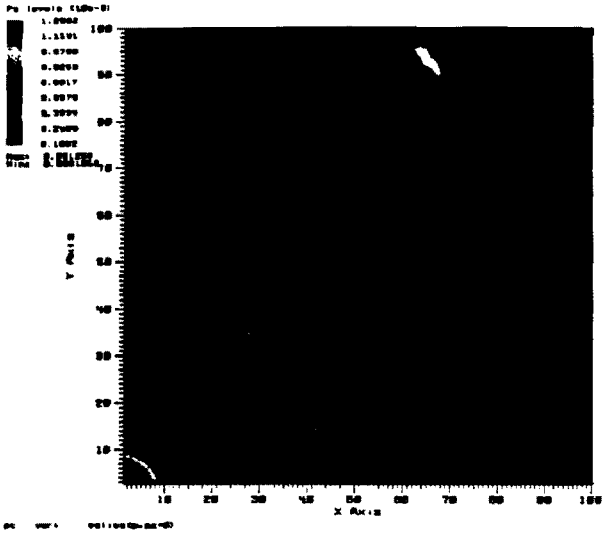

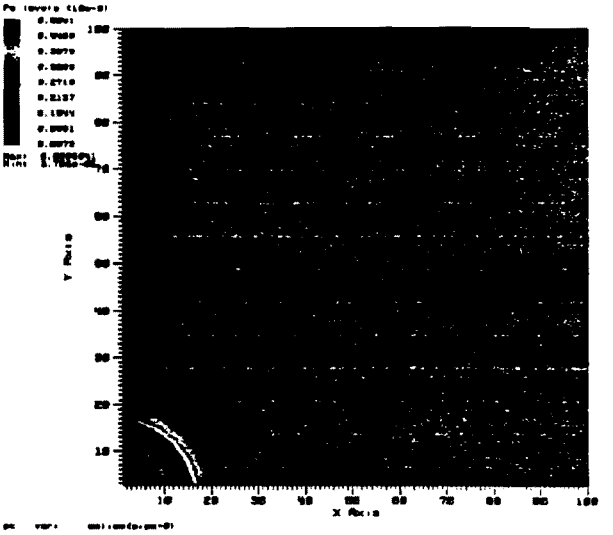

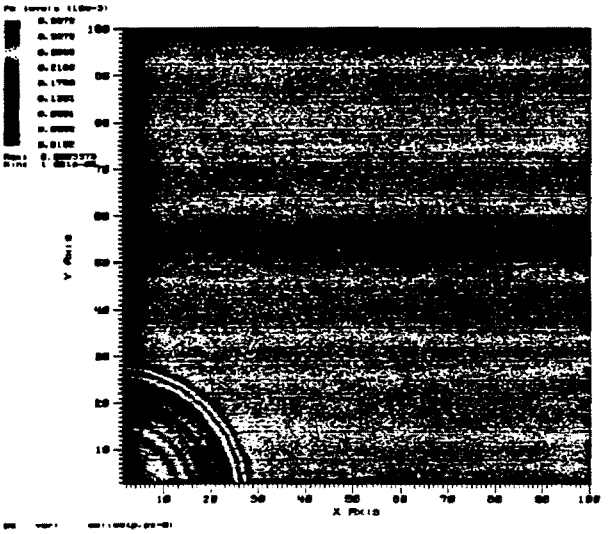

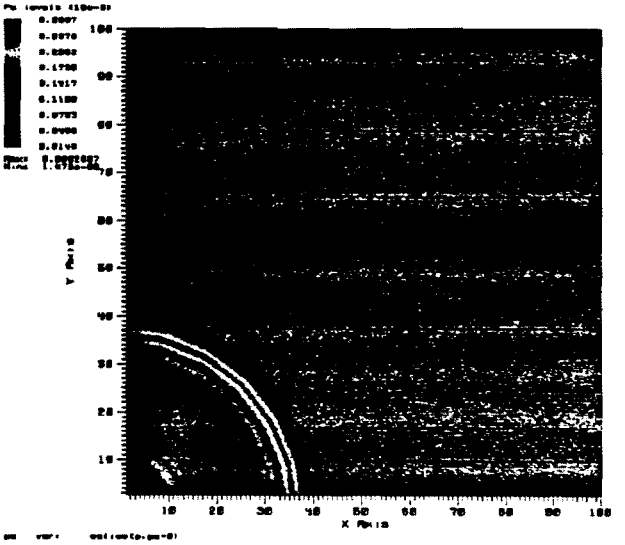

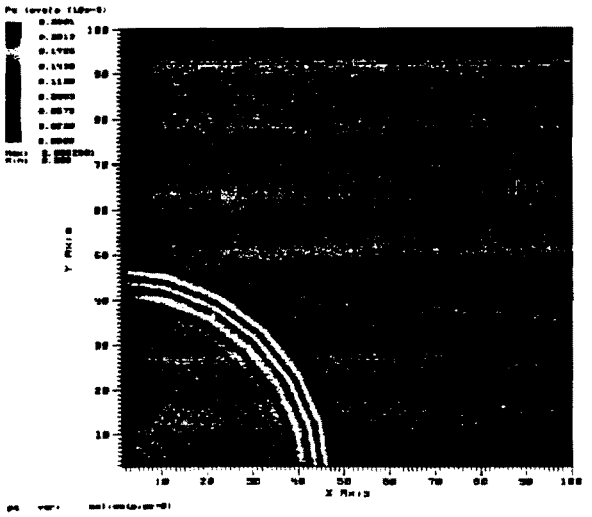

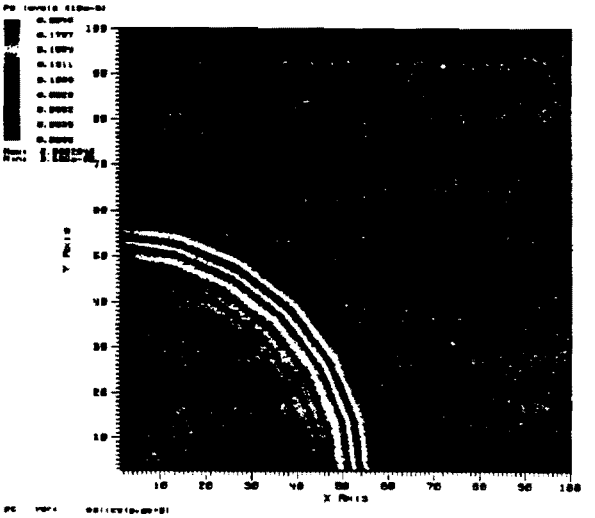

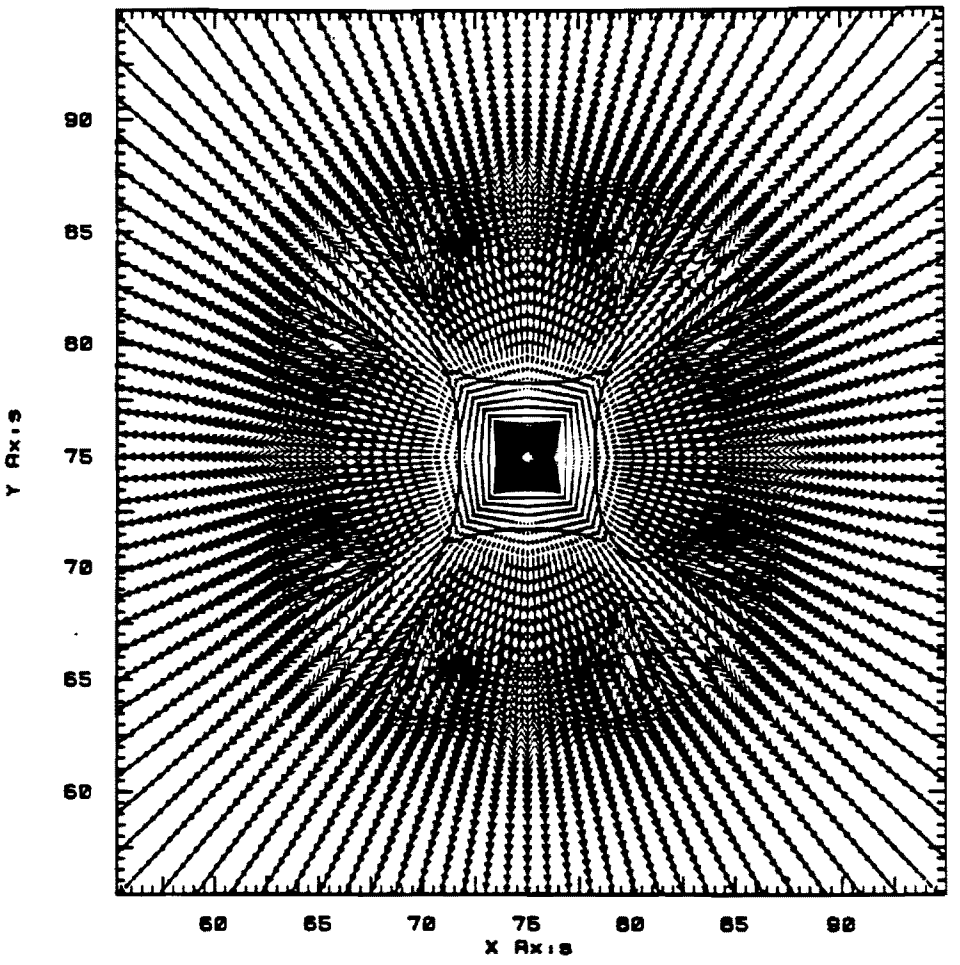

a) t = 4·5

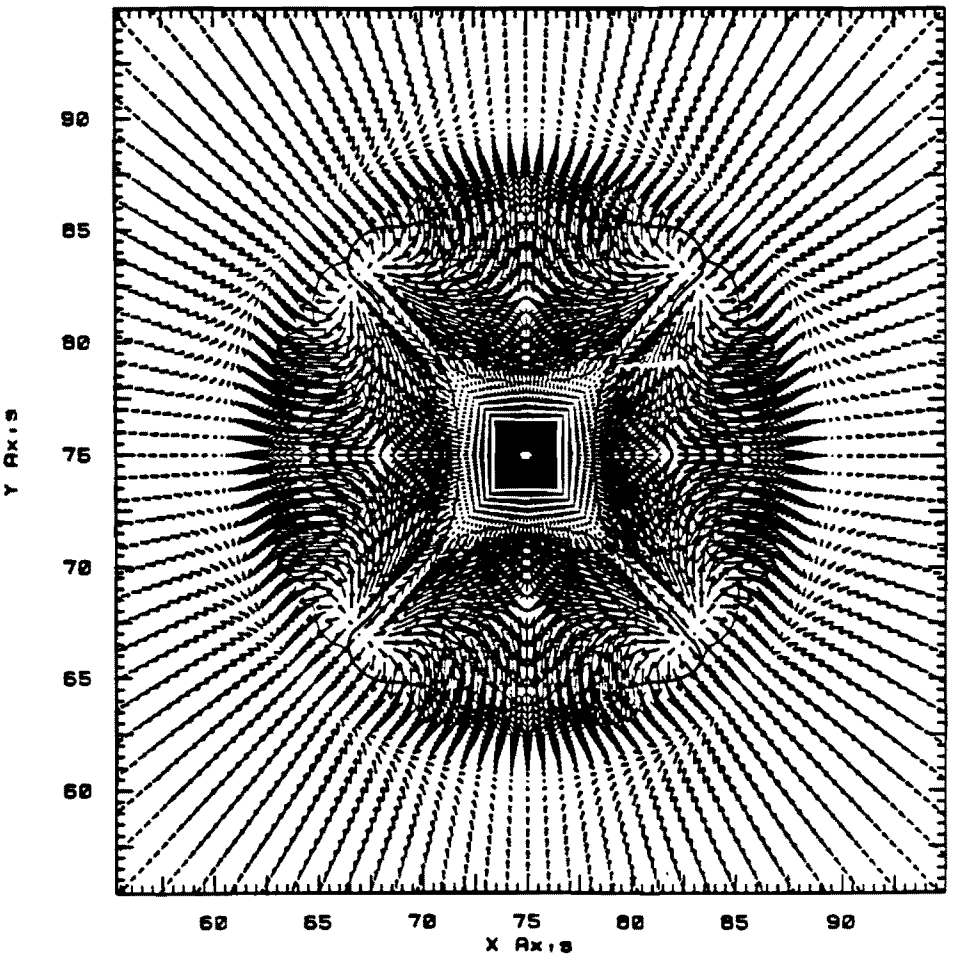

b) t = 9 ms

re 3

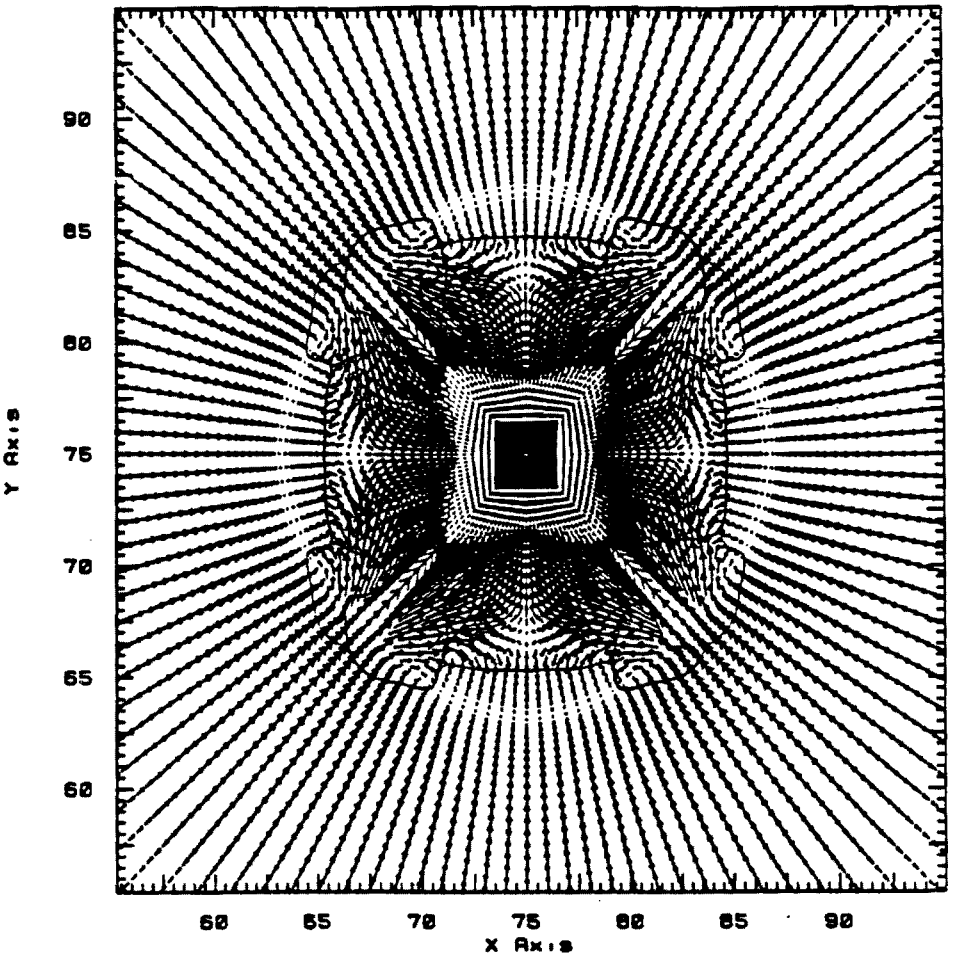

c) t = 12 ms

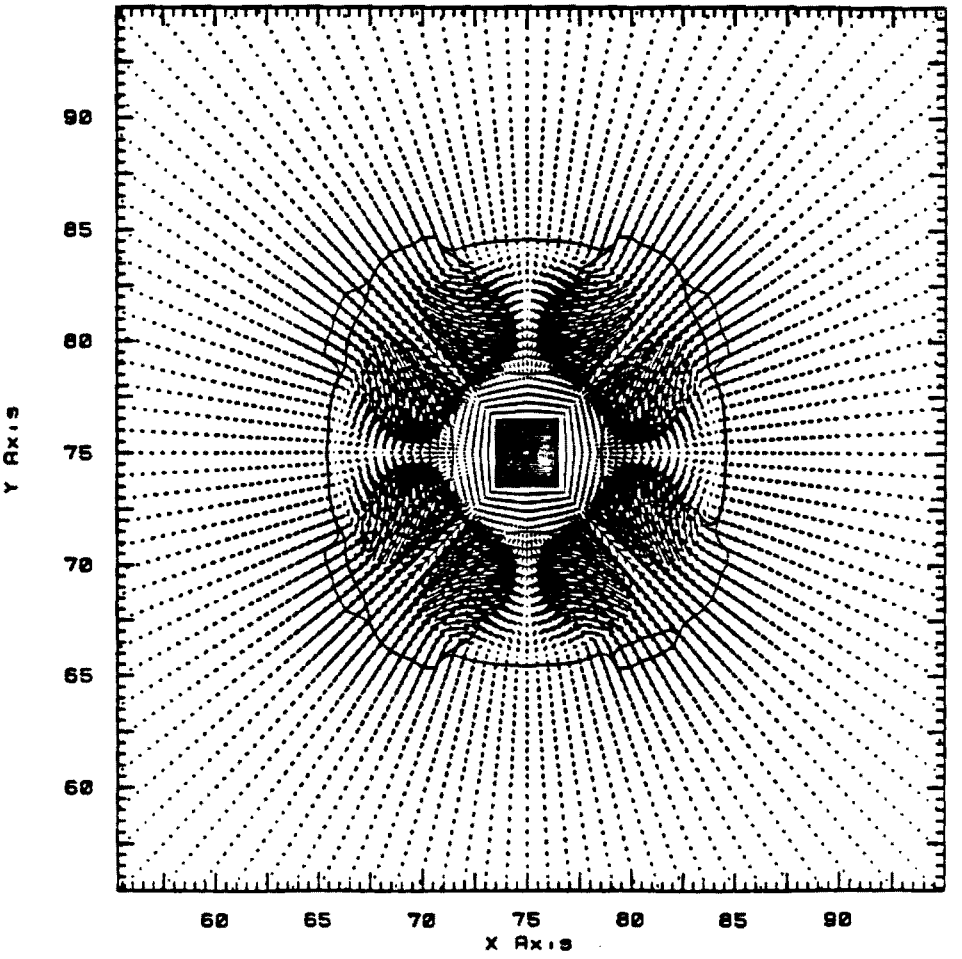

d) t = 15 ms

re 3 (cont)

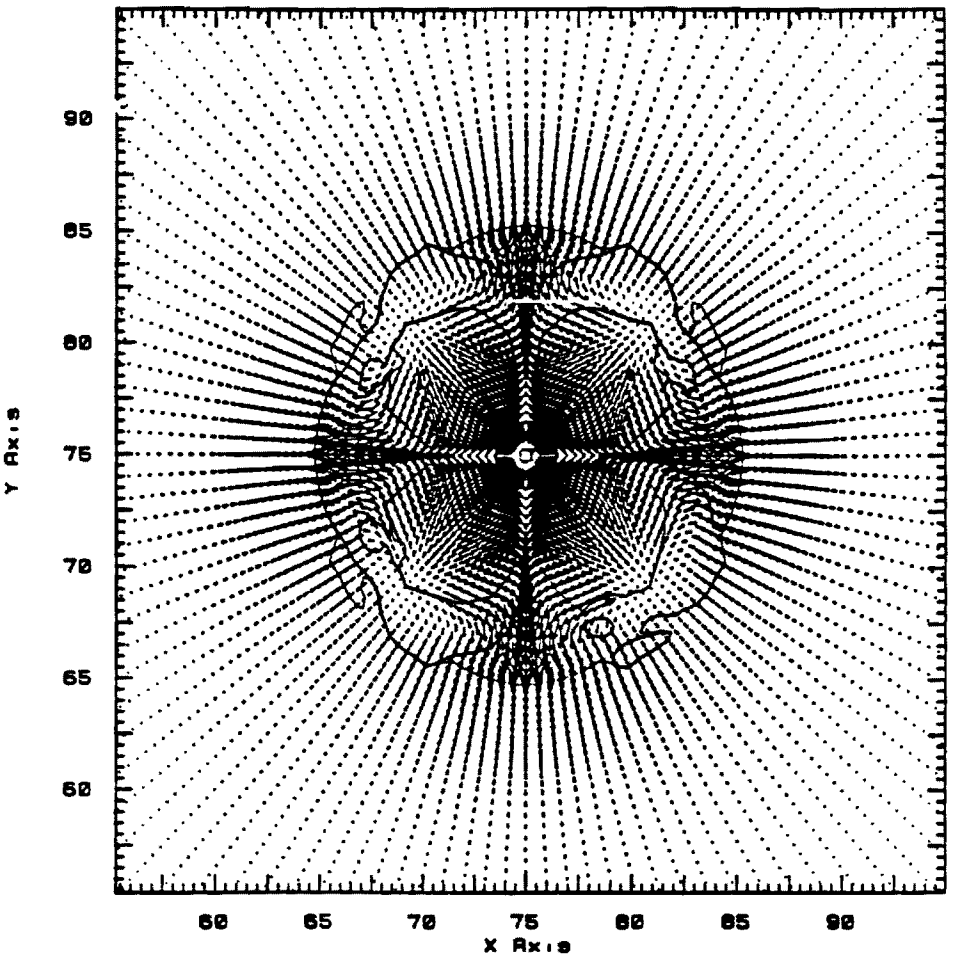

e) t=18 ms

Figure 3 (cont.)

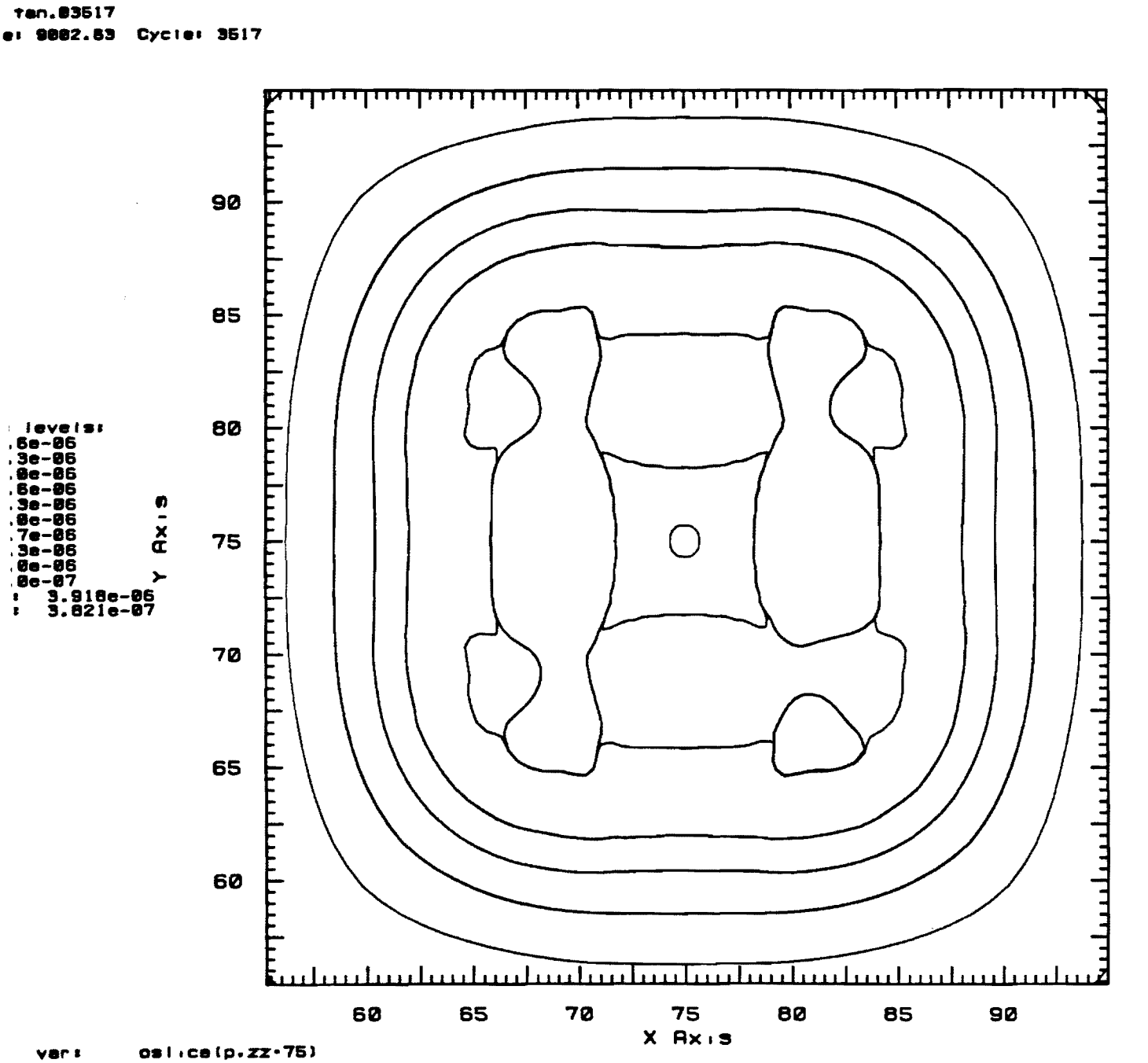
tan.03517
e: 9002.69 Cycle: 3517
levels:
.6e-06
.3e-06
.0e-06
.6e-06
.3e-06
.0e-06
.7e-06
.3e-06
.0e-06
.0e-07
: 3.918e-06
: 3.821e-07
Y Axis
90
85
80
75
70
65
60
60
65
70
75
80
85
90
X Axis
var: osl:ce(p.zz*75)
var: osl:ce(met1.zz*75)
s 1 2 3 4 5
(a) t = 9 ms
user:ale
Wed Jan 28 16:35:01 1998

Figure 4

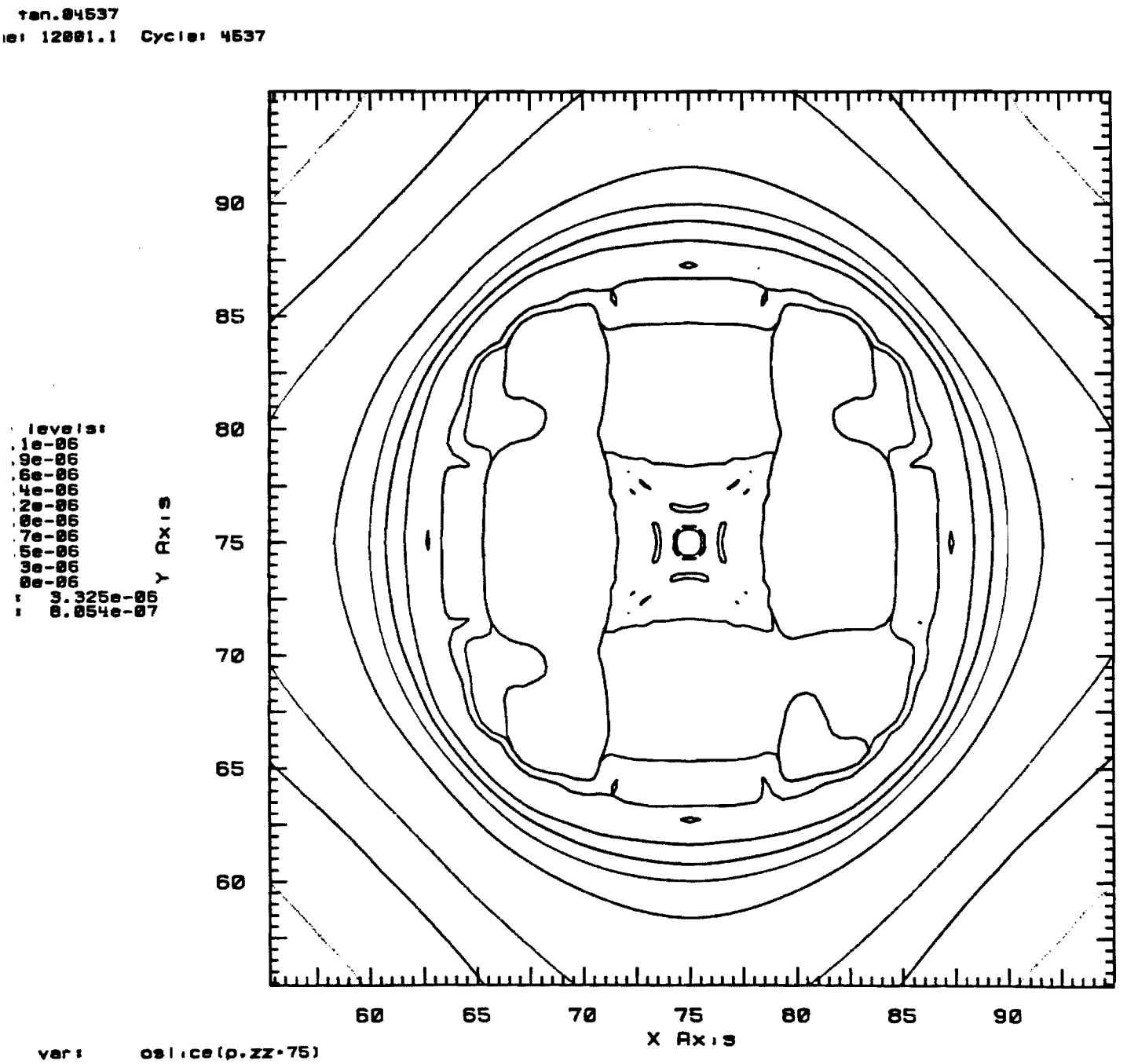

(b) $t = 12$ ms

Figure 4 (cont.)

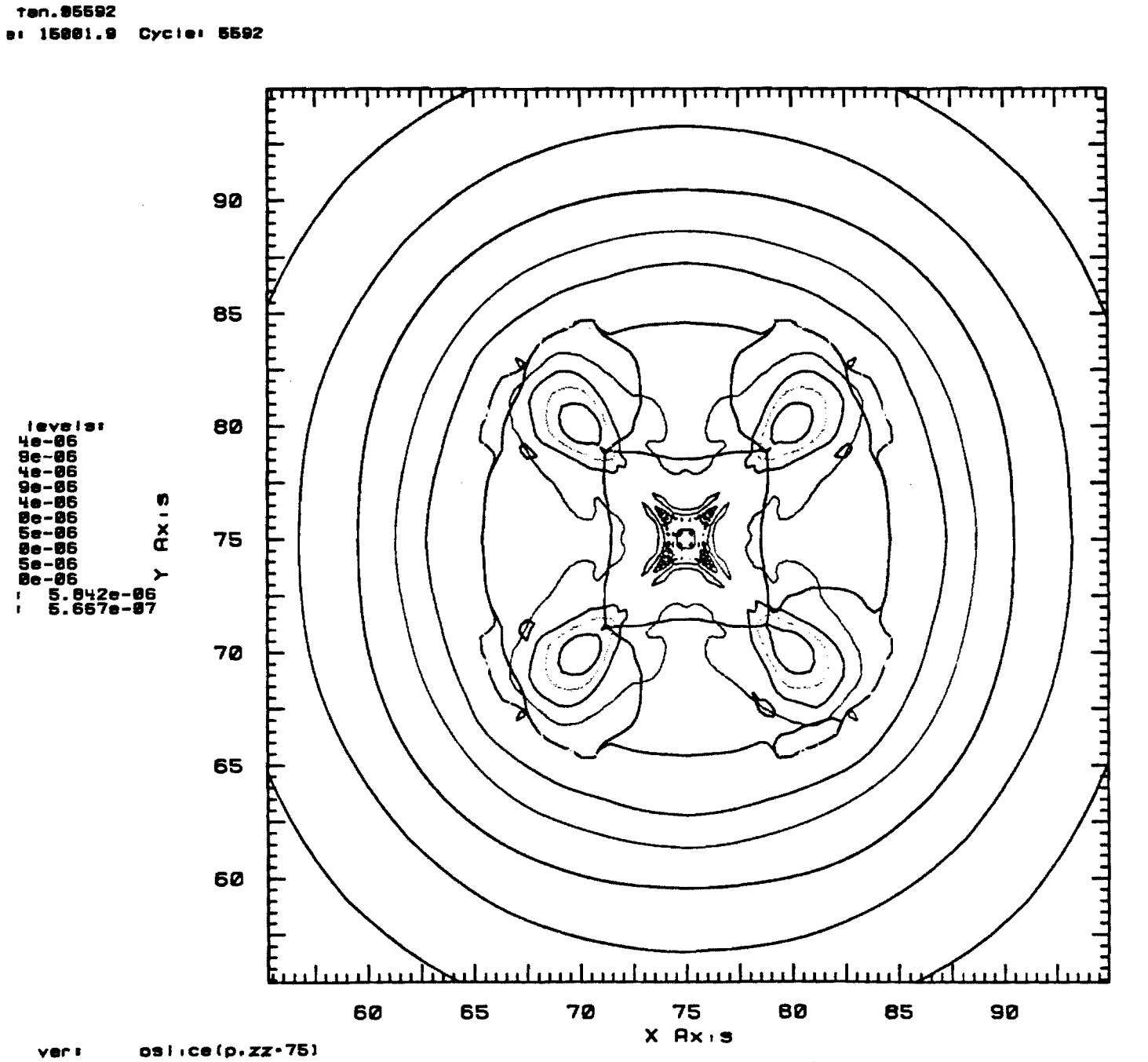

(c) $t = 15$ ms

Figure 4

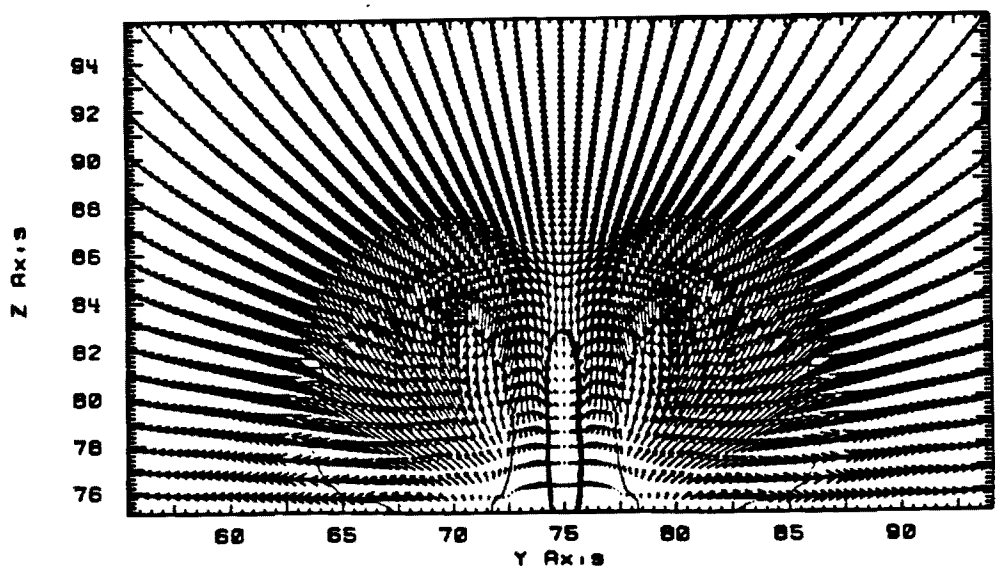

a) $t = 4.5$

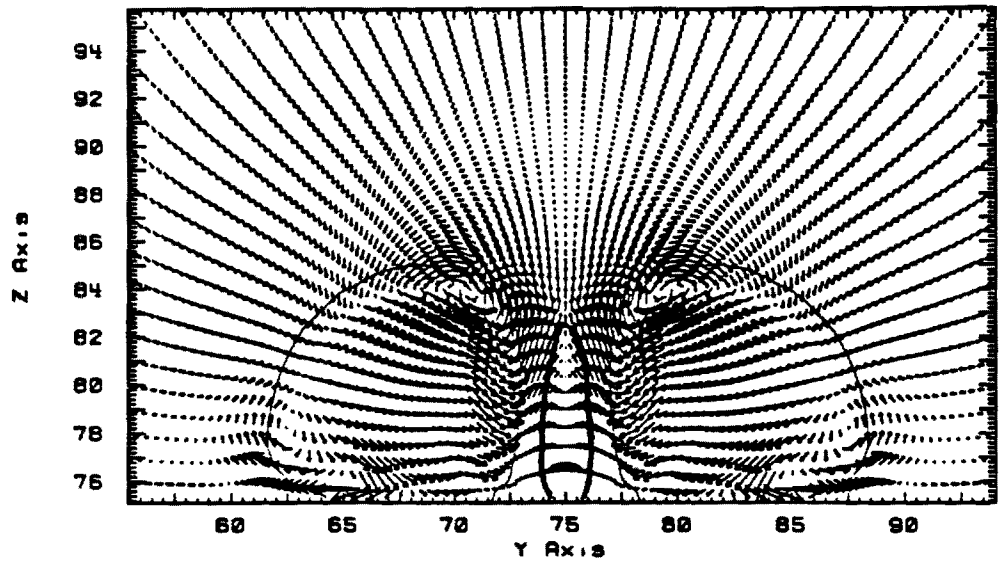

(b) $t = 9$ m

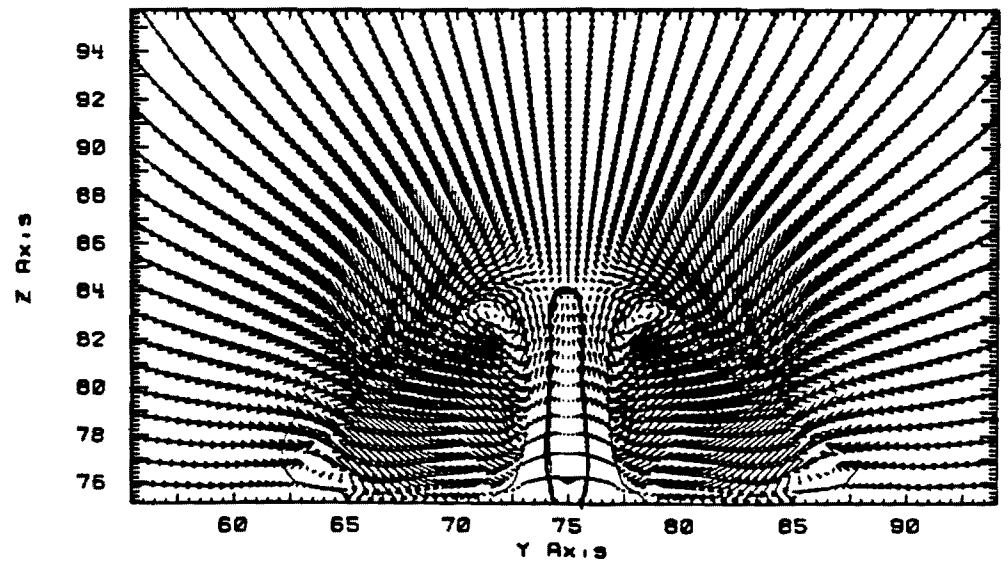

c) $t = 12$

Figure 5

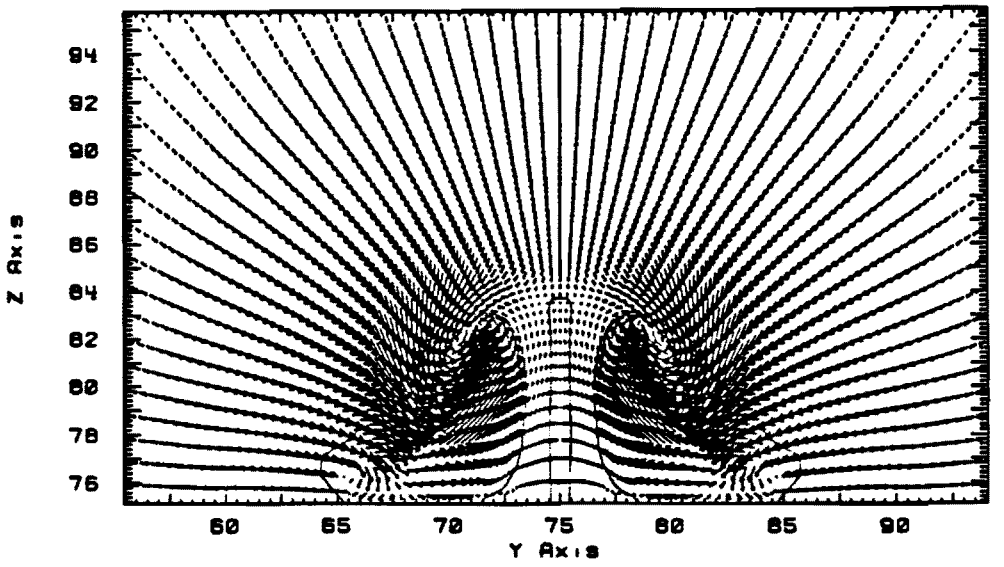

d) t=15 m

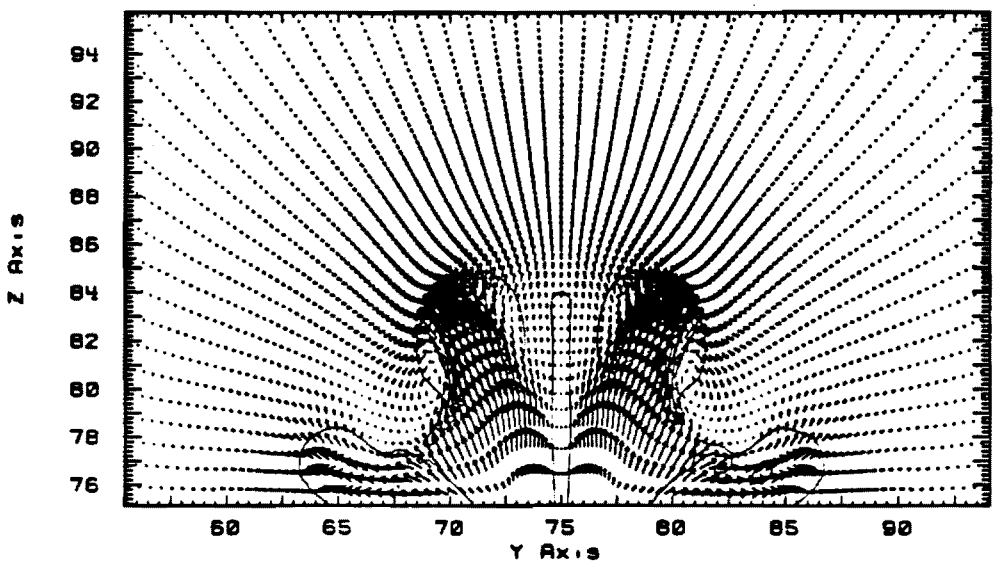

e) t=18 n

Figure 5 (cont.)

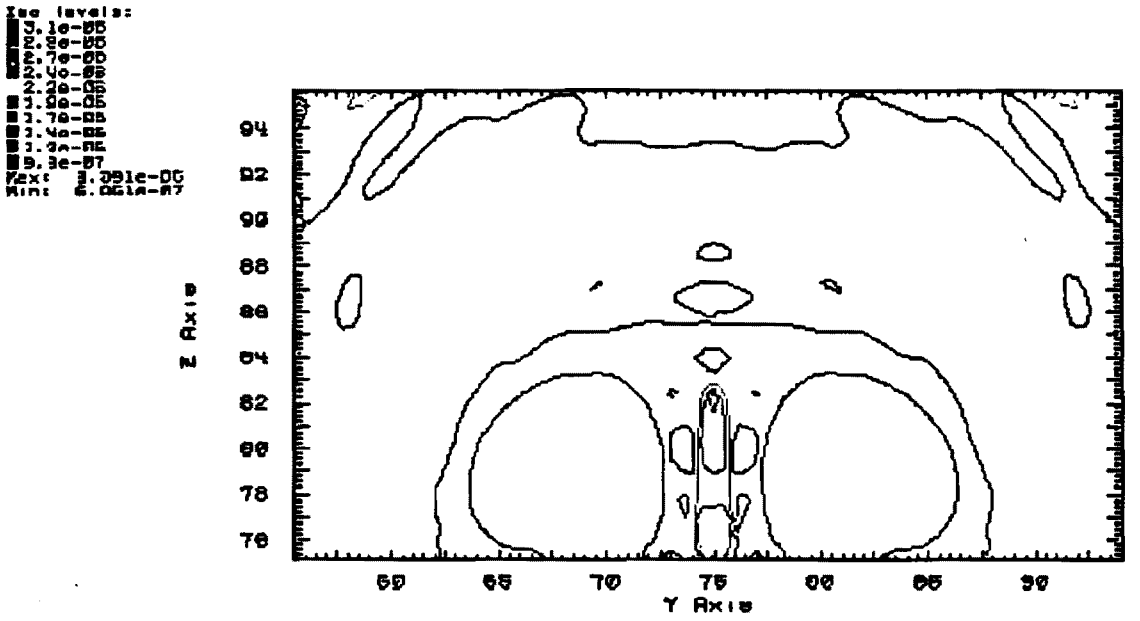

a) $t = 4.5$ ms

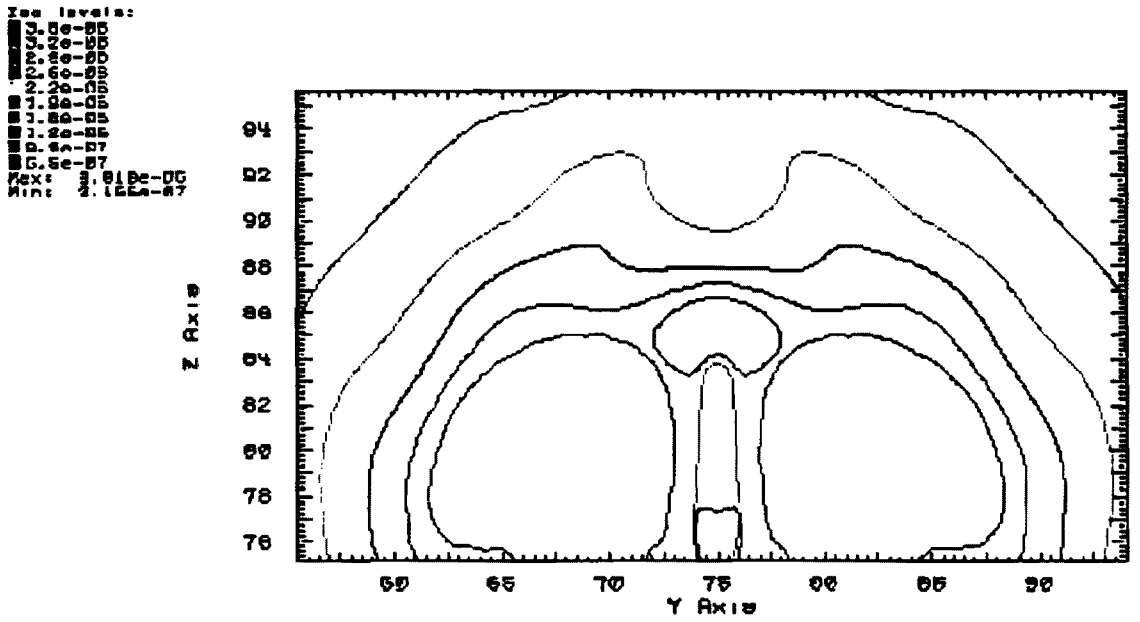

b) $t = 9$ ms

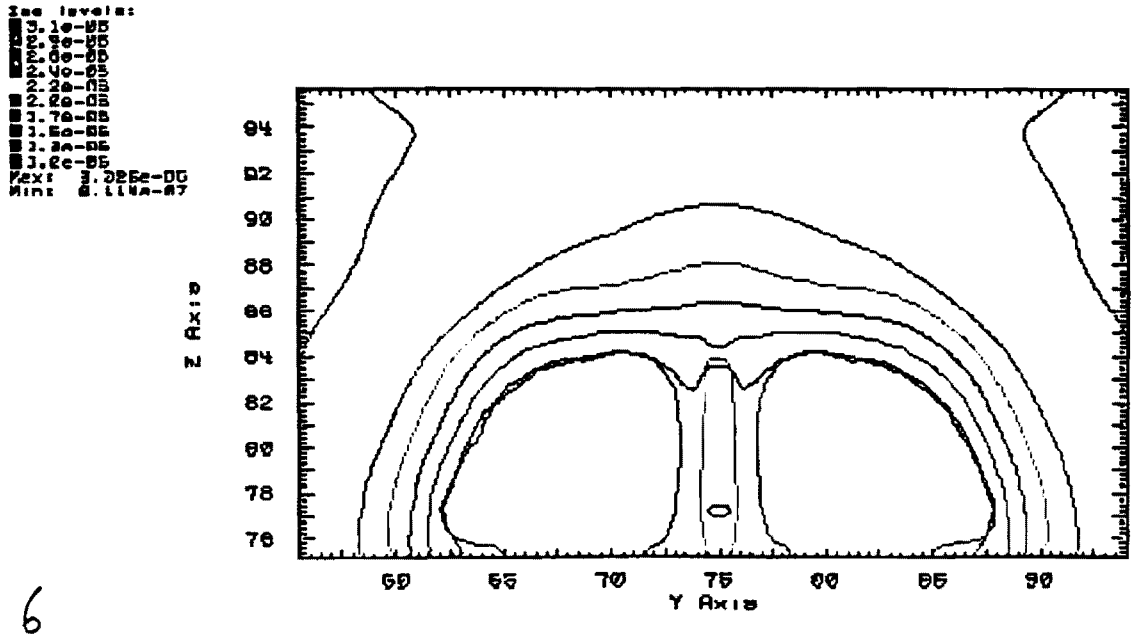

c) $t = 12$ ms

Fig 6

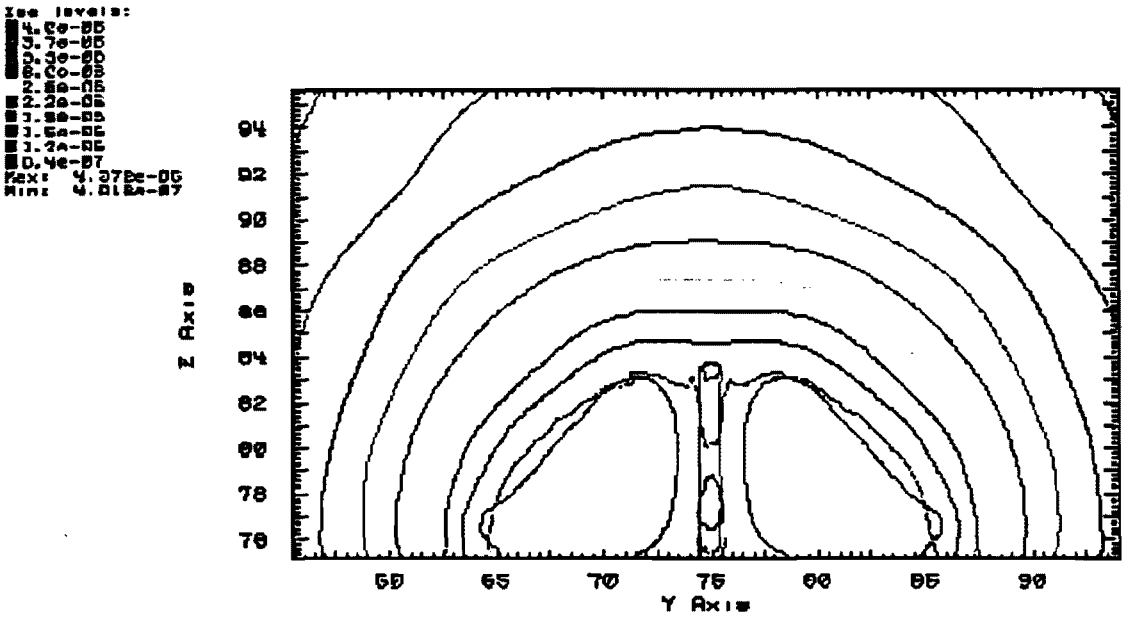

d) t=15 ms

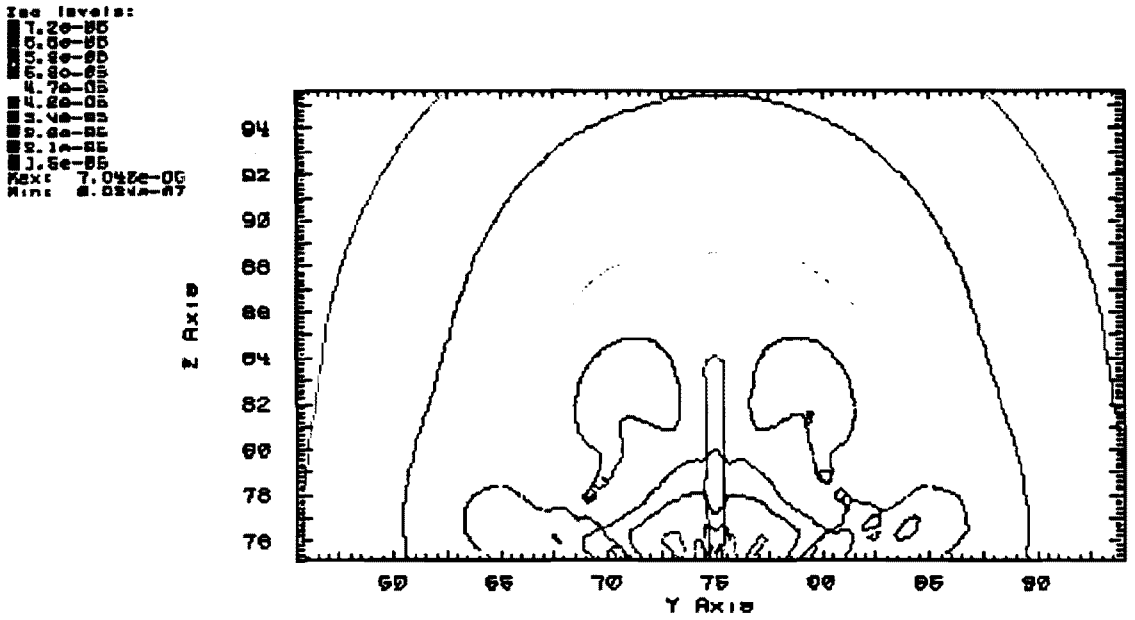

e) t=18 ms

Figure 6 (cont.)

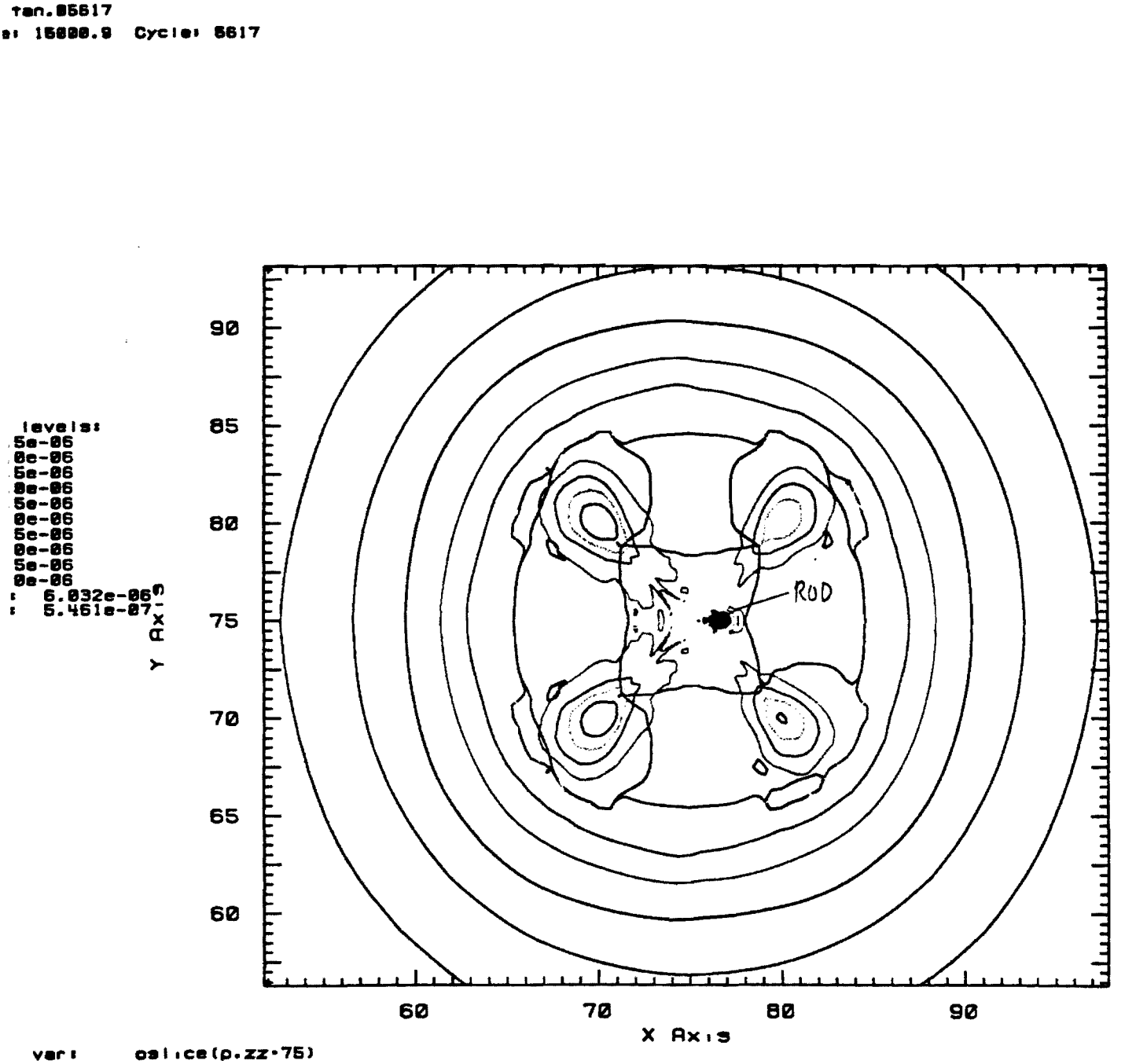

a) Off-Center, $t = 15$ ms

Figure 7

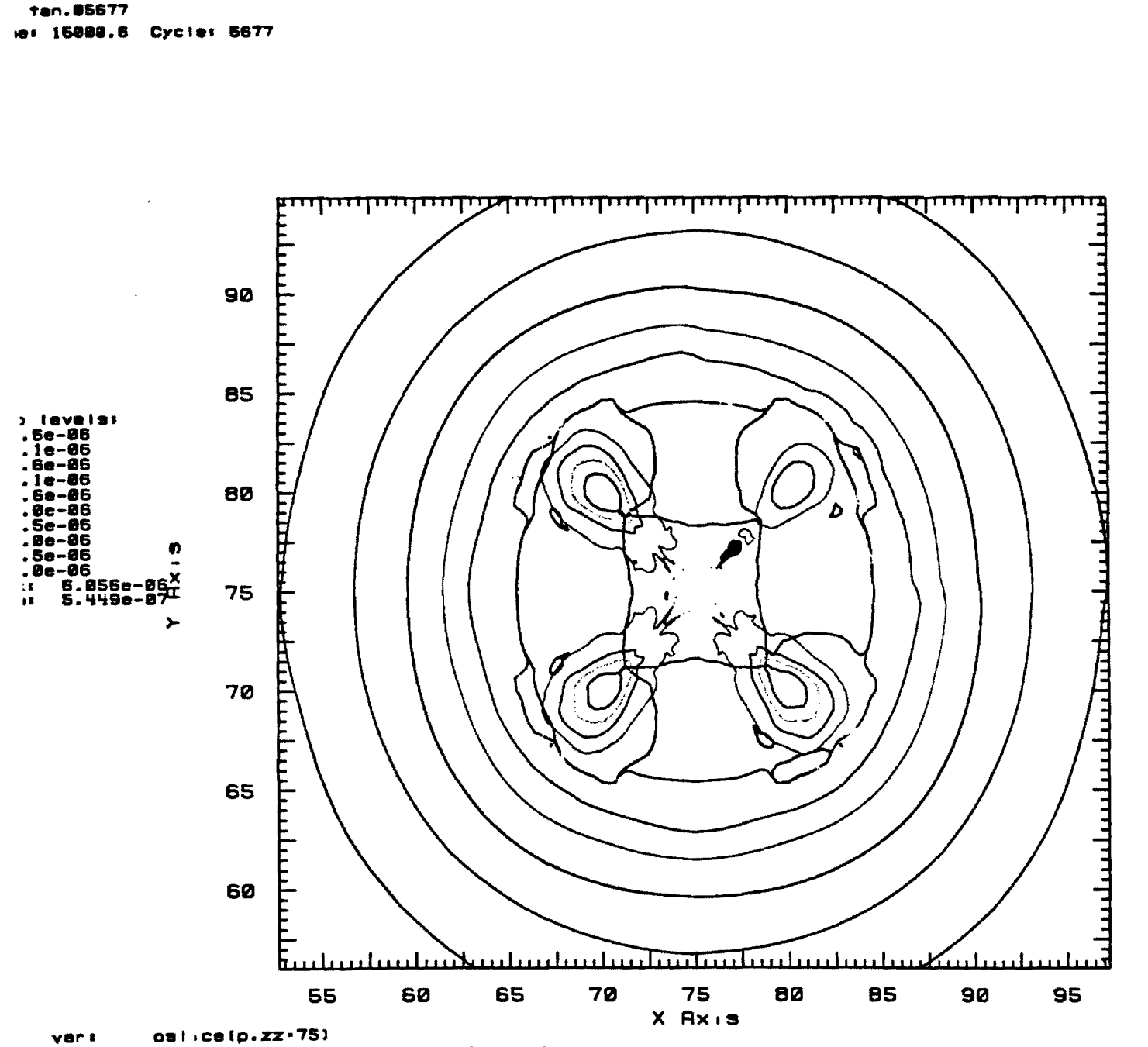

b) Corner, t = 15 ms

Figure 7 (cont.)

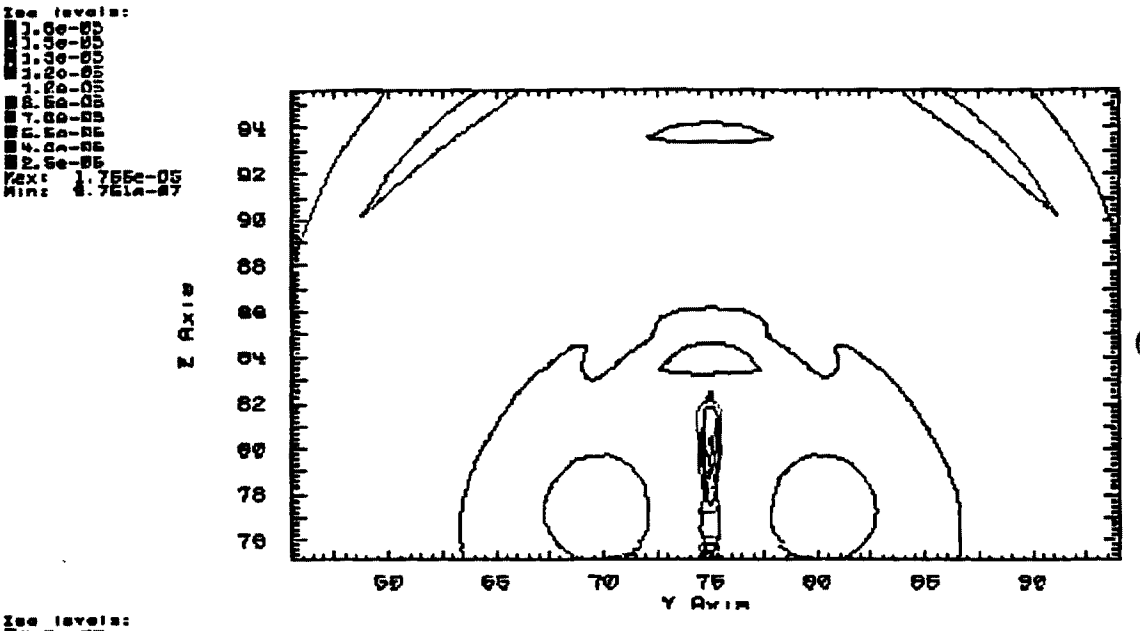

a) t = 4.5 ms

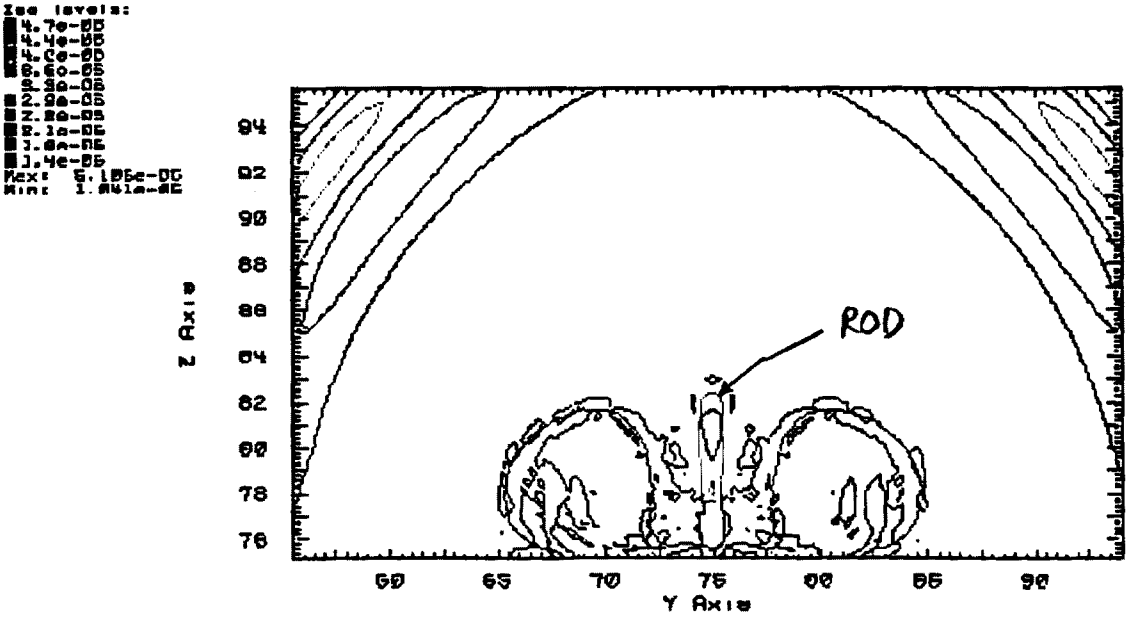

b) t = 9 ms

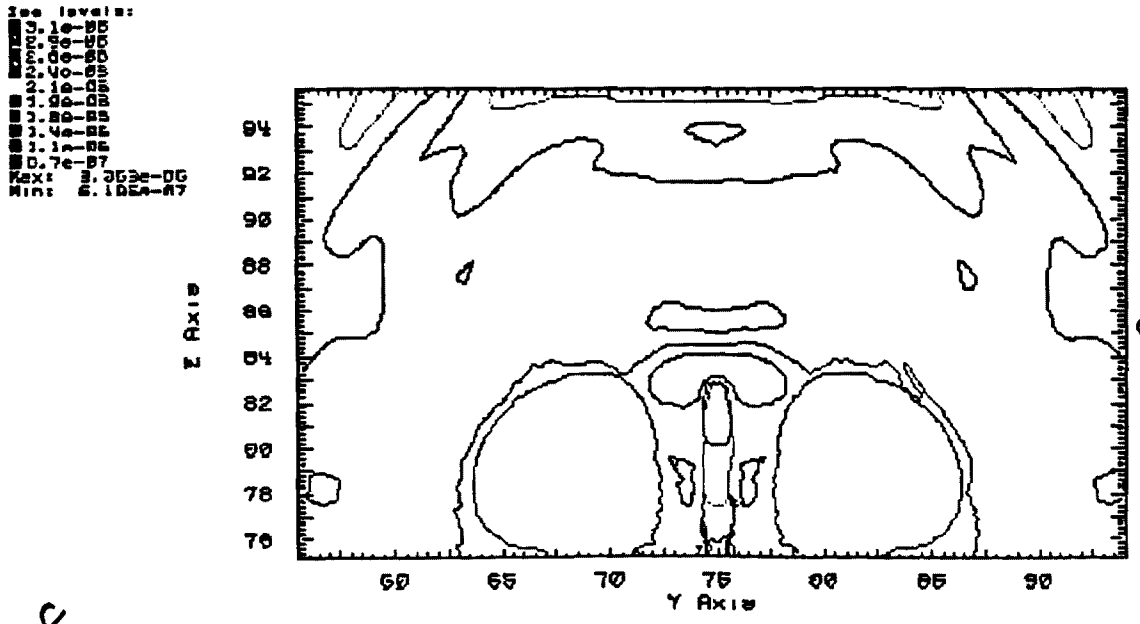

c) t = 12 ms

ure 8

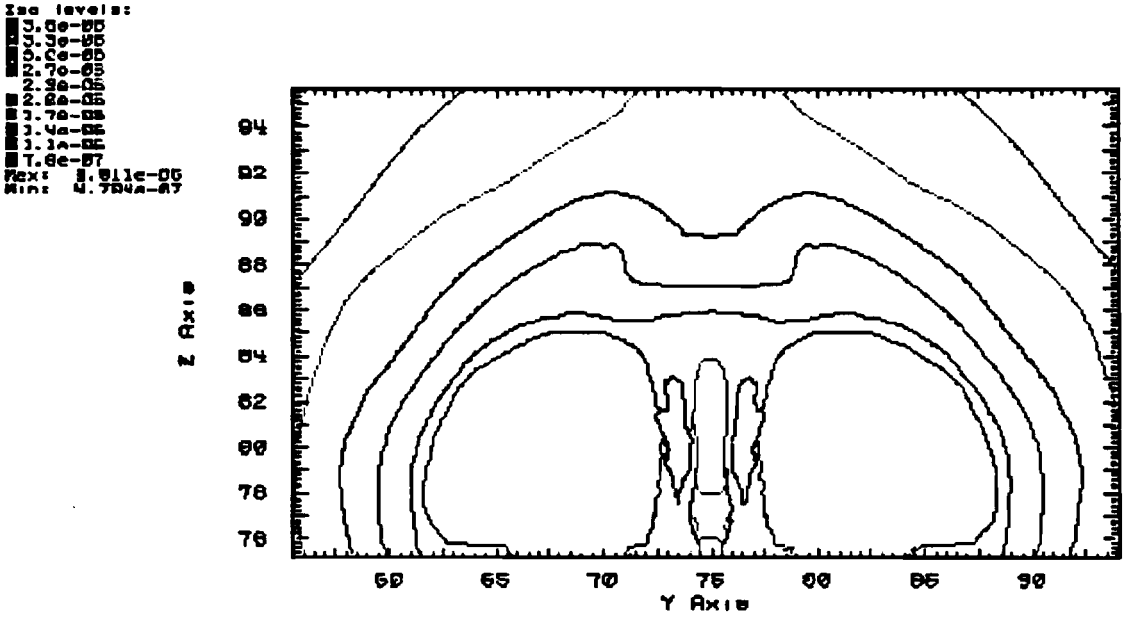

d) t = 15 ms

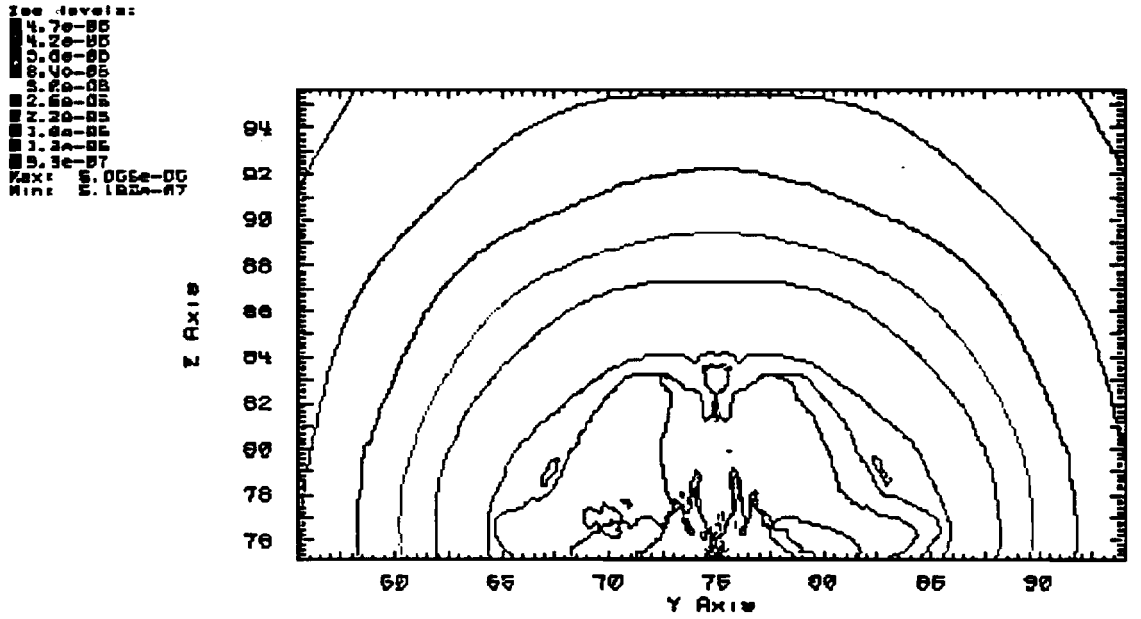

e) t = 18 ms

Figure 8 (cont.)

1997 ASME Fluids Engineering Division Summer Meeting
FEDSM'97
June 22 - 26, 1997

FEDSM97-3492

SIMULATIONS OF UNDERWATER EXPLOSION BUBBLE DYNAMICS USING AN ARBITRARY LAGRANGIAN-EULERIAN FORMULATION

Suresh Menon
Georgia Institute of Technology
Atlanta, Georgia 30332-0150
(404)-894-9126
(404)-894-2760(FAX)
menon@falcon.ae.gatech.edu

Sreekanth Pannala
Georgia Institute of Technology
Atlanta, Georgia 30332-0150
(404)-894-1409
(404)-894-2760(FAX)
gt5960b@prism.ae.gatech.edu

ABSTRACT

The dynamics of bubbles formed during underwater explosions are numerically investigated using an Arbitrary Lagrangian-Eulerian three-dimensional finite-element code and compared with experimental data. Both experimental and numerical results show good qualitative and quantitative agreement and suggests that the excitation of Rayleigh-Taylor instability is a major cause of interface instability. Simulations have also been carried out to investigate bubble-bubble interactions. Results show the formation of a water jet as one bubble collapses into the other, in agreement with recent experimental observation. Finally, the collapse of a bubble near a rigid wall and the formation of high velocity re-entrant jet onto the wall have been successfully simulated. The well known vortex ring bubble during the collapse process has been numerically captured.

1. INTRODUCTION

Vapor and gas bubble dynamics are of great practical interest in the prediction and prevention of cavitation erosion of marine propeller and turbine blades. The destructive nature of strong underwater explosions near walls is well known. Detailed reviews (e.g., Blake and Gibson, 1987; Prosperetti, 1982) have summarized past experimental and numerical results. Experimental studies are too many to list completely; however, most past studies focused on cavitation (small) bubbles. Among the studies that focused on large scale explosions are the studies reported in Cole (1948) for freely oscillating, deep sea explosion bubbles and the studies of bubble collapse near walls (e.g., Tomita and Shima, 1986). Bubble-bubble interactions have also been studied in the past e.g., Warren and Rice, 1964). However, in most cases, due to difficulties in acquiring detailed data, only limited information has been obtained. Recently, experiments were carried out to investigate large-scale bubble explosions (Menon and Lal, 1996; Lal and Menon, 1996a, b). These experiments were conducted in shallow water due to an interest in understanding the dynamics of bubble-wall interaction in such flows and to investigate the feasibility of targeting buried mines for destruction in beaches. The data obtained from these experiments have been used to validate the numerical model discussed in this paper.

Numerical studies in the past range from simple 1-D analytic solutions (e.g., Lauterborn, 1976; Plesset, 1971; Prosperetti, 1982) to more complex 2D/3D studies. Many studies employed the Boundary Element Method (BEM) or its variants (e.g., Chahine and Perdue, 1988; Duncan and Zhang, 1991; Blake et al., 1986, Plesset and Chapman, 1970). This method has some inherent limitations. For example, compressibility in the gas cannot be included and in the study of bubble collapse near a surface, BEM can be used only up to the point of jet formation. To model the flow beyond the point of bubble collapse, BEM has been modified by introducing vortex elements (e.g., Zhang and Duncan, 1994; Zhang et al., 1993; Best, 1993). Furthermore, to set up this problem, recourse to experimental observation is required to obtain characteristic parameters. Such an approach is not general and cannot be used when the details of the explosion dynamics is unknown.

There are other assumptions used in past studies that are known to be in error. For example, significant compressible effects are known to occur in the collapse phase especially in deep sea strong explosions. Bubble shape is also known to quickly deviate from sphericity at bubble maximum, thereby, violating axisymmetric assumptions used in the past (e.g., Szymczak et al., 1993; Zhang and Duncan, 1994) and requiring full 3D treatment. Thus, simple 1-D or 2-D/axisymmetric analysis or incompressible methods cannot completely resolve the bubble and the flow dynamics. Furthermore, such simplified treatments also do not to provide details of the flow field inside and outside the bubble and cannot account for the interaction between the vapor and the liquid phases. Conventional numerical treatments (even using full 3D) such as Lagrangian or Eulerian techniques are also not practical, since the

expansion and collapse of bubbles create severe fluid motion so that a Lagrangian approach (in which the grid points move with the fluid resulting in severe grid distortion) becomes inappropriate, while in an Eulerian approach, adequate resolution in the regions of interest is very difficult to achieve since the bubble's shape changes very rapidly.

A numerical method that includes both compressibility and an ability to capture the entire bubble collapse in complex configuration is used in this study. This numerical code (ALE3D) combines lagrangian and eulerian features and is based on the Arbitrary Lagrangian-Eulerian (ALE) scheme developed at the Lawrence Livermore Lab. Past applications include the 2D (e.g., Tipton, et al., 1992) and the full 3D (Milligan et al., 1995) studies of bubble collapse. This paper reports some recent results using ALE3D, of both single and double bubble explosions in free field and in the vicinity of a rigid wall.

2. THE NUMERICAL METHOD

ALE3D (Anderson et al., 1994) is an explicit, 3D finite element code that simulates the fluid motion and elastic-plastic response on an unstructured grid. The grid may consist of arbitrarily connected hexahedral shell and beam elements. The ALE algorithm is implemented by carrying out a complete lagrangian calculation followed by an advection step. After each lagrangian step, a new mesh is created using a finite element based equipotential method to relax the distorted grid. In the eulerian advection step, the fluid variables such as mass, density, energy, momentum and pressure are reevaluated on the new mesh by allowing fluid motion. The details of the constitutive models are described elsewhere (e.g., Steinberg, 1991) and, therefore, are not described here for brevity.

The advection step uses a second order, monotonic advection algorithm. This can create mixed material elements (i.e., liquid and vapor). Material interfaces are not explicitly tracked but for the purpose of carrying out mixed element advection, they are inferred from volume fractions. Separate state variables are kept for each component of a mixed element.

3. RESULTS AND DISCUSSION

In this section, the results obtained for the various test cases are summarized and discussed. These studies serve to identify the capabilities and limitations of the ALE3D code and to identify areas for further study.

3.1 Free Field Single Bubble Oscillation

These simulations employed test conditions similar to the experimental set-up of Menon and Lal (1996). A freely oscillating bubble is modeled in the center of a 1.5 m x 1.5 m x 1.5 m tank filled with water. The initial bubble diameter is 5.34 cm and the initial explosion pressure is 9.34 atmospheres. The water pressure is 1 atmosphere. The ALE mesh treatment is applied to all the elements in the bubble and in the vicinity of the bubble. But away from the bubble where the bubble explosion does not cause much grid distortion, lagrangian mesh treatment is used. The number of elements used to resolve the bubble and the surrounding water was varied to confirm that the results are grid independent. For a typical 3D simulation, 64512 elements were used to discretize the domain., but as many as 150000 elements were used for carrying out the grid independence tests for this test case. Although various cases have been simulated, only characteristic results are discussed below.

The bubble grows after the explosion due to the high vapor pressure inside the bubble. Because of inertia, this results in an over expansion and the pressure inside the bubble falls below the ambient(water) pressure. As a result, the bubble collapses and reaches a bubble minimum at which time the internal pressure again exceeds the external pressure. Thus, a oscillation process is set up and continues as long as there is sufficient energy available. However, energy is continuously lost during the oscillation due to irreversible mechanical work done on water and vapor and due to the onset of various instabilities. Analysis of the losses and the instability mechanisms (Menon and Lal, 1996) suggest that during the collapse process the Rayleigh-Taylor (R-T) instability occurs at the interface. This results in a distortion of the vapor-water interface. This phenomenon has been captured in the numerical study. For example, Figs. 1a and 1b show snapshots of bubble at the first maximum and the first minimum. As can be seen, near the bubble minimum, wave-like distortion appears along the bubble interface. Figures 2a-b show the corresponding velocity vector field inside and outside the bubble. Figure 2a shows the outward motion of the bubble just before the bubble maximum and Fig. 2b shows the outward motion of the bubble just after the first bubble minimum. The magnitude of the velocity vectors also indicate that the acceleration of the fluid is minimum at the beginning and end of compression or expansion phases.

The deviation from sphericity and the formation of waves on the bubble interface are characteristics of Rayleigh-Taylor instability. To ensure that this interface distortion is not due to acoustic reflections from the wall, calculations were carried out by moving the wall further and by replacing the rectangular domain by a spherical domain. Results showed that, although there are changes in the bubble oscillation period, the interface distortion appears near the bubble minimum in all cases. The R-T instability can also be inferred by analyzing the variation of the radius with time. For example, Fig. 3 shows the region (near bubble minimum) where $d^2R/dt^2 > 0$ (which is a necessary condition for R-T instability).

Figure 4 compares the pressure history in the bubble with experimental data (Menon and Lal, 1996). It can be seen that the computed first period of oscillation (around 15 ms), the peak pressure and the maximum radius agrees well with data. It can also be seen that the acoustics do not play a important role in dictating bubble dynamics as the time period and peak pressure hardly changed even when the walls are moved away by approximately eight times. During the contraction phase there are some differences between the calculations and experiments.. However, the experimental set-up employed a glass globe (which contained the stoichiometric fuel-air mixture) with a metal insert that contained the pressure transducer and the spark generator while these features were ignored in the numerical model. In addition, the effect of glass fragments have not been included in the numerical model.

Figure 5a shows the time trace of pressure in the tank away from the bubble and close to a wall. It is very similar to the high frequency pressure oscillations as recorded by the tank transducer in the experiments (Menon and Lal, 1996) and is shown in Fig. 5b. The slight differences in the two plots may be attributed to the idealization of the tank as a cube with walls

all around(whereas, for the experiment, the top surface was a free surface; see below).

As mentioned earlier, simulations were carried out to ensure grid independence, and to confirm that the walls do not effect the overall dynamics. It has been determined that the presence of walls does effect (decrease) the oscillation period (Fig. 4); however, the bubble dynamics are captured relatively accurately. To simulate true free field explosion will require using outflow boundary conditions. However, at present, the ALE3D code requires that the far field boundary be modeled as a solid reflecting wall. This limitation of the code can be removed only by modifying the source code. This is will be investigated in the future.

To extend the applicability of ALE3D to real underwater explosions is quite trivial. To demonstrate this capability a deep sea underwater explosion was simulated using pentolite as the explosive. The time period (not shown) scales as approximately two times the non dimensional time based on the maximum radius of the bubble, the ambient(water) pressure and the water density $\left(R_{max} / \sqrt{\frac{P_\infty}{\rho_w}} \right)$, as found in the above simulations and in earlier studies (e.g., Chahine and Perdue, 1988).

3.2 Bubble-Bubble Interactions

To investigate bubble-bubble interactions, a series of studies were carried out using bubbles of various sizes. A limitation of the current ALE3D code is that it does not allow phase difference between the two explosions to be incorporated into the model. However, by using different bubble sizes (or using different explosive strength) the net effective energy release from each bubble can be varied. The effect of inter-bubble distance on the interaction process was also studied. Due to space limitation only characteristic results are discussed below.

When two identical bubbles (of initial radii 3.17 cm and placed 8 cm apart) are exploded the bubbles expand and then collapse onto each other and a reentrant water jet with a high speed (30 m/s) is formed in both vertical and horizontal directions. Figures 6a-c show snapshots of the bubble-bubble interaction and the corresponding velocity fields are shown in Figs. 7a-c, respectively. Fig. 8a-c show photographs from the experiments (Lal and Menon, 1996a) for the present case with two bubbles of same size exploding in phase with each other. Although not clearly seen in the experimental Fig. 8c, studies have show the presence of vortex ring bubble. The jet directed towards the adjacent bubble impinges on its counterpart as in a stagnation point flow. As the bubble-bubble process continues, two counter vortex rings are formed with the velocity between the bubble increasing to as high as 50 m/s. There is reasonable agreement between the experimental observations and the present computations.

When same size bubbles were exploded at the same distance as before, but with one bubble containing four time more energy than the other, a similar result was obtained except that in this case, the weaker bubble is sucked into the other bubble with a velocity reaching a maximum of around 85 m/s (not shown). The reentrant waterjet is first formed in the weaker bubble during the first oscillation and the vortex ring thus formed merges into the (still coherent) stronger bubble. The jet formation in the stronger bubble is delayed until the second oscillation, at which time the second bubble also collapses.

When two bubbles of different size (e.g., of radii 3.17 cm and 2.17 cm (and thus, with different total explosion energy) are exploded, the results are quite similar to the case discussed above. During the expansion phase, the greater inertia and explosion strength of the bigger bubble inhibits the smaller bubble. During the collapse, the pressure drop in-between the bubbles is more than on the other sides and this pressure differential causes the smaller bubble to be engulfed into the larger bubble. The center of motion of the water jet directed towards the bubbles does not immediately adjust to the motion of the bubbles and, thus, the water motion is directed off-center of the bubble. This creates a high pressure on the side of the smaller bubble away from the larger bubble. This high pressure and the low pressure in-between the bubbles creates enough momentum to form a water jet through the bubbles which penetrates to the other side of the bubble. Final stage of the jet formation is shown in Figs. 9a and 9c.

The velocity vector field shows the formation of the water jet in agreement with experimental study (Lal and Menon, 1996a). A water jet was also observed in the experiments when two identical bubbles were exploded out-of-phase, as shown in Fig. 9b. Out-of-phase explosion essentially changes the relative strength of the bubble explosion during interaction and is, therefore, similar to the present case with two unequal bubbles exploding simultaneously and the similarities can be seen in Figs. 9a-c. At present, the ALE3D code cannot simulate phase difference between the adjacent explosions. This feature will be included in the code at a later date.

Finally, Fig. 10 compares the pressure between the two bubbles for the various test cases. All cases have the same period of oscillation. However, the case with increased energy content shows the strongest water jet formation (around 85 m/s) and the largest impact pressure at the first bubble minimum.

3.3 Bubble-Wall Interactions

Bubble collapse near a rigid wall is of significant interest due to a variety of reasons related to its ability to cause serious damage to the structure. This is because when the bubble collapses near a rigid surface, a strong reentrant water jet is formed that is directed towards the wall. The peak impact pressure on the wall due to this water jet can be substantially higher that the explosion pressure especially when the initial explosion energy is very large. Various simulations were performed by varying the explosion strength and distance of the bubble from the rigid plate. However, only characteristic results are discussed here to highlight the pertinent observations.

Two cases are discussed here with bubble placed 8.34 cm above (buoyancy inhibiting jet formation) and 8.34 cm below (buoyancy aiding the jet formation) the wall. Figures 11a-d show the velocity field at various stages of the collapse for the first case. Initially, the bubble is almost spherical but begins to distort as it collapses. The physics of the jet formation is quite similar to the bubble-bubble case. Since there is less volume of water between the wall and the bubble during the collapse, the pressure drop is quite large relative to the pressure on other sides of the bubble. This pressure differential further forces the bubble towards the wall. Since steam is lighter, the bubble tends to move further away from the wall (due to buoyancy) for the case where the gravitational force is inhibiting the jet formation, while for the second case, the bubble is further

accelerated towards the wall (Fig. 12). The water surrounding the bubble is directed off-center relative to the bubble geometric center, thereby, creating a higher pressure on the side of the bubble away from the wall. The combination of these effects causes the water to penetrate the bubble from the high pressure side and to form a high-speed water jet that impacts the rigid surface. As this jet impacts on the rigid plate, a ring bubble vortex is formed as shown. The maximum jet velocity obtained is around 70m/s. It scales as approximately 7 times the non-dimensional velocity scale based on the ambient(water) pressure and water density $\left(\sqrt{P_\infty/\rho_w}\right)$ and this scaling is in good agreement with earlier results (e.g., Chahine and Perdue, 1988).

The effect of buoyancy in the formation of jet is very evident in Fig. 13 where the impact pressure on the wall is plotted versus time. The buoyancy aided case increases the impact pressure than for the buoyancy inhibited case and is as much as two times that of the peak explosion pressure.

The present study captures the vortex ring bubble after the jet impact, as shown above. This ring bubbles have been also observed both in experiments (e.g., Tomita and Shima, 1986; Vogel, et al., 1989) and in numerical studies (Best, 1993; Szymczak, et al., 1993; Zhang and Duncan 1994).

4. CONCLUSIONS

These studies show that the ALE3D code can be used for bubble explosions. The basic code has been validated using shallow water explosion data. In addition to isolated bubbles, bubble-bubble and bubble-wall interaction studies were also performed. It has been shown that all the features observed in experiments have been captured in these studies. The formation of reentrant waterjet when the bubble collapses near a rigid surface and the formation of a ring vortex bubble have been captured and are in good agreement with experimental data.

Some limitations of the current ALE3D code have also been identified. For example, the current code is unable to simulate bubble-bubble interaction with a phase difference between the explosions. However, such features can be incorporated by proper modifications to the code.

ACKNOWLEDGMENTS

This work is supported by the Office of Naval Research under grant No. N00014-91-J-1993. ALE3D, a product of Lawrence Livermore National Laboratories was used for the simulations in this paper.

REFERENCES

Anderson, S., Dube, E., Futral, S., Otero , I., and Sharp, R. (1994) " Users Manual For ALE3D," Lawrence Livermore National Lab., CA.

Best, J. (1993) "The Formation of Toroidal Bubbles upon the Collapse of Transient Cavities", J. Fluid Mech., 251, pp. 79-107.

Blake, J. R., Taib, B. B., and Doherty, G. (1986) "Transient Cavities Near Boundaries. Part I. Rigid Boundary," J. Fluid Mech., 170, pp. 479-497.

Chahine, G. L., and Perdue, T. O. (1988) "Simulation of the Three-Dimensional Behavior of an Unsteady Large Bubble near a Structure," 3rd International Colloquium on Bubbles and Drops, Monterey, CA.

Cole, R. H. (1948) "Underwater Explosions," Princeton University Press, Princeton.

Duncan, J. H., and Zhang, S. (1991) " On the Interaction of a Collapsing Cavity and a Compliant Wall," J. of Fluid Mech., 226, pp. 401-423.

Lal, M. K., and Menon, S. (1996a) "Interaction of Two Underwater Explosion Bubbles", ASME, Fluids Engg. Div. Conf., Vol. 1, pp. 595-600.

Lal, M. K. and Menon, S., (1996b) "Experiments in Underwater Explosions near rigid surface", under preparation.

Lauterborn, W., (1976) "Numerical Investigation of Nonlinear Oscillations of Gas Bubbles in Liquids," J. Acoust.. Soc. Am., 59, pp. 283-293.

Menon, S., and Lal, M. K., (1996) "On the Dynamics and Instability of Bubbles Formed During Underwater Explosions," submitted to Experimental Thermal and Fluid Science Journal.

Milligan, C. D., Duncan, J. H, and Stillman, D. J. (1995) "A Numerical Study of Underwater Explosion Bubble Phenomena," preprint.

Plesset, M. S. (1971) "The Dynamics of Cavitation Bubbles," Trans. ASME, J. Appl. Mech., 16, pp. 277-282.

Plesset, M. S. and Chapman, R. B. (1971) " Collapse of an initially spherical cavity in the neighbourhood of a solid boundary," J. of Fluid Mech., 47(2), pp. 283-290.

Prosperetti, A. (1982)"A Generalization of the Rayleigh-Plesset Equation of Bubble Dynamics. Phys. Fluids, 25, pp. 409-410.

Steinberg, D. (1991) "Equation of State and Strength Properties of Selected Materials," Lawrence Livermore Natn. Lab., Livermore, CA, UCRL-MA-106439.

Szymczak, W. G., Rogers, J. C. W., Solomon, J. M. and Berger A. E. (1993) "A numerical algorithm for hydrodynamic free boundary problems," J. Comput. Phys., 106, pp. 319-336.

Tomita. Y., and Shima. A. (1986) "Mechanisms of Impulsive Pressure Generation and Damage Pit Formation by Bubble Collapse," J. Fluid Mech., 169, pp. 535-564.

Tipton, R. E., Steinberg, D. J., and Tomita, Y. (1992) "Bubble Expansion and Collapse Near a Rigid Wall," JSME , 35, pp. 67-75.

Vogel, A., Lauterborn, W. and Timm, R., 1989, "Optical and acoustic investigations of the dynamics of the dynamics of laser-produced cavitation bubbles near a solid boundary", J. Fluid Mech., 206, pp. 299-338.

Warren, G. R. and Rice, T. W (1964) "The Interaction of the Gas Bubbles from Two Adjacent Underwater Explosions," Foulness Division Note 9-64, Atomic Weapons Research Establishment, United Kingdom Atomic Energy Authority.

Zhang, S., Duncan, J. H. and Chahine, G. L. (1993) "The final stage of the collapse of a cavitation bubble near a rigid wall," J. Fluid Mech., 257, pp. 147-181.

Zhang, S. and Duncan, J. H., (1994) "On the non spherical collapse and rebound of a cavitation bubble," Phys. Fluids, 6, pp. 2352-2362.

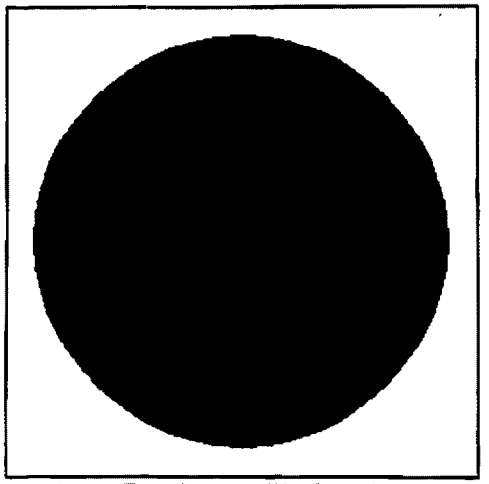

Figure 1a : Freely oscillating bubble at 8ms(Near Maximum)

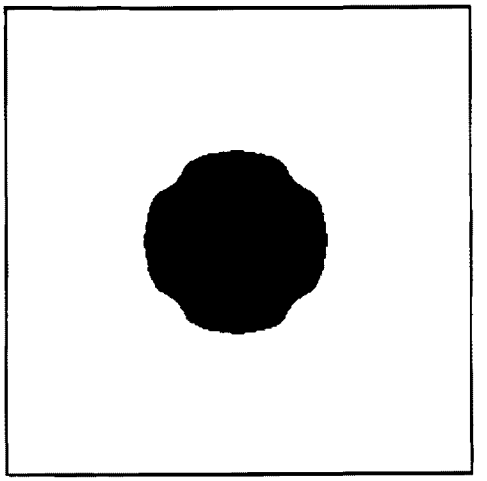

Figure 1a : Freely oscillating bubble at 15ms(Minimum)

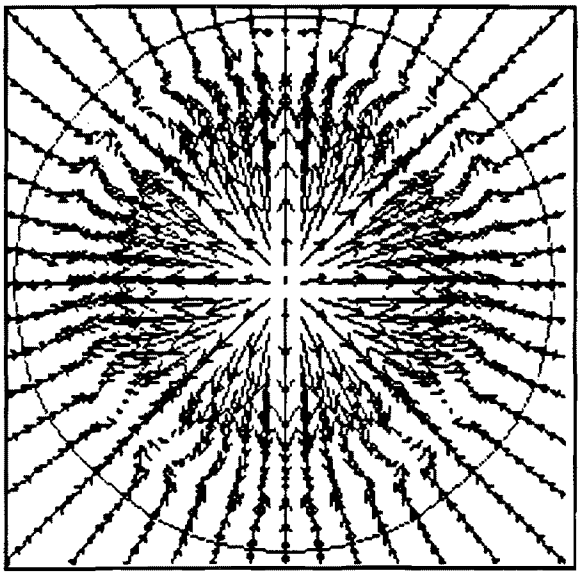

Figure 2a : Vector field corresponding to Fig.1a.

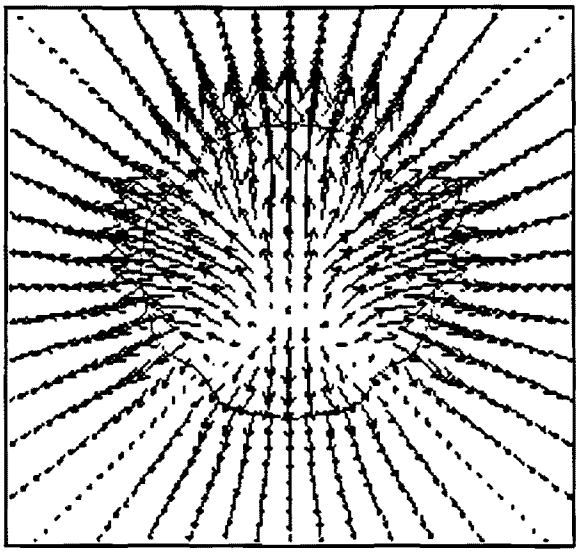

Figure 2b : Vector field corresponding to Fig.1b.

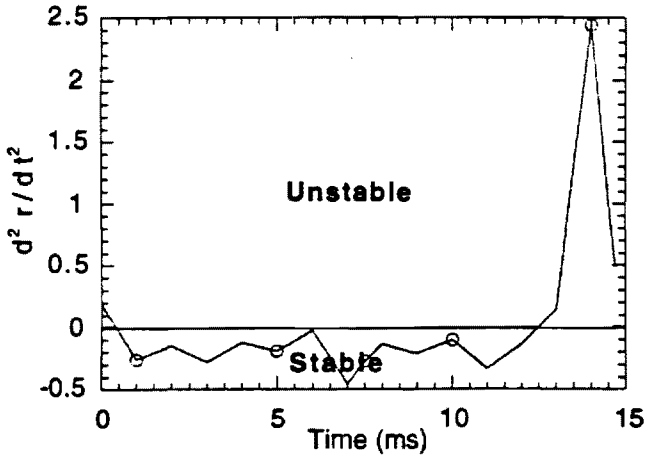

Figure 3: d^2r/dt^2 versus timeplot to identify the regions of R-T stable and unstable regions.

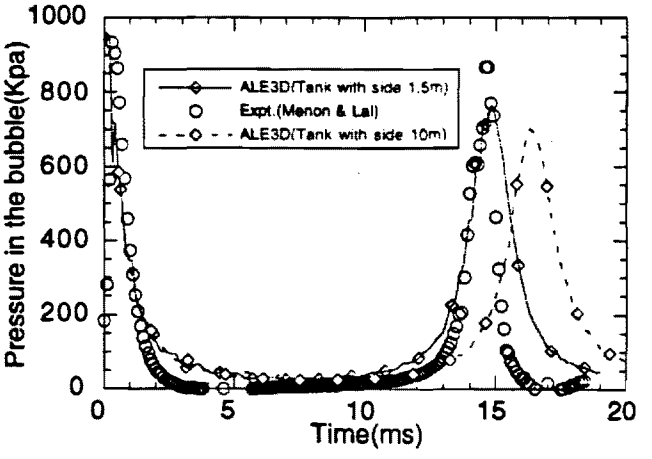

Figure 4: Time trace of pressure in the freely oscillating bubble(for near and far walls) compared with the experiment.

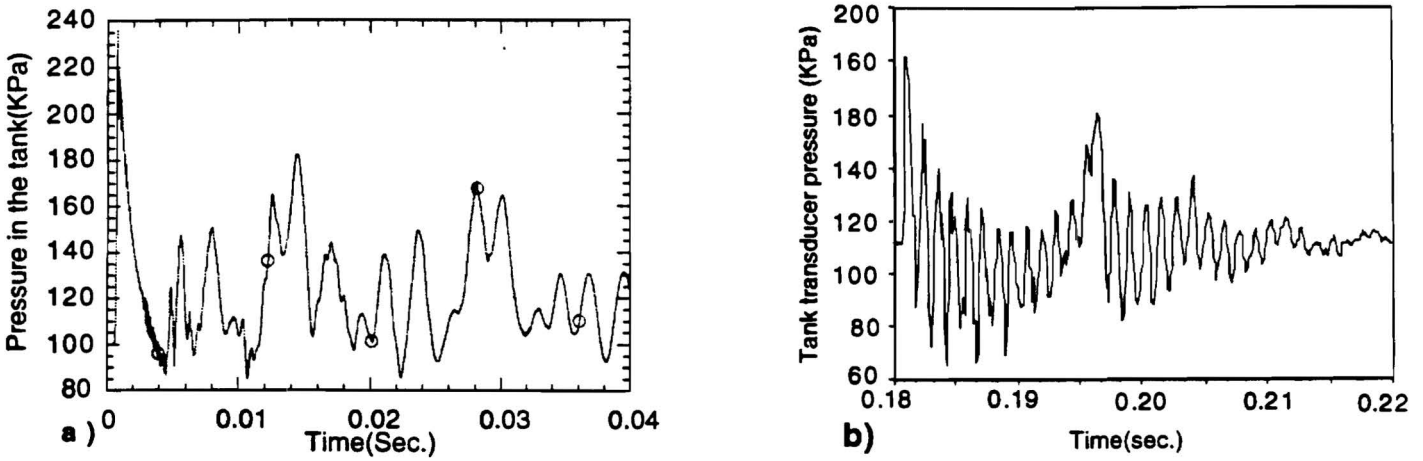

Figure 5: The acoustic pressure signature in the tank away from the bubble and near the walls. a) Numerical Simulation and b) Experiments(Menon and Lal, 1996).

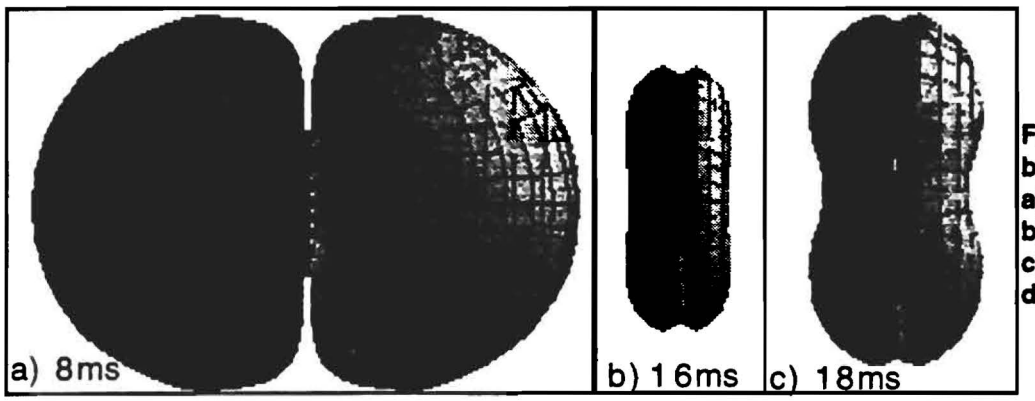

Figure 6: Time sequence of two bubbles of same size interacting: a) At bubble maximum, b) Just before the jet formation c) Formation of the toroidal double ring bubble.

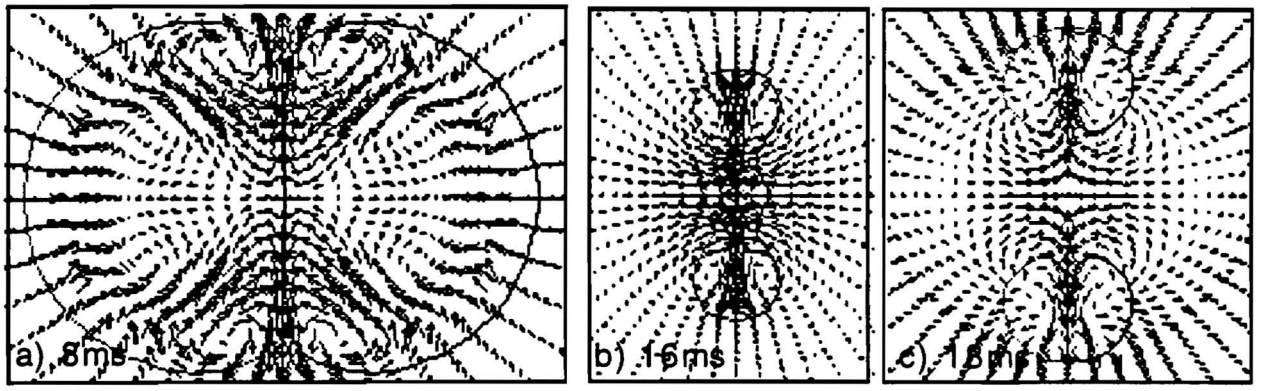

Figure 7: Velocity vectors for the cases discussed in fig. 6.

Figure 8: Snapshots of the bubbles in the expt.(Lal and Menon,1996) for in-phase explosions of same size. a) Corresponds to bubble maximum, b) During Collapse & c) During rebound.

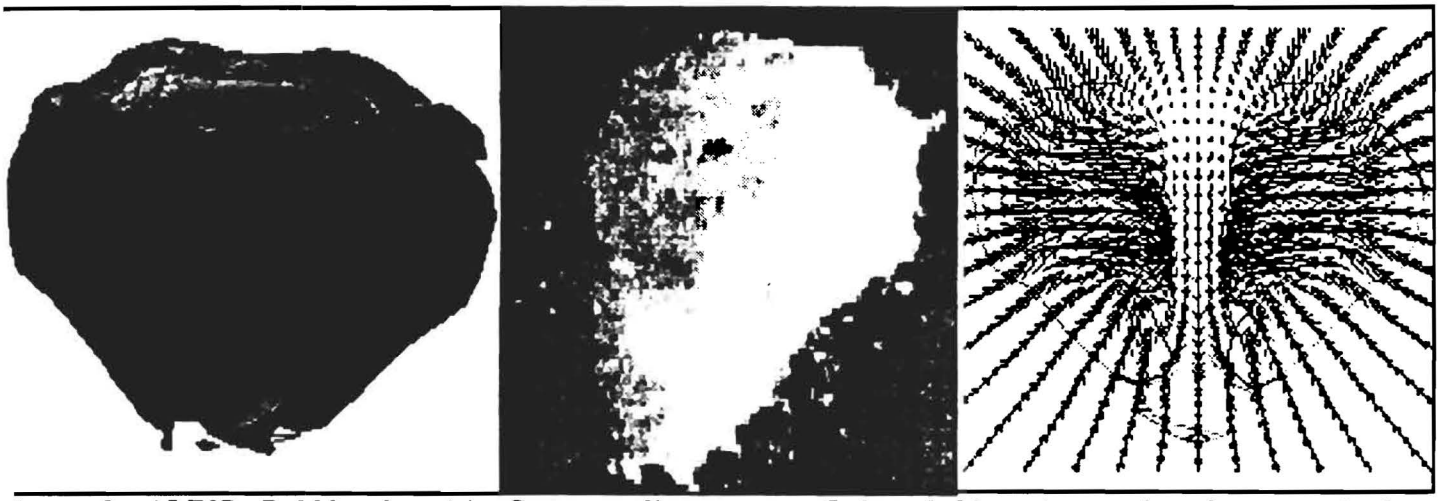

igure 9: ALE3D Bubble shape(a), Corresponding to expt.(Lal and Menon) snapshot for out of phase xplosion(b) and corresponding velocity field(c) at the time of jet formation for the bubbles of different izes interacting.

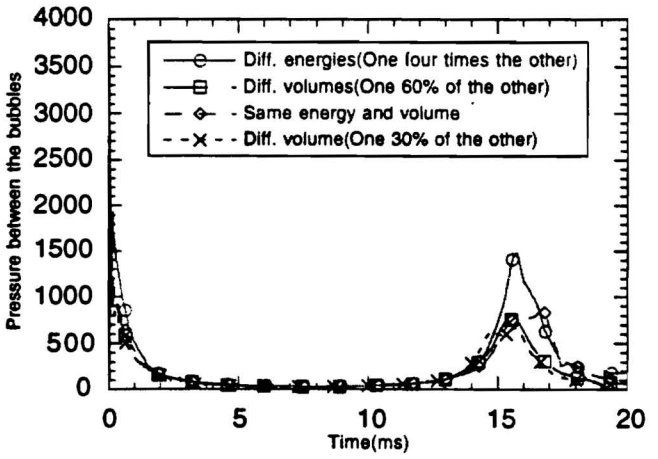

Figure 10: Time trace of the pressure in between the bubbles for different cases of double bubble interactions

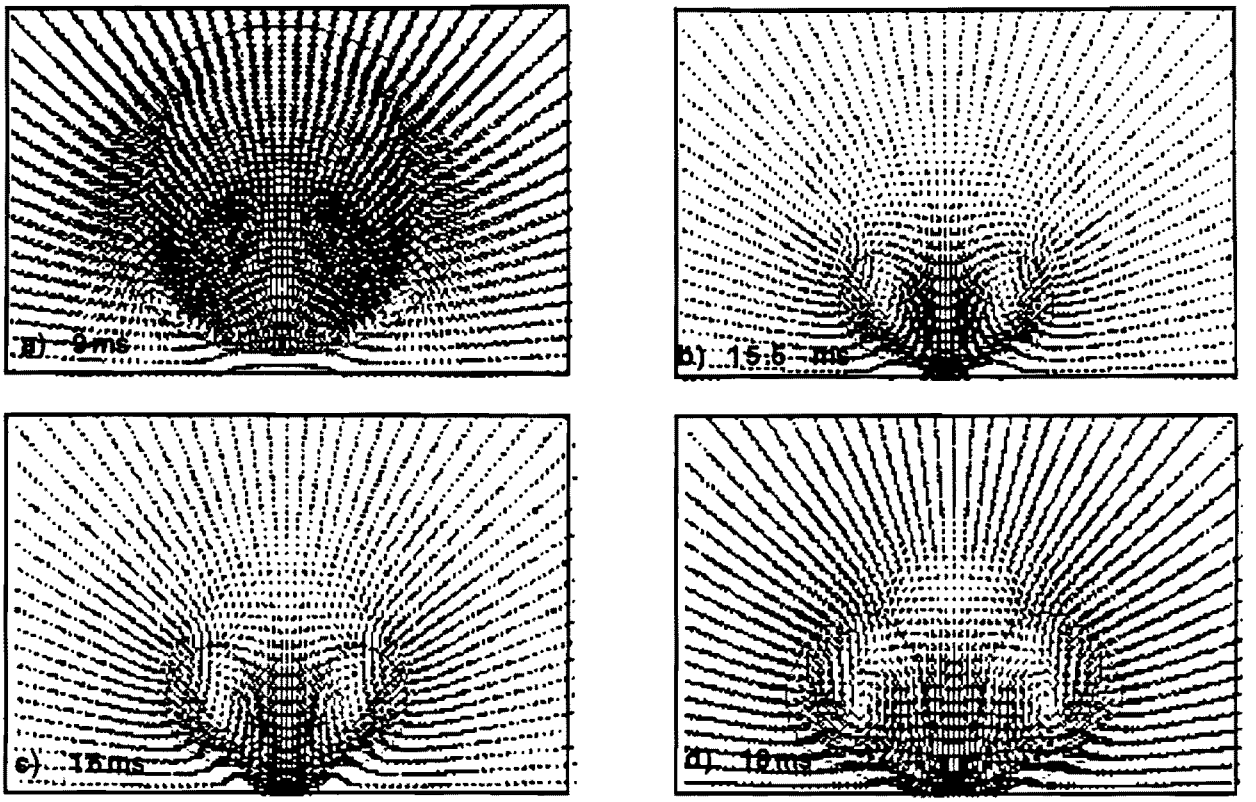

Figure 11: Velocity field around a bubble collapsing near a wall(Buoyancy Inhibiting). a) At bubble maximum, b) & c) Just before the jet formation and d) After the toroidal bubble is formed during rebound.

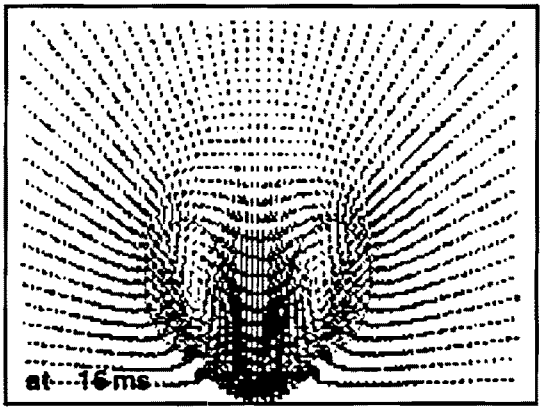

Figure 12: Velocity field around the bubble collapsing near a rigid wall with buoyancy aiding the collapse.

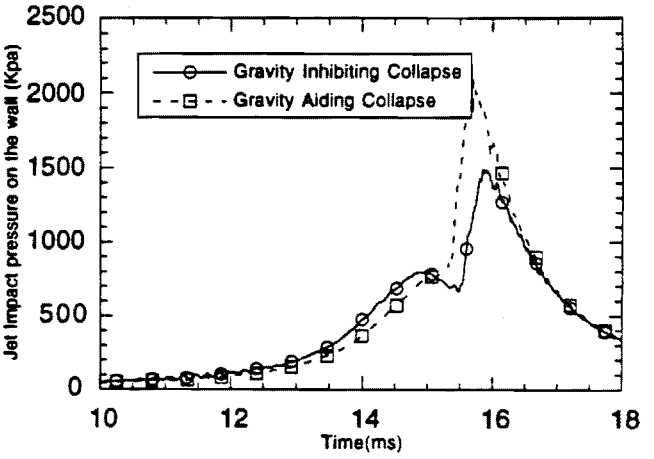

Figure 13: Impact pressure on the wall for both the buoyancy aiding and inhibiting cases.

1997 ASME Fluids Engineering Division Summer Meeting
FEDSM'97
June 22 - 26, 1997

FEDSM97-3244

NUMERICAL STUDY OF BUBBLE COLLAPSE AND REBOUND NEAR A WALL

Sreekanth Pannala
Georgia Institute of Technology
Atlanta, Georgia 30332-0150
(404)-894-1409
(404)-894-2760(FAX)
gt5960b@prism.ae.gatech.edu

Suresh Menon
Georgia Institute of Technology
Atlanta, Georgia 30332-0150
(404)-894-9126
(404)-894-2760(FAX)
menon@falcon.ae.gatech.edu

ABSTRACT

The collapse and rebound of an explosion bubble near a wall are numerically investigated using an Arbitrary Lagrangian Eulerian three-dimensional code and the results are compared with the experimental data. The final stages of the collapse including the formation of a high velocity re-entrant jet are successfully captured in the simulations. The jet velocity and the impact pressure on the wall are functions of the explosion pressure and the distance of the bubble from the wall and to some extent on gravity. The results indicate that, for a given explosion pressure and initial conditions (gravity aided or inhibited), there is an optimal distance of the bubble from the wall, which gives the maximum impact pressure. This trend is in very good agreement with the experimental results. The evolution of the vortex ring bubble, reported in earlier experimental and numerical studies is accurately predicted. The applicability of the available scaling laws for the time period and peak velocities is also reviewed.

INTRODUCTION:

The physics of cavitation erosion of marine propellers and turbine blades and the destruction caused by underwater explosions is of great practical interest but is not very well understood. Bubble (cavitation or explosion) collapse near a rigid wall is of significant interest due to a variety of reasons related to its ability to cause serious damage to the structure. This is because when the bubble collapses near a rigid surface, a strong reentrant water jet is formed that is directed towards the wall. The peak impact pressure on the wall due to this water jet can be substantially higher than the initial explosion pressure (especially when it is very large). Detailed reviews (e.g., Blake and Gibson, 1987; Prosperetti, 1982) have summarized past experimental and numerical results. Experimental studies are too many to list completely; however, in general, only limited amount of information can be obtained due to various difficulties encountered in acquiring data. The most recent and notable experiments conducted to study bubble-wall interactions are those reported by Vogel et. al. (1989) and Tomita and Shima (1986). Recently, experiments were also carried out to investigate large-scale bubble explosions (Menon and Lal, 1996; Lal and Menon, 1996a, b). These experiments were conducted in shallow water due to interest in understanding the dynamics of bubble-wall interaction in such flows and to investigate the feasibility of targeting buried mines for destruction in beaches. The data obtained from these bubble-wall experiments is used in this paper to validate the numerical results.

Numerical studies in the past range from simple 1-D analytic solutions to more complex 2D/3D studies. Most of the earlier work has been done using the Boundary Element Methods(BEM) (e.g., Chahine and Perdue, 1988; Duncan and Zhang, 1991; Blake et. al., 1986; Wilkerson, 1989). The original BEM methodology cannot handle the phenomena of jet formation as the geometry changes from simple domain to a doubly connected domain. To overcome this short coming, many variants of the BEM methodology are used to capture the collapse and rebound of (e.g., Zhang and Duncan, 1994; Zhang et. al., 1993; Best and Kucera, 1992; Best, 1993) the bubble. Such procedures are often *ad hoc*. and recourse to the experiments is required to model the problem correctly. Further they cannot be easily extended to other complex problems like the collapse of bubbles near deformable surface or collapse of non-spherical bubbles. Incompressible flow assumption made in these studies is not completely valid for the collapse of bubble near a wall as the pressures and velocities encountered are very high. The axisymmetric assumption also can not be generally used without apriori knowledge of the problem at hand.

Conventional Lagrangian or Eulerian techniques (even using full 3D) are also not practical, since the expansion and collapse of bubbles, the jet formation and the rebound of the ring vortex bubble create severe fluid motion. In a Lagrangian approach grid points move with the fluid, resulting in severe grid distortion (skewness, overlap of grid etc.,), becomes inappropriate. In an Eulerian approach, adequate resolution in

the regions of interest (e.g., the bubble surface) is very difficult to achieve since the bubble's shape changes very rapidly.

A numerical method that includes both compressibility and an ability to capture the entire bubble collapse and rebound in complex configuration is used in this study. This numerical code (ALE3D), developed at the Lawrence Livermore National Laboratory, combines lagrangian and eulerian features and is based on the Arbitrary Lagrangian-Eulerian (ALE) scheme. Past applications of this method include the 2D (e.g., Tipton, et al., 1992) and the full 3D (Milligan et al., 1995 and Couch et al., 1996) studies of bubble collapse. This paper reports results of the interactions of the explosion bubbles with a rigid wall. The affects of various parameters are also analyzed.

NUMERICAL METHODOLOGY

ALE3D (Anderson et al., 1994) is an explicit, 3D finite element code that simulates the fluid motion and elastic-plastic response on an unstructured grid. The grid may consist of arbitrarily connected hexahedral shell and beam elements. The ALE algorithm is implemented by carrying out a complete Lagrangian calculation followed by an advection step. After each lagrangian step, a new mesh is created using a finite element based equipotential method to relax the distorted grid. In the eulerian advection step, the fluid variables such as mass, density, energy, momentum and pressure are reevaluated on the new mesh by allowing fluid motion. The details of the constitutive models are described elsewhere (e.g., Steinberg, 1991) and, therefore, are not described here for brevity.

The advection step uses a second order, monotonic advection algorithm. This can create mixed material elements (i.e., liquid and vapor). Material interfaces are not explicitly tracked but for the purpose of carrying out mixed element advection, they are inferred from volume fractions. Separate state variables are kept for each component of a mixed element.

RESULTS AND DISCUSSION

In this section, the various test cases studied are summarized and specific trends are discussed.

The simulations employed here are similar to the experimental set-up of Lal and Menon (1996b). The experimental case is modeled as a bubble placed at a distance (d) above the wall in the vertical direction in a 1.5m x 1.5m x .75m tank filled with water. The initial diameter of the bubble is 6.34 cm and the initial explosion pressure is 13 atmospheres.. The water pressure is 1 atmosphere. The experimental set-up employed a glass globe with a metal insert that contained pressure transducer and the spark generator, while these features were ignored in the numerical model. There are inherent limitations in the models employed for the equations of state for water and vapor. Further it is assumed that viscosity and surface tension are negligible. The ALE mesh treatment is applied to all the elements in the bubble, in the vicinity of the bubble and in between the bubble and the nearby wall. The other parts of the domain, where the bubble explosion and collapse does not cause much grid distortion, the standard lagrangian mesh treatment is used. The resolution of the grid is varied to ensure grid independence. The full 3D simulation of the bubble collapse against a rigid wall is carried out and the results compare well with the simulation using only one-quarter of the domain and using two symmetry planes. This indicates that the present problem is symmetric about the axis and the results reported here are from the reduced problem.

Three cases are analyzed here to highlight the various physical phenomena associated with the bubble collapse near a wall and its dependence on the proximity to the wall. These cases correspond to an initial bubble location of 5 cm, 6.34 cm and 4 cm above the wall (gravity inhibiting case as in the experiments), respectively. Figures 1a-c show the velocity field at various stages of the collapse for the first case. At the bubble maximum, the bubble is almost spherical but begins to distort as it collapses. Since there is less volume of water between the wall and the bubble during the collapse, the pressure drop is quite large relative to the drop on other sides of the bubble. This pressure differential further forces the bubble towards the wall. This migration of bubble causes the water surrounding the bubble to be directed off-center relative to the bubble geometric center, thereby, creating a higher pressure on the side of the bubble away from the wall. This results in the well known Bjerknes force. The iterative combination of these effects causes the water to penetrate the bubble from the high pressure side and to form a high-speed water jet that impacts the rigid surface. As this jet impacts the rigid plate, a toroidal vortex ring bubble is formed, as shown in the Fig. 3. This ring bubble qualitatively compares well with those observed in both experiments (e.g., Tomita and Shima, 1986; Vogel, et al., 1989) and in numerical studies (Best, 1993; Szymczak, et al., 1993; Zhang and Duncan, 1994). In Fig. 4, the two different views of the bubble are shown after the jet has penetrated it and compares well with the recent data reported in Jin et al. (1996). In Fig. 5, the velocity fields for the cases 2 and 3 are shown at a time before the jet formation. Comparison of Fig. 1b and Fig. 5, indicates that for case 2, where the bubble is the farthest has the provision to collapse to a smaller volume and thus the higher velocities. In case 3, the bubble cannot collapse as much as the other two cases and thus, lower velocities and in turn the lower pressures are observed.

Figure 6 compares the time traces of peak impact pressure on the rigid wall for the three cases. The time periods scaled with non dimensional time based on the maximum radius of the bubble, the ambient(water) pressure and the water density $\left(R_{max} / \sqrt{\frac{P_\infty}{\rho_w}} \right)$, are 2.021, 2.017 and 2.048 respectively for the three cases. The peak velocities are observed slightly before the jet impacts the wall. These velocities scaled with non-dimensional velocity scale based on the ambient(water) pressure and water density $\left(\sqrt{P_\infty / \rho_w} \right)$ are 6.9, 7 and 6.4 respectively.. These scaling laws compare well with earlier results(e.g., Chahine and Perdue, 1988; Blake et al., 1986). It is observed that even though maximum velocities are seen in case 2, it does not correspond to the maximum peak impact pressure as the jet formed loses some of its energy as it impinges on the wall through the water layer between the toroidal bubble and the wall. In case 1, the lower surface and the upper surfaces are attached to the wall before the impingement of the jet and thus, the jet does not transmit energy to the water layer as in case 2. This explains the higher impact pressures observed. The other fact to be noted in this figure is that the impact pressure on the wall due to the first pressure pulse is higher for case 3, and is inversely proportional to proximity of the bubble from the wall. The strength of the pressure wave generated by the bubble decreases radially outwards and thus, a greater impact pressure is felt on the wall in case 3. It can be seen that the time periods of

jet formation is not a strong function of the bubble distance from the wall. since the pressure peak is very steep, appropriately small time steps have to be taken to ensure numerical accuracy.

Figure 7 compares the variation of peak impact pressure (scaled with initial explosion pressure) versus separation distance (scaled with the initial radius of the bubble) of the present simulations to that of the experiments (Lal and Menon, 1996b). It can be seen clearly that the present numerical study captures the trends and the magnitudes of the peak impact pressures. The differences between the gravity inhibiting case and the experiment can be due to many reasons associated with the idealization of the experimental setup in addition to numerical errors. The gravity aided case (bubble placed below the wall) shows similar behavior to the gravity inhibited case and the impact pressure peaks at a distance slightly greater than for the other case. This follows the physical intuition that the bouyancy aids the migration of the bubble towards the wall and thus the peak shifts to the right.

Figure 8 shows the variation of impact pressure along the wall for case 1, just after the jet formation. This indicates that the jet is very narrow and even millimeters away from the jet center the pressure falls of very rapidly. This kind of behavior is very typical of stagnation point flows and makes it very difficult to simulate the process accurately, unless the jet is properly resolved.

CONCLUSIONS

The above studies demonstrate the potential of ALE3D code to capture the physical phenomena associated with the collapse and rebound of bubble near a rigid wall. The procedure adopted is general and the code is applicable to more complex cases than those discussed here. The results obtained are in good quantitative and qualitative agreement with the experiments and other numerical work. In addition the formation of re-entrant jet and a ring vortex bubble has been captured without any ad hoc. procedure.

ACKNOWLEDGMENTS

This work is supported by the Office of Naval Research under grant No. N00014-91-J-1993. ALE3D, a product of Lawrence Livermore National Laboratories was used for the simulations in this paper.

REFERENCES

Anderson, S., Dube, E., Futral, S., Otero, I., and Sharp, R., 1994, "Users Manual For ALE3D," Lawrence Livermore National Lab., CA.

Best, J. 1993, "The formation of toroidal bubbles upon the collapse of transient cavities," J. Fluid Mech., 251,79-107.

Best, J.P., and Kucera, A., 1992, "A numerical investigation of non-spherical rebounding bubbles," J. Fluid Mech.,245, 137-154.

Blake, J. R., Taib, B. B., and Doherty, G., 1986, "Transient Cavities Near Boundaries. Part I. Rigid Boundary," J. Fluid Mech., 170, 479-497.

Chahine, G. L., and Perdue, T. O., 1988, "Simulation of the Three-Dimensional Behavior of an Unsteady Large Bubble near a Structure," 3rd International Colloquium on Bubbles and Drops, Monterrey, CA.

Couch, R., and Faux, D., 1996, "Simulation of Underwater Explosion Benchmark Experiments with ALE3D," Lawrence Livermore Natn. Lab., Livermore, CA, UCRL-CR-123819.

Duncan, J. H., and Zhang, S., 1991, "On the Interaction of a Collapsing Cavity and a Compliant Wall," J. of Fluid Mech., 226, pp. 401-423.

Jin, Y. H., Shaw, S. J., and Emmony, D. C., 1996, "Observations of a Cavitation Bubble Interacting with a Solid Boundary from Below," Phys. Fluids, 8, 1699-1701.

Lal, M. K., and Menon, S.,1996a, "Interaction of Two Underwater Explosion Bubbles", ASME, Fluids Engg. Div. Conf., Vol. 1, pp. 595-600.

Lal, M. K., and Menon, S., 1996b, "Experiments in Underwater Explosions near rigid surface", Under Preparation.

Menon, S., and Lal, M. K., 1996, "On the Dynamics and Instability of Bubbles Formed During Underwater Explosions," Submitted to Thermal and Fluids Journal.

Milligan, C. D., Duncan, J. H, and Stillman, D. J., 1995, "A Numerical Study of Underwater Explosion Bubble Phenomena" preprint.

Plesset, M. S., 1971, "The Dynamics of Cavitation Bubbles," Trans. ASME, J. Appl. Mech., 16, 277-282.

Prosperetti, A., 1982, "A Generalization of the Rayleigh-Plesset Equation of Bubble Dynamics," Phys. Fluids, 25, 409-410.

Steinberg, D., 1991, "Equation of State and Strength Properties of Selected Materials," Lawrence Livermore Natn. Lab., Livermore, CA, UCRL-MA-106439.

Szymczak, W. G., Rogers, J. C. W., Solomon, J. M. and Berger A. E., 1993, "A numerical algorithm for hydrodynamic free boundary problems," J. Comput. Phys., 106,319-336.

Tomita. Y., and Shima. A., 1986, "Mechanisms of impulsive pressure generation and damage pit formation by bubble collapse," J. Fluid Mech., 169, 535-564.

Tipton, R., 1990, "CALE User's Manual," Lawrence Livermore Natn. Lab., B-Division Internal Document, Livermore, CA, 1990.

Tipton, R. E., Steinberg, D. J., and Tomita, Y.,1992, "Bubble Expansion and Collapse Near a Rigid Wall," JSME, Vol. 35. No. 1, pp. 67-75.

Vogel, A., Lauterborn, W. and Timm, R., 1989, "Optical and acoustic investigations of the dynamics of laser-produced cavitation bubbles near a solid boundary," J. Fluid Mech., 206, 299-338.

Wikerson, S. A., 1989, "Boundary Integral Technique for Explosion Bubble Collapse Analysis," ASME, Energy-Sources Technology Conference and Exhibition, Houston, 1989.

Zhang, S., Duncan, J. H. and Chahine, G.L., 1993, "The final stage of the collapse of a cavitation bubble near a rigid wall," J. Fluid Mech., 257, 147-181.

Zhang, S. and Duncan, J. H., 1994, "On the nonspherical collapse and rebound of a cavitation bubble," Phys. Fluids, 6(7), 2352-2362.

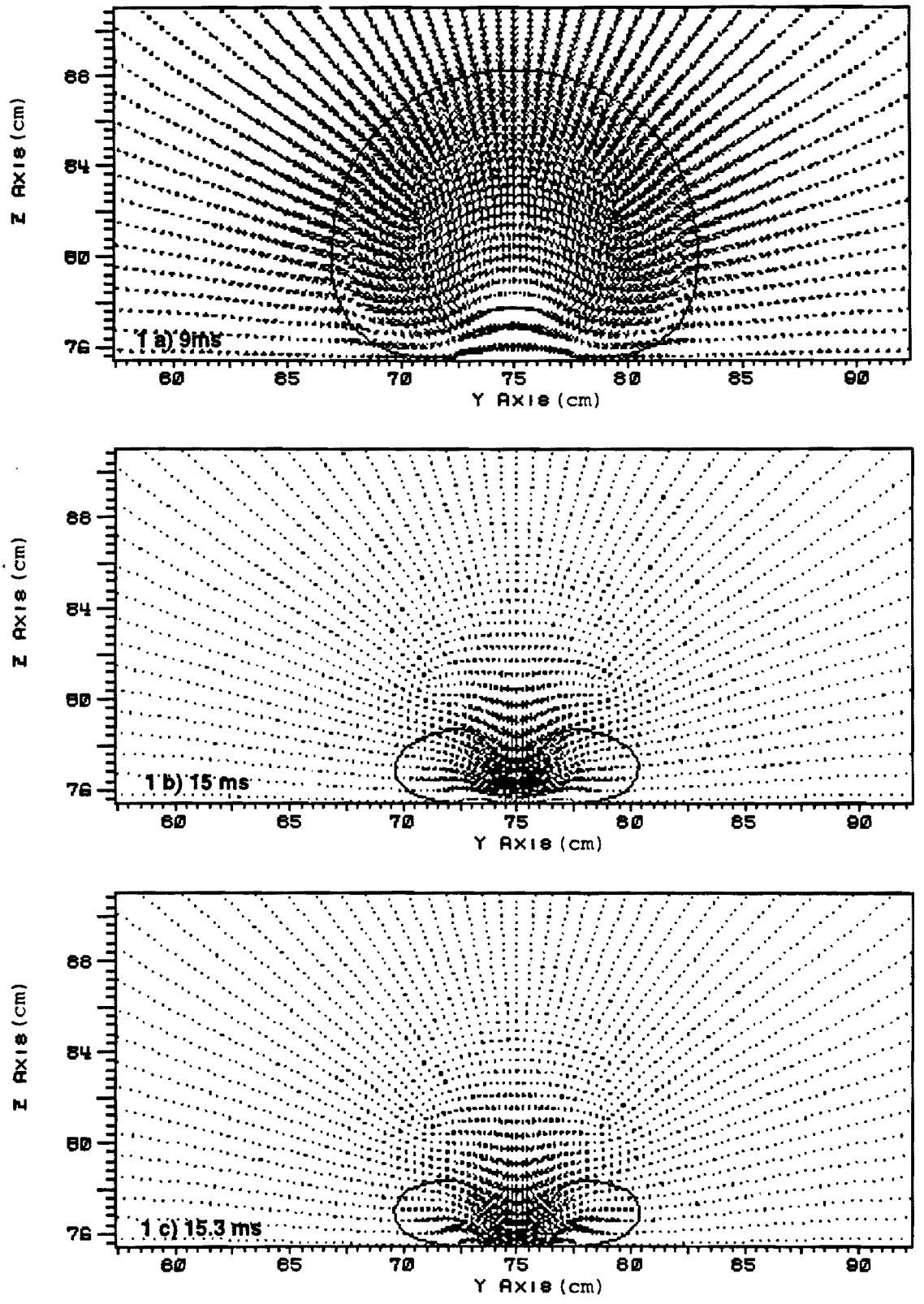

Figure 1: Velocity vector field around the bubble collapsing near wall(5cm). a) Initial phase of collapse, b) & c) Just before the jet formation.

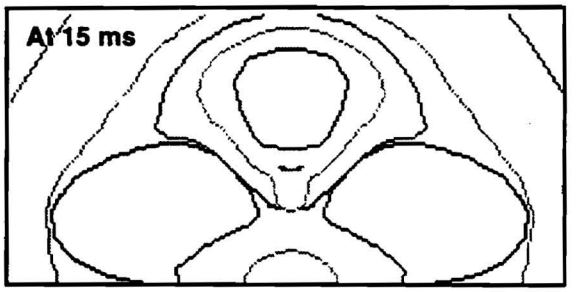

Figure 2: Pressure contours showing the pressure build on the side of the bubble away from the wall (case 1).

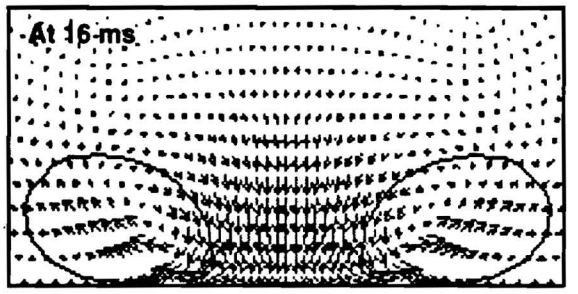

Figure 3: Velocity vector field in and around the vortex ring bubble formed during rebound.

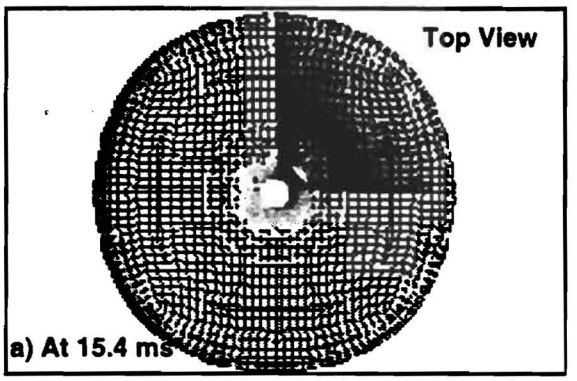

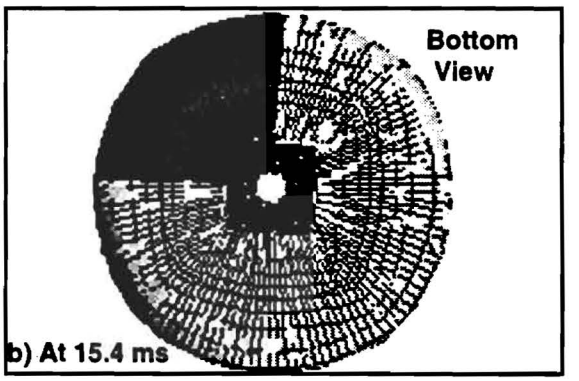

Figure 4: Different views of the bubble just after the jet formation.

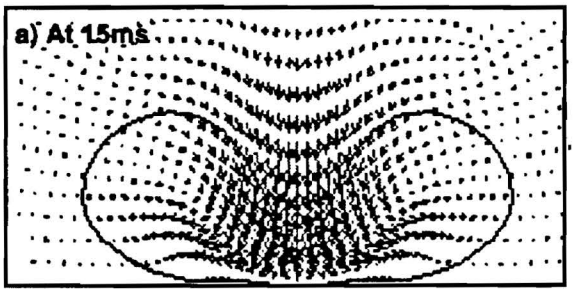

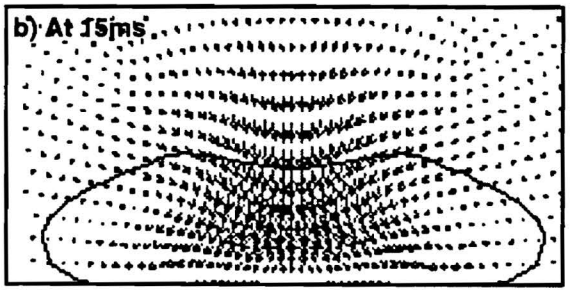

Figure 5: The velocity field in and around the bubble just before the jet formation. a) Case 2 and b) case 3

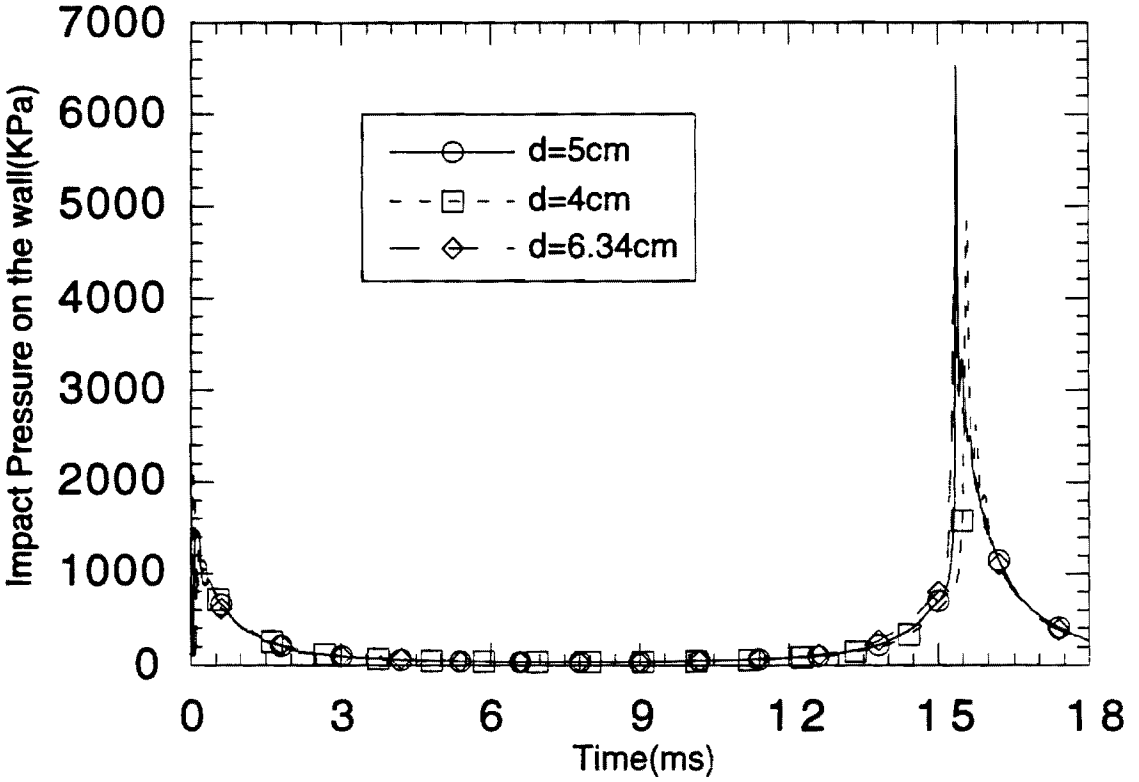

Figure 6: Comparision of the time traces of the impact pressure on the wall for different distances of the bubble center from the wall.

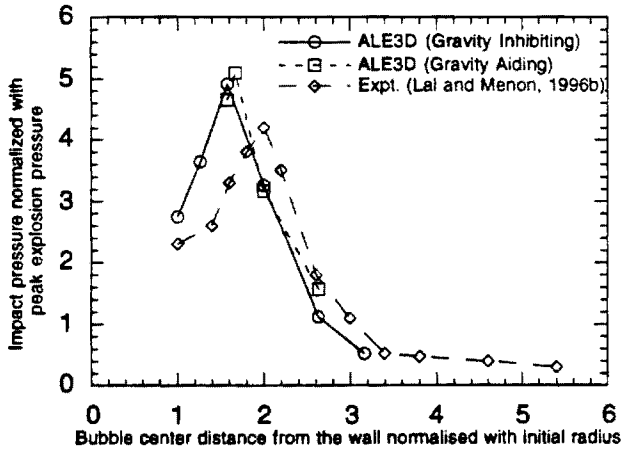

Figure 7: Variation of peak impact pressures on the wall with distance of the bubble from wall for simulations (gravity aiding and inhibiting) and experiments.

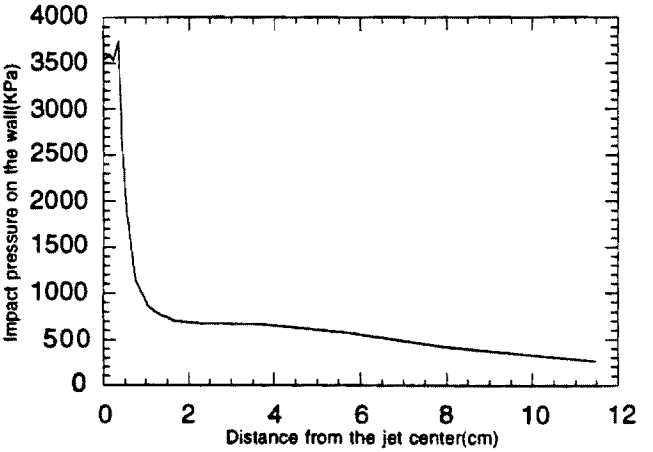

Figure 8: Variation of the impact pressure along the wall from the stagnation point of the reentrant jet showing the spread of impact.

Proceedings of the 1996 ASME Fluids Engineering Division Summer Meeting
San Diego, California; July 7-11, 1996, FED Vol. II, pp. 595-600

INTERACTION OF TWO UNDERWATER EXPLOSION BUBBLES

Mihir K. Lal

Suresh Menon

School of Aerospace Engineering
Georgia Institute of Technology
Atlanta, Georgia 30332
Phone: (404) 894-9126
Fax: (404) 894-2760
E-mail: menon@falcon.ae.gatech.edu

ABSTRACT

Underwater explosion bubbles are created by detonating a mixture of oxygen and Carbon Monoxide or Hydrogen in glass globes submerged in a water tank. A cinematographic technique is employed to capture entire interaction process in both horizontal and vertical configurations. Depending on the delay between two explosions and inter-bubble distance, the bubbles may either attract each other to form a single coalesced bubble, or they may violently repel each other. A violent interaction leads to an increased instability of the bubbles. When a coalesced bubble is formed by merging the energies of two bubbles, the resulting bubble has more residual energy and is more stable for successive oscillations. An out-of-phase oscillation generates a reentrant water jet which pierces the bubble. Water free surface repels the bubble and the bubble migration speed and direction change smoothly as the explosion depth is continuously decreased.

INTRODUCTION

Much of the research activities in the area of underwater bubble dynamics has been focused on the behavior of cavitation bubbles. Cavitation bubble dynamics play a very important role in underwater acoustics and in predicting and preventing propeller and turbine blade damage. These bubbles, however, seldom occur singly. Actual cavitation fields contain several thousands of oscillating and translating microbubbles. Study of the behavior of a cloud of bubbles thus becomes inevitable and experimental (Chahine and Sirian 1985), numerical (Chahine and Liu, 1985; Chahine, 1991; Chahine and Duraiswami, 1992) and analytical (Van Wijngaarden, 1972) techniques have all been developed. The simplest model that has been studied by the researchers is the interaction between two bubbles. Theoretical and numerical studies of the interaction of two spherical or nonspherical bubbles of same or different sizes (Fujikawa et al., 1985; Fujikawa and Takahira, 1986; Fujikawa and Takahira, 1988; Morioka, 1974; Shima, 1971) have been carried out. Interesting experimental observations of the interaction of a gas bubble with a pressure wave (Shima and Tomita, 1988) or with a vapor bubble (Smith and Mesler, 1972) have also been made.

Large bubbles, such as those formed during underwater explosion, owing to their tremendous inherent destructive capabilities upon collapse near a rigid boundary, find practical applications in underwater weaponry. These bubbles were recently simulated experimentally on a laboratory scale in a free field configuration (Menon and Lal, 1996).

The interaction of two underwater explosion bubbles is a very interesting and complex phenomenon, because of the fact that one bubble is influenced by time-delayed pressure or shock wave radiated from the adjacent bubble. Radial motion of the bubble may be greatly excited or subdued due to the interaction depending on their spatial and temporal separations. Though some experimental work have been done on the interaction of gas bubbles with two adjacent underwater explosion bubbles, and it has been shown that strong and complicated interactions ensue, it appears that no detailed results on the interaction of two underwater explosion bubbles have been published in the public domain literature.

This paper reports the results of the experiments carried out in a laboratory water tank to study the interaction between two adjacent bubbles created by underwater explosion of flammable gas contained in glass globes. The globes were placed side-by-side either in a horizontal or a vertical plane. The distance between the two globes and their sizes were both varied. This paper will also deal with the interaction of single and double explosion bubble(s) with the water free surface.

EXPERIMENTAL PROCEDURES

Underwater explosion experiments were conducted in a wooden tank of dimension 2 m×1.5 m×1.5 m, coated with fiberglass resin from inside. The tank, as shown in Fig. 1, has three windows on three sides. The underwater explosion bubble is generated by centrally igniting a mixture of an explosive gas (either Hydrogen or Carbon Monoxide) and oxygen contained in a hand-blown glass globe. Three different sizes of glass globes have been used for present experiments with average radii of 2.9 cm, 3.2 cm, and 3.8

cm. The glass globe, as shown in Fig. 2, has an electric spark ignition system connected to a 3000V DC power supply. The explosion takes place at a constant volume until the globe bursts. It has been shown (Menon and Lal, 1996) with the help of geometric and dynamic scaling rules that the explosion bubble thus formed is a reasonable subscale approximation of the deep sea underwater explosion bubble.

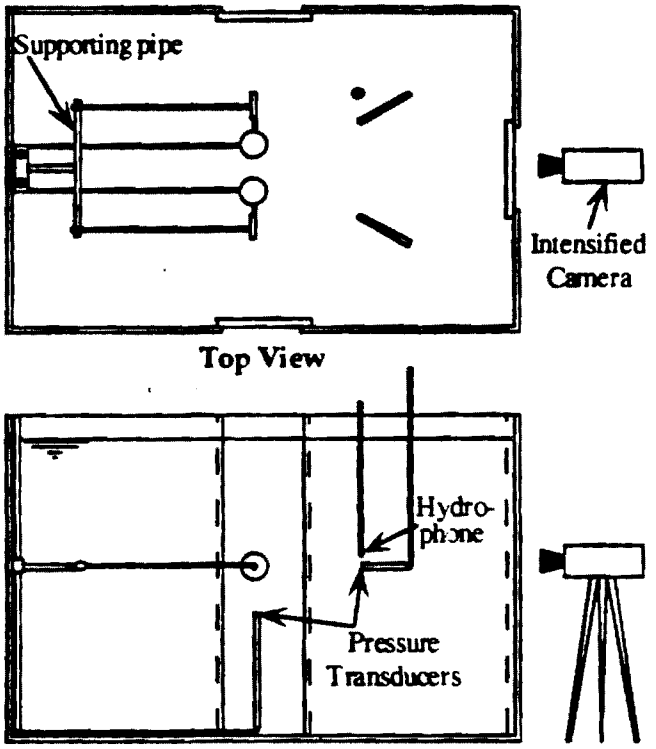

Fig. 1. Experimental setup

The pressure responses in the water around the bubbles are recorded during the experiments by means of 4 KISTLER dynamic piezoelectric pressure transducers fitted at the ends of 4 stainless steel (1.27 cm diameter) tubes bent at right angle, as shown in Fig. 1. A hydrophone is also mounted in the tank and is used for measuring acoustic pressure. Pressure inside the bubble during its oscillation is measured by another KISTLER transducer which is mounted inside the plug, as shown in Fig. 2. Signals from these six pressure transducers and the hydrophone are digitized using National Instrument's AT-MIO-16X analog-to-digital converter board, and are recorded into a microcomputer. Eight channel data recording are performed with a sustained sampling rate of 10,000 samples per second per channel.

The tank is illuminated by either direct overhead flood lights or an argon-ion laser sheet which lies in a vertical plane perpendicular to the camera axis. The optical recording of the bubble motion is performed by a CCD enhanced digital video camera with a maximum speed of 6000 frames per second. Since the viewable picture size is inversely proportional to the recording speed, the maximum speed was limited to 2000 frames per second as the image size reduces to half at this speed. Most of the experiments, however, were performed at the speed of 1000 frames per second (full screen image).

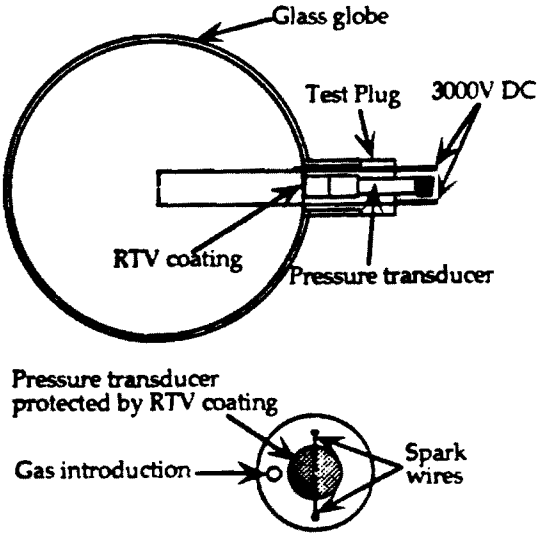

Fig. 2. Glass bulb and test plug instrumentation

The two glass globes are supported inside the tank by means of a modified sting which makes the pressure transducers mounted inside the two globes to face each other. This facilitates the direct measurement of the fluctuation in the pressure inside one bubble due to its interaction with the other. In order to provide a means for altering the distance between the two bubbles, six holes were drilled in the supporting copper pipe (1.6 cm diameter) of Fig. 1 at equal spatial separation from either ends. Experiments were conducted in primarily two configurations; a horizontal configuration, when the supporting pipe was horizontal, and a vertical configuration, when it was vertical. The former configuration prohibited the use of laser light sheet and only the flood lights were used for imaging, while the latter allowed the use of laser light sheet.

Experiments were also conducted to study the interaction of water free surface with the explosion bubble(s). The motivation for this kind of experiments has obvious reasons as detailed in the next section. The free surface provides a constant pressure boundary in close proximity of the oscillating bubble. It is known that the bubble moves away from the free surface and a reentrant jet is formed which pierces the bubble in the direction of its migration (Birkhoff, 1957; Blake and Gibson, 1981; Chahine, 1982; Wilkerson, 1989). Wilkerson (1989) developed a boundary integral technique for the analysis of expansion and collapse of an explosion bubble in free field, near a rigid surface, or near a free surface. To verify the accuracy of his method for predicting reentrant water jet tip velocities for a bubble near a free surface, he compared his results with a PISCES code calculation and expressed his inability to predict an accurate estimation of the error involved in his method because of the unavailability of any such experimental data. This observed lack of data motivated the current experiments to study the interaction of a free surface with an explosion bubble.

RESULTS AND DISCUSSION

The interaction process is highly dependent on the time delays between the two explosions. These time delays are related to a variety of hardware and bubble response characteristics. The two globes have independent power supplies and there is always a time delay between the occurrence of the spark and when the bubble starts expanding. The bubble expansion occurs immediately after the glass globe bursts. The time delay depends primarily on the gas volume (globe size) and the nature of gas mixture inside the globe. A bigger globe size will create a larger time delay. Similarly, fuel-rich or fuel-lean mixtures will also create larger delays as compared to the one associated with a stoichiometric mixture. In addition to this delay, there is another time delay which is associated with the spark system itself. This delay is between the instant when the power is turned on and when the spark actually fires. This delay primarily depends on the actual gap between the two spark wires since a bigger gap creates a larger delay. The actual delay (temporal separation) between two explosions is therefore measured from the recorded video images as the time elapsed between the instant when the individual globe bursts. It was therefore deemed necessary to conduct several experiments to collect statistical information about the range of bubble behavior with respect to the delay between two explosions.

The entire spectrum of delay can be classified into two broad regions and they are called in-phase oscillation and out-of-phase oscillation (Morioka, 1974; Shima, 1971; Smith and Mesler, 1972). In most of the past analytical, numerical or even experimental work on the interaction of two cavitation bubbles, interest has been focused primarily on the contraction phase of the bubble oscillation. This yields an in-phase oscillation of the bubbles as they both start collapsing at the same time following a sudden change in the ambient pressure. In-phase oscillation is obtained when there is strictly no delay between the explosions and both the bubbles start their oscillation cycle at the same time. Of course, it is assumed that the two bubbles have identical time period of oscillation and they are in identical phase at any instant throughout their oscillation cycle. This is the simplest scenario and has been analyzed comprehensively.

Another interesting scenario is 180° out-of-phase oscillation and it can be best understood in the interaction of two identical explosion bubbles as a case where one bubble starts its oscillation cycle when the other has already reached its maximum radius. In fact, these are the two scenarios predicted by the analytical theories (Morioka, 1974). Morioka's (1974) theoretical analysis of natural frequencies of two pulsating bubbles predicts the existence of two natural frequencies corresponding to in-phase and 180° out-of-phase oscillations, respectively. Of course, in an experimental setup one can have any amount of delay between zero to 180°, or beyond.

The behavior of explosion bubbles under these two scenarios have long been predicted (Birkhoff, 1957; Bjerknes, 1906; Cole, 1948; Young, 1989) and it is called the laws of Bjerknes. Bjerknes showed in 1868 that two spheres pulsating in-phase attract each other, and those pulsating 180° out-of-phase repel each other. Two spheres collapsing in-phase are equivalent to a single sphere collapsing near a rigid surface at a distance which is exactly equal to be half of the distance between two spheres. Similarly, two spheres oscillating 180° out-of-phase are equivalent to a single sphere pulsating near a free surface at a distance equal to half of the distance between two spheres. It has been shown (Birkhoff, 1957) that the migration speed of the bubble towards a rigid surface or away from a free surface is inversely proportional to r^3, where r is the instantaneous bubble radius. Therefore, most of the migration would take place when the bubble radius is small (i.e., when the bubble is collapsing and approaching its minimum radius). Also, Bjerknes (Bjerknes, 1906; Young, 1989) showed as an analogy with gravitational and electromagnetic forces that the attractive force, F, between two bubbles of volumes V_1 and V_2 a distance d apart in a pressure field is given by $F \propto V_1 V_2 / d^2$. Since the bubble migration velocity is directly proportional to the attractive force, its magnitude is expected to increase for bigger bubbles pulsating out-of-phase at a shorter inter-bubble distance, and decrease for smaller bubbles at a larger distance.

Fig. 3 shows a perfect example for two underwater explosion bubbles oscillating in-phase. The numbers in the parentheses denote the frame numbers, with frame number 1 corresponding to the instant when the sparks are visible for the first time. The initial volume of the right glass globe is 94 ml and that of the left glass globe is 90.5 ml. They are in a horizontal configuration and are initially separated by a distance d, where $d/R_o = 2.32$. Here R_o is the initial bubble radius, which is taken to be the radius of the glass globe. Both are filled with stoichiometric mixture of Carbon Monoxide and Oxygen. It can be seen in Fig. 3 that there is virtually no delay between two explosions. Since the initial spatial separation between the globes was intentionally kept to a very small value so that a violent interaction can ensue, the bubbles soon come in contact with each other. They deviate more and more from sphericity as they expand with time. Fig. 4(a) shows how different radii of the left bubble change with time. A similar behavior is exhibited by the right bubble. The deviation from sphericity is more clearly demonstrated in Fig. 4(b), where the time history of the ratio of major and minor radii is plotted. As is evident from this figure, the bubbles quickly deviate from sphericity and the maximum deviation is attained at around frame no. 11. This deviation slowly diminishes and the bubbles become nearly spherical at around frame no. 21. When the bubbles merge together to form a single coalesced bubble, it becomes difficult to isolate them individually.

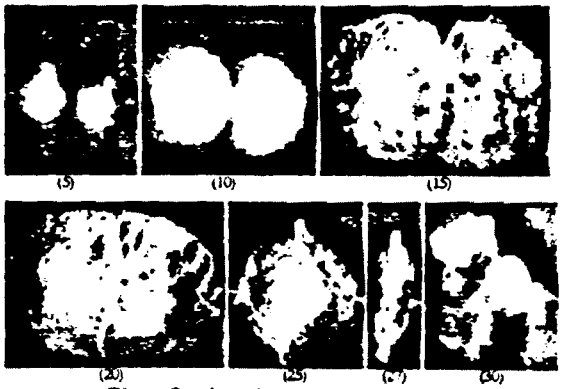

Fig. 3. In-phase oscillation

The surface where the two bubbles come in contact in Fig. 3 grows in size as the bubbles grow and is initially curved. The bubbles reach their maximum radii at around frame no. 18 and start collapsing thereafter. The surface of contact slowly becomes a plane surface around frame no. 21 and remains so thereafter until the bubbles collapse near frame no. 28. This plane surface of contact may be considered as a rigid surface in an equivalent single bubble

analogy. This surface is almost perpendicular to the line joining the initial globes' centers and is located almost midway.

The frames shown in Fig. 3 have been recorded at a speed of 1000 frames per second. The time period of oscillation of the bubbles is found to be about 21 ms, while that of an identical bubble in free-field is less than 15 ms (Menon and Lal, 1996). Therefore, for two identical bubbles oscillating in-phase, an increase in the bubble period is observed (Chahine, 1991).

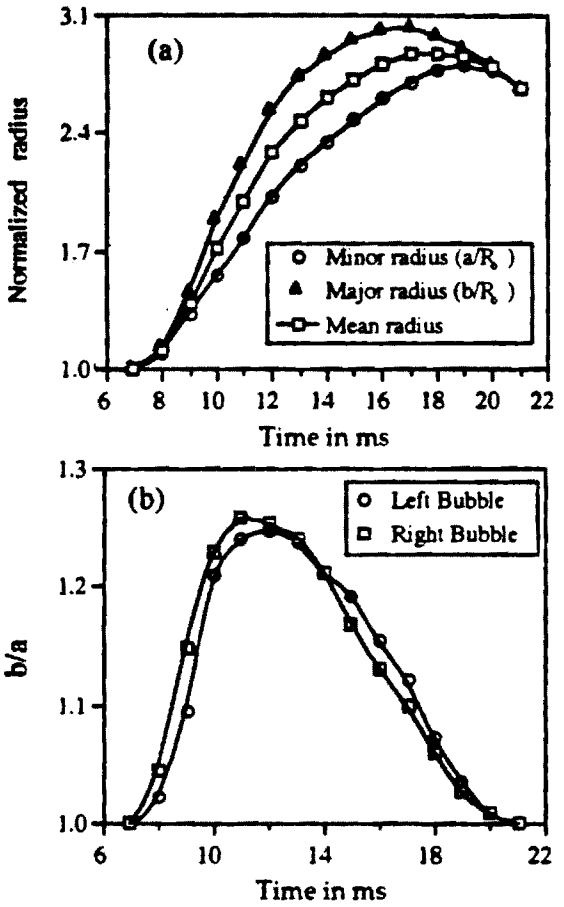

Fig. 4. (a) Different radii of the left bubble. (b) Ratio of major and minor radii.

The collapse is very violent (as recorded by two plug transducers) and the coalesced bubble quickly disintegrates into a cloud of bubbles. The bubble contour is traced and 360 bubble radii are obtained at equal azimuth locations. A mean radius is obtained from this data, which is used to normalize the radii data. These data are then Fourier analyzed and the results are shown in Fig. 5, which shows the power spectral density of the coalesced bubble's interface at three instants: just after it is formed and 1 and 5 ms after it collapses. Here c is the bubble circumference and λ is the wavelength. The coalesced bubble is therefore very unstable.

The pressure traces measured around the bubbles show that the bubble behavior is symmetrical. A pressure fluctuation of about 700 kPa exhibited by the plug transducers near bubble minimum demonstrates the severity of the collapse of the jets formed in the two bubbles onto each other. The pressure drops exponentially as one moves away from the bubble (Cole, 1948). A pressure drop of 70% (from 1000 kPa to 300 kPa) over a distance of 14 cm, and that of 80% (from 1000 kPa to 200 kPa) over a distance of 34 cm from the bubble center have been recorded by tank transducers.

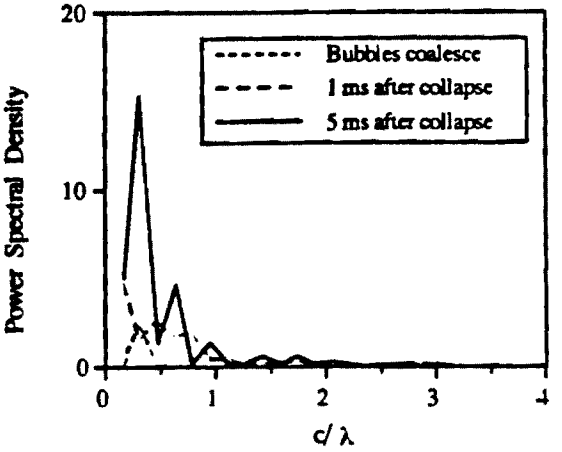

Fig. 5. Power spectral density of the bubble.

A single coalesced bubble does not form only in an in-phase oscillation. Another situation where the formation of a single coalesced bubble has been observed repeatedly and most surprisingly, is associated with a nonzero time delay and a very short inter-bubble distance. This case is shown in Fig. 6. The initial volume of the right glass globe is 125 ml and that of the left glass globe is 127 ml. They are almost touching each other such that the initial separation distance between them, d, is given by $d/R_o = 2.1$. Both of them are filled with stoichiometric mixture of Carbon Monoxide and Oxygen. The right globe explodes first (around frame no. 11) and tries to encompass the left globe as the bubble grows. The left globe explodes near frame no. 19 and the shock wave emitted by this bubble travels through the right bubble as is evident by its protruding pieces (frames 21,24). The right bubble, however, maintains its coherence and sphericity. It seems that the energy of the left bubble is substantially transferred to the right bubble. A force field is generated such that when the right bubble starts to collapse, the left bubble just merges into its predecessor to form a single coalesced bubble, which continues the oscillation cycle as a single explosion bubble. Since no jets are formed and the coalesced bubble is formed by merging the energies of two bubbles, it has more residual energy than that of the previous example and does not disintegrate into smaller bubbles so quickly. In fact, it is even more stable than a single explosion bubble in free field.

The effect of the shock wave generated during the formation of the right bulb is reflected by a 150 kPa peak in the left plug transducer pressure trace. On the other hand, the expanding right bubble acts as a screen for the propagation of the shock wave generated during the formation of the left bubble, and this is reflected by a tiny fluctuation of 10 kPa in the right plug transducer pressure trace. It is very interesting to note that the explosion pressure for the left bubble (200 kPa) is only about 20% of what it would have been in a free field case. Thus, an expanding bubble inhibits the formation of another explosion bubble in its close proximity by reducing its explosion pressure. This is the reason

why the left bubble does not have sufficient energy to expand to its maximum radius. But, it certainly aids its predecessor to form a coalesced bubble with a greater energy to collapse violently and this fact is captured by all the transducers and hydrophone in the form of elevated collapse peaks. This time, the right plug transducer lies inside the coalesced bubble as it collapses (see Fig. 6, frame no. 27). The collapse pressure recorded by this transducer is very high (2500 kPa). The pressure traces recorded by the right and left transducers are once again almost identical, indicating a symmetrical bubble behavior.

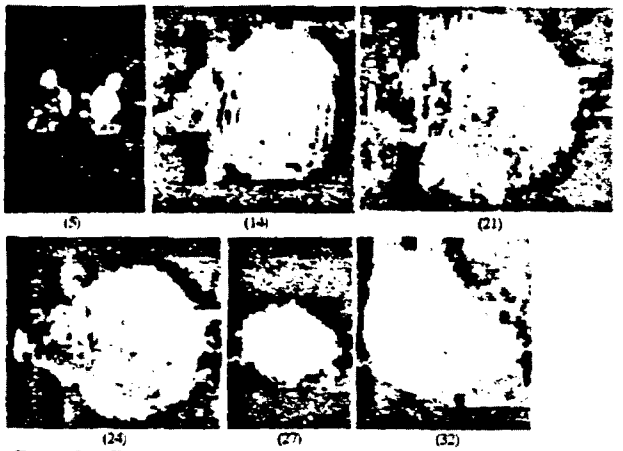

Fig. 6. Bubble formation by merging energies.

Similar dynamic behavior is exhibited by the interaction of bubbles formed by glass globes of initially different sizes. It is not possible, however, to obtain an in-phase oscillation because of a simple reason that the two bubbles have different time periods of oscillation. On the other hand, the bubble dynamics observed where the coalesced bubble is formed by merging the energies of two bubbles have been exhibited by the bubbles of different sizes where the small bubble has been gobbled up by its predecessor large bubble. This kind of bubble dynamics is not feasible for large inter-bubble distance.

When the inter-globe distance is sufficiently large, the bubbles start repelling each other for a nonzero time delay. The repulsion force increases with the delay between the explosions, up to the point when they are oscillating 180° out-of-phase. In such cases, the formation of a strong reentrant water jet in the successor bubble is observed with increasing magnitude. Figure 7 shows how this reentrant jet travels with time for a case of 180° out-of-phase oscillation. Here x denotes the location of the jet tip relative to the inertial frame (the tank) and x = 0 corresponds to the instant when the jet tip becomes visible for the first time. As the phase delay between two explosions increase beyond 180°, the repulsion force as well as the water jet velocity decrease in magnitude. If the phase delay between two explosions increase beyond 360° (i.e., if one bubble has already completed one oscillation cycle when the other bubble forms), the resulting interaction is very weak. In this case, though the predecessor bubble manages to create a depression in successor bubble at its maximum radius, neither a jet nor a repulsion force is formed.

The horizontal configuration is very important from a practical standpoint, as it can set a catastrophic bending vibration to a nearby rigid body if tuned properly. The research effort is being pursued in this direction. The vertical configuration is also equally important, as it can dramatically enhance the impact pressure of a single bubble when collapsed near a rigid body. If two bubbles are placed close to each other along an axis perpendicular to a nearby rigid body, and if these two bubbles are tuned to oscillate 180° out-of-phase with each other, a water jet will be formed and directed towards the rigid surface with a velocity which will be higher than that formed by the collapse of a single bubble under similar circumstances. This is also being studied.

The bubble dynamics in vertical configuration in the present study (in the absence of any nearby rigid body), however, does not show a remarkable difference from that of horizontal counterpart. This is because of the fact that only the orientation of the gravitational force changes between two configurations. In practical cases, the force field generated by the bubbles is much more stronger to be affected negligibly by the gravitational force.

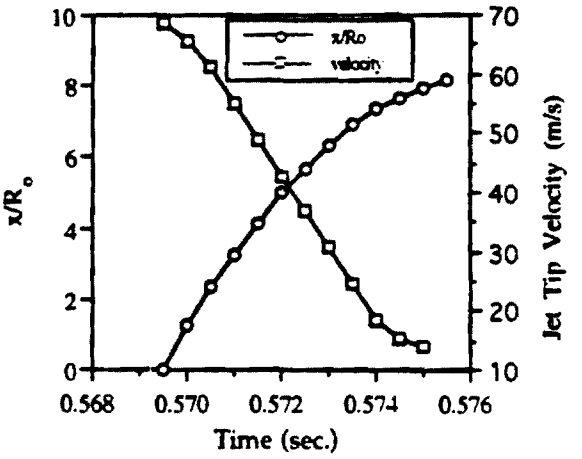

Fig. 7. Water jet tip location and velocity

Bubble(s)-Free Surface Interaction

Since it was shown earlier that two bubbles oscillating 180 ° out-of-phase are equivalent to a single bubble oscillating near a free surface, experiments were carried out to study the interaction of a free surface with explosion bubble(s). Figure 8 shows the transition of bubble migration velocity with water depth.

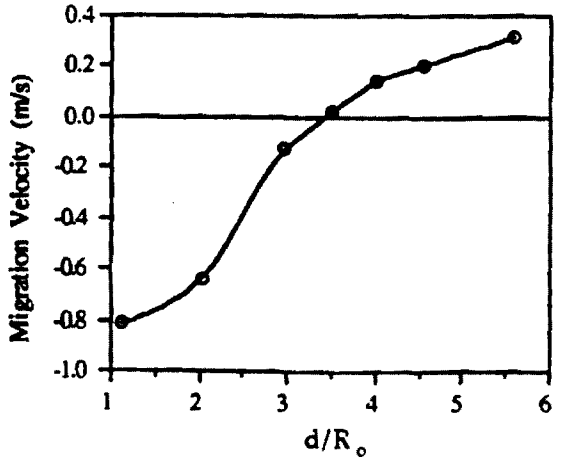

Fig. 8. Bubble migration velocity with water depth.

A simple sting mount was used to support a glass globe and the depth of water in the tank was decreased in a step of 2.54 cm. It was found that the bubble migration velocity smoothly changes its direction as well as its magnitude. The transition point determines the maximum inter-bubble distance *(2d)* for which two identical bubbles will start interacting while oscillating 180° out-of-phase with each other. It is found that $d \approx 3.4R_o$.

Both out-of-phase and in-phase oscillation of two explosion bubbles in a horizontal configuration near a free surface were also studied. The bubbles oscillating out-of-phase with each other repel each other and the effect of the free surface becomes apparent only after they have been repelled by each other. This once again indicates that the force field generated by the interaction between two bubbles is much stronger than that of a free surface and there have been instances where one of the bubbles actually migrates upward.

CONCLUSIONS

This paper discusses results obtained in an experimental investigation of the dynamical interaction of two underwater explosion bubbles in both horizontal and vertical configurations. The former configuration can excite a nearby submerged structure in bending vibration mode, while the latter can easily be tailored for the directionality and enhancement of the impact pressure resulting from the collapse of an underwater explosion bubble near a solid boundary. Depending on the delay between two explosions and inter-bubble distance, the bubbles may either attract each other to form a single coalesced bubble, or they may violently repel each other. A violent interaction between the bubbles leads to an increased instability of the bubbles. If a coalesced bubble is formed by merging the energies of two bubbles, the resulting bubble has more residual energy and is more stable for successive oscillations. An out-of-phase oscillation generates a reentrant water jet which pierces the bubble. Water free surface repels the bubble and the transition point of bubble migration velocity determines the maximum inter-bubble distance required for the initiation of interaction between two out-of-phase pulsating bubbles.

ACKNOWLEDGMENT

This work is supported by the Office of Naval Research under Grant No. N00014-91-J-1963 and monitored by Drs. Richard Miller and Judah Goldwasser.

REFERENCES

Birkhoff, G., and Zarantonello, E. H., 1957, "Jets, Wakes, and Cavities," Academic Press Inc, New York, pp. 241-243.

Bjerknes, V. F. J., 1906, "Fields of Force," Columbia University Press, New York.

Blake, J. R., and Gibson, D. C., 1981, "Growth and Collapse of a Vapor Cavity near a Free Surface," Journal of Fluid Mechanics, Vol. 111, pp. 123-140.

Chahine, G. L., 1977, "Interaction Between an Oscillating Bubble and a Free Surface," Journal of Fluids Engineering, Vol. 38, pp. 709-716.

Chahine, G. L., 1982, "Experimental and Asymptotic Study of Nonspherical Bubble Collapse," Applied Scientific Research, Vol. 38, pp. 187-197.

Chahine, G. L., and Liu, H. L., 1985, "A Singular Perturbation Theory of the Growth of a Bubble Cluster in a Superheated Liquid," Journal of Fluid Mechanics, Vol. 156, pp. 257-279.

Chahine, G. L., and Sirian, C. R., 1985, "Collapse of a Simulated Multibubble System," ASME, Cavitation and Multiphase Flow Forum, Albuquerque, New Mexico, pp. 78-81.

Chahine, G. L., 1991, "Dynamics of the Interaction of Non-Spherical Cavities," Mathematical approaches in Hydrodynamics, T. Miloh, ed., Society for Industrial Applications of Mathematics, Philadelphia, pp. 51-67.

Chahine, G. L., and Duraiswami, R., 1992, "Dynamical Interactions in a Multi-Bubble Cloud," Transactions of the ASME, Vol. 114, pp. 680-686.

Cole, R. H., 1948, "Underwater Explosions," Princeton University Press, Princeton.

Fujikawa, S., Takahira, H., and Akamatsu, T., 1985, "Underwater Explosion of Two Spherical or Nonspherical Bubbles and Their Interaction With Radiated Pressure Waves," Shock Waves and Shock Tubes, Proceedings of the Fifteenth International Symposium, Berkeley, CA, pp. 737-744.

Fujikawa, S., and Takahira, H., 1986, "A Theoretical Study on the Interaction between Two Spherical Bubbles and Radiated Pressure Waves in a Liquid," Acustica, Vol. 61, pp. 188-199.

Fujikawa, S., and Takahira, H., 1988, "Dynamics of Two Nonspherical Cavitation Bubbles in Liquids," Fluid Dynamics Research, Vol. 4, pp. 179-194.

Menon, S., and Lal, M. K., 1996, "On the Dynamics and Instability of Bubbles Formed During Underwater Explosions," Submitted to International Journal of Engineering Fluid Mechanics.

Moroika, M., 1974, "Theory of Natural Frequencies of Two Pulsating Bubbles in Infinite Liquid," Journal of Nuclear Science and Technology, Vol. 11, pp. 554.

Shima, A., 1971, "The Natural Frequencies of Two Spherical Bubbles Oscillating in Water," Journal of Basic Engineering, Vol. 93, pp. 426-432.

Shima, A., and Tomita, Y., 1988, "Impulsive Pressure Generation by Bubble/Pressure-Wave Interaction," AIAA Journal, Vol. 26, No. 4, pp. 434-437.

Smith, R. H., and Mesler, R. B., 1972, "A Photographic Study of the Effect of an Air Bubble on the Growth and Collapse of a Vapor Bubble near a Surface," Journal of Basic Engineering, pp. 933-942.

Van Wijngaarden, L., 1972, "On the Collective Collapse of a Large Number of Gas Bubbles in Water," Proceedings of the 11th International Congress of Applied Mechanics, Springer, Berlin, pp. 854-865.

Wilkerson, S. A., 1989, "Boundary Integral Technique for Explosion Bubble Collapse Analysis," Energy-Sources Technology Conference and Exhibition, 89-OCN-2, Houston, Texas, pp. 1-12.

Young, F. R., 1989, "Cavitation," McGraw-Hill Book Company (UK), The Alden Press, Oxford.